UNIVERSIDADE DE LISBOA

FACULDADE DE FARMÁCIA

Targeting human aquaporin function: physiological and chemical approaches

Doutoramento em Farmácia

(Especialidade em Bioquímica)

Andreia Filipa Bonecas Mósca

Orientador(es):

- Prof.ª Doutora Maria da Graça Tavares Rebelo de Soveral Rodrigues
- Prof.ª Doutora Angela Casini

Documento especialmente elaborado para a obtenção do grau de Doutor

2018

UNIVERSIDADE DE LISBOA

FACULDADE DE FARMÁCIA

Targeting human aquaporin function: physiological and chemical approaches

Doutoramento em Farmácia

(Especialidade em Bioquímica)

Andreia Filipa Bonecas Mósca

Orientador(es):

- Prof.ª Doutora Maria da Graça Tavares Rebelo de Soveral Rodrigues
- Prof.ª Doutora Angela Casini

Júri:
Presidente:

- Doutora Cecília Maria Pereira Rodrigues

Vogais:

- Doutora Alberta Paula Lobo Machado Gameiro dos Santos
- Doutor Hernâni Varanda Gerós
- Doutora Catarina Paula Guerra Geoffroy Prista
- Doutora Maria da Graça Tavares Rebelo de Soveral Rodrigues

Instituição Financiadora: Fundação para a Ciência e Tecnologia (FCT) (SFRH/BD/52384/2013)
Documento especialmente elaborado para a obtenção do grau de Doutor

2018

Andreia Filipa Bonecas Mósca foi bolseira de doutoramento no âmbito do Programa Doutoral "Medical Biochemistry and Biophysics Doctoral Programme (M2B-PhD)" da Faculdade de Farmácia da Universidade de Lisboa, financiado pela Fundação para a Ciência e Tecnologia do Ministério da Educação e Ciência, Bolsa FCT / SFRH / BD / 52384 / 2013.

De acordo com o disposto no artigo 24º do Regulamento de Estudos de Pós-Graduação da Universidade de Lisboa, Despacho nº 7024/2017, publicado no Diário da República – 2ª Série – nº 155 – 11 de Agosto de 2017, foram utilizados nesta dissertação resultados incluídos nos seguintes artigos:

[2015] Madeira A, **Mósca AF**, Moura TF, Soveral G. Aquaporin-5 is expressed in adipocytes with implications in adipose differentiation. IUBMB Life, 67(1): 54-60. DOI 10.1002/iub.1345

[2016] de Almeida A, Martins AP, **Mósca AF**, Soveral G, Casini A. Exploring the gating mechanisms of aquaporin-3: new clues for inhibitors design? Mol. Biosyst. 12(5): 1564-73. DOI 10.1039/c6mb00013d

[2016] Rodrigues C*, **Mósca AF***, Martins AP, Nobre T, Prista C, Antunes F, Cipak Gasparovic A, Soveral G. Rat aquaporin-5 is pH-gated induced by phosphorylation and is implicated in oxidative stress. Int J Mol Sci. (17). DOI 10.3390/ijms1712090
*equal contribution

[2017] de Almeida A*, **Mósca AF***, Wragg D, Wenzel M, Kavanagh P, Barone G, Leoni S, Soveral G, Casini A. The mechanism of aquaporin inhibition by gold compounds elucidated by biophysical and computational methods. Chem Commun (27): 3830-3833. DOI 10.1039/c7cc00318h
*equal contribution

[2018] Gotfryd K, **Mósca AF***, Missel JW*, Truelsen SF, Wang K, Spulber M, Krabbe S, Nielsen CH, Laforenza U, Soveral G, Pedersen PA, Gourdon P. Human adipose glycerol flux is regulated by a pH gate in AQP10.
(submitted for peer review)
*equal contribution

[2018] **Mósca AF***, de Almeida A*, Wragg D, Martins AP, Sabir F, Leoni S, Moura TF, Prista C, Casini A, Soveral G. Human aquaporin-7 behaves as a glycerol efflux channel at acidic pH.
(submitted for peer review)
*equal contribution

No cumprimento do disposto da referida deliberação, a autora esclarece serem da sua responsabilidade, exceto quando referido o contrário, a execução das experiências que permitiram a elaboração dos resultados apresentados, assim como da interpretação e discussão dos mesmos. Os resultados obtidos por outros autores foram incluídos para facilitar a compreensão dos trabalhos e estão assinalados nas respetivas figuras.

Contents

Abstract

Aquaporins (AQPs) are a group of small membrane proteins belonging to a highly conserved family of membrane proteins called MIPs (Major Intrinsic Proteins) that are responsible for the bidirectional transport of water (orthodox aquaporins) and also small uncharged solutes (aquaglyceroporins) across cell membranes, in response to osmotic or solute gradients.

Rapid water flux across membranes is crucial to maintain the water homeostasis in many epithelia and endothelia involved in fluid transport. In addition, due to the unique ability of aquaglyceroporins to transport glycerol in addition to water, they have important roles in glycerol metabolism and skin hydration in non-fluid transporting tissues such as skin, fat and liver. The thesis introduction (Chapter 1) presents an overview of aquaporins structure, their main biological functions and related pathologies, with special emphasis on the so far described mechanisms of regulation.

In the first part of this thesis (Chapter 2), we report the discovery of a new role for Aquaporin-5 (AQP5, an orthodox aquaporin) in adipocyte biology, where Aquaporin-7 (AQP7, an aquaglyceroporin) has been the mainly characterized protein in adipose tissue responsible for glycerol efflux.

A better understanding of aquaporin regulation and gating would allow manipulation of their activity facilitating the identification of new putative modulators. A cellular model optimized to assess the function of aquaporins and discriminate individually each isoform, instead of mammalian cells where more than one isoform is usually expressed, is a useful tool to study aquaporin regulation.

The second part of this thesis (Chapter 3) is dedicated to the functional characterization of different mammalian aquaporin isoforms (AQP3, AQP5, AQP7

and AQP10), using a yeast heterologous expression system devoided of endogenous aquaporins, a background where analysis is unlikely to be compromised by the co-expression of other aquaporin isoforms. Using the stopped-flow technique to evaluate the channel permeability for water and for glycerol, we were able to disclose gating mechanisms of aquaporin isoforms, being given special emphasis to the regulation by pH and phosphorylation.

In the third part of this thesis (Chapter 4), a screening of several small gold compounds as inhibitors for Aquaporin-3 (AQP3, an aquaglyceroporin) was performed aiming at identifying new modulators with potential therapeutic use.

Keywords: aquaporins, regulation, pH, heterologous expression, *Saccharomyces cerevisiae*

Resumo

A água possui um papel crucial para a vida devido às suas propriedades únicas. Todos os processos bioquímicos e fisiológicos de um organismo dependem da presença de água, sendo esta o componente fundamental na manutenção da homeostase celular. Nas células eucarióticas, a água encontra-se distribuída pelos vários compartimentos intracelulares separados entre si por membranas intracelulares e do meio extracelular pela membrana plasmática. Estas membranas de composição bilipídica são normalmente impermeáveis à maioria dos solutos polares e/ou carregados, cuja passagem é facilitada através de canais membranares específicos. No entanto estas membranas são bastante permeáveis à água, sendo então propostas três vias de transporte: por difusão simples, por transporte passivo associado ao transporte de iões e solutos e por canais específicos para a água.

Atualmente sabe-se que a maioria das células de um organismo possui proteínas específicas – as aquaporinas – que conferem à membrana uma permeabilidade à água de cerca de 5 a 10 vezes superior às membranas que não possuem estas proteínas.

Devido às suas características estruturais, as aquaporinas permitem um rápido transporte bidirecional de água, seletivo e regulado, em resposta a gradientes osmóticos, ao mesmo tempo que previnem a passagem de protões e iões através da membrana plasmática. Em mamíferos, são conhecidas até à data treze isoformas (AQP0-AQP12) que são classificadas em três grupos de acordo com a sua sequência primária, localização celular e seletividade em *1)* aquaporinas ortodoxas, primariamente seletivas à água; *2)* aquagliceroporinas, para além de água também transportam pequenos solutos neutros, como glicerol e ureia; e *3)* super-aquaporinas, que são encontradas em membranas intracelulares e possuem menor homologia.

No entanto, a lista de substâncias que são capazes de permear as diferentes aquaporinas tem aumentado ao longo do tempo. Recentemente, para além de água e glicerol, foi também descrito o transporte facilitado através de algumas isoformas de arsenito, amoníaco e peróxido de hidrogénio.

Devido à grande diversidade de tecidos onde são encontradas as aquaporinas, o seu papel de facilitar o transporte de água e/ou solutos através das membranas plasmáticas é importante em vários processos fisiológicos, tais como: secreção de fluido glandular, mecanismo de concentração urinária, excitabilidade neuronal, metabolismo dos lípidos, hidratação epidérmica e balanço de água no cérebro. A observação do fenótipo de ratinhos geneticamente modificados com *knock-out* de determinadas aquaporinas revelou funções fisiológicas muito importantes no aparecimento e desenvolvimento de várias patologias, como epilepsia, edema cerebral, glaucoma, cancro e obesidade.

No Capítulo 1 é apresentada uma introdução geral que visa proporcionar um conhecimento abrangente sobre as principais funções das aquaporinas humanas e patologias associadas, dando especial atenção aos diferentes mecanismos de regulação já conhecidos.

Na primeira parte dos resultados desta tese (Capítulo 2), através da construção de linhas celulares de pré-adipócitos de ratinho 3T3-L1 com diferentes níveis de expressão da Aquaporin-5 (cenário de ganho e perda de função) foi possível estabelecer um novo e determinante papel desta aquaporina na diferenciação dos adipócitos.

Na segunda parte dos resultados desta tese (Capítulo 3), pretendeu-se usar um sistema de expressão heteróloga em *Saccharomyces cerevisiae* (*S. cerevisiae*) para permitir avaliar de forma individual a função de cada aquaporina. A levedura *S. cerevisiae* é considerada um valioso sistema de expressão heteróloga para estudar inúmeras proteínas devido à elevada homologia funcional entre esta e os

eucariontes superiores, incluindo mamíferos. Pelo facto de existir uma grande biblioteca de estirpes disponíveis, ser de fácil manipulação genética, ser pouco dispendioso em comparação com as culturas de células animais e poderem ser testadas uma variedade de condições externas, este sistema oferece condições experimentais ótimas para estudar a especificidade e regulação das aquaporinas.

Após a expressão e confirmação da sua localização celular, procedeu-se à caracterização da função de cada isoforma, utilizando a técnica de interrupção brusca de fluxo, seguindo a variação de volume celular por fluorescência quando se introduz uma perturbação no meio extracelular. Os fluxos de água através da membrana celular causados por gradientes de pressão osmótica (de solutos impermeantes ou permeantes) provocam alterações transitórias de volume, até se atingir um novo volume final de equilíbrio osmótico. A velocidade com que as alterações de volume ocorrem e o tempo que a célula leva a re-estabelecer o seu novo equilíbrio osmótico dependem diretamente das características intrínsecas de transporte da membrana, em particular da quantidade de canais específicos para a água e para o soluto em questão. No Capítulo 3 foram estudadas quatro isoformas diferentes (AQP3, AQP5, AQP7 e AQP10) e os seus mecanismos de regulação por pH e fosforilação foram revelados pela primeira vez.

Vários esforços têm vindo a ser feitos com o intuito de desenvolver possíveis fármacos para tratamento das aquaporinopatias, mas até agora nenhum composto se revelou qualificado para estudos *in vivo*, quer pela sua fraca solubilidade quer pela sua baixa capacidade de inibição. Na terceira parte dos resultados desta tese (Capítulo 4), deu-se especial atenção à descoberta de novos compostos organometálicos, inibidores da função da Aquaporina-3, que poderão ser usados para benefício clínico na prevenção ou tratamento das várias patologias associadas.

Palavras-chave: aquaporinas, regulação, pH, expressão heteróloga, *Saccharomyces cerevisiae*

General aims and outline of this thesis

Being AQPs recognized as promising drug targets for several pathological conditions, detection and characterization of AQP function is critical to understand its regulatory mechanisms as well to identify efficient AQP modulators with potential for drug development.

In general terms, the work developed in this thesis aimed to deep our knowledge in AQPs physiology and mechanisms of regulation, by **(1)** functional characterization of AQPs (analysis of water/glycerol transport); **(2)** investigation of post-translational regulatory mechanisms that can affect AQPs' activity, such as pH and phosphorylation, and **(3)** screening of new chemical inhibitors and elucidation of its structure-activity relationship.

This thesis is organized in five chapters. In **Chapter 1**, a general introduction is presented with the state-of-art of the subject of this thesis. **Chapter 2** describes studies where the expression of endogenous AQP5 was detected in adipocytes, so far never reported. Using a gain / loss of function scenario, we found that AQP5 is important for cell differentiation, thus revealing a novel physiological role of AQP5 in adipose cells. This discovery brings new insights into AQP5 biological functions.

Chapter 3 is divided in four separate studies, where yeast cells were used to express and characterize mammalian AQPs. Mammalian cell lines frequently express more than one aquaporin isoform at the plasma membrane and, unless a specific isoform is silenced or overexpressed, its function is not easily discriminated. Using the yeast cell system, water/glycerol transport of particular mammalian AQP isoforms was evaluated, as well as their putative mechanisms of regulation. In the first part (**subchapter 3.1**), AQP5 ability to be short-term regulated either by pH and phosphorylation was investigated. Our data show that AQP5 can be gated by pH in a phosphorylation dependent manner, with higher

water permeability at physiological pH 7.4. In the second part (**subchapter 3.2**), pH regulation of rat and human AQP3 were compared and our data show that both isoforms are inactive at pH 5. In the third part (**subchapter 3.3**), pH regulation of human AQP7 was disclosed and discussed within its well-known physiological role in adipose tissue. In the fourth part (**subchapter 3.4**), pH regulation of AQP10, also abundantly expressed in human adipocytes, was investigated and the mechanism of pore gating was elucidated by structural studies.

In **Chapter 4**, divided in two complementary studies, human red blood cells (RBC) were used as a screening system for several series of small molecules as AQP3 inhibitors. In the first part (**subchapter 4.1**) the mechanism of aquaporin inhibition by a gold-compound is elucidated by biophysical and computational methods. In the second part (**subchapter 4.2**), two new series of gold compounds were tested in order to fine-tune specificity and potency.

Finally, in **Chapter 5**, the results obtained along this thesis are discussed and future considerations are presented.

List of Abbreviations

AQP(s)	Aquaporin(s)
AQP3	Aquaglyceroporin-3 or aquaporin-3
AQP5	Aquaporin-5
AQP7	Aquaglyceroporin-7 or aquaporin-7
AQP10	Aquaglyceroporin-10 or aquaporin-10
cAMP	Cyclic adenosine monophosphate
DFT	Density functional calculations
DMSO	Dimethyl sulphoxide
E_a	Activation energy
ER	Endoplasmic reticulum
FFA	Free fatty acid
MD	Molecular dynamics
PBS	Phosphate buffered saline
pdb	Protein Database
P_f	Osmotic Permeability Coefficient
P_{gly}	Glycerol Permeability Coefficient
PKA	Protein kinase A
r.t.	Room temperature
RBC	Human red blood cells
TG	Triglycerides
β	Cellular non-osmotic volume
Λ	Tonicity

CHAPTER 1

General Introduction

Movement of water through cells is a prerequisite for all life forms. In eukaryotic cells, water needs to flow into and out of the cell and between intracellular compartments through plasma membrane and intracellular membranes, respectively, to maintain homeostasis.

Aquaporins (AQPs) are a family of small integral membrane proteins found in almost every organism, from bacteria to humans, that act primarily as water channels conferring high water permeability to membranes. AQPs facilitate bi-directional water movement across cellular membranes in response to osmotic gradients, playing a crucial role in water homeostasis through transcellular and transepithelial pathways.

In the next sections, a comprehensive overview about AQP structure, function and regulation will be presented. Due to the variety of AQP related pathologies they are now considered to be drug targets and the importance of potential modulators will be also addressed.

1.1 Discovery of water channels – Historical perspective

The first studies of water transport began in the early 50s when the high water permeability of human red blood cells (RBC) was detected after imposing an osmotic pressure gradient [1]. Although no water channels were identified at this date, these studies suggested that specialized water channels should be present in the RBC membrane to account for the high water permeability measured.

The fundamental discovery and characterization of the abundant protein of the erythrocyte membrane CHIP28 (presently termed as Aquaporin-1 (AQP1)) by Peter Agre, who was acknowledged with a Nobel Prize in Chemistry in 2003, represented a paradigm shift in the understanding of membrane water transport [2]. Several studies have shown that AQP1 is a member of a conserved and widespread family of water and solute-permeable membrane proteins – Major Intrinsic Proteins (MIPs) - which have been demonstrated to be ubiquitous in all types of organisms [3].

1.2 Overview of aquaporins: structure and function

Three-dimensional structural studies of AQPs from different species revealed a homotetrameric assembly in the plasma membrane (Figure 1.2.1 A) [4,5,6,7] that is assumed to be preserved among all AQP family members. Each monomer, with an hourglass conformation, functions independently as a water channel (Figure 1.2.1 B). Figure 1.2.1 C illustrates the topology of the AQP monomer, which comprises six α-helical transmembrane domains (TM1-6) connected by three extracellular and two intracellular loops (Loop A-E), with a cytoplasmic N- and C-terminal [8].

The intracellular and extracellular entry of the pore is constituted by several carbonyl groups that offer hydrophilic interaction sites for water molecules. The transport specificity of AQPs is achieved by the presence of two highly conserved

regions within the pore channel: *1)* an aromatic/arginine selectivity filter (Ar/R SF) at the extracellular vestibule which forms the narrowest point along the channel pore, acting mainly as a size filter and *2)* a pair of Asn-Pro-Ala boxes considered to be the signature of the AQP family (NPA motifs), located in loop B and E, which reenter into the lipid bilayer from opposite sites at the centre of the channel, behaving as dipoles forcing water molecules to acquire a specific orientation [9,10]. The combination of both size and charge restriction sites endorses AQPs with unique properties that allow water molecules to pass through the channel while preventing the permeation of protons and ions [11], and differentiate AQPs from other channels and transporters.

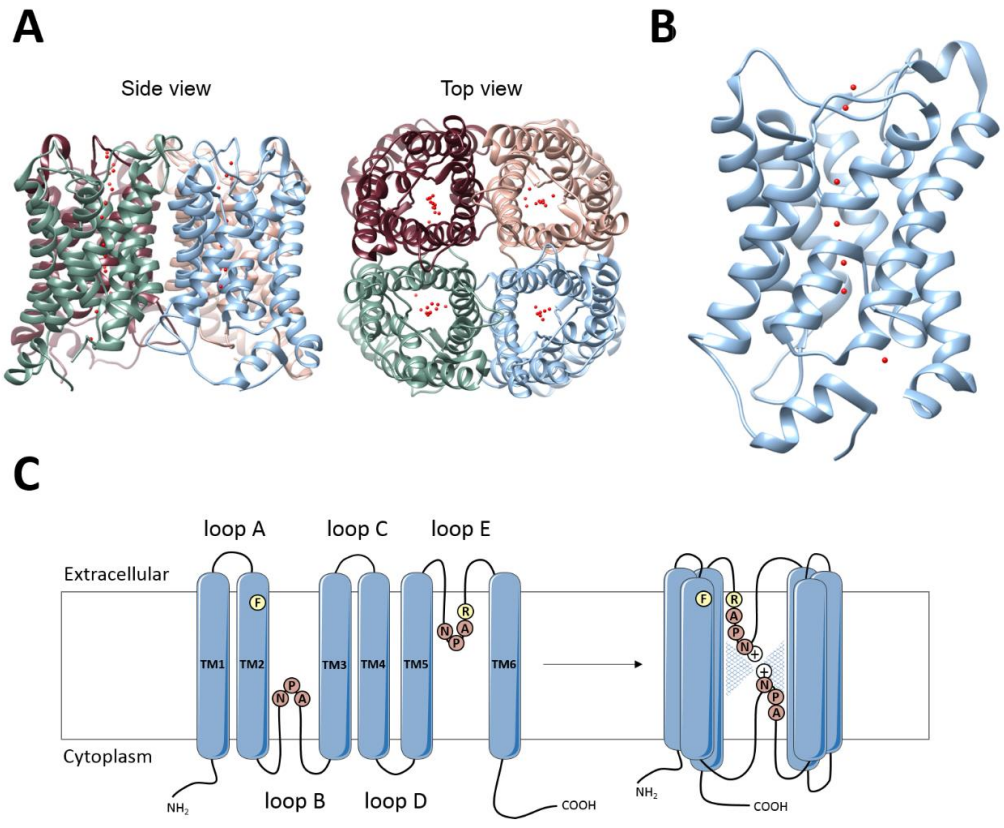

Figure 1.2.1 | General structure of aquaporins. Crystal structure of human AQP5 (PDB code 3D9S) in ribbon representation showing the **(A)** tetrameric organization viewed perpendicular to the plasma membrane (side view) and from the extracellular side (top view) and the **(B)** monomer hourglass conformation viewed parallel to the membrane.

Water molecules along the channel pore are shown as red spheres. **(C)** Schematic representation of AQP topology with six transmembrane α-helices (TM1-6), five connecting loops (loop A-E), ar/R selectivity filter and NPA motifs.

Despite the conserved molecular structure, it has been demonstrated that some members of AQP family have different channel selectivity which are directly related with structural differences in the ar/R region. For some isoforms, the diameter of ar/R region is slightly larger and more hydrophobic and these are able to transport larger molecules such as glycerol and urea [12].

In humans, 13 AQPs isoforms (AQP0-12) are presently known which have been divided in three main subgroups on the basis of their primary sequence, localization and substrate selectivity: *1)* orthodox AQPs (AQP0, AQP1, AQP2, AQP4, AQP5, AQP6 and AQP8) that are primarily selective for water permeation; *2)* aquaglyceroporins (AQP3, AQP7, AQP9 and AQP10) that also facilitate the movement of small neutral solutes such as glycerol and urea; and *3)* superaquaporins (AQP11 and AQP12), that are found in intracellular membranes, showing unusual NPA boxes and lower sequence homology [13] as its function is still not clear; while AQP11 water and glycerol permeation was detected [14,15], function of AQP12 remains to be clarified.

Interestingly a few aquaporins do not fit in only one sole category; for example, AQP6 and AQP8 are both classified as orthodox aquaporins, even though AQP6 is an intracellular isoform found in vesicles and AQP8 is also permeated by urea, ammonia and hydrogen peroxide [16,17,18]. AQP9 is the isoform with the most wide-ranging selectivity, facilitating the passage of monomethylselenic acid, selenite, lactate, ionic arsenic species and neutral solutes such as urea, carbamides, polyols, purines and pyrimidines [19,20]. The presence of AQP9 in highly metabolically active tissues [21] that accumulate several metabolites may provide

an exit pathway for their elimination. On the other hand, when compared to other AQP members, AQP0 has a limited water permeability. To compensate its poor water channel function, a secondary function has been suggested for AQP0 as a cell-to-cell adhesion protein, forming membrane junctions [22].

Also interestingly is the fact that the central pore formed by the homotetrameric structure has been recently described to be permeated by gases and cations [23]. Particularly, it has been proposed that AQP1 is the major pathway for CO_2 permeation in human red blood cells [24] and can also permeate cations, independently from the aqueous pore in individual monomers [25,26,27,28]. In general terms, emerging evidences show that AQPs are not simply water channels but can act as multifunctional channels [29].

1.3 Aquaporin physiological roles and related pathologies

Much of our understanding of AQPs function in mammalian physiology has come from phenotype analysis of mice lacking one of the AQP isoforms. These studies have confirmed the anticipated involvement of AQPs in the mechanism of urine concentration (AQP2, Figure 1.3.1 A), glandular fluid secretion (AQP5, Figure 1.3.1 B) [30] and cell migration (AQP1, Figure 1.3.1 C) [31,32]. On the other hand, the aquaglyceroporins subgroup gave rise to surprising roles in regulating glycerol content in epidermis preventing dehydration (AQP3, Figure 1.3.1 D) [33], adipocyte metabolism and obesity (AQP7, Figure 1.3.1 F) [34] and cell proliferation promoting carcinogenesis (AQP3, Figure 1.3.1 E) [35].

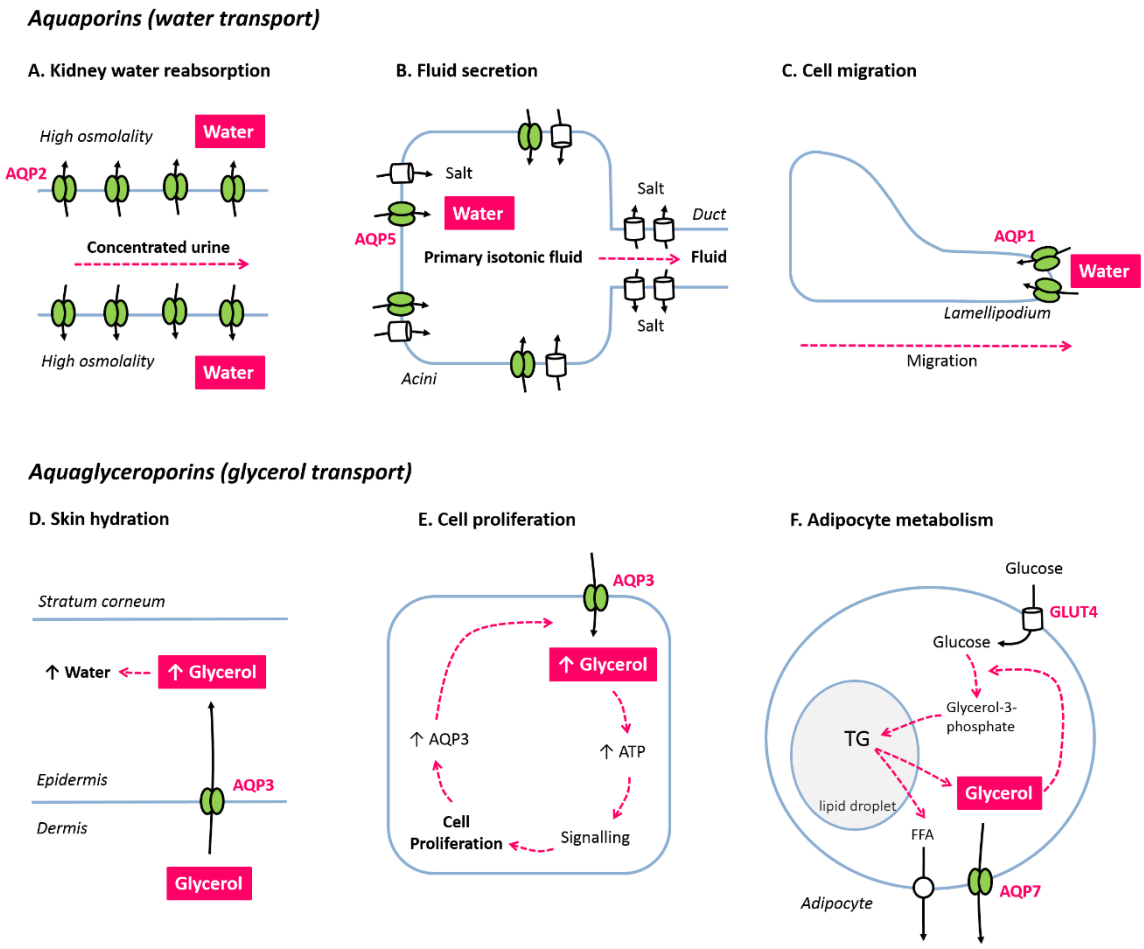

Figure 1.3.1 | Main physiological roles of aquaporins. Water-selective aquaporins are involved in **(A)** water reabsorption for urine concentration in kidney tubules; **(B)** fluid secretion in epithelial cells; and **(C)** cell migration. Glycerol transport through aquaglyceroporins is crucial for **(D)** skin hydration by maintaining high glycerol levels in epidermis which retains water; **(E)** cell proliferation by high ATP generation; and **(F)** adipocyte metabolism by facilitating efflux of glycerol from triglycerides (TG) hydrolysis. Adapted from [36].

Other studies led to the discovery of unexpected roles for AQPs in brain water balance and neural function (AQP4) [37], ocular function (AQP0) [38], macrophage immune function (AQP3) [39], as reviewed in [36]. Mutations and/or dysfunction of AQPs have been associated with several human pathologies, such as congenital

cataracts (AQP0) [38], palmoplantar keratoderma (AQP5) [40] and nephrogenic diabetes insipidus (AQP2) [41].

Overexpression of several AQPs isoforms has been reported in many types of tumor cells and associated with tumor aggressiveness and clinical prognosis [42,43]. It is proposed that AQP-mediated water fluxes may facilitate changes in cell volume and shape that are crucial for cell migration, and are involved in cell invasion, metastasis and angiogenesis [31,44]. Recently, AQP5 gained attention due its potential implication in carcinogenesis in different organs and systems [45]. AQP5 was found overexpressed in cancer cells and tumor tissues, strongly suggesting that it may be implicated in tumor formation by contributing to cell differentiation and migration. In fact, AQP5 downregulation in hepatocellular carcinoma inhibited cell invasion and tumor metastasis which may result from impaired water uptake by tumor cells [46]. Implantation of tumor cells in AQP1-null mice resulted in reduced tumor vascularity and subsequent impairment of tumor growth [31], and AQP3-null mice were remarkably resistant to the development of skin tumors [35].

However, in human hepatocellular carcinoma, AQP9 mRNA and protein levels were significantly lower [47]. Interestingly, overexpression of AQP9 in a human hepatoma cell line inhibited cellular proliferation through cell cycle arrest and apoptosis, and also reduced tumor growth in mice [47]. In general, the pathological importance of AQPs and the mechanisms that are behind carcinogenesis and other diseases remain poorly understood [48].

In addition, it is now well established that reactive oxygen species (ROS), particularly H_2O_2, participate in cell signaling transduction pathways affecting cellular growth and proliferation mechanisms involved in cancer development [49,50]. Recently, permeation of H_2O_2 by some AQPs revealed that these channels could influence regulatory complex signaling pathways involved in pathological

states. In mammalian cells, AQP3, AQP8, and AQP9 were shown to mediate H_2O_2 membrane transport [51,52,53], which may be used for intracellular signaling in cancer cells [54].

1.4 Regulation of mammalian aquaporins

As many other channels and transporters, there are emergent evidences that AQPs are subject to a very tight regulation in different cells and organs, either by transcriptional/translational mechanisms, protein trafficking, or by channel short-term regulation also known as gating. The latter is often achieved by mechanisms directly affecting the protein channel conformation after its insertion in the plasma membrane, when a rapid regulation of water permeability is required.

Furthermore, sequence alignment of aquaporins demonstrates that C-terminal is the most diverse region of these proteins and is often crucial to achieve channel regulation. In the particular case of AQPs, these domains are thought to regulate membrane targeting, interaction with other proteins and aquaporin function in a tissue-specific manner.

1.4.1 Membrane trafficking

The classical examples of this regulatory mechanism are the redistribution of AQP2 in kidney-collecting ducts and AQP7 in adipocytes, both in response to a hormonal stimuli. Trafficking of AQP5 is also regulated by the neurotransmitter acetylcholine.

1.4.1.1 Aquaporin-2

Aquaporin-2 (AQP2) is one of the most characterized AQP isoforms which plays the important role of water reabsorption and urine concentration in kidney-collecting ducts to maintain the overall body water homeostasis. Mutations and insufficient membrane abundance of AQP2 results in nephrogenic diabetes insipidus in humans [41,55]. Thus, insertion at the plasma membrane and retrieval of AQP2 are important processes that need to be precisely controlled (Figure 1.4.1). Briefly, AQP2 is stored intracellularly in vesicles and upon anti-diuretic hormone arginine-vasopressin (AVP) secretion, a cAMP signaling cascade is initiated which results in human AQP2 phosphorylation by PKA [56]. Phosphorylation of S256 appears to be required for the fusion of AQP2-containing vesicles with the apical membrane [57].

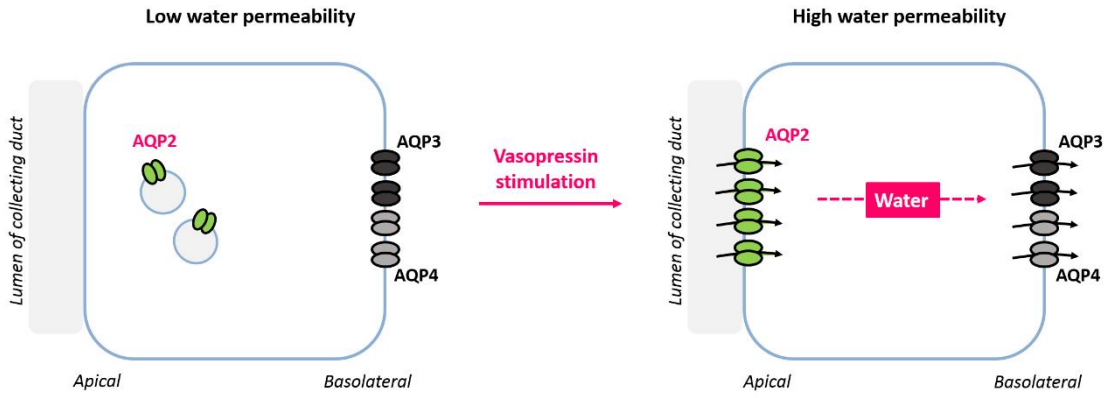

Figure 1.4.1 | Schematic representation of transcellular water transport in kidney collecting ducts through AQPs. AQP2 is stored in intracellular vesicles and upon vasopressin stimulation its trafficking to the apical plasma membrane is triggered. With AQP2 at the apical membrane, water is reabsorbed from the lumen of collecting duct and exits through the basolateral membrane via AQP3/AQP4.

When AVP levels decrease, internalization of AQP2 by endocytosis is triggered to restore the basal water permeability of the apical membrane. AQP2 in the cell

surface is short-chain-ubiquitinated on a single lysine residue (K270) enhancing its endocytosis and targeting to multivesicular bodies (MVB) [58]. Once in MVB, AQP2 can be subjected to 1) lysosomal degradation; 2) the next AVP-induced insertion cycle into apical membrane, after being deubiquitinated or 3) release as exosomes from renal cells into the urine [56].

Strikingly, AQP2 is also highly expressed in rat vas deferens where it is constitutively present on the apical membrane of epithelial cells and is not regulated by AVP [59]. This is a clear example that AQP targeting signals can be interpreted differently depending on the cell type or tissue.

1.4.1.2 Aquaporin-5

Aquaporin-5 (AQP5) is responsible for the majority of water secretion in exocrine glands such as lacrimal, salivary and sweat glands [60,61]. Abnormalities in AQP5 trafficking toward the apical membrane of salivary and lacrimal acinar cells are supposed to play a crucial role in development of Sjögren's Syndrome (SS) [62]. Patients suffering from SS experience severe mucous dryness and have a higher risk of developing a B-cell (non-Hodgkin's) lymphoma [62].

Normal saliva secretion by acinar cells is triggered by acetylcholine stimulation of M3 muscarinic receptors that leads to an increase in cytosolic [Ca^{2+}] and Cl^- and K^+ channels opening. The efflux of Cl^- and K^+ ions create an osmotic gradient that results in cell shrinkage mediated by AQP5. AQP5 trafficking is induced from intracellular vesicles to apical membrane upon neurotransmitter stimulation to increase water permeability in acinar cells [63,64,65], similarly to AQP2 upon AVP stimulation. In the case of AQP5, a PKA consensus site is found in C-terminal region and some studies describe a phosphorylation event; however, is still controversial if it is crucial for membrane trafficking.

1.4.1.3 Aquaporin-7

In feeding conditions, adipocytes accumulate triacylglycerols (TAGs) in lipid droplets while, during fasting, TAGs are hydrolyzed into free fatty acids (FFA) and glycerol that are release into the bloodstream. AQP7 is highly expressed in adipocytes plasma membranes being crucial for glycerol efflux into the blood stream, which will then be taken up by liver AQP9 for gluconeogenesis [66].

Balance between formation (lipogenesis) and breakdown (lipolysis) of TAGs in adipocytes are hallmarks of body fat homeostasis [67]. As well, glycerol and aquaglyceroporin-induced glycerol fluxes are likely central elements of fat accumulation in the pathophysiology of obesity [34,68], since mice AQP7 knockout accumulate glycerol and TAGs, and develop enlarged adipocytes and obesity with age.

Human aquaglyceroporin-7 (AQP7) is controlled by cathecolamine/insulin levels [69]. Briefly, during lipogenesis, pancreatic β-cells secrete insulin in response to increased glucose blood levels. Insulin stimulates glucose transporter 4 (GLUT4) trafficking to the adipocyte plasma membrane, promoting uptake of glucose to be converted into glycerol-3-phosphate and esterification into TAGs (Figure 1.4.2). Conversely, during fasting or exercise, lipolysis is stimulated by catecholamines promoting TAGs hydrolysis into free fatty acids and glycerol that are released into the bloodstream to provide energy in other tissues (Figure 1.4.2). During the fed state AQP7 is found intracellularly, regulated by insulin [70], whereas it is trafficked to the plasma membrane in response to a lipolytic stimuli by catecholamines [71].

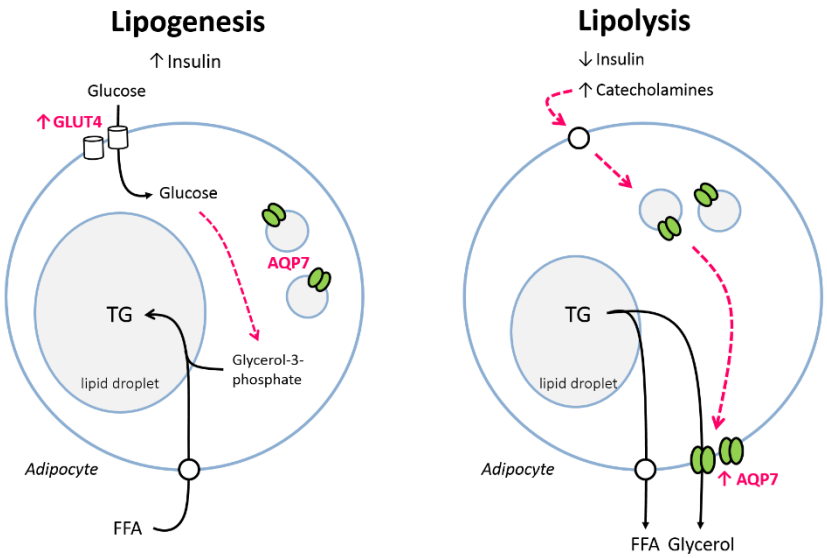

Figure 1.4.2 | AQP7 trafficking and its contribution for glycerol metabolism in adipose tissue. In lipogenesis, AQP7 is found intracellularly. During lipolysis, triglycerides (TG) are hydrolyzed in free fatty acids (FFA) and glycerol. Efflux of glycerol is facilitated by AQP7 which is trafficked to the plasma membrane in response to an increase in catecholamines and a decrease in insulin levels.

1.4.2 Mechanisms of aquaporin channel gating

AQPs can be subjected to regulation via different mechanisms. For example, some orthodox aquaporins are regulated by posttranslational modifications, as phosphorylation [72,73,74,75], as well as gated by sudden osmotic changes and membrane surface tension [72,76,77,78], divalent cations [79,80] and pH [81,82]. The orthodox water channels AQP0 (expressed in the lens) and AQP6 (expressed in the intercalated cells of the kidney collecting ducts) are gated by pH and appear to have low permeability at physiological pH, increasing below pH 7 and with a maximum of permeability at about pH 6.5 [18,79].

As far as aquaglyceroporins are concerned, information about gating mechanisms is only available for AQP3, which can be regulated by both pH and divalent cations [83,84,85]. Interestingly, at variance with AQP0 and AQP6, AQP3 shows an

overall maximum of permeability for water and glycerol above pH 6.5, decreasing with lower pH, until complete pore closure at pH 5 [83,85]. As AQP0 and AQP6 are both orthodox aquaporins and AQP3 is permeated by glycerol, these differences may be correlated with protein function in different cells and organs.

Remarkably, more than one regulatory mechanism is found in the same isoform pointing to a complex level of regulation. For example, water channel permeability of AQP0 is gated by either low pH, phosphorylation at C-terminal residues and/or Ca^{2+} concentration [79]. In vasopressin-regulated water reabsorption through AQP2 in the kidney, phosphorylation of AQP2 S256 that appears to be crucial for its apical membrane trafficking is also responsible for an increase channel itself water permeability [86].

Interestingly, AQP1 can function as a cation channel when gated by cGMP [25,27,28,87]. The reversible cGMP-induced activation that requires the direct binding of the secondary messenger cGMP is thought to occur at C-terminal since truncation of AQP1 at position 237 abolished the cation permeation without affecting water permeability [27]. However, it appears that the presence of cGMP is not sufficient since only a small fraction of AQP1 channels in the plasma membrane, that are constitutively open for water permeation, are active for cation conductance [27]. Phosphorylation of a tyrosine residue in C-terminal (Y253) is required for AQP1 ion function to be available for activation [25].

1.4.3 Interaction with regulatory proteins

Several protein interaction partners have been identified for mammalian AQPs in the last years [88]. Some regulatory proteins including carbonic anhydrase II (CAII) [89] and calmodulin (CaM) [79] directly affect AQP channel permeability, whereas others often control membrane trafficking and protein complex assembly, such as

SPA-1 [90], prolactin inducible protein (PIP) [91], perilipin-1 (PLIN1) [92] and Na+/H+ Exchange Regulatory Factor-1 (NHERF1) [93].

AQP0 water permeability is inhibited by an allosteric mechanism in response to increased Ca^{2+} concentration, which promote the binding of calmodulin (CaM) [79,94], whereas renal carbonic anhydrase II (CAII) is known as to interact physically and functionally with AQP1 C-terminal enhancing its water permeability, crucial for urine concentration in thin descending limp of the loop of Henle [89]. CAII-deficient mice displayed a lower ability to concentrate urine due to the reduced water flux through AQP1 [89].

Both AQP2 and AQP9 possess PDZ-binding domains at the C-terminal. PDZ proteins are involved in targeting, anchoring and stabilizing membrane proteins. SPA-1, a PDZ protein, directly bounds to AQP2 in kidney papilla and regulates its trafficking to apical membrane [90]. The PDZ binding motif of AQP9 binds NHERF1 [93], which is a cytoplasmic scaffolding protein that facilitates the assembling of multiprotein complexes at the plasma membrane. Also CFTR (Cystic Fibrosis Transmembrane Conductance Regulator, a cAMP-activated Cl^- channel) co-immunoprecipitated with AQP9 in rat epididymis and Sertoli cells [93,95]. It is thought that cAMP-activated CFTR is required for normal AQP9 permeability [96] probably via NHERF1 complex formation and a disruption of this protein complex might contribute to male infertility observed in cystic fibrosis [93]. This interaction is further supported by studies in human preeclamptic placentas where a decrease in CFTR protein expression with an AQP9 apparent lack of functionality for water and mannitol permeability is found [97,98]. It seems that decreases or defects in CFTR lead to defective regulation of AQP9 permeability.

Some regulatory proteins are important for AQP trafficking. As formerly described, AQP7 trafficking in adipocytes is controlled by hormone stimulation. During feeding state, it is suggested that AQP7 is kept intracellularly by a physical

interaction with PLIN1 while, during stimulated lipolysis, a PKA-mediated phosphorylation prevents the interaction, allowing AQP7 translocation to the plasma membrane for glycerol efflux [92]. Another example is the prolactin-inducible protein (PIP) that was found to interact with murine AQP5 C-terminal in lacrimal glands promoting the localization of the water channel in apical membrane [91].

In other cases, AQPs can also determine the function of other proteins. An example is the functional interaction between AQP5 and the transient receptor potential cation channel (TRPV4). In fluid secretion of salivary glands, AQP5 is crucial for the initial rate of cell swelling but also for the subsequent cell volume recovery - regulatory volume decrease (RVD) [60]. Both channels are required for the regulatory response but deletion of AQP5 N-terminal showed that a physical interaction is required for TRPV4 activation [99].

1.5 Aquaporins as drug targets

Numerous roles of AQPs in physiology and pathological conditions make these proteins essential for health, suggesting that AQPs can be considered as potential targets for drug development. Modulators of AQPs are expected to be of broad interest for diagnostic and therapeutic approaches, as well as a tool to investigate AQP molecular features and mechanisms of gating.

The effect of sulfhydryl-reactive compounds such as $HgCl_2$ on water permeability inhibition is well described in the literature [2,100] and these compounds are considered benchmark inhibitors of orthodox AQPs [2,100] and aquaglyceroporins [101,102]. Despite mercurial compounds have been typically used to block AQP activity, they are extremely toxic and nonspecific due to its high affinity towards cysteine and methionine residues, and thus not suitable for *in vivo* experiments and

therapeutic application.

In the past years, several chemical compounds such as acetazolamide [103,104], tetraethylammonium [105,106], inorganic salts [107], aromatic sulfonamides and dihydrobenzofurans [108,109] were reported as inhibitors of AQPs permeability. The inhibitory effect of other transition compounds, that are also able to interact with sulfhydryl groups such silver (as silver nitrate and silver-sulfadiazine) [110] and copper [84] were reported.

Recently, our group selected some metallodrugs well-known by their anticancer, antimetastatic, antirheumatic and antibacterial properties to evaluate their ability to inhibit AQP3 glycerol transport, using human red blood cells (RBC) as a screening model [101]. Only the water-soluble Au(III) compound [Au(phen)Cl2]Cl (phen = 1,10-phenanthroline) (Auphen) showed to be effective by reducing AQP3 glycerol permeability in 90% and highly selective since it poorly affected AQP1-mediated water permeability [101]. Auphen selectivity towards AQP3 can be explained by the favorable interactions that can occur between the hydrophobic phenanthroline ligand and the hydrophobic AQP3 pore entrance region, in contrast to the highly hydrophilic region of AQP1 [101].

1.6 References

[1] V.W. Sidel, A.K. Solomon, Entrance of water into human red cells under an osmotic pressure gradient, J Gen Physiol 41 (1957) 243-257.

[2] G.M. Preston, T.P. Carroll, W.B. Guggino, P. Agre, Appearance of water channels in Xenopus oocytes expressing red cell CHIP28 protein, Science 256 (1992) 385-387.

[3] G. Soveral, A. Casini, S. Nielsen, Aquaporins in health and disease: new molecular targets for drug discovery, CRC Press

Taylor & Francis Group, 2015.

[4] D. Fu, A. Libson, L.J. Miercke, C. Weitzman, P. Nollert, J. Krucinski, R.M. Stroud, Structure of a glycerol-conducting channel and the basis for its selectivity, Science 290 (2000) 481-486.

[5] T. Gonen, P. Sliz, J. Kistler, Y. Cheng, T. Walz, Aquaporin-0 membrane junctions reveal the structure of a closed water pore, Nature 429 (2004) 193-197.
[6] W.E. Harries, D. Akhavan, L.J. Miercke, S. Khademi, R.M. Stroud, The channel architecture of aquaporin 0 at a 2.2-A resolution, Proc Natl Acad Sci U S A 101 (2004) 14045-14050.
[7] D. Ruiz Carrillo, J. To Yiu Ying, D. Darwis, C.H. Soon, T. Cornvik, J. Torres, J. Lescar, Crystallization and preliminary crystallographic analysis of human aquaporin 1 at a resolution of 3.28 A, Acta Crystallogr F Struct Biol Commun 70 (2014) 1657-1663.
[8] G.M. Preston, J.S. Jung, W.B. Guggino, P. Agre, Membrane topology of aquaporin CHIP. Analysis of functional epitope-scanning mutants by vectorial proteolysis, J Biol Chem 269 (1994) 1668-1673.
[9] K. Murata, K. Mitsuoka, T. Hirai, T. Walz, P. Agre, J.B. Heymann, A. Engel, Y. Fujiyoshi, Structural determinants of water permeation through aquaporin-1, Nature 407 (2000) 599-605.
[10] H. Sui, B.G. Han, J.K. Lee, P. Walian, B.K. Jap, Structural basis of water-specific transport through the AQP1 water channel, Nature 414 (2001) 872-878.
[11] B.L. de Groot, T. Frigato, V. Helms, H. Grubmuller, The mechanism of proton exclusion in the aquaporin-1 water channel, J Mol Biol 333 (2003) 279-293.
[12] E. Beitz, D. Becker, J. von Bulow, C. Conrad, N. Fricke, A. Geadkaew, D. Krenc, J. Song, D. Wree, B. Wu, In vitro analysis and modification of aquaporin pore selectivity, Handb Exp Pharmacol (2009) 77-92.
[13] G. Benga, On the definition, nomenclature and classification of water channel proteins (aquaporins and relatives), Molecular Aspects of Medicine 33 (2012) 514-517.
[14] K. Yakata, K. Tani, Y. Fujiyoshi, Water permeability and characterization of aquaporin-11, J Struct Biol 174 (2011) 315-320.
[15] A. Madeira, S. Fernandez-Veledo, M. Camps, A. Zorzano, T.F. Moura, V. Ceperuelo-Mallafre, J. Vendrell, G. Soveral, Human aquaporin-11 is a water and glycerol channel and localizes in the vicinity of lipid droplets in human adipocytes, Obesity (Silver Spring) 22 (2014) 2010-2017.
[16] A. Almasalmeh, D. Krenc, B. Wu, E. Beitz, Structural determinants of the hydrogen peroxide permeability of aquaporins., The FEBS journal 281 (2014) 647-656.
[17] L.R. Soria, E. Fanelli, N. Altamura, M. Svelto, R.A. Marinelli, G. Calamita, Aquaporin-8-facilitated mitochondrial ammonia transport, Biochem Biophys Res Commun 393 (2010) 217-221.
[18] M. Yasui, A. Hazama, T.-H. Kwon, S. Nielsen, W.B. Guggino, P. Agre, Rapid gating and anion permeability of an intracellular aquaporin, Nature 402 (1999) 184-187.
[19] X. Geng, J. McDermott, J. Lundgren, L. Liu, K.J. Tsai, J. Shen, Z. Liu, Role of AQP9 in transport of monomethyselenic acid and selenite, Biometals (2017).
[20] H. Tsukaguchi, C. Shayakul, U.V. Berger, B. Mackenzie, S. Devidas, W.B. Guggino, A.N. van Hoek, M.A. Hediger, Molecular characterization of a broad selectivity neutral solute channel, J Biol Chem 273 (1998) 24737-24743.
[21] M. Elkjaer, Z. Vajda, L.N. Nejsum, T. Kwon, U.B. Jensen, M. Amiry-Moghaddam, J. Frokiaer, S. Nielsen, Immunolocalization of AQP9 in liver, epididymis, testis, spleen, and brain, Biochem Biophys Res Commun 276 (2000) 1118-1128.

[22] G.A. Zampighi, S. Eskandari, J.E. Hall, L. Zampighi, M. Kreman, Micro-domains of AQP0 in lens equatorial fibers, Exp Eye Res 75 (2002) 505-519.
[23] A.J. Yool, A.M. Weinstein, New roles for old holes: ion channel function in aquaporin-1, News Physiol Sci 17 (2002) 68-72.
[24] V. Endeward, R. Musa-Aziz, G.J. Cooper, L.M. Chen, M.F. Pelletier, L.V. Virkki, C.T. Supuran, L.S. King, W.F. Boron, G. Gros, Evidence that aquaporin 1 is a major pathway for CO2 transport across the human erythrocyte membrane, FASEB J 20 (2006) 1974-1981.
[25] E.M. Campbell, D.N. Birdsell, A.J. Yool, The activity of human aquaporin 1 as a cGMP-gated cation channel is regulated by tyrosine phosphorylation in the carboxyl-terminal domain, Mol Pharmacol 81 (2012) 97-105.
[26] M. Kourghi, S. Nourmohammadi, J.V. Pei, J. Qiu, S. McGaughey, S.D. Tyerman, C.S. Byrt, A.J. Yool, Divalent Cations Regulate the Ion Conductance Properties of Diverse Classes of Aquaporins, Int J Mol Sci 18 (2017).
[27] S.M. Saparov, D. Kozono, U. Rothe, P. Agre, P. Pohl, Water and ion permeation of aquaporin-1 in planar lipid bilayers. Major differences in structural determinants and stoichiometry, J Biol Chem 276 (2001) 31515-31520.
[28] T.L. Anthony, H.L. Brooks, D. Boassa, S. Leonov, G.M. Yanochko, J.W. Regan, A.J. Yool, Cloned human aquaporin-1 is a cyclic GMP-gated ion channel, Mol Pharmacol 57 (2000) 576-588.
[29] D. Gomes, A. Agasse, P. Thiebaud, S. Delrot, H. Geros, F. Chaumont, Aquaporins are multifunctional water and solute transporters highly divergent in living organisms, Biochim Biophys Acta 1788 (2009) 1213-1228.
[30] T. Matsuzaki, T. Suzuki, H. Koyama, S. Tanaka, K. Takata, Aquaporin-5 (AQP5), a water channel protein, in the rat salivary and lacrimal glands: immunolocalization and effect of secretory stimulation, Cell Tissue Res 295 (1999) 513-521.
[31] S. Saadoun, M.C. Papadopoulos, M. Hara-Chikuma, A.S. Verkman, Impairment of angiogenesis and cell migration by targeted aquaporin-1 gene disruption, Nature 434 (2005) 786-792.
[32] A.S. Verkman, M. Hara-Chikuma, M.C. Papadopoulos, Aquaporins--new players in cancer biology, J Mol Med (Berl) 86 (2008) 523-529.
[33] T. Ma, M. Hara, R. Sougrat, J.M. Verbavatz, A.S. Verkman, Impaired stratum corneum hydration in mice lacking epidermal water channel aquaporin-3, J Biol Chem 277 (2002) 17147-17153.
[34] T. Hibuse, N. Maeda, T. Funahashi, K. Yamamoto, A. Nagasawa, W. Mizunoya, K. Kishida, K. Inoue, H. Kuriyama, T. Nakamura, T. Fushiki, S. Kihara, I. Shimomura, Aquaporin 7 deficiency is associated with development of obesity through activation of adipose glycerol kinase, Proc Natl Acad Sci U S A 102 (2005) 10993-10998.
[35] M. Hara-Chikuma, A.S. Verkman, Prevention of skin tumorigenesis and impairment of epidermal cell proliferation by targeted aquaporin-3 gene disruption, Mol Cell Biol 28 (2008) 326-332.
[36] A.S. Verkman, M.O. Anderson, M.C. Papadopoulos, Aquaporins: important but elusive drug targets, Nat Rev Drug Discov 13 (2014) 259-277.

[37] A.S. Verkman, A.J. Smith, P.W. Phuan, L. Tradtrantip, M.O. Anderson, The aquaporin-4 water channel as a potential drug target in neurological disorders, Expert Opin Ther Targets 21 (2017) 1161-1170.
[38] K. Varadaraj, S.S. Kumari, R. Patil, M.B. Wax, R.T. Mathias, Functional characterization of a human aquaporin 0 mutation that leads to a congenital dominant lens cataract, Exp Eye Res 87 (2008) 9-21.
[39] N. Zhu, X. Feng, C. He, H. Gao, L. Yang, Q. Ma, L. Guo, Y. Qiao, H. Yang, T. Ma, Defective macrophage function in aquaporin-3 deficiency, FASEB J 25 (2011) 4233-4239.
[40] X. Cao, J. Yin, H. Wang, J. Zhao, J. Zhang, L. Dai, J. Zhang, H. Jiang, Z. Lin, Y. Yang, Mutation in AQP5, encoding aquaporin 5, causes palmoplantar keratoderma Bothnia type, J Invest Dermatol 134 (2014) 284-287.
[41] A.J. Loonen, N.V. Knoers, C.H. van Os, P.M. Deen, Aquaporin 2 mutations in nephrogenic diabetes insipidus, Semin Nephrol 28 (2008) 252-265.
[42] C. Moon, J.C. Soria, S.J. Jang, J. Lee, M. Obaidul Hoque, M. Sibony, B. Trink, Y.S. Chang, D. Sidransky, L. Mao, Involvement of aquaporins in colorectal carcinogenesis, Oncogene 22 (2003) 6699-6703.
[43] S. Saadoun, M.C. Papadopoulos, D.C. Davies, B.A. Bell, S. Krishna, Increased aquaporin 1 water channel expression in human brain tumours, Br J Cancer 87 (2002) 621-623.
[44] J. Hu, A.S. Verkman, Increased migration and metastatic potential of tumor cells expressing aquaporin water channels, FASEB J 20 (2006) 1892-1894.
[45] I. Direito, A. Madeira, M.A. Brito, G. Soveral, Aquaporin-5: from structure to function and dysfunction in cancer, Cell Mol Life Sci 73 (2016) 1623-1640.
[46] Z. He, W. Dong, J. Hu, X. Ren, AQP5 promotes hepatocellular carcinoma metastasis via NF-kappaB-regulated epithelial-mesenchymal transition, Biochem Biophys Res Commun 490 (2017) 343-348.
[47] C.F. Li, W.G. Zhang, M. Liu, L.W. Qiu, X.F. Chen, L. Lv, Z.C. Mei, Aquaporin 9 inhibits hepatocellular carcinoma through up-regulating FOXO1 expression, Oncotarget 7 (2016) 44161-44170.
[48] M.C. Papadopoulos, S. Saadoun, Key roles of aquaporins in tumor biology, Biochim Biophys Acta 1848 (2015) 2576-2583.
[49] B.C. Dickinson, C.J. Chang, Chemistry and biology of reactive oxygen species in signaling or stress responses, Nat Chem Biol 7 (2011) 504-511.
[50] S.G. Rhee, Cell signaling. H2O2, a necessary evil for cell signaling, Science 312 (2006) 1882-1883.
[51] E.W. Miller, B.C. Dickinson, C.J. Chang, Aquaporin-3 mediates hydrogen peroxide uptake to regulate downstream intracellular signaling, Proc Natl Acad Sci U S A 107 (2010) 15681-15686.
[52] F. Vieceli Dalla Sega, L. Zambonin, D. Fiorentini, B. Rizzo, C. Caliceti, L. Landi, S. Hrelia, C. Prata, Specific aquaporins facilitate Nox-produced hydrogen peroxide transport through plasma membrane in leukaemia cells, Biochim Biophys Acta 1843 (2014) 806-814.
[53] S. Watanabe, C.S. Moniaga, S. Nielsen, M. Hara-Chikuma, Aquaporin-9 facilitates membrane transport of hydrogen peroxide in mammalian cells, Biochem Biophys Res Commun 471 (2016) 191-197.

[54] H. Satooka, M. Hara-Chikuma, Aquaporin-3 Controls Breast Cancer Cell Migration by Regulating Hydrogen Peroxide Transport and Its Downstream Cell Signaling, Mol Cell Biol 36 (2016) 1206-1218.
[55] J. Cen, M. Nie, L. Duan, F. Gu, Novel autosomal recessive gene mutations in aquaporin-2 in two Chinese congenital nephrogenic diabetes insipidus pedigrees, Int J Clin Exp Med 8 (2015) 3629-3639.
[56] K. Takata, T. Matsuzaki, Y. Tajika, A. Ablimit, T. Hasegawa, Localization and trafficking of aquaporin 2 in the kidney, Histochem Cell Biol 130 (2008) 197-209.
[57] T. Katsura, C.E. Gustafson, D.A. Ausiello, D. Brown, Protein kinase A phosphorylation is involved in regulated exocytosis of aquaporin-2 in transfected LLC-PK1 cells, Am J Physiol 272 (1997) F817-822.
[58] E.J. Kamsteeg, G. Hendriks, M. Boone, I.B. Konings, V. Oorschot, P. van der Sluijs, J. Klumperman, P.M. Deen, Short-chain ubiquitination mediates the regulated endocytosis of the aquaporin-2 water channel, Proc Natl Acad Sci U S A 103 (2006) 18344-18349.
[59] A.L. Stevens, S. Breton, C.E. Gustafson, R. Bouley, R.D. Nelson, D.E. Kohan, D. Brown, Aquaporin 2 is a vasopressin-independent, constitutive apical membrane protein in rat vas deferens, Am J Physiol Cell Physiol 278 (2000) C791-802.
[60] C.M. Krane, J.E. Melvin, H.V. Nguyen, L. Richardson, J.E. Towne, T. Doetschman, A.G. Menon, Salivary acinar cells from aquaporin 5-deficient mice have decreased membrane water permeability and altered cell volume regulation, J Biol Chem 276 (2001) 23413-23420.
[61] T. Ma, Y. Song, A. Gillespie, E.J. Carlson, C.J. Epstein, A.S. Verkman, Defective secretion of saliva in transgenic mice lacking aquaporin-5 water channels, J Biol Chem 274 (1999) 20071-20074.
[62] S. Yoshimura, H. Nakamura, Y. Horai, H. Nakajima, H. Shiraishi, T. Hayashi, T. Takahashi, A. Kawakami, Abnormal distribution of AQP5 in labial salivary glands is associated with poor saliva secretion in patients with Sjogren's syndrome including neuromyelitis optica complicated patients, Mod Rheumatol 26 (2016) 384-390.
[63] I.S. Ambudkar, Ca(2)(+) signaling and regulation of fluid secretion in salivary gland acinar cells, Cell Calcium 55 (2014) 297-305.
[64] Y. Ishikawa, T. Eguchi, M.T. Skowronski, H. Ishida, Acetylcholine acts on M3 muscarinic receptors and induces the translocation of aquaporin5 water channel via cytosolic Ca2+ elevation in rat parotid glands, Biochem Biophys Res Commun 245 (1998) 835-840.
[65] B.H. Lee, A.E. Gauna, G. Perez, Y.J. Park, K.M. Pauley, T. Kawai, S. Cha, Autoantibodies against muscarinic type 3 receptor in Sjogren's syndrome inhibit aquaporin 5 trafficking, PLoS One 8 (2013) e53113.
[66] N. Maeda, Implications of aquaglyceroporins 7 and 9 in glycerol metabolism and metabolic syndrome, Mol Aspects Med 33 (2012) 665-675.
[67] I.V. da Silva, G. Soveral, Aquaporins in Obesity, Adv Exp Med Biol 969 (2017) 227-238.
[68] M. Hara-Chikuma, E. Sohara, T. Rai, M. Ikawa, M. Okabe, S. Sasaki, S. Uchida, A.S. Verkman, Progressive adipocyte hypertrophy in aquaporin-7-deficient mice:

adipocyte glycerol permeability as a novel regulator of fat accumulation, J Biol Chem 280 (2005) 15493-15496.
[69] A. Rodriguez, V. Catalan, J. Gomez-Ambrosi, S. Garcia-Navarro, F. Rotellar, V. Valenti, C. Silva, M.J. Gil, J. Salvador, M.A. Burrell, G. Calamita, M.M. Malagon, G. Fruhbeck, Insulin- and leptin-mediated control of aquaglyceroporins in human adipocytes and hepatocytes is mediated via the PI3K/Akt/mTOR signaling cascade, J Clin Endocrinol Metab 96 (2011) E586-597.
[70] K. Kishida, I. Shimomura, H. Kondo, H. Kuriyama, Y. Makino, H. Nishizawa, N. Maeda, M. Matsuda, N. Ouchi, S. Kihara, Y. Kurachi, T. Funahashi, Y. Matsuzawa, Genomic structure and insulin-mediated repression of the aquaporin adipose (AQPap), adipose-specific glycerol channel, J Biol Chem 276 (2001) 36251-36260.
[71] K. Kishida, H. Kuriyama, T. Funahashi, I. Shimomura, S. Kihara, N. Ouchi, M. Nishida, H. Nishizawa, M. Matsuda, M. Takahashi, K. Hotta, T. Nakamura, S. Yamashita, Y. Tochino, Y. Matsuzawa, Aquaporin adipose, a putative glycerol channel in adipocytes, J Biol Chem 275 (2000) 20896-20902.
[72] G. Fischer, U. Kosinska-Eriksson, C. Aponte-Santamaria, M. Palmgren, C. Geijer, K. Hedfalk, S. Hohmann, B.L. de Groot, R. Neutze, K. Lindkvist-Petersson, Crystal structure of a yeast aquaporin at 1.15 angstrom reveals a novel gating mechanism, PLoS Biol 7 (2009) e1000130.
[73] L. Janosi, M. Ceccarelli, The gating mechanism of the human aquaporin 5 revealed by molecular dynamics simulations, PLoS One 8 (2013) e59897.
[74] K. Kalman, K.L. Nemeth-Cahalan, A. Froger, J.E. Hall, Phosphorylation determines the calmodulin-mediated Ca2+ response and water permeability of AQP0, J Biol Chem 283 (2008) 21278-21283.
[75] S. Törnroth-Horsefield, K. Hedfalk, G. Fischer, K. Lindkvist-Petersson, R. Neutze, Structural insights into eukaryotic aquaporin regulation., FEBS letters 584 (2010) 2580-2588.
[76] L. Leitao, C. Prista, M.C. Loureiro-Dias, T.F. Moura, G. Soveral, The grapevine tonoplast aquaporin TIP2;1 is a pressure gated water channel, Biochem Biophys Res Commun 450 (2014) 289-294.
[77] M. Ozu, R.A. Dorr, F. Gutierrez, M.T. Politi, R. Toriano, Human AQP1 is a constitutively open channel that closes by a membrane-tension-mediated mechanism, Biophys J 104 (2013) 85-95.
[78] G. Soveral, A. Madeira, M.C. Loureiro-Dias, T.F. Moura, Membrane tension regulates water transport in yeast, Biochim Biophys Acta 1778 (2008) 2573-2579.
[79] K.L. Nemeth-Cahalan, J.E. Hall, pH and calcium regulate the water permeability of aquaporin 0, J Biol Chem 275 (2000) 6777-6782.
[80] L. Verdoucq, A. Grondin, C. Maurel, Structure-function analysis of plant aquaporin AtPIP2;1 gating by divalent cations and protons, Biochem J 415 (2008) 409-416.
[81] L. Leitao, C. Prista, T.F. Moura, M.C. Loureiro-Dias, G. Soveral, Grapevine aquaporins: gating of a tonoplast intrinsic protein (TIP2;1) by cytosolic pH, PLoS One 7 (2012) e33219.

[82] C. Tournaire-Roux, M. Sutka, H. Javot, E. Gout, P. Gerbeau, D.-T. Luu, R. Bligny, C. Maurel, Cytosolic pH regulates root water transport during anoxic stress through gating of aquaporins., Nature 425 (2003) 393-397.
[83] M. Zelenina, A.A. Bondar, S. Zelenin, A. Aperia, Nickel and extracellular acidification inhibit the water permeability of human aquaporin-3 in lung epithelial cells, J Biol Chem 278 (2003) 30037-30043.
[84] M. Zelenina, S. Tritto, A.A. Bondar, S. Zelenin, A. Aperia, Copper inhibits the water and glycerol permeability of aquaporin-3, J Biol Chem 279 (2004) 51939-51943.
[85] T. Zeuthen, D.A. Klaerke, Transport of water and glycerol in aquaporin 3 is gated by H(+), J Biol Chem 274 (1999) 21631-21636.
[86] K. Eto, Y. Noda, S. Horikawa, S. Uchida, S. Sasaki, Phosphorylation of aquaporin-2 regulates its water permeability, J Biol Chem 285 (2010) 40777-40784.
[87] D. Boassa, A.J. Yool, Single amino acids in the carboxyl terminal domain of aquaporin-1 contribute to cGMP-dependent ion channel activation, BMC Physiol 3 (2003) 12.
[88] J. Sjohamn, K. Hedfalk, Unraveling aquaporin interaction partners, Biochim Biophys Acta 1840 (2014) 1614-1623.
[89] D. Krishnan, W. Pan, M.R. Beggs, F. Trepiccione, R. Chambrey, D. Eladari, E. Cordat, H. Dimke, R.T. Alexander, Deficiency of Carbonic Anhydrase II Results in a Urinary Concentrating Defect, Front Physiol 8 (2017) 1108.
[90] Y. Noda, S. Horikawa, T. Furukawa, K. Hirai, Y. Katayama, T. Asai, M. Kuwahara, K. Katagiri, T. Kinashi, M. Hattori, N. Minato, S. Sasaki, Aquaporin-2 trafficking is regulated by PDZ-domain containing protein SPA-1, FEBS Lett 568 (2004) 139-145.
[91] Y. Ohashi, K. Tsuzaka, T. Takeuchi, Y. Sasaki, K. Tsubota, Altered distribution of aquaporin 5 and its C-terminal binding protein in the lacrimal glands of a mouse model for Sjogren's syndrome, Curr Eye Res 33 (2008) 621-629.
[92] J.S. Hansen, C. Krintel, M. Hernebring, T.J. Haataja, S. de Mare, S. Wasserstrom, U. Kosinska-Eriksson, M. Palmgren, C. Holm, K.G. Stenkula, H.A. Jones, K. Lindkvist-Petersson, Perilipin 1 binds to aquaporin 7 in human adipocytes and controls its mobility via protein kinase A mediated phosphorylation, Metabolism 65 (2016) 1731-1742.
[93] C. Pietrement, N. Da Silva, C. Silberstein, M. James, M. Marsolais, A. Van Hoek, D. Brown, N. Pastor-Soler, N. Ameen, R. Laprade, V. Ramesh, S. Breton, Role of NHERF1, cystic fibrosis transmembrane conductance regulator, and cAMP in the regulation of aquaporin 9, J Biol Chem 283 (2008) 2986-2996.
[94] S.L. Reichow, D.M. Clemens, J.A. Freites, K.L. Nemeth-Cahalan, M. Heyden, D.J. Tobias, J.E. Hall, T. Gonen, Allosteric mechanism of water-channel gating by Ca2+-calmodulin, Nat Struct Mol Biol 20 (2013) 1085-1092.
[95] T.T. Jesus, R.L. Bernardino, A.D. Martins, R. Sa, M. Sousa, M.G. Alves, P.F. Oliveira, Aquaporin-9 is expressed in rat Sertoli cells and interacts with the cystic fibrosis transmembrane conductance regulator, IUBMB Life 66 (2014) 639-644.
[96] K.H. Cheung, C.T. Leung, G.P. Leung, P.Y. Wong, Synergistic effects of cystic fibrosis transmembrane conductance regulator and aquaporin-9 in the rat epididymis, Biol Reprod 68 (2003) 1505-1510.

[97] M. Castro-Parodi, L. Levi, V. Dietrich, E. Zotta, A.E. Damiano, CFTR may modulate AQP9 functionality in preeclamptic placentas, Placenta 30 (2009) 642-648.
[98] A.E. Damiano, E. Zotta, C. Ibarra, Functional and molecular expression of AQP9 channel and UT-A transporter in normal and preeclamptic human placentas, Placenta 27 (2006) 1073-1081.
[99] X. Liu, B.C. Bandyopadhyay, T. Nakamoto, B. Singh, W. Liedtke, J.E. Melvin, I. Ambudkar, A role for AQP5 in activation of TRPV4 by hypotonicity: concerted involvement of AQP5 and TRPV4 in regulation of cell volume recovery, J Biol Chem 281 (2006) 15485-15495.
[100] R.I. Macey, R.E. Farmer, Inhibition of water and solute permeability in human red cells, Biochim Biophys Acta 211 (1970) 104-106.
[101] A.P. Martins, A. Marrone, A. Ciancetta, A. Galán Cobo, M. Echevarría, T.F. Moura, N. Re, A. Casini, G. Soveral, Targeting aquaporin function: potent inhibition of aquaglyceroporin-3 by a gold-based compound., PloS one 7 (2012) e37435.
[102] A. Spinello, A. de Almeida, A. Casini, G. Barone, The inhibition of glycerol permeation through aquaglyceroporin-3 induced by mercury(II): A molecular dynamics study, Journal of Inorganic Biochemistry (2016).
[103] J. Gao, X. Wang, Y. Chang, J. Zhang, Q. Song, H. Yu, X. Li, Acetazolamide inhibits osmotic water permeability by interaction with aquaporin-1, Anal Biochem 350 (2006) 165-170.
[104] B. Ma, Y. Xiang, S.M. Mu, T. Li, H.M. Yu, X.J. Li, Effects of acetazolamide and anordiol on osmotic water permeability in AQP1-cRNA injected Xenopus oocyte, Acta Pharmacol Sin 25 (2004) 90-97.
[105] H.L. Brooks, J.W. Regan, A.J. Yool, Inhibition of aquaporin-1 water permeability by tetraethylammonium: involvement of the loop E pore region, Mol Pharmacol 57 (2000) 1021-1026.
[106] F.J. Detmers, B.L. de Groot, E.M. Muller, A. Hinton, I.B. Konings, M. Sze, S.L. Flitsch, H. Grubmuller, P.M. Deen, Quaternary ammonium compounds as water channel blockers. Specificity, potency, and site of action, J Biol Chem 281 (2006) 14207-14214.
[107] Y. Yukutake, Y. Hirano, M. Suematsu, M. Yasui, Rapid and reversible inhibition of aquaporin-4 by zinc, Biochemistry 48 (2009) 12059-12061.
[108] V.J. Huber, M. Tsujita, M. Yamazaki, K. Sakimura, T. Nakada, Identification of arylsulfonamides as Aquaporin 4 inhibitors, Bioorg Med Chem Lett 17 (2007) 1270-1273.
[109] R.V. Patil, S. Xu, A.N. van Hoek, A. Rusinko, Z. Feng, J. May, M. Hellberg, N.A. Sharif, M.B. Wax, M. Irigoyen, G. Carr, T. Brittain, P. Brown, D. Colbert, S. Kumari, K. Varadaraj, A.K. Mitra, Rapid Identification of Novel Inhibitors of the Human Aquaporin-1 Water Channel, Chem Biol Drug Des (2015).
[110] C.M. Niemietz, S.D. Tyerman, New potent inhibitors of aquaporins: silver and gold compounds inhibit aquaporins of plant and human origin, FEBS Lett 531 (2002) 443-447.

CHAPTER 2

New insights into the physiological roles of aquaporins

In mammalian cells, multiple AQP isoforms are usually co-expressed and their individual contribution to biological processes is difficult to ascertain. The use of gain of function / loss of function strategies helps to disclose novel physiological roles of AQPs. In the adipose tissue where aquaglyceroporins are mainly expressed, AQPs coordinated activity might be crucial to assure lipid homeostasis. Recently, AQP5 was described as a regulator of other AQP isoforms. We hypothesized for a role of AQP5 in adipocyte biology.

This chapter is adapted from one published manuscript:

Madeira A, **Mósca AF**, Moura TF and Soveral G. "Aquaporin-5 is expressed in adipocytes with implications in adipose differentiation"
IUBMB Life (2015) 67(1): 54-60; DOI: 10.1002/iub.13

2.1 Role of aquaporin-5 in adipocyte differentiation

2.1.1 Abstract

Aquaporins (AQPs) are membrane channels widely distributed in nature. Typically, multiple isoforms are expressed in a single tissue. The adipose tissue is no exception where several AQP members have been identified. The importance of overlapped AQPs expression is unclear, yet interisoforms interactions might be required for key cellular functions. Recently, AQP5 was described as a regulator of other AQP isoforms. Therefore, we hypothesized for a role of AQP5 in adipocyte biology.

Gene expression analysis revealed the presence of AQP5 in both 3T3-L1 fibroblasts and adipocytes, being more abundant in the later. AQP5 depletion impaired adipocyte differentiation, which was confirmed by decreased expression of specific differentiation markers. By overexpressing the human AQP5 in mature adipocytes it was possible to ascertain its role as a water channel in a gain-of-function scenario. To our knowledge, this is the first time that AQP5 is reported on adipose tissue. Our data revealed AQP5 as a new player in adipose tissue biology.

2.1.2 Introduction

For a long time, AQP7 has been the only aquaporin isoform associated with the adipose tissue. Evidences that AQP7 is involved in obesity were found in AQP7 knockout mice presenting adipocyte hypertrophy and in obese humans showing dysregulated AQP7 expression [1,2].

Recently, other AQP isoforms were reported in human adipocytes, namely AQP3, 9, 10, and 11 [3,4,5]. Although the role of these novel adipose AQPs is still unclear, their dysregulation seems to be mostly associated with metabolic disorders [6]. The need for overlapped AQPs expression in tissues, including the adipose, is not yet

understood but it is speculated that the establishment of interisoform physical interactions is required for important cellular functions [7,8].

Recently, AQP5 was described as participating in protein–protein interactions, controlling another aquaporin isoform in kidney [9]. AQP5 is highly expressed in corneal epithelium, alveolar type I cells, epidermis, and in several glandular epithelia [10]. AQP5 dysfunction has been associated with a vast array of phenotypes: AQP5-null mice present reduced saliva production [11] and airway submucosal fluid secretion [12]; two recent studies showed that AQP5 missense mutations are associated with the development of palmoplantar keratoderma [13,14] and interestingly, there are many evidences suggesting the importance of AQP5 upregulation in promoting tumor cell proliferation [15].

The evidences correlating AQP5 to adipose tissue biology are scarce. In favor of AQP5 involvement in adipose tissue biology is the surprising link discovered between hypothalamus *AQP5* and 169 adipose genes, strongly indicating a possible regulatory coordination [16]. Interestingly, AQP5-depleted mice are 10–15% smaller by weight than controls [17], yet the precise mechanisms have not yet been explored. With these discoveries in mind, we hypothesized for the presence of AQP5 in adipocytes.

In this work, we silenced AQP5 expression in mice 3T3-L1 adipocytes and observed an impairment of cell differentiation that was confirmed by quantification of specific differentiation markers. Further, by overexpressing the human AQP5 isoform, we unveiled its activity as a functional water channel when expressed in adipocytes.

2.1.3 Results and Discussion

AQP5 is expressed in 3T3-L1 cells

For a long time AQP7 has been the only AQP associated with the adipose tissue, but in recent years AQPs expression profile in adipose tissue broadened with the identification of many other AQP members, namely AQP3, AQP9 [5], AQP10 [3] and AQP11 [4].

Within the search for AQP5 association with adipose tissue biology, gene expression analysis revealed the presence of *AQP5* in both 3T3-L1 fibroblasts and mature adipocytes (Figure 2.1.1). As expected, AQP7 expression was only detected in adipocytes, roughly two-fold the level of AQP5. In addition, increased *AQP5* levels in adipocytes were observed, indicating that its expression might also be related to adipose cells differentiation.

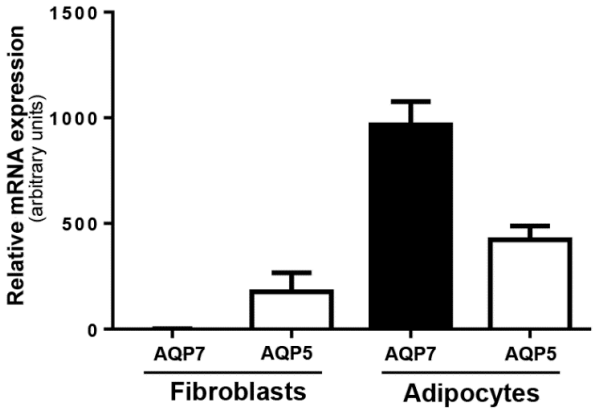

Figure 2.1.1 | AQP7 and AQP5 gene expression analysis in 3T3-L1 cells. AQP mRNA levels are expressed relative to the reference gene *β*-actin and to AQP7 expression. Data are presented as mean ± SEM of three independent measurements. [Data obtained by Ana Madeira]

AQP5 depletion affects adipocyte morphology reducing lipid droplets

According to AQPs solute specificity, AQP5 is described as a selective water channel [10]. To establish the direct role between AQP5 expression levels and the adipocyte membrane water permeability, we obtained 3T3-L1 stable cell lines in which AQP5 was downregulated (mice AQP5 knockdown phenotype, AQP5-shRNA) or upregulated (overexpressing phenotype for human AQP5, hAQP5) (Table 2.1.1). The knockdown cell line showed a 68% reduction of AQP5 transcript whereas enhanced levels of human AQP5 were detected in the overexpression cell line (Table 2.1.1).

Table 2.1.1 | AQP5 expression in the generated 3T3-L1 cell lines. AQP5 expression in 3T3-L1 adipocytes: control, AQP5-shRNA (AQP5 knockdown), and hAQP5 (human AQP5 overexpression). β-actin was used as reference gene. Data represent mean ± SEM of three independent measurements. nd, not detected. *P < 0.05 vs. Control. [Data obtained by Ana Madeira]

3T3-L1 generated cell lines		*Gene*	*Relative mRNA expression*
Knocked down	Control	Mouse AQP5	0.544 (±0.086)
	AQP5-shRNA		0.176 (±0.034)*
Overexpression	Control	Human AQP5	nd
	hAQP5		0.337 (±0.133)

After differentiating these cell lines expressing different amounts of *AQP5*, distinct morphologies were noticeable amongst them. We observed that *AQP5* knockdown adipocytes presented smaller lipid droplets, when compared with both control and human *AQP5*-overexpressing cells (Figure 2.1.2 A).

To further explore the mechanisms underlying these observations we assessed the relative non-osmotic volume (β) [18], which represents the fraction of the cell that is osmotically unresponsive. In adipocytes, besides the intracellular organelles, the

increase in osmotically inactive portion is greatly due to the existence of large lipid droplets that occupy most of the cytoplasm. In fact, a positive correlation between adipocytes nonosmotic volume (β) and triglyceride content was previously established [18]. Figure 2.1.2 B shows significantly lower β values for AQP5-depleted adipocytes (AQP5-shRNA), in comparison with control and hAQP5, indicating lower triglyceride content in these cells. No differences were detected between control and hAQP5-overexpressing adipocytes. However, considering that the control cell line already expresses endogenous AQP5 (mouse AQP5) and has the capacity of fully differentiation, further differentiation promoted by hAQP5 overexpression would not be expected.

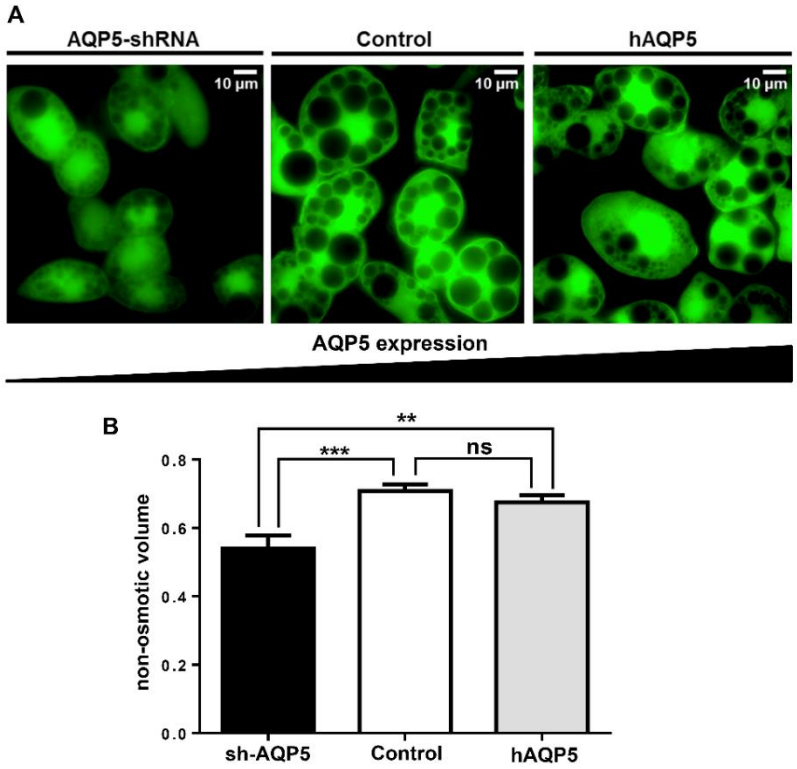

Figure 2.1.2 | AQP5 depletion affects adipocyte morphology reducing lipid droplets. **(A)** Representative illustration of 3T3-L1 adipocytes with different levels of AQP5 [controls, AQP5 knockdown (sh-AQP5) and human AQP5 overexpression (hAQP5)]. **(B)** Nonosmotic volumes β of control and human AQP5-overexpressing adipocytes (hAQP5). Bars show

mean ± SEM from 20 to 25 cells. Significance levels: ns, not significant; $^{**}P < 0.01$; $^{***}P < 0.001$ vs. control.

These observations led us to speculate for a generalized defect in adipocytes differentiation as a consequence of AQP5 depletion. To confirm this hypothesis, we quantified specific markers of adipocyte differentiation (fatty acid-binding protein, aP2; hormone-sensitive lipase, HSL; and glucose transporter type 4, Glut4) in both control and AQP5-depleted cells (Table 2.1.2). A tendency toward lower adipogenic markers levels was observed in regard to control. Thus, these data point towards a perturbation in adipocytes maturation related to the absence of AQP5.

Table 2.1.2 | Expression of specific mature adipocyte markers. Expression in control and AQP5 knockdown (AQP5-shRNA) 3T3-L1 adipocytes. GAPDH was used as reference gene. Data represent mean ± SEM of three independent measurements. [Data obtained by Ana Madeira]

Gene	*Cell line*	*Adipocytes*
Mouse aP2	Control	0.096 (±0.033)
	AQP5-shRNA	0.085 (±0.014)
Mouse HSL	Control	0.152 (±0.090)
	AQP5-shRNA	0.076 (±0.002)
Mouse Glut4	Control	0.229 (±0.168)
	AQP5-shRNA	0.114 (±0.011)

Previous studies have correlated elevated AQP5 expression levels with increased proliferation in several cancer cell lines [19,20,21,22,23]. In the course of differentiation, 3T3-L1 preadipocytes undergo multiple rounds of proliferation, referred as mitotic clonal expansion [24]. Whether AQP5 interferes with this process still needs to be further elucidated.

Human AQP5 is a functional water channel in adipocytes

Water permeability P_f was determined by computing the time course of cell volume change (V/V_0) after a hyperosmotic challenge with a non-diffusible solute (mannitol), inducing water outflow and cell shrinkage. A faster volume change is depicted for hAQP5-overexpressing cells (Figure 2.1.3 A), giving a P_f of (1.6 ± 0.1) × 10^{-3} cm s^{-1} for hAQP5 and of (0.9 ± 0.1) × 10^{-3} cm s^{-1} for control adipocytes (Figure 2.1.3 B).

It is well documented that upon differentiation, adipocytes plasma membrane undergoes striking changes to accommodate the unique functions carried out by these cells [25,26]. Significant alterations in both lipid/protein composition and arrangement impart changes in plasma membrane properties, including membrane permeability. It was previously reported that AQPs expression (AQP3,7) is intrinsically related to adipocytes differentiation [5,27] and specifically, the involvement of AQP7 in water permeation in mature adipocytes was shown [18]. Therefore, given that AQP5 depletion compromises adipocytes differentiation with predicted impact on the overall plasma membrane properties, for comparison purposes P_f was only assessed in control and hAQP5 overexpressing adipocytes. Our results show that human AQP5 is a functional water channel when expressed in adipocytes. Further studies are required to clarify if water transport through AQP5 is associated with adipocytes differentiation, which seems to be compromised in the absence this protein (Figure 2.1.3).

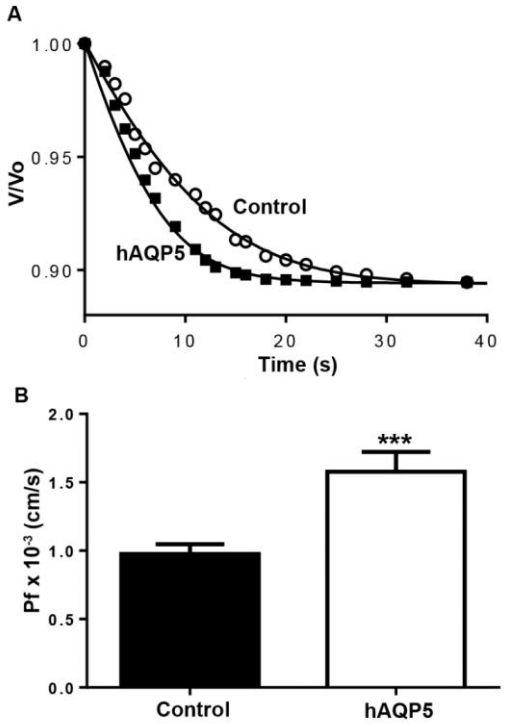

Figure 2.1.3 | Functional assessment of human AQP5 water transport. (A) Representative time course of the relative cell volume change V/V_0 after an osmotic shock with mannitol. All data points were from cells presenting equivalent nonosmotic volumes (*ϐ*). **(B)** Osmotic water permeability coefficient (P_f). Bars show mean ± SEM from 20 to 25 cells. Significance levels: ***P < 0.001 vs. control.

2.1.4 Conclusions

AQP5 has been classified as specific for water transport and thus its contribution to adipocyte differentiation is not probably related with glycerol permeation. hAQP5 high-resolution structure [28] displayed a pore that narrows to an average radius of 1.02 Å near the highly conserved ar/R constriction region, which is marginally narrower than that of AQP1 [29]. This feature renders the channel unable to permeate molecules much larger than water, such as glycerol. Thus, it is not expected any effect on glycerol permeability due to AQP5 expression nor a direct effect on glycerol metabolism.

Alternatively, AQP5 role in adipocytes may rely on the coordination with specific functional partners. Transient receptor potential vanilloid 4 (TRPV), a Ca^{2+}-permeable nonselective cation channel described as a sensor of many stimuli, including osmolarity [30], was reported as functionally linked to AQP5 [14,31,32]. Remarkably, adipose tissue expresses high levels of TRPV4 [30] and a relation between obesity and *TRPV4* has been proposed: deletion of mouse TRPV4 results in reduced glucose levels, improved insulin sensitivity and resistance against diet-induced obesity [33]. In human and murine salivary gland cells, activation of TRPV4 upon hypoosmotic conditions is dependent on the presence of AQP5 [31], whereas in lung epithelial cells TRPV4 activation by hypotonicity leads to a reduction in AQP5 abundance [32]. Despite the mechanism(s) associating TRPV4 activation and AQP5 still remain untangled in adipose tissue, a deeper involvement of AQP5 with TRPV4 or other interaction partners cannot be disregarded.

2.1.5 Experimental Section

Cell culture and differentiation - 3T3-L1 preadipocytes (CCL 92.1; American Type Culture Collection, Manassas, VA) were grown to confluence and induced to differentiate into adipocytes essentially as previously described [34]. Fully mature adipocytes were used 10-15 days after initiation of differentiation.

cDNA and shRNA constructs - Human AQP5 was subcloned from the pDONR223 (Invitrogen, Carlsbad, CA) into the lentiviral expression vector pWPI-DEST (Adaptation by Trono Lab) using the recombination Gateway® Technology as described [18]. For mouse AQP5 silencing, five different target shRNA constructs inserted within the lentiviral vector pLKO.1-puro were tested [35]. The effective target sequence of the sense

shRNA was as follows: 5′ – GCTGTGGTCAAAGGCACATAT – 3′ (Clone ID TRCN0000105621). shRNA lentiviral non-target plasmid (MISSION pLKO.1-puro Control Transduction Particles, Sigma-Aldrich, St. Louis, MO) was used as a control and contains a puromycin resistance marker for selection of successfully infected cells.

Lentivirus production and infection of 3T3-L1 preadipocytes - To generate the lentivirus, shRNA or cDNA lentiviral expression constructs were co-transfected into Human kidney 293T cells with pCMVR8.74 (Addgene plasmid 22036) and pMD2G (Addgene plasmid 22036) using the polyethilenimine method [36] as described [18]. The HIV derived constructs (pCMVR8.74 helper packaging vector and pMD2G vector encoding for envelop protein) were kindly provided by Dr. D. Trono, EPFL (Switzerland). Levels of human AQP5 overexpression were determined by RT-PCR and expressed relative to control cells infected with the empty plasmid (GFP control).

RNA extraction and RT-PCR - Total RNA was extracted with RNeasy Mini Kit (Qiagen, Hiden, Germany) as described [18]. Quantification of PCR products was accomplished by measuring the fluorescence of specific probes for each target sequence (Taqman ® pre-designed gene expression assays, Applied Biosystems, Carlsbad, CA) or by measuring fluorescence from the progressive binding of SYBR green I dye to double-stranded DNA. Amplification and detection of specific products were performed with the 7500 Real-Time PCR System (Applied Biosystems) following the manufacturer's protocol. Relative quantification value of PCR transcripts was calculated either using the comparative Ct method (manufacture's protocol) or the standard curve method [12] with normalization to β-actin or glyceraldehyde 3-phosphate dehydrogenase (GAPDH) endogenous controls. The set of specific primers and TaqMan® pre-designed gene expression assays were as follows: AQP5 (Mm00437578_m1); AQP7 (Mm00431839_m1); β-actin (Mm02619580_g1); GLUT4 (5′- ACTTCATTGTCGGCATGGGT-3′ and 5′-AGATCTGGTCAAACGTCCGG- 3′); aP2 (fatty acid binding protein 4) (5′-TTCGATGAAATCACCGCAGA-3′ and 5′-GGTCGACTTTCCATCCCACTT-3′); HSL (Hormone sensitive lipase) (5′-

GGCTTACTGGGCACAGATACCT-3′ and 5′-CTGAAGGCTCTGAGTTGCTCAA-3′); and GAPDH (5′-GGCCATCCACAGTCTTCTGG-3′ and 5′-ACCACAGTCCATGCCATCACTGCCA-3′).

Permeability assays - Water permeability (P_f) was measured in individual adherent cells on a coverslip as previously described [18]. Briefly, 3T3-L1 adipocytes were loaded with 5 μM calceinacetoxymethyl ester (calcein-AM) (Sigma Aldrich) (a volume sensitive fluorophore) for 90 min at 37°C in 5% CO2/95% air. The coverslips with the adhered cells were mounted in a closed perfusion chamber (Warner Instruments, Hamden, CT) on the stage of a Zeiss Axiovert 200 inverted microscope. Fluorescence was excited at 495/10 nm and the emission fluorescence was collected with a 535/25nm bandpass filter coupled with a 515 nm dichroic beam splitter. Images were captured using a ×40/1.6 epifluorescence oil immersion objective and a digital camera (CoolSNAP EZ, Photometrics, Tucson, AZ) and were recorded by the Metafluor Software (Molecular Devices, Sunnyvale, CA). For the permeability assays the strategy developed in our previous work was used [18]. Briefly, for the Pf assessment, cells were perfused with HEPES [135 mM NaCl, 5 mM KCl, 2.5 mM $CaCl_2$, 1.2 mM $MgCl_2$, 10 mM glucose, 5 mM HEPES, pH 7.4, and initial osmolarity $(osmout)_0$ = 300 mosM] for 60 sec, after which 300 mM mannitol (nondiffusible solute) was added, being achieved an external osmolarity $(osmout)_\infty$ = 600 mosM and thus a tonicity of the osmotic shock (Λ) of 2 [Λ is defined as the ratio between final and initial media osmolarities, $\Lambda = (osmout)_\infty/(osmout)_0$]. Permeability coefficient P_f was evaluated from the measured time-dependent volume changes, $v_{rel}=V/V_0$, obtained by adding mannitol (impermeant solute) to the external media achieving an osmotic challenge of Λ=2. The relative nonosmotic volume $\beta=V_{Nosm}/V_0$ was considered in all calculations. Parameters (P_f and β) were evaluated by numerically integrating and curve fitting the time dependent v_{rel} data, using the model equations detailed in [18] and the Berkeley Madonna software (http://www.berkeleymadonna.com/).

Cell volume measurement - Cell volume V was measured at selected time points from 2D images obtained during the permeability assay to evaluate the initial volume (prior to the osmotic challenge V_0) and the final equilibrium volume. For each assay three coverslips were analyzed (approximately 25 cells). The cross-sectional area of calcein-loaded cells was measured using the Image J software [37] and cells were assumed to have a spherical shape for volume calculations. A linear relationship between relative changes in cell osmotic volume $(V-\beta)/(V_0-\beta)$ (thus of V/V_0) and calcein fluorescence intensity (F/F_0) was previously reported [38] and validated for these 3T3-L1 cells [18] allowing the calibration of the fluorescence output after the mannitol osmotic challenge. This linear correlation indicates that the overestimation of cellular volume V when considering a spherical rather than a disc-like shape of adherent cells can be disregarded for relative volume changes V/V_0 [18]. Cell fluorescence traces F/F_0 were converted into (V/V_0) after subtracting the bleaching given by the initial fluorescence decay before the mannitol osmotic shock. F_0 was calculated in each signal as the averaged initial values of fluorescence prior to the osmotic challenge.

Statistical analysis - Results were expressed as mean ± SEM of n individual experiments. Statistical analysis between groups was performed by one-way ANOVA followed by Tukey's multiple comparisons test or unpaired t-test. P values < 0.05 were considered statistical significant. Statistical analyses were performed using the Graph Prism software (GraphPad Software).

2.1.6 References

[1] M. Hara-Chikuma, E. Sohara, T. Rai, M. Ikawa, M. Okabe, S. Sasaki, S. Uchida, A.S. Verkman, Progressive adipocyte hypertrophy in aquaporin-7-deficient mice: adipocyte glycerol permeability as a novel regulator of fat accumulation, J Biol Chem 280 (2005) 15493-15496.

[2] N. Maeda, Implications of aquaglyceroporins 7 and 9 in glycerol metabolism and metabolic syndrome, Mol Aspects Med 33 (2012) 665-675.

[3] U. Laforenza, M.F. Scaffino, G. Gastaldi, Aquaporin-10 represents an alternative pathway for glycerol efflux from human adipocytes, PLoS One 8 (2013) e54474.
[4] A. Madeira, S. Fernandez-Veledo, M. Camps, A. Zorzano, T.F. Moura, V. Ceperuelo-Mallafre, J. Vendrell, G. Soveral, Human aquaporin-11 is a water and glycerol channel and localizes in the vicinity of lipid droplets in human adipocytes, Obesity (Silver Spring) 22 (2014) 2010-2017.
[5] A. Rodriguez, V. Catalan, J. Gomez-Ambrosi, S. Garcia-Navarro, F. Rotellar, V. Valenti, C. Silva, M.J. Gil, J. Salvador, M.A. Burrell, G. Calamita, M.M. Malagon, G. Fruhbeck, Insulin- and leptin-mediated control of aquaglyceroporins in human adipocytes and hepatocytes is mediated via the PI3K/Akt/mTOR signaling cascade, J Clin Endocrinol Metab 96 (2011) E586-597.
[6] A. Madeira, T.F. Moura, G. Soveral, Aquaglyceroporins: implications in adipose biology and obesity, Cell Mol Life Sci 72 (2015) 759-771.
[7] K. Fetter, V. Van Wilder, M. Moshelion, F. Chaumont, Interactions between plasma membrane aquaporins modulate their water channel activity, Plant Cell 16 (2004) 215-228.
[8] J. Sjohamn, K. Hedfalk, Unraveling aquaporin interaction partners, Biochim Biophys Acta 1840 (2014) 1614-1623.
[9] H. Wu, L. Chen, X. Zhang, Q. Zhou, J.M. Li, S. Berger, Z. Borok, B. Zhou, Z. Xiao, H. Yin, M. Liu, Y. Wang, J. Jin, M.R. Blackburn, Y. Xia, W. Zhang, Aqp5 is a new transcriptional target of Dot1a and a regulator of Aqp2, PLoS One 8 (2013) e53342.
[10] A.S. Verkman, M.O. Anderson, M.C. Papadopoulos, Aquaporins: important but elusive drug targets, Nat Rev Drug Discov 13 (2014) 259-277.
[11] T. Ma, Y. Song, A. Gillespie, E.J. Carlson, C.J. Epstein, A.S. Verkman, Defective secretion of saliva in transgenic mice lacking aquaporin-5 water channels, J Biol Chem 274 (1999) 20071-20074.
[12] Y. Song, A.S. Verkman, Aquaporin-5 dependent fluid secretion in airway submucosal glands, J Biol Chem 276 (2001) 41288-41292.
[13] D.C. Blaydon, L.K. Lind, V. Plagnol, K.J. Linton, F.J. Smith, N.J. Wilson, W.H. McLean, C.S. Munro, A.P. South, I.M. Leigh, E.A. O'Toole, A. Lundstrom, D.P. Kelsell, Mutations in AQP5, encoding a water-channel protein, cause autosomal-dominant diffuse nonepidermolytic palmoplantar keratoderma, Am J Hum Genet 93 (2013) 330-335.
[14] X. Cao, J. Yin, H. Wang, J. Zhao, J. Zhang, L. Dai, J. Zhang, H. Jiang, Z. Lin, Y. Yang, Mutation in AQP5, encoding aquaporin 5, causes palmoplantar keratoderma Bothnia type, J Invest Dermatol 134 (2014) 284-287.
[15] M.C. Papadopoulos, S. Saadoun, Key roles of aquaporins in tumor biology, Biochim Biophys Acta 1848 (2015) 2576-2583.
[16] R. Dobrin, J. Zhu, C. Molony, C. Argman, M.L. Parrish, S. Carlson, M.F. Allan, D. Pomp, E.E. Schadt, Multi-tissue coexpression networks reveal unexpected subnetworks associated with disease, Genome Biol 10 (2009) R55.
[17] A.S. Verkman, B. Yang, Y. Song, G.T. Manley, T. Ma, Role of water channels in fluid transport studied by phenotype analysis of aquaporin knockout mice, Exp Physiol 85 Spec No (2000) 233S-241S.

[18] A. Madeira, M. Camps, A. Zorzano, T.F. Moura, G. Soveral, Biophysical assessment of human aquaporin-7 as a water and glycerol channel in 3T3-L1 adipocytes, PLoS One 8 (2013) e83442.
[19] Y.K. Chae, S.K. Kang, M.S. Kim, J. Woo, J. Lee, S. Chang, D.W. Kim, M. Kim, S. Park, I. Kim, B. Keam, J. Rhee, N.H. Koo, G. Park, S.H. Kim, S.E. Jang, I.Y. Kweon, D. Sidransky, C. Moon, Human AQP5 plays a role in the progression of chronic myelogenous leukemia (CML), PLoS One 3 (2008) e2594.
[20] S.K. Kang, Y.K. Chae, J. Woo, M.S. Kim, J.C. Park, J. Lee, J.C. Soria, S.J. Jang, D. Sidransky, C. Moon, Role of human aquaporin 5 in colorectal carcinogenesis, Am J Pathol 173 (2008) 518-525.
[21] H. Shimizu, A. Shiozaki, D. Ichikawa, H. Fujiwara, H. Konishi, H. Ishii, S. Komatsu, T. Kubota, K. Okamoto, M. Kishimoto, E. Otsuji, The expression and role of Aquaporin 5 in esophageal squamous cell carcinoma, J Gastroenterol 49 (2014) 655-666.
[22] J. Woo, J. Lee, Y.K. Chae, M.S. Kim, J.H. Baek, J.C. Park, M.J. Park, I.M. Smith, B. Trink, E. Ratovitski, T. Lee, B. Park, S.J. Jang, J.C. Soria, J.A. Califano, D. Sidransky, C. Moon, Overexpression of AQP5, a putative oncogene, promotes cell growth and transformation, Cancer Lett 264 (2008) 54-62.
[23] Z. Zhang, Z. Chen, Y. Song, P. Zhang, J. Hu, C. Bai, Expression of aquaporin 5 increases proliferation and metastasis potential of lung cancer, J Pathol 221 (2010) 210-220.
[24] Q.Q. Tang, M.D. Lane, Adipogenesis: from stem cell to adipocyte, Annu Rev Biochem 81 (2012) 715-736.
[25] J.Y. Fan, J.L. Carpentier, E. van Obberghen, C. Grunfeld, P. Gorden, L. Orci, Morphological changes of the 3T3-L1 fibroblast plasma membrane upon differentiation to the adipocyte form, J Cell Sci 61 (1983) 219-230.
[26] J. Storch, S.L. Shulman, A.M. Kleinfeld, Plasma membrane lipid order and composition during adipocyte differentiation of 3T3F442A cells. Studies in intact cells with 1-[4-(trimethylamino)phenyl]-6-phenylhexatriene, J Biol Chem 264 (1989) 10527-10533.
[27] K. Kishida, H. Kuriyama, T. Funahashi, I. Shimomura, S. Kihara, N. Ouchi, M. Nishida, H. Nishizawa, M. Matsuda, M. Takahashi, K. Hotta, T. Nakamura, S. Yamashita, Y. Tochino, Y. Matsuzawa, Aquaporin adipose, a putative glycerol channel in adipocytes, J Biol Chem 275 (2000) 20896-20902.
[28] R. Horsefield, K. Norden, M. Fellert, A. Backmark, S. Tornroth-Horsefield, A.C. Terwisscha van Scheltinga, J. Kvassman, P. Kjellbom, U. Johanson, R. Neutze, High-resolution x-ray structure of human aquaporin 5, Proc Natl Acad Sci U S A 105 (2008) 13327-13332.
[29] K. Murata, K. Mitsuoka, T. Hirai, T. Walz, P. Agre, J.B. Heymann, A. Engel, Y. Fujiyoshi, Structural determinants of water permeation through aquaporin-1, Nature 407 (2000) 599-605.
[30] W. Liedtke, Y. Choe, M.A. Marti-Renom, A.M. Bell, C.S. Denis, A. Sali, A.J. Hudspeth, J.M. Friedman, S. Heller, Vanilloid receptor-related osmotically activated channel (VR-OAC), a candidate vertebrate osmoreceptor, Cell 103 (2000) 525-535.
[31] X. Liu, B.C. Bandyopadhyay, T. Nakamoto, B. Singh, W. Liedtke, J.E. Melvin, I. Ambudkar, A role for AQP5 in activation of TRPV4 by hypotonicity: concerted involvement of

AQP5 and TRPV4 in regulation of cell volume recovery, J Biol Chem 281 (2006) 15485-15495.
[32] V.K. Sidhaye, A.D. Guler, K.S. Schweitzer, F. D'Alessio, M.J. Caterina, L.S. King, Transient receptor potential vanilloid 4 regulates aquaporin-5 abundance under hypotonic conditions, Proc Natl Acad Sci U S A 103 (2006) 4747-4752.
[33] L. Ye, S. Kleiner, J. Wu, R. Sah, R.K. Gupta, A.S. Banks, P. Cohen, M.J. Khandekar, P. Bostrom, R.J. Mepani, D. Laznik, T.M. Kamenecka, X. Song, W. Liedtke, V.K. Mootha, P. Puigserver, P.R. Griffin, D.E. Clapham, B.M. Spiegelman, TRPV4 is a regulator of adipose oxidative metabolism, inflammation, and energy homeostasis, Cell 151 (2012) 96-110.
[34] S.C. Frost, M.D. Lane, Evidence for the involvement of vicinal sulfhydryl groups in insulin-activated hexose transport by 3T3-L1 adipocytes, J Biol Chem 260 (1985) 2646-2652.
[35] J. Moffat, D.A. Grueneberg, X. Yang, S.Y. Kim, A.M. Kloepfer, G. Hinkle, B. Piqani, T.M. Eisenhaure, B. Luo, J.K. Grenier, A.E. Carpenter, S.Y. Foo, S.A. Stewart, B.R. Stockwell, N. Hacohen, W.C. Hahn, E.S. Lander, D.M. Sabatini, D.E. Root, A lentiviral RNAi library for human and mouse genes applied to an arrayed viral high-content screen, Cell 124 (2006) 1283-1298.
[36] L. Naldini, U. Blomer, F.H. Gage, D. Trono, I.M. Verma, Efficient transfer, integration, and sustained long-term expression of the transgene in adult rat brains injected with a lentiviral vector, Proc Natl Acad Sci U S A 93 (1996) 11382-11388.
[37] C.A. Schneider, W.S. Rasband, K.W. Eliceiri, NIH Image to ImageJ: 25 years of image analysis, Nat Methods 9 (2012) 671-675.
[38] S. Hamann, J.F. Kiilgaard, T. Litman, F.J. Alvarez-Leefmans, B.R. Winther, T. Zeuthen, Measurement of cell volume changes by fluorescence self-quenching, Journal of Fluorescence 12 (2002) 139-145.

CHAPTER 3

Exploring the pH regulation of aquaporins by heterologous expression in yeast

A better understanding of human aquaglyceroporin regulation in biological environments by different stimuli and the identification of mechanisms of modulation of water/glycerol fluxes may help the design of novel inhibitors with potential therapeutic applications.

An excellent tool to investigate AQP's function and regulation is the yeast heterologous expression system. In the current chapter, AQP3, AQP5, AQP7 and AQP10 isoforms were functional characterized in the yeast *Saccharomyces cerevisiae* and their channel activity regulation by external pH were investigated.

This chapter is adapted from two published and two submitted manuscripts:

Rodrigues C*, **Mósca AF***, Martins AP, Nobre T, Prista C, Antunes F, Gasparovic AC & Soveral G. "Rat Aquaporin-5 Is pH-Gated Induced by Phosphorylation and Is Implicated in Oxidative Stress"
International Journal of Molecular Sciences (2016) 17, 2090; DOI: 10.3390/ijms17122090

de Almeida A, Martins AP, **Mósca AF**, Hein J. Wijma, Prista C, Soveral G & Casini A. "Exploring the gating mechanisms of aquaporin-3: new clues for the design of inhibitors?"
Molecular Biosystems (2016) 12(5): 1564-73; DOI: 10.1039/c6mb00013

Mósca AF*, de Almeida A*, Wragg D, Martins AP, Sabir F, Leoni S, Moura TF, Prista C, Casini A & Soveral G. "Human aquaporin-7 behaves as a glycerol efflux channel at acidic
pH"
Submitted

Gotfryd K, **Mósca AF***, Missel JW*, Truelsen SF, Wang K, Spulber M, Krabbe S, Hélix-Nielsen C, Laforenza U, Soveral G, Pedersen PA & Gourdon P. "Human adipose glycerol flux is regulated by a pH gate in AQP10"
Submitted

*Equal contribution

3.1 pH gating induced by phosphorylation of Aquaporin-5

3.1.1 Abstract

Aquaporin-5 (AQP5) is a membrane water channel widely distributed in human tissues that was found up-regulated in different tumors and considered implicated in carcinogenesis in different organs and systems. However, AQP5 short-term regulation was not reported and mechanisms underlying its involvement in cancer are not well defined. In this work, we expressed rat AQP5 in yeast and investigated mechanisms of gating. Our data shows that AQP5 does not change its water permeability by external acidification, but AQP5 can be gated by pH in a phosphorylation-dependent manner, with higher activity at physiological (pH 7.4).

3.1.2 Introduction

Besides being widely distributed among the human body, AQP5 was found expressed in salivary and lacrimal glands and showed to play a major role in saliva secretion [1]. AQP5 transport defect was also associated with Sjögren's syndrome, a chronic autoimmune disease that destroys the salivary and lacrimal glands [1].

Interestingly, a recent study showed that AQP5 membrane abundance is regulated by phosphorylation [2], and in fact, the contrasting phosphorylation status between cancer and normal tissues suggests that AQP5 role in tumorigenesis is related with its phosphorylation [3]. However, besides its post-translational modification by phosphorylation, gating mechanisms for AQP5 channel activity regulation have not been reported so far.

3.1.3 Results and Discussion

Subcellular localization and water permeability of rat AQP5 expressed in yeast

Yeast cells made devoid of endogenous aquaporins (*aqy*-null) were transformed with either the empty plasmid pUG35 (control cells) or the plasmid containing the rat AQP5 gene (mentioned as AQP5 cells, for clarity). The expression of AQP5 in the *S. cerevisiae* model was assessed by fluorescence microscopy, using GFP tagging. In transformed cells, AQP5–GFP is localized at the cellular membrane, as depicted in Figure 3.1.1 A.

The permeability of yeast expressing AQP5 was evaluated by stopped-flow fluorescence after loading cells with the volume sensitive dye carboxyfluorescein. When cells are exposed to hyperosmotic shock with impermeant solutes, water outflow induces cell shrinkage. Water permeability is then evaluated by monitoring the time course of fluorescence output that reflects the transient volume change. As depicted in Figure 3.1.1 B, cells expressing AQP5 show a much faster volume change after a hyperosmotic shock. The water permeability coefficient P_f was 12-fold higher for AQP5 cells ($(4.94 \pm 0.40) \times 10^{-3}$ cm s^{-1} and $(0.41 \pm 0.05) \times 10^{-3}$ cm s^{-1} for AQP5 and control, respectively) (Figure 3.1.1 C). The activation energy for water transport E_a was concomitantly lower for AQP5 cells (6.52 ± 0.82 kcal mol^{-1}) compared to the control (15.16 ± 0.85 kcal mol^{-1}) (Figure 3.1.1 D), corroborating the increase in membrane water permeability conferred by AQP5 expression. Although AQP5 behavior as a water channel is well known in the literature, these data validate the use of the yeast system to detect AQP5 function and further explore mechanisms of regulation.

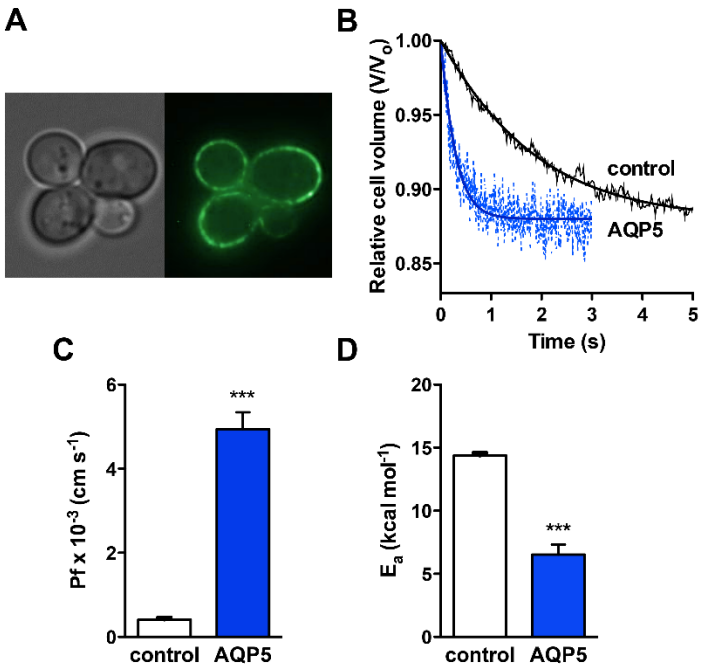

Figure 3.1.1 | Expression and function of rat Aquaporin-5 (AQP5) in yeast. (A) Epifluorescence images of GFP-tagged AQP5 localization (green) in yeast cells (100x objective); **(B)** Representative time course of the relative cell volume (V/V_0) changes after a hyperosmotic shock inducing cell shrinkage (pH 7.4); **(C)** Water permeability coefficients of control (P_f = (0.41 ± 0.05) × 10^{-3} cm s^{-1} and cells expressing AQP5 (P_f = (4.94 ± 0.40) × 10^{-3} cm s^{-1}), measured at 23 °C and pH 7.4. Data are mean ± SD of 10 measurements; **(D)** Activation energies (E_a) for water permeation of control and AQP5 cells (15.16 ± 0.85 and 6.52 ± 0.82 kcal mol^{-1}, respectively). Data are mean ± SD. *** $p < 0.001$.

Effect of pH and glucose-stimulated phosphorylation on rat AQP5 permeability

A gating mechanism regulating human AQP5 activity has been proposed by molecular dynamics simulations [4]. This study revealed that the AQP5 channel could change between an open and closed state by a tap-like mechanism at the cytoplasmic end, induced by a translation of the His67 inside the pore, blocking the entrance of the channel. Moreover, when in the open state, the selectivity filter (SF) can regulate the flow rate of water molecules by exhibiting two different conformations (wide or narrow). These two conformations are decided by the side chain orientation of His173 and the proximity to Ser183—when His173 is close to

Ser183, the SF is in the narrow conformation and the water passage is restricted. The trigger for this gating mechanism has not been described; in addition, this in silico approach has not been so far experimentally validated. A similar gating mechanism for human AQP4 was recently described [5], where two putative gate regions formed by two residues on the cytoplasmic side (His95 and Cys178) and the other two on the SF region (Arg216 and His201) modulate opening and closure of the AQP4 pore along four possible conformational states. The relative stability of the two resulting states, open and closed, may depend on small changes in the microenvironment, such as variations of pH. Indeed, a pH-dependent gating mechanism was recently obtained from in silico and in vitro studies [6], ascribing to His95 located in AQP4 cytoplasmic end the role of regulating channel permeability. Phosphorylation of AQP4 has also been demonstrated with opposed effects depending on the residue that is phosphorylated. AQP4 is inhibited when Ser180 is phosphorylated in loop D and is activated when Ser111 in loop B is phosphorylated [7]. These observations prompted us to investigate if AQP5 would be gated by pH or by phosphorylation. Thus, we first decided to investigate the effect of external pH on AQP5 activity of rat AQP5-transformed yeasts. Although our yeast cells express rat AQP5, sequence alignment of human and rat AQP5 isoforms showed a sequence identity of 91% [8]. From the analyses of the amino acid sequences, we can infer that human and rat AQP5 may share the same gating mechanism.

Since the physiological pH of yeast's natural environment is acidic (3.5–6.5) [9], and conditions at which cells show optimal growth and expression and trafficking mechanisms are expected to be fully active, we chose the external pH 5.1 to test yeast membrane water permeability. In addition, considering that a mammalian aquaporin is being expressed, permeability was also measured at the mammalian physiological pH 7.4. Permeability experiments with AQP5 and control cells

incubated at pH 5.1 and 7.4 showed that, by changing external pH channel, activity was not altered (Figure 3.1.2 A). At pH 5.1, P_f = (0.35 ± 0.01) × 10^{-3} cm s^{-1} and E_a = 14.38 ± 0.22 kcal mol^{-1} for control cells, and P_f = (4.77 ± 0.32) × 10^{-3} cm s^{-1} and E_a = 7.69 ± 0.86 kcal mol^{-1} for AQP5 cells, were not different from the respective values at pH 7.4 (detailed above, Figure 3.1.1). These results indicate that the acidic external pH does not affect AQP5 water permeability.

It is known that AQP5 expression and trafficking can be regulated by phosphorylation, but whether phosphorylation also regulates channel activity and contributes to gating still remains uncertain. Several studies reported AQP5 redistribution in plasma membrane of animal cells initiated by phosphorylation [2,10]. Post-transcriptional regulation of AQP5 function in response to stimuli such as neurotransmitters, hormones, and cyclic adenosine monophosphate (cAMP), has been reported (for a review see [3]). cAMP regulates aquaporin-5 expression at both transcriptional and post-transcriptional levels through a protein kinase A (PKA) pathway [11], increasing AQP5 abundance on the apical membrane of lung epithelial cells after long-term exposure [12]. Besides translocation to the plasma membrane, phosphorylation of AQP5 was shown to promote cell proliferation [13] and, interestingly, AQP5 Ser156 was found preferentially phosphorylated in tumor cells [14], supporting AQP5 phosphorylation involvement in cell proliferation.

In yeast *S. cerevisiae*, the basal intracellular cAMP concentration is low [15]. However, addition of glucose or related fermentable sugars after a period of glucose-starvation triggers the Ras/PKA pathway, creating a sudden and transient increase in intracellular cAMP levels that induce a protein phosphorylation cascade [16,17]. Activation of this pathway by glucose mimics the well-known hormonal-induced phosphorylation pathways that occur in animal cells [18]. Therefore, to examine the effect of phosphorylation on AQP5 water permeability, glucose starved yeast cells were incubated with 100 mM glucose for 5 min before P_f

measurements. As shown in Figure 3.1.2 B, glucose addition did not affect P_f of control or AQP5 cells at pH 5.1. However, at pH 7.4, glucose pulse resulted in a significantly two-fold increased P_f in AQP5 cells (P_f = (10.60 ± 0.53) × 10^{-3} cm s^{-1}) and a 30-fold increase compared with basal levels of control cells (Figure 3.1.2 B).

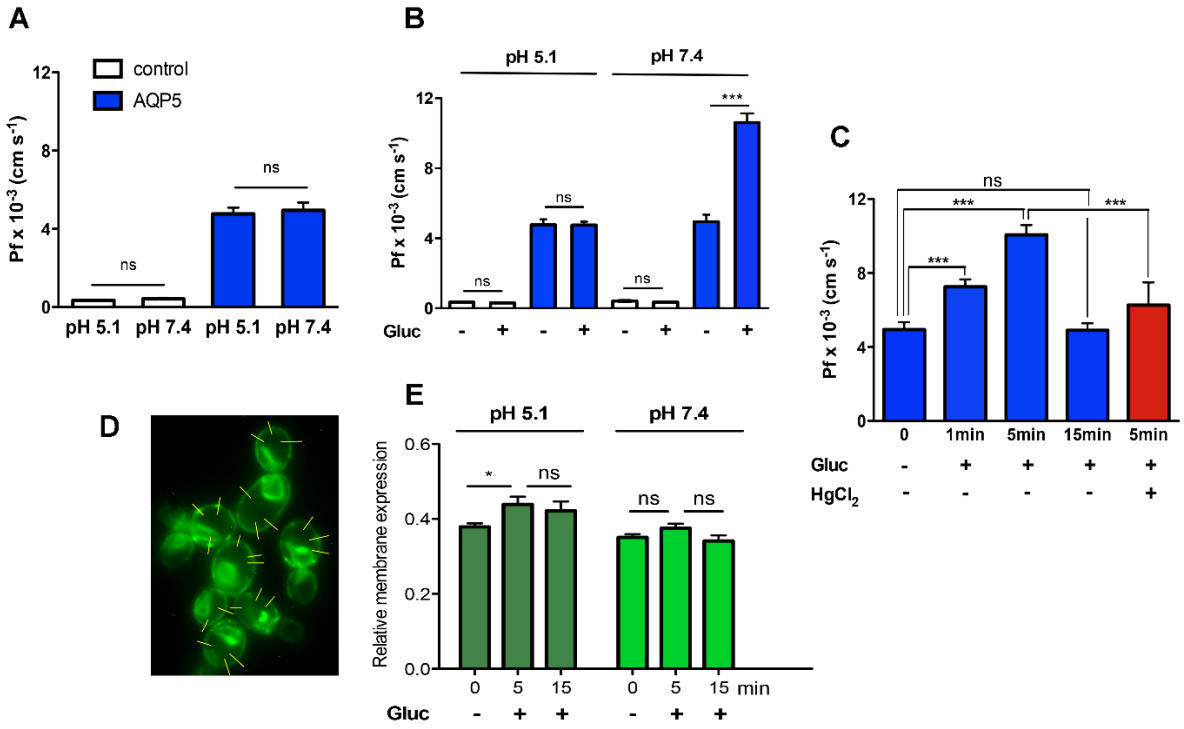

Figure 3.1.2 | Regulation of AQP5 water permeability. (A) Water permeability P_f at pH 5.1 and pH 7.4 of control cells (P_f = (0.35 ± 0.01) × 10^{-3} and (0.41 ± 0.05) × 10^{-3} cm s^{-1}, respectively) and yeast cells expressing AQP5 (P_f = (4.77 ± 0.32) × 10^{-3} and (4.94 ± 0.40) × 10^{-3} cm s^{-1}, respectively); **(B)** Water permeability P_f at pH 5.1 and pH 7.4 upon an external glucose pulse **(C)** Time course of glucose-induced phosphorylation (1, 5 and 15 min, pH 7.4) and inhibition of AQP5 by $HgCl_2$ 0.05 mM. Data are mean ± SD of 10 measurements; **(D)** Representative epifluorescence images of GFP-tagged AQP5 localization in yeast cells (100x objective); linear intensity profiles are indicated (yellow lines); and (E) Relative membrane expression of AQP5 calculated from fluorescence intensity profiles (30 cells in each experimental condition, 3 profiles for each cell, from at 3 independent experiments). ns, non significant, * p < 0.5, *** p < 0.001.

In addition, we investigated the time course of AQP5 activation after glucose addition at pH 7.4 (Figure 3.1.2 C). Following a glucose pulse, a transient strong increase of cAMP with peak values around 1–2 min that progressively decay to about their basal levels, was previously reported in yeast cells [19,20]. Our data show a significant increase of AQP5 water permeability after 1 min that was further increased at 5 min; after 15 min, glucose exposure no longer produces effect on AQP5 permeability, possibly due to the decay of cAMP synthesis. Yeast cells were subsequently incubated for 5 min simultaneously with glucose and $HgCl_2$, a well-known aquaporin inhibitor (Figure 3.1.2 C). In this case, the glucose-induced increase in P_f of AQP5 cells was partially abolished (P_f = (6.26 ± 1.23) × 10^{-3} cm s^{-1}. The inhibitor alone had no effect on P_f of control cells.

Afterwards, to determine whether cAMP-mediated increase in water permeability was due to AQP5 increased trafficking and abundance or to opening of the channel, we measured GFP-tagged AQP5 relative membrane expression (Figure 3.1.2 D). Before glucose addition, the membrane abundance measured at pH 5.1 and pH 7.4 was not significantly different (0.37 ± 0.07 and 0.35 ± 0.07, respectively) (Figure 3.1.2 E). Although membrane abundance was slightly increased after 5 min glucose pulse (implying that also trafficking is triggered by phosphorylation, as previously reported by Kitchen et al. [2]), this effect was only detected at extracellular pH 5.1 (0.49 ± 0.08 and 0.47 ± 0.12 at 5 and 15 min, respectively). Interestingly, at pH 7.4, no significant difference could be detected after 5 min (0.37 ± 0.07), and at both pHs the membrane abundance was kept stable at least for 15 min (Figure 3.1.2 E).

Also to consider is the fact that, if a carbon source is available, external shifts in proton concentration in the pH range from 3.0 to 7.5 do not significantly affect yeast internal pH values due to ATPase activity [9]. However, a two-fold increase in P_f with concomitant reduction of E_a after glucose addition only happened at pH

7.4 (Figure 3.1.2 B). No increase was seen at pH 5.1. Interestingly, pH 5.1 is in the range of yeast physiological pH at which the machineries for protein expression, transcription, and trafficking are expected to be in place. If the increase in Pf observed would be simply due to an increase in AQP5 membrane abundance, then it should also be detected at pH 5.1. Hence, since we observe differences in permeability mediated by phosphorylation when the external pH is changed, changes in the channel structure activity rather than in AQP5 membrane abundance might be responsible for the measured difference in permeability.

Figure 3.1.3 A displays the structure of human AQP5 with several consensus phosphorylation sites at cytoplasmic loop D (Ser152 and Ser156) and at C-terminal (Ser231, Ser233, and Thr242) [21]. In Figure 3.1.3 B the top view of the monomer is depicted, with His173 and Ser183 located in the selectivity filter (SF). The distance between these two residues (8.4 Å) was proposed to correspond to the pore wide conformation [4]. All these residues are conserved in rat AQP5 sequence with the exception of Ser233. Phosphorylation of Ser156 was reported to play an important role in AQP5 translocation to the plasma membrane in HEK293 cells [2]. In contrast, another study observed that a mutation on Ser156 had no effect on membrane trafficking but instead affected cell proliferation [14].

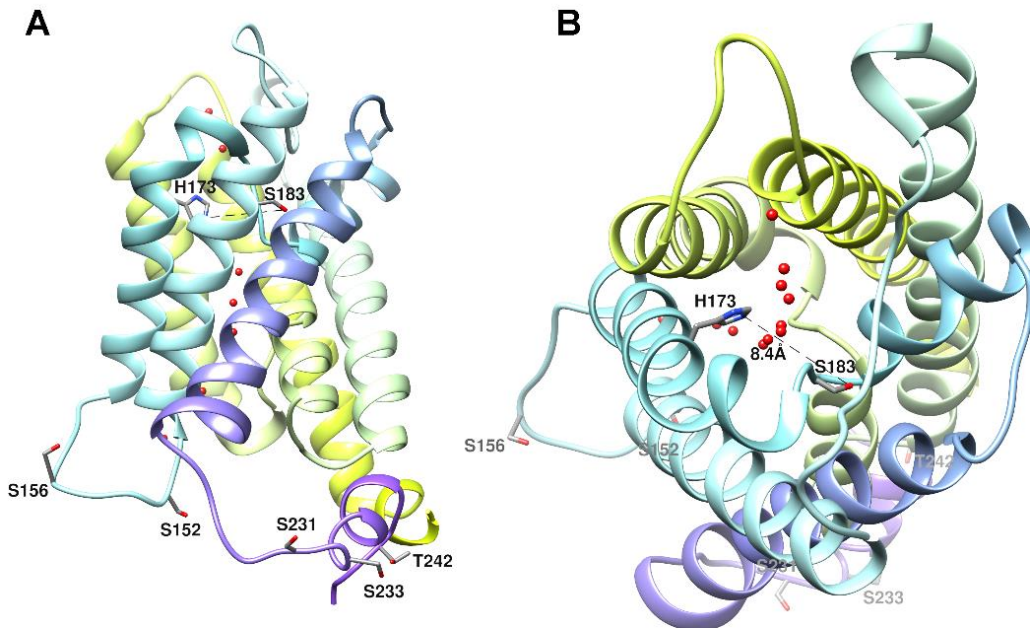

Figure 3.1.3 | Structure of human AQP5 monomer. (A) Side view of the monomer with several phosphorylation consensus sites in the cytoplasmic region (Ser152, Ser156, Ser231, Ser233, and Thr242) shown in licorice representation. Thr259, also a phosphorylation site, is not represented due to the inexistent electron density beyond Pro245 for hAQP5 structure [49]; **(B)** Top view of the monomer with His173 and Ser183 in the selectivity filter (SF) shown in licorice representation. The distance between these two residues (8.4 Å) corresponds to the proposed distance for the SF wide conformation [33]. Water molecules are shown as red spheres along the channel pore. Structures were generated with Chimera (http://www.cgl.ucsf.edu/chimera) and are based on AQP5 X-ray structure (PDB databank code 3D9S).

Thr259 is not represented in Figure 3.1.3 A due to the inexistent electron density beyond Pro245 in hAQP5 structure. However, this residue is also an interesting phosphorylation site due to the homology to Ser256 in hAQP2. It has been demonstrated that phosphorylation of Ser256, besides triggering AQP2 insertion at apical plasma membrane, is also essential to modulate AQP2 function, increasing water permeability of the individual channel [22,23]. In a recent study, extracellular acidic pH was shown to attenuate AQP2 hormone-induced

phosphorylation and membrane apical trafficking, probably by inhibition of vasopressin V2 receptor-G protein-cAMP-PKA actions [24].

From a structural point of view, Ser152 and Ser156 are strong candidates prone to induce conformation changes at loop D with impact on the protein channel monomeric conformation. However, phosphomimetic mutations of Ser156 were able to increase membrane expression but did not cause any significant structural change [2]. It is thus reasonable to anticipate that more than one phosphorylation site is necessary to produce a measurable conformation change. Phosphorylated AQP5 (Ser and Thr residues facing the cytoplasmic region, Figure 3.1.3 A) may induce a change in channel conformation, and in this new conformation de-protonation of His183 residue (facing the outer membrane) may occur at pH 7.4, with widening of the channel pore (Figure 3.1.3 B). While at pH 7.4 the channel is wide open, at pH 5.1 the protonated residues and putative hydrogen-bond interactions hold the channel in the narrow open conformation, with lower permeability. Interestingly, the human AQP5 crystals were obtained at pH 7.0–7.6, the pH range where, in this study, phosphorylated AQP5 shows increased permeability.

3.1.4 Conclusions

Human AQP5 was the first aquaporin crystalized in full tetrameric assembly [21] and its trafficking and membrane expression are known to be regulated by phosphorylation [2] through PKA and RAS signaling pathways that promote cell proliferation [13]. The fact that AQP5 was found preferentially phosphorylated in tumor cells strongly suggests that its regulation might be involved in tumorigenesis.

Our data provides experimental evidences for the direct regulation of AQP5 water permeability by pH dependent on phosphorylation. We observed that AQP5 does

not change its activity by external acidification, but phosphorylation makes the AQP5 channel prone to pH sensing.

At mammalian physiologic conditions (pH 7.4) phosphorylated AQP5 enables larger fluxes of water through membranes, which may contribute to rapid changes in cell volume and shape and thus facilitate cell migration and proliferation as seen in cancer cells. In this context, AQP5 modulation by phosphorylation may represent a novel strategy with potential application in cancer treatment. On the other hand, acidic conditions favors channel narrowing, allowing fine-tuning of cell volume. Notably, although natural for yeast cells, the low pH tested is far below the pH found in mammalian tissues, even in solid tumors where it can reach pH 6.5 [25]. There are, however, a few mammalian acidic physiological conditions where pH gets close to this value. For instance, sweat shows acidic pH levels, between 4.6 and 5.4 [26], and in the skin the protective sweat acid mantle acidity ranges from 4 to 5.5 [26]; the pH of human stomach is highly acidic, usually from 1 to 2; osteoclasts' acidic microenvironment below pH 5.5 is critical for the bone resorption [27]; an acidic pH luminal fluid microenvironment is important for sperm maturation [28]. Interestingly, AQP5 was found expressed in sweat glands [29], gastric mucosa [30], bone cells [31], and in the epididymis [28]. In all these tissues, effective mechanisms of water flux regulation induced by pH fluctuations might be advantageous to prevent excessive water reabsorption and control cell volume and shape.

3.1.5 Experimental Section

Yeast Strains and Growth Conditions - Plasmid (pcDNA3) with *Rattus norvegicus* AQP5 cDNA (pcDNA3-AQP5), kindly provided by Prof. Miriam Eschevarria, Virgen del Rocio University Hospital, Seville, Spain, was used for AQP5 cDNA amplification. The centromeric plasmid pUG35 was used for cloning AQP5, conferring C-terminal GFP

tagging, MET25 promoter, and CYC1-T terminator [32]. For plasmids propagation, *Escherichia coli* DH5α was used as host [33]. *E. coli* transformants were maintained and grown in Luria-Bertani broth (LB) supplemented with ampicillin (100 μg/mL), at 37 °C [34]. Plasmid DNA was extracted from *E. coli* using a GenElute™ Plasmid Miniprep Kit (Sigma-Aldrich, St. Louis, MO, USA).

Saccharomyces cerevisiae (10560-6B MATa leu2::hisG tpr1::hisG his3::hisG ura3-52 aqy1D::KanMX aqy2D::KanMX) from now on designated as aqy-null, was used as host strain for heterologous expression of AQP5. The aqy-null strain was grown and maintained in YPD medium (2% w/v peptone, 1% w/v yeast extract, 2% w/v glucose). Transformed yeast strain was grown in YNB medium (2% w/v glucose, 0.67% (DIFCO) Yeast Nitrogen Base) supplemented with the adequate requirements for prototrophic growth [35] and maintained in the same medium with 2% (w/v) agar. For stopped-flow assays, the same medium was used for yeast cell growth. For all experiments, cells were grown to mid exponential phase (OD_{600nm} 1-2).

Cloning and Heterologous Expression of AQP5 in *S. cerevisiae* - Briefly, after propagation, isolation, and purification of pcDNA3_AQP5, AQP5-specific primers modified to incorporate restriction sites for *Spe*I (underlined) and *Cla*I (underlined) (5'-GGACTAGTCCT ATGAAAAAGGAGGTGTGCTCCCTTGC-3' and 5'-CCATCGATGGAGTGTGC CGTCAG CTCGATG-3', respectively) were designed and used for PCR amplification of AQP5 cDNA (carried out in an Eppendorff thermocycler using Taq Change DNA polymerase from NZYTech, Lisbon, Portugal). The PCR product was digested with *Spe*I and *Cla*I restriction enzymes, purified (using a Wizard® SV Gel and the PCR Clean-Up System kit Promega) and cloned (using T4 DNA Ligase Roche) into the corresponding restriction sites of pUG35 digested with the same restriction enzymes, behind the MET25 promoter and in frame with the GFP sequence and CYC1-T terminator, according to standard protocols [34], to construct the expression plasmid pUG35-AQP5. This plasmid was propagated in *E. coli* DH5α. After extraction and purification, fidelity of constructs and correct orientation of AQP5-cDNA were verified by PCR amplification and

DNA sequencing. Transformation of the *S. cerevisiae* aqy-null strain with pUG35-AQP5 was performed using the lithium acetate method described in [36]. The same strain was also transformed using an empty pUG35 vector (which does not contain AQP5 cDNA) to be used as a control (further indicated as control strain). Transformants were selected on YNB medium without uracil as auxotrofic marker.

AQP Subcellular Location by Fluorescence Microscopy - For subcellular localization of GFP-tagged AQPs in *S. cerevisiae*, yeast cells in the mid-exponential phase were observed using a Zeiss Axiovert 200 fluorescence microscope (Zeiss, Jena, Germany), at 495 nm excitation and 535 nm emission wavelengths. Fluorescence microscopy images were captured with a digital camera (CoolSNAP EZ, Photometrics, Tucson, AZ, USA) and using the Metafluor software (Molecular Devices, Sunyvale, CA, USA).

AQP5 membrane expression was measured by evaluating GFP-protein fluorescence intensity according to [2,37]. A linear profile that crosses the cell membrane was generated and analyzed using the software ImageJ (https://imagej.net). The intensity profile along the line path from at least 30 cells in each experimental condition (n = 3) was recorded and for each cell three profile lines were taken. The background intensity along the same distance was measured and subtracted from the peak fluorescence intensity over each line, and the obtained difference divided by the maximal fluorescence to calculate the relative membrane expression.

Cell Sampling and CFDA Loading - For water permeability assays, yeast transformants grown up to OD_{600nm} 1-2, were harvested by centrifugation (5000 g; 5 min; 4 °C) (Allegra® 6 Series Centrifuges, Beckman Coulter®, Brea, CA, USA), washed 3 times and resuspended in ice cold sorbitol (1.4 M) K^+-citrate (50 mM pH 5.1 or 7.4) buffer up to a concentration of 0.3 g/mL wet weight and cells were incubated on ice for at least 90 min. Prior to permeability assays, cells were preloaded with the non-fluorescent precursor 5(6)-carboxyfluorescein diacetate (CFDA, 1 mM, 10 min at 30 °C), which is intracellularly

hydrolyzed yielding the impermeable fluorescent form (CF). Cells were then diluted (1:10) in 1.4 M sorbitol buffer and immediately used for experiments.

Cell Volume Measurements - Equilibrium cell volumes (V_o) were obtained after loading the cells with CFDA under an epifluorescent microscope (Zeiss Axiovert, Zeiss, Jena, Germany) equipped with a digital camera. Cells were assumed to have a spherical shape with a diameter calculated as the average of the maximum and minimum dimensions of each cell.

Water Permeability Assays - Permeability assays were performed by stopped-flow fluorescence spectroscopy as previously described [38], using a HI-TECH Scientific PQ/SF-53 stopped-flow apparatus, which has a 2-ms dead time, controlled temperature, interfaced with a microcomputer. Experiments were performed at temperatures ranging from 9 to 34 °C. Four runs were usually stored and analyzed in each experimental condition. In each run, 0.1 mL of cell suspension was mixed with an equal volume of hyperosmotic sorbitol buffer (2.1 M sorbitol, 50 mM K-citrate, pH 5.1 or 7.4) producing an inwardly directed gradient of the impermeant sorbitol solute that induces water outflow and cell shrinkage. Fluorescence was excited using a 470 nm interference filter and detected using a 530 nm cut-off filter. The time course of cell volume change was followed by fluorescence quenching of the entrapped fluorophore (CF). The recorded fluorescence signals were fitted to a single exponential from which the rate constant (k) was calculated. The osmotic water permeability coefficient, P_f, was estimated from the linear relationship between P_f and k [38], $P_f = k(V_o/A)(1/V_w(osm_{out}))$, where V_w is the molar volume of water, V_o/A is the initial volume to area ratio of the cell population, and (osm_{out}) is the final medium osmolarity after the osmotic shock. The osmolarity of each solution was determined from freezing point depression by a semi-micro-osmometer (Knauer GmbH, Berlin, Germany). The activation energy (E_a) of water transport was evaluated from the slope of the Arrhenius plot (ln P_f as a function of 1/T) multiplied by the gas constant R.

External pH Dependence and *In Vivo* PKA Phosphorylation - Yeast cells were grown and prepared as above-described and incubated in isotonic sorbitol buffer (1.4 M sorbitol, 50 mM K^+-citrate) at two different pH (5.1 and 7.4) for at least 90 min. Deprived of a carbon source and incubated in ice for a long period, yeast cells are considered in starvation. The production of intracellular cAMP and phosphorylation was triggered immediately before water permeability measurements by the addition of 0.1 M glucose (adjusted to pH 5.1 or 7.4) to starved cells [16,17].

Statistical Analysis - All experiments and assays were carried out in triplicate. Mean values were compared using ANOVA followed by unpaired t-test. p-values < 0.05 were considered significantly different.

3.1.6 References

[1] C. Delporte, A. Bryla, J. Perret, Aquaporins in Salivary Glands: From Basic Research to Clinical Applications, Int J Mol Sci 17 (2016).

[2] P. Kitchen, F. Oberg, J. Sjohamn, K. Hedfalk, R.M. Bill, A.C. Conner, M.T. Conner, S. Tornroth-Horsefield, Plasma Membrane Abundance of Human Aquaporin 5 Is Dynamically Regulated by Multiple Pathways, PLoS One 10 (2015) e0143027.

[3] I. Direito, A. Madeira, M.A. Brito, G. Soveral, Aquaporin-5: from structure to function and dysfunction in cancer, Cell Mol Life Sci 73 (2016) 1623-1640.

[4] L. Janosi, M. Ceccarelli, The gating mechanism of the human aquaporin 5 revealed by molecular dynamics simulations, PLoS One 8 (2013) e59897.

[5] D. Alberga, O. Nicolotti, G. Lattanzi, G.P. Nicchia, A. Frigeri, F. Pisani, V. Benfenati, G.F. Mangiatordi, A new gating site in human aquaporin-4: Insights from molecular dynamics simulations, Biochim Biophys Acta 1838 (2014) 3052-3060.

[6] S. Kaptan, M. Assentoft, H.P. Schneider, R.A. Fenton, J.W. Deitmer, N. MacAulay, B.L. de Groot, H95 Is a pH-Dependent Gate in Aquaporin 4, Structure 23 (2015) 2309-2318.

[7] Y. Yukutake, M. Yasui, Regulation of water permeability through aquaporin-4, Neuroscience 168 (2010) 885-891.

[8] S.F. Altschul, T.L. Madden, A.A. Schaffer, J. Zhang, Z. Zhang, W. Miller, D.J. Lipman, Gapped BLAST and PSI-BLAST: a new generation of protein database search programs, Nucleic Acids Res 25 (1997) 3389-3402.

[9] R. Orij, J. Postmus, A. Ter Beek, S. Brul, G.J. Smits, In vivo measurement of cytosolic and mitochondrial pH using a pH-sensitive GFP derivative in Saccharomyces cerevisiae reveals a relation between intracellular pH and growth, Microbiology 155 (2009) 268-278.

[10] C. Kosugi-Tanaka, X. Li, C. Yao, T. Akamatsu, N. Kanamori, K. Hosoi, Protein kinase A-regulated membrane trafficking of a green fluorescent protein-aquaporin 5 chimera in MDCK cells, Biochim Biophys Acta 1763 (2006) 337-344.
[11] F. Yang, J.D. Kawedia, A.G. Menon, Cyclic AMP regulates aquaporin 5 expression at both transcriptional and post-transcriptional levels through a protein kinase A pathway, J Biol Chem 278 (2003) 32173-32180.
[12] V. Sidhaye, J.D. Hoffert, L.S. King, cAMP has distinct acute and chronic effects on aquaporin-5 in lung epithelial cells, J Biol Chem 280 (2005) 3590-3596.
[13] J. Woo, J. Lee, M.S. Kim, S.J. Jang, D. Sidransky, C. Moon, The effect of aquaporin 5 overexpression on the Ras signaling pathway, Biochem Biophys Res Commun 367 (2008) 291-298.
[14] J. Woo, J. Lee, Y.K. Chae, M.S. Kim, J.H. Baek, J.C. Park, M.J. Park, I.M. Smith, B. Trink, E. Ratovitski, T. Lee, B. Park, S.J. Jang, J.C. Soria, J.A. Califano, D. Sidransky, C. Moon, Overexpression of AQP5, a putative oncogene, promotes cell growth and transformation, Cancer Lett 264 (2008) 54-62.
[15] R. Van Wijk, T.M. Konijn, Cyclic 3', 5'-amp in Saccharomyces carlsbergensis under various conditions of catabolite repression, FEBS Lett 13 (1971) 184-186.
[16] K. Mbonyi, L. van Aelst, J.C. Arguelles, A.W. Jans, J.M. Thevelein, Glucose-induced hyperaccumulation of cyclic AMP and defective glucose repression in yeast strains with reduced activity of cyclic AMP-dependent protein kinase, Mol Cell Biol 10 (1990) 4518-4523.
[17] J.M. Thevelein, J.H. de Winde, Novel sensing mechanisms and targets for the cAMP-protein kinase A pathway in the yeast Saccharomyces cerevisiae, Mol Microbiol 33 (1999) 904-918.
[18] M. Johnston, J.H. Kim, Glucose as a hormone: receptor-mediated glucose sensing in the yeast Saccharomyces cerevisiae, Biochem Soc Trans 33 (2005) 247-252.
[19] F. Rolland, V. Wanke, L. Cauwenberg, P. Ma, E. Boles, M. Vanoni, J.H. de Winde, J.M. Thevelein, J. Winderickx, The role of hexose transport and phosphorylation in cAMP signalling in the yeast Saccharomyces cerevisiae, FEMS Yeast Res 1 (2001) 33-45.
[20] J.B. van der Plaat, Cyclic 3',5'-adenosine monophosphate stimulates trehalose degradation in baker's yeast, Biochem Biophys Res Commun 56 (1974) 580-587.
[21] R. Horsefield, K. Norden, M. Fellert, A. Backmark, S. Tornroth-Horsefield, A.C. Terwisscha van Scheltinga, J. Kvassman, P. Kjellbom, U. Johanson, R. Neutze, High-resolution x-ray structure of human aquaporin 5, Proc Natl Acad Sci U S A 105 (2008) 13327-13332.
[22] K. Eto, Y. Noda, S. Horikawa, S. Uchida, S. Sasaki, Phosphorylation of aquaporin-2 regulates its water permeability, J Biol Chem 285 (2010) 40777-40784.
[23] M. Kuwahara, K. Fushimi, Y. Terada, L. Bai, F. Marumo, S. Sasaki, cAMP-dependent phosphorylation stimulates water permeability of aquaporin-collecting duct water channel protein expressed in Xenopus oocytes, J Biol Chem 270 (1995) 10384-10387.
[24] H.J. Choi, H.J. Jung, T.H. Kwon, Extracellular pH affects phosphorylation and intracellular trafficking of AQP2 in inner medullary collecting duct cells, Am J Physiol Renal Physiol 308 (2015) F737-748.

[25] V. Estrella, T. Chen, M. Lloyd, J. Wojtkowiak, H.H. Cornnell, A. Ibrahim-Hashim, K. Bailey, Y. Balagurunathan, J.M. Rothberg, B.F. Sloane, J. Johnson, R.A. Gatenby, R.J. Gillies, Acidity generated by the tumor microenvironment drives local invasion, Cancer Res 73 (2013) 1524-1535.
[26] F. Herrmann, L. Mandol, Studies of pH of sweat produced by different forms of stimulation, J Invest Dermatol 24 (1955) 225-246.
[27] Y. Kato, S. Ozawa, C. Miyamoto, Y. Maehata, A. Suzuki, T. Maeda, Y. Baba, Acidic extracellular microenvironment and cancer, Cancer Cell Int 13 (2013) 89.
[28] N. Da Silva, C. Pietrement, D. Brown, S. Breton, Segmental and cellular expression of aquaporins in the male excurrent duct, Biochim Biophys Acta 1758 (2006) 1025-1033.
[29] Q. Du, M. Lin, J.H. Yang, J.F. Chen, Y.R. Tu, Overexpression of AQP5 Was Detected in Axillary Sweat Glands of Primary Focal Hyperhidrosis Patients, Dermatology 232 (2016) 150-155.
[30] M.N. Parvin, K. Tsumura, T. Akamatsu, N. Kanamori, K. Hosoi, Expression and localization of AQP5 in the stomach and duodenum of the rat, Biochim Biophys Acta 1542 (2002) 116-124.
[31] F. Yi, M. Khan, H. Gao, F. Hao, M. Sun, L. Zhong, C. Lu, X. Feng, T. Ma, Increased differentiation capacity of bone marrow-derived mesenchymal stem cells in aquaporin-5 deficiency, Stem Cells Dev 21 (2012) 2495-2507.
[32] U. Guldener, S. Heck, T. Fielder, J. Beinhauer, J.H. Hegemann, A new efficient gene disruption cassette for repeated use in budding yeast, Nucleic Acids Res 24 (1996) 2519-2524.
[33] D. Hanahan, Techniques for transformation of Escherichia coli, in: D.M. Glover (Ed.), DNA cloning: a practical approach,, IRL Press, Oxford, United Kingdom, 1985, pp. 109-135.
[34] J. Sambrook, E.F. Fritsch, T. Maniatis, Molecular Cloning: A Laboratory Manual, 2nd edn ed., Cold Spring Harbor, NY, 1989.
[35] J.T. Pronk, Auxotrophic yeast strains in fundamental and applied research, Appl Environ Microbiol 68 (2002) 2095-2100.
[36] R.D. Geitz, R.H. Schiestl, Transforming Yeast with DNA, Methods in Molecular and Cellular Biology 5 (1995) 255–269.
[37] S.D. Joshi, L.A. Davidson, Live-cell imaging and quantitative analysis of embryonic epithelial cells in Xenopus laevis, J Vis Exp (2010).
[38] G. Soveral, A. Madeira, M.C. Loureiro-Dias, T.F. Moura, Water transport in intact yeast cells as assessed by fluorescence self-quenching, Appl Environ Microbiol 73 (2007) 2341-2343.

3.2 Gating mechanism of Aquaporin-3

3.2.1 Abstract

The pH gating of human AQP3 and its effects on both water and glycerol transport permeability have been fully characterized for the first time using a human red blood cell model (RBC). For comparison, the effects of pH on the gating of rat AQP3 have also been characterized in yeast. The obtained results highlight similarities as well as differences between the two isoforms. Our data show that both human and rat AQP3 are gated by pH, the latter with the pH gating parameters here described for the first time. However, different features were observed for glycerol and water permeation in the two cases. Through molecular modelling studies, we could study the pH dependent closure/opening of the hAQP3 channel at a molecular level, allowing us to predict gating mechanisms of this isoform and possibly of other aquaglyceroporins. The obtained results are discussed in terms of the putative physiological roles of pH gating in aquaglyceroporins and the opening of new possibilities to inhibitors design.

3.2.2 Introduction

Aquaporin-3 (AQP3) has a wide tissue distribution in the epithelial cells of kidneys, airways and skin, suggesting a role in water reabsorption, mucosal secretions, skin hydration, and cell volume regulation [1]. Moreover, recent studies demonstrated an aberrant AQP3 expression in tumour cells of different origins, particularly in aggressive tumours [2], suggesting this enhanced protein expression to be of diagnostic and prognostic value.

The first publication in 1999, describing AQP3 gating by pH, used Xenopus oocytes expressing rat AQP3 (rAQP3) and revealed only a slightly different pK_a for water and glycerol permeability (6.4 and 6.1, respectively) but a markedly different

Hill coefficient. In fact, the Hill slope was calculated to be ca. 3 for water and 6 for glycerol permeability, respectively [3]. At the time of this first study, little was understood about the possible conformation or residue distribution in the folded functional AQP3, leading the authors to speculate that the pH sensitive residues would be along the channel. Instead, in a later report by Zelenina et al. [4], who studied the mechanism of pH gating of human AQP3 (hAQP3) transfected into lung cells, thanks to the availability of additional sequence information, it could be hypothesized that the pH sensitive residues are likely to be located in loops at the monomers' interfaces, within the AQP3 tetrameric assembly, instead of lining the protein channel. Moreover, four main amino acid residues were identified as pH-sensitive residues by site-directed mutagenesis: His53, His154, Tyr124 and Ser152, all located in extracellular loops. Mutations in these residues led to loss of pH sensitivity, a decrease in water permeability or a shift in the pH sensitivity range [4]. However, in this study the effects of pH gating on permeation by glycerol were not described. Interestingly, both papers postulate that the differences in Hill slope values for water and glycerol are mainly due to different hydrogen bonding capability of the two substrates, while permeating the monomeric aquaporin pore [3,4]. However, so far, this idea remains to be validated.

Thus, we investigated the pH gating of rAQP3, in a different system than previously reported, using this isoform homolog expressed in yeast. Furthermore, we extended our study to human AQP3 and its effects on both water and glycerol permeability using human red blood cells (hRBC), considered a very good model to assess AQP3 activity [5].

3.2.3 Results and Discussion

pH gating of rat AQP3 in yeast

In our study we first evaluated rAQP3 gating, in a yeast model, using stopped-flow spectroscopy. Yeast cells were transformed with either the empty plasmid (control cells) or the plasmid containing the rat AQP3 gene (mentioned as rAQP3 cells, for clarity). The expression of rAQP3 in the *S. cerevisiae* model was assessed by fluorescence microscopy, using GFP tagging. In transformed cells, rAQP3-GFP is localized at the cellular membrane, while cells with empty plasmid have a homogeneous cytoplasmic distribution (Supplementary Figure S3.2.1). Stopped-flow technique allows volume monitoring of cells subjected to hypo and hyperosmotic stress: when cells are exposed to hyperosmotic shock with impermeant solutes, water outflow induces cell shrinkage. Conversely, when the osmotic shock is provided by a permeable solute as glycerol, cells first shrink due to water outflow and afterwards swell again due to glycerol passage. Thus, water and glycerol permeability is then evaluated according to cell swelling or shrinkage monitored by 90° light scattering, detected by the stopped-flow. In the case of the yeast cell model, the cells are pre-loaded with carboxyfluorescein, and the fluorescence intensity reflects volume changes.

At first, in order to evaluate if the observed effect was due to AQP3 being expressed in the yeast cells, both groups of control and rAQP3 were incubated at two different pH values, namely pH 5 and 7. These pH conditions were chosen based on previous literature [3,4], to have closed (pH 5) and open (pH 7) AQP3. In Figure 3.2.1 the water and glycerol permeability (P_f and P_{Gly}, respectively) of control and rAQP3 cells are shown. It is possible to observe that, while control cells have no glycerol permeability, they do show basal water permeability at both tested pH conditions, due to the intrinsic water permeability of the membrane

lipid bilayer. Interestingly, from panel C of Figure 3.2.1 it is evident that, at pH 5, there is no permeation by glycerol, with a significant increase at pH 7, which clearly demonstrate the close and open states of rAQP3.

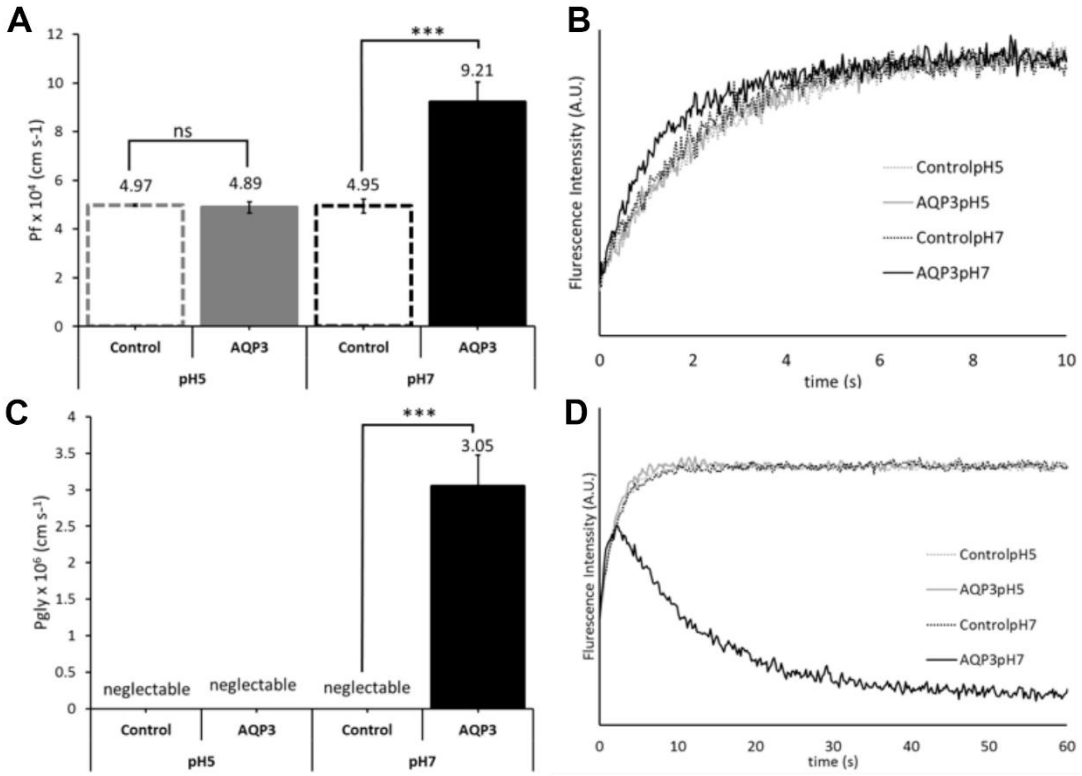

Figure 3.2.1 | Water (**A**,**B**) and glycerol (**C**, **D**) permeability (P_f and P_{Gly}) in control yeast cells (transformed with the empty vector) (dashed) and in yeast expressing rAQP3 (solid) at pH 5 (grey) and 7 (black). Panel **A** shows the water permeability (P_f) of control and AQP3-expressing cells, at pH 5 and pH 7. Panel **B** shows the changes in fluorescence intensity obtained when yeast transformants are confronted with a hyperosmotic sorbitol solution of tonicity 1.25 triggering cell shrinkage due water outflow. Panel **C** shows the glycerol permeability (P_{Gly}) of control and AQP3-expressing cells, at pH 5 and pH 7, while panel **D** shows the changes of fluorescence intensity obtained when cells are confronted with a hyperosmotic glycerol solution. After a first water outflow due to the osmotic gradient, the AQP3-expressing cells re-swell due to glycerol entrance at pH7. *** $p<0.001$. [Data obtained jointly with Ana Paula Martins]

Since the control cells present a basal water permeability that is not altered by the expression of rAQP3 when incubated at pH 5, it is possible to normalize the P_f that corresponds to the permeability of rAQP3 alone. Knowing from these results (Figure 3.2.1) and previous studies that hAQP3 is in a closed state at low pH (ca. 5) [3], the normalized water permeability via rAQP3 was obtained by subtracting the permeability values of control cells at each pH value. For P_{Gly}, this subtraction was not necessary since the control cells show no glycerol permeability at any pH. The rAQP3 permeability for both water and glycerol are shown in Figure 3.3.2. We can observe that the channel is closed for both water and glycerol between pH 5 and 6 and has maximum permeability at pH 6.5 (glycerol) and pH 7 (water), respectively. This behaviour and Hill slope values found for water and glycerol in the rAQP3 isoform (see Table 3.2.1) are similar to those reported previously [3].

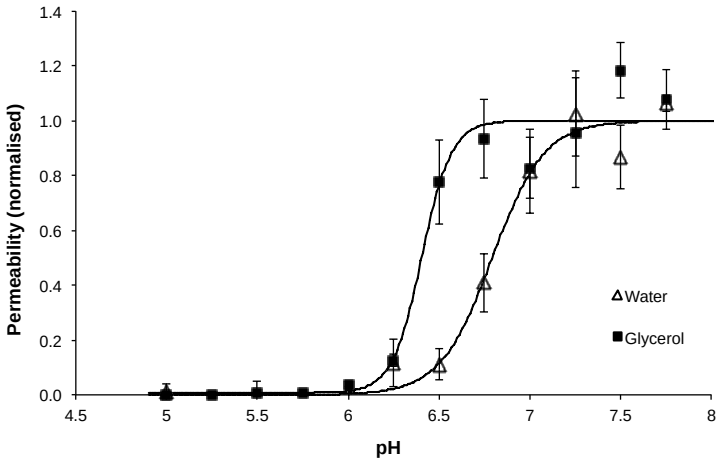

Figure 3.2.2 | Water and glycerol permeability (P_f and P_{Gly}, normalized) in yeast cells expressing rAQP3 versus pH. The fit is according to Hill equation. [Data obtained jointly with Ana Paula Martins]

Table 3.2.1 | pKa and Hill slope values for water and glycerol, of human and rat AQP3, obtained by fitting the data presented in Figures 3.21 and 3.2.2. [Data obtained jointly with Ana Paula Martins]

AQP3 variant	**pK_a**		**Hill slope**	
	Water	*Glycerol*	*Water*	*Glycerol*
rat	6.80 ±	6.40 ±	3.00 ±	5.30 ±
human	6.08 ±	6.12 ±	1.64 ±	3.93 ±

pH gating of human AQP3 in hRBC

Afterwards, we evaluated hAQP3 gating in RBC. RBC co-express hAQP1 (selective for water) and hAQP3 (permeating water and glycerol) and thus both isoforms contribute for water permeability. Previous studies showed that human AQP1 is not gated by pH [3,6] and thus any pH-dependent effect on hRBC water permeability would be due to individual gating of hAQP3. Knowing that pH does not influence water permeation via lipid bilayer nor via hAQP1, water permeability corresponding exclusively to hAQP3 was obtained by subtracting the total cell permeability at pH 5 (where AQP3 is in the closed state [3,4]) from the total permeability at each pH value (Figure 3.2.3). In accordance with previous studies [3,4], we observed a maximum permeability for both water and glycerol between pH 6.5 and 7.5, and a decreased permeability and pore closure at lower pH, with the pore completely closed at pH 5.

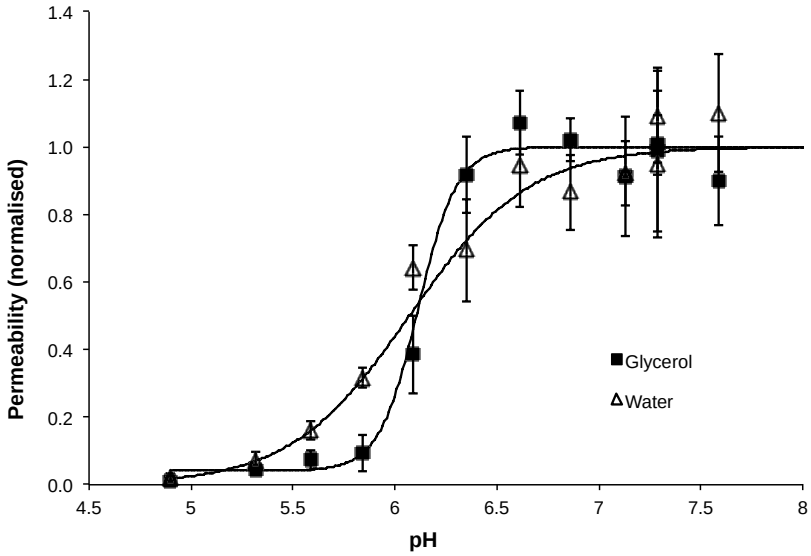

Figure 3.2.3 | Water and glycerol permeability (P_f and P_{Gly} normalized) in human red blood cells (RBC) versus pH. The fit is according to Hill equation. [Data obtained by Ana Paula Martins]

The calculated pK_a values for both water and glycerol were found to be approximately the same, ca. 6.1, with Hill slopes of about 2 and 4, respectively. While the pK_a for glycerol permeability is in accordance with our data on rAQP3, the pK_a value for water is slightly lower (6.1 vs 6.8). Notably, while the Hill coefficients vary from those calculated for rAQP3 - which may be due to both differences in protein sequence or in the selected cellular model - they have the same 2-fold difference (Table 3.2.1). It is worth mentioning that in spite of the strong sequence homology (ca. 95%) between the two isoforms still the 5% difference in sequence may account for a different mechanism of inhibition, as will be discussed further.

Hill coefficients, as black boxes parameters, may be subjected to different interpretations. One explanation found in literature for this difference of half the value for water, when compared to glycerol, is based on the Eyring energy barrier model [7], and explained by the differences in activation energy (E_a) of both

solutes. Interestingly, the measured activations energies for water and glycerol in RBC evidenced a two-fold value for glycerol permeability [8]. It was hypothesized that, as E_a for water permeability is low, water molecules cross the channel by forming a single line of hydrogen bonds, while glycerol, with higher E_a, and having three OH groups, will establish more hydrogen bonds than water molecules when passing through the channel [7]. In fact, such hydrogen bond network for both water and glycerol is evidenced by X-ray studies of the bacterial glycerol facilitator (bGlpF) channel [9] and of the *P. falciparum* isoform (pfAQP) [10] (Figure 3.2.4). Moreover, glycerol molecules have their OH groups pointing towards the hydrophilic side of the channel, favouring such hydrogen bond network. In the case of hAQP3, we can also observe this phenomenon in molecular dynamics (MD) simulations [11]. Remarkably, in this latter study the number of hydrogen bonds in the crystal structures, as well as in the MD simulations, is similar to the Hill slopes found by us for hAQP3 in RBC, approximately 1.5 for water and 4 for glycerol.

Although the importance of H-bonding interactions between substrates and amino acid residues inside the AQP3 channel cannot be underestimated, and certainly plays a role in determining the activation energies of each substrate, recent experimental findings from our groups on the pH gating of aquaglyceroporin-7 (hAQP7) (unpublished data) indicate that the Hill slope is similar for water and glycerol. Therefore, other factors may influence the overall pH gating mechanisms of AQPs, in addition to the number of H-bonds between substrates and the protein channel.

A second explanation for the observed difference in Hill coefficient values is the amount of titrable residues inside the channel, as postulated previously by Zeuthen et al [3]. This theory is based on the possible competition between the H^+ and glycerol molecules for the protonable side-chains. A phenomenon of

noncompetitive inhibition of glycerol binding, by two protons, has been observed in RBC [12]. The limitation of this theory is the fact that the titrable residues would be located in the channel lining, where they could affect glycerol H-bond formation. Later work on aquaporin sequencing and structure showed that hydrophilic and hydrophobic sides constitute the aquaporin lining and few to no residues are actually titrable.

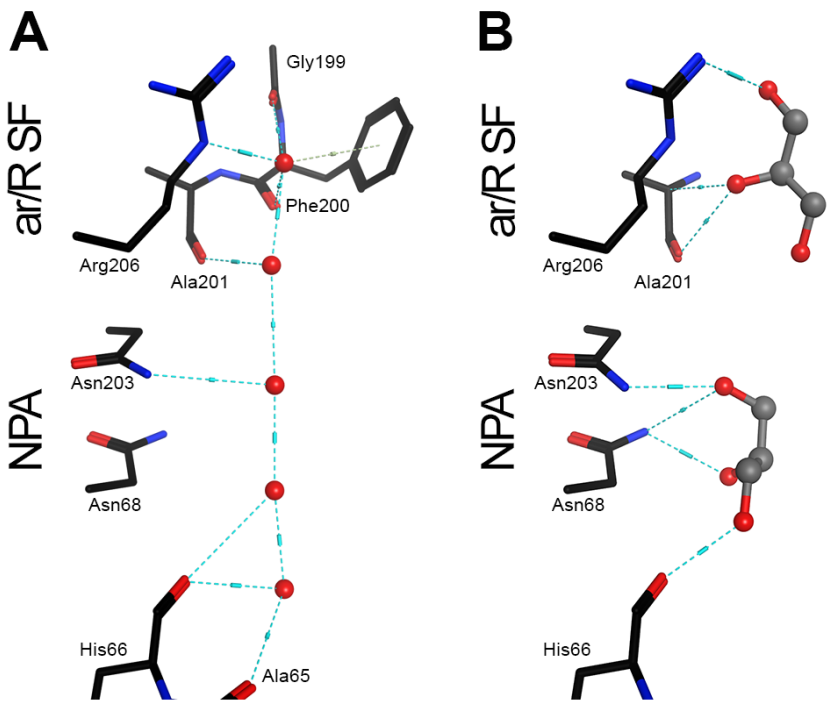

Figure 3.2.4 | H-bond network of water **(A)** and glycerol **(B)**, X-ray structure of bacterial glycerol facilitator (bGlpF) with water **(A)**, pdb1LDA, and glycerol **(B)**, pdb1FX8. [Data obtained by Andreia de Almeida]

Interestingly, analysing not only the Hill slope but also the raw data of the titration curve (shown in Figure 3.2.3) the decrease in water permeability appears to have an earlier onset, but also seems to be more gradual than that of glycerol as a function of pH. However, it is important to distinguish between the steepness of

the titration curves (Hill slope), which is related to how abruptly the channel stops permeating a substrate, and the exact pH at which we observe a change in permeability. Regarding the different steepness of water and glycerol permeability, the phenomenon may be explained by the smaller size of a water molecule, when compared to glycerol. In fact, protonation of certain residues in the protein, even in loops, may cause structural changes in hAQP3, as seen in other aquaporins [12,13,14,15], which lead to channel's closure. Such changes may abruptly hinder the passage of a bulkier glycerol molecule at a pH where some water molecules can still flow through. This hypothesis is in line with our studies on aquaporin inhibition by Hg^{2+}, where we described the closure of hAQP3 for glycerol passage, but not for water passage, upon structural changes caused by metal binding [11].
Based on these considerations, we suggest that the different protonation states of hAQP3 correspond to different structural conformations. Moreover, since the activation energies of water and glycerol have a two-fold difference, higher for glycerol, it suggests that glycerol permeation is much slower. In fact, in our studies on Hg^{2+} inhibition of hAQP3, we observed an unbiased passage of a glycerol molecule and its permeation was much slower than observed for water [11]. This difference is mainly due to the formation of a higher number of hydrogen bonds inside the channel with lining residues by glycerol.

Investigation of the pH gating mechanism of hAQP3 by molecular modelling

In order to investigate the molecular mechanism of pH gating of hAQP3, a molecular modelling approach previously developed by our group was used [16]. However, in the case of the present study, a homology model of human AQP3 in the tetrameric form was built, instead of the monomeric form, based on the available structure of the bacterial glycerol facilitator (GlpF, pdb code 1LDI) [9].

The final model was obtained by averaging 50 individual models, using MOE software (MOE 2012.10; CCG 2012) [17], as described in the Experimental section.

Analysis of the model shows the common fold, shared by the aquaporin family, containing six transmembrane helices and two half-helices, for each monomer. The two half-helices are located inside of the pore of each monomer and contain the typical NPA (Asp-Pro-Ala) motif that constitutes one of the aquaporin's selectivity filters. The residues in these two NPA motifs are Asn83-Pro84-Ala85, and Asn215-Pro216-Ala217 (Supplementary Figure S3.2.2). Another selectivity filter, the narrowest part of the channel lining, is located near the extracellular entrance and is named ar/R SF (aromatic/arginine selectivity filter). This selectivity filter is an important structural feature of aquaporins, where the arginine is fully conserved in all mammalian aquaporins (Supplementary Figure S3.2.2). The ar/R SF also serves as a distinctive feature among aquaporins, as the composition in amino acids may vary in water and glycerol channels: classical aquaporins have an ar/R SF formed by 4 residues, including commonly a phenylalanine and histidine, while aquaglyceroporins' ar/R SF comprises only three residues. Thus, these differences account for pore size and selectivity among aquaporin isoforms. All these features are observed in our model of hAQP3, where Phe63, Tyr212 and Arg218 constitute the ar/R SF (Supplementary Figure S3.2.2).

According to the previously reported site-directed mutagenesis studies, the molecular mechanism behind the gating of AQP3 involves four titrable residues, namely His53, Tyr124, Ser152 and His154 [4]. However, the lack of structural information about this isoform led the authors only to speculate on the type of interactions these residues could possibly establish with unknown surrounding residues, based on possible similar behaviours of histidines, tyrosines and serines in enzymes. Using our homology model of the tetrameric form of hAQP3, it is possible to locate the pointed residues at the interface of the monomers, closer to

the extracellular side of the protein (Figure 3.2.5). These residues may be involved in important monomer–monomer interactions and their protonation/deprotonation may affect the overall assembly of the tetramer and, consequently, of the water and glycerol permeability. In detail, at pH 7 in our model His53 is located at the central pore lining and its side-chain appears to have the possibility to form H-bonds with residues Thr58, Thr52 and Gln45 in the same monomer while interacting also with the aromatic ring of Phe56, located in an adjacent monomer. These interactions are different in each monomer. Interestingly, mimicking the protonation state of the protein at pH 5 leads to the formation of new H-bonds, namely a second H-bond with Thr52 (this time with its side-chain) Thr204, Gly51 and Thr62. The formation of new H-bonds may cause loop A to move closer to the monomer pore and cause structural modifications in transmembrane-helix 5 (TM5).

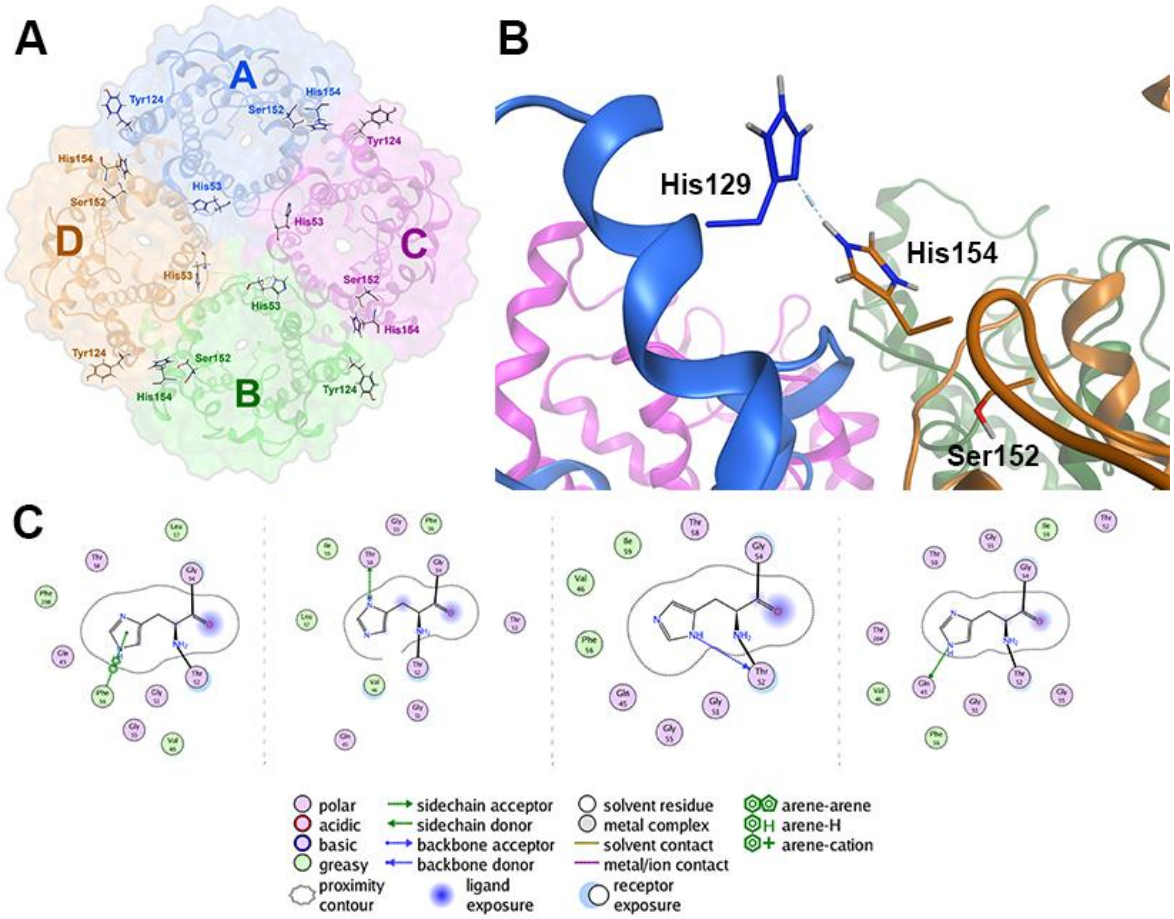

Figure 3.2.5 | Homology model of tetrameric human AQP3. (A) Extracellular top view of the tetrameric form of hAQP3 and position of residues involved in pH regulation. **(B)** Positions of His129 from monomer A and His154 from monomer D, as well as Ser152. The dashed blue line represents the H-bond formed between the two histidines at pH 7. **(C)** Scheme of the interactions of His154 with neighbouring residues, at pH 7, for each of the 4 monomers. [Data obtained by Andreia de Almeida]

On the other hand, Tyr124 does not appear to have a clear role or to be particularly sensitive to pH changes. Due to its very high pKa (typical range for a Tyr side-chain in proteins is 9–12 [18]), it is unlikely that its side-chain is affected by changes in the pH range from 5 to 8. In addition, the side-chain of Tyr124 appears to be pointing out in the direction of the membrane, not participating in any interaction with other residues. The only apparent interactions of this residue are between its

backbone and the backbones of Trp128 and Phe120, contributing to the maintenance of the helical structure. Interestingly, at pH 5, in one monomer it is possible to see the formation of a new H-bond with the backbone of Ile127. This cannot explain the influence of pH on Tyr124 and the possible changes it may induce.

Regarding Ser152 and His154, these residues are located in the region between two adjacent monomers. At pH 7, while the backbone of His154 forms a H-bond with the backbone of Ser152, located in the same loop (loop C), the His154 side-chain forms a H-bond with the side-chain of His129, at the opposite end of loop C of another monomer (Figure 3.2.5 B).

At lower pH, the same interactions appear to be maintained and a new H-bond may be formed with the backbone of Gly153. The formation of this new bond in the same loop may weaken the interaction between the two histidines, leading to a movement of loop C towards the channel opening. This disruption, together with the above-described movement of loop A due to protonation of His53, may be the cause for blockage of the channel for water and glycerol permeability. This structural change of movement of loop C was also observed in the MD studies on mercury inhibition of hAQP3, which leads to a collapse of the ar/R SF [11]. This movement may not be simultaneous as, due to neighbouring amino acid side-chains, the pKa of His53 and His154 may be subjected to small variation, causing a gradual conformational change with a pH decrease (or increase).

Previous studies by Zelenina et al. show that a mutation of His129 to an alanine residue does not affect water permeability or change the pH sensitivity range [4]. However, glycerol permeability was not measured and the contribution of this residue to the mechanism of inhibition of hAQP3 by pH, regarding glycerol permeability, cannot be excluded.

Interestingly, loop movement upon pH changes was also observed for the orthodox water channel bovine AQP0 (bAQP0). This isoform has a maximum of permeability similar to that of hAQP3 at pH 6.5; however it is closed at pH 8.5 [19]. The residues responsible for pH sensibility were identified by site-directed mutagenesis as two histidines: His40 and His122, in loops A and C, respectively. While His40 in bAQP0 is in a similar position to His53 in our model of hAQP3, His122 is in the position corresponding to Ser152 (and close to His154) in hAQP3 (Supplementary Figure S3.2.3). Overall, as described for bAQP0, we propose that key histidines in loops A and C that span the outer vestibule contribute to pH sensitivity in hAQP3. Moreover, insertion of two histidines in similar positions in hAQP1, a non pH-gated aquaporin, induced pH sensitivity in the same range as bAQP0 [19], further confirming the key role of these residues in pH gating.

As observed for the MD study on Hg^{2+} inhibition of hAQP3, by Spinello et al. [11], the closed state of bAQP0 involves the movement of a loop (in this case loop A) and a collapse of the ar/R SF (Supplementary Figure S3.2.4), shown in the X-ray structures of the open and closed bAQP0 [20]. This collapse in the SF appears to be different from the one described for hAQP3, most likely due to differences in amino acid composition and diameter of the channel. Mutations in the histidine of loop A – His40 in AQP0 [19] and His53 in AQP3 [21] – showed a shift of the pH sensitivity towards a more alkaline range. This effect supports the idea that the pKa of histidine residues in different regions of the same protein may be very different, leading to different levels of channel regulation. Other studies reported that the orthodox water channel AQP4 also shows pH-sensitivity, which was recently attributed to one particular histidine residue, His95, predicted by in silico methodologies [22]. His95, located inside the channel and facing the intracellular side, is conserved in all aquaporins, including those that do not show pH-

sensitivity, such as AQP1. Therefore, it is difficult to conclude that it is the only one responsible for the observed pH gating mechanism.

rAQP3 versus hAQP3

Molecular modelling was useful also to explain observed differences among the Hill slope values of hAQP3 with respect to rAQP3 (see Table 3.2.1). Human AQP3 shares a sequence identity higher than 80% with most mammalian AQP3 isoforms. Nonetheless, changes in key residues may change permeability and regulatory features. When compared human and rat AQP3 isoforms, although a sequence similarity of about 95% is observed, they do not share one of the residues that may be involved in the pH gating of the hAQP3, namely His129, which is substituted by an alanine (Supplementary Figure S3.2.5). Even though this mutation does not seem to affect water permeability of hAQP3 [4] its effect on glycerol permeability is unknown. Moreover, a mutation of the same residue on a human and rat isoform may not have the same effect, as a network of hydrogen bonds is a very delicate system and is highly dependent on the neighbouring residues. Therefore, we can only conclude that the mutation H129A is able to produce a functional rAQP3 glycerol and water channel. Additionally, it is possible that the differences in the observed pKa and Hill slope for the human and rat isoforms are due to species differences, even though we cannot exclude the possibility of cell-model differences.

3.2.4 Conclusions

In the present study we investigated the pH gating of rat and human AQP3 by stopped flow spectroscopy. For the first time we were able to fully characterize not only the effects of pH gating on water, but also on glycerol permeability in this

human isoform. In the case of water, the obtained results confirm the previous observations of hAQP3 gating in oocytes [3].

Interestingly, previous reports on rAQP3 pH gating were confirmed in our yeast model, which highlighted differences with the human isoform. In fact, while hAQP3 shows the same pKa for both water and glycerol, the pKa values are similar for water, but different for glycerol in the rAQP3 system. These differences may be due to species differences, even though we cannot exclude that the selected investigational system itself may partly lead to this variation.

In the light of the experimental Hill slope values for water and glycerol, a few theories on differences in the pH gating mechanisms of aquaporin permeation have been postulated. Current knowledge about the aquaporin sequence and structure allows us to discard the hypothesis of protonation of residues inside the channel.

Previous mutagenesis studies highlighted four key residues -- His53, Tyr124, Ser152 and His154 – in hAQP3 pH gating and their effects on water permeability, but could not give a comprehensive analysis of the role of these residues [4]. Based on our experimental data (pKa and the Hill slope of hAQP3), and using a tetrameric homology model of hAQP3, we investigated the AQP3 gating mechanisms at a molecular level, disclosing the interactions of the four key amino acidic residues in the context of the functional aquaporin quaternary-structure. Specifically, we can now conclude the following:

- The four key amino acids are located in extracellular loops (A and C) in each hAQP3 monomer.
- Protonation of pH-sensitive residues of hAQP3 may not occur simultaneously, but gradually, causing progressive structural changes as a function of pH.

- Movement of loop C in the outer vestibule of hAQP3, as observed previously in MD studies [11], may cause a blockage of the larger glycerol molecule, while still allowing the permeation of water. A similar movement may occur in loop A.
- hAQP3 monomers may not behave in a concerted fashion, but rather independently, and fluxes of solutes may be different in each monomer, upon pH changes. The observable effect of pH on AQP3 permeation is a sum of the effects in all the four monomers and, as a consequence, our observation of the differences in the Hill slope for water and glycerol may not be the same for each independent monomer, but an ''average'' effect of the tetrameric assembly.

Overall, *in silico* methodologies have allowed us and others [13,22] to perform a detailed molecular analysis of the gating mechanism of AQPs, providing a more physiological view of such processes. Moreover, the movement of loops, intra or extracellular, was observed in the gating mechanism of several AQPs [12,13,14,15] and appears to be a crucial feature in channel closure. Histidine residues in such loops can ''tune'' the pH sensitivity towards certain pH values [4,19].

Notably, metal compounds have also been shown to modulate the function of AQPs. For example, among the endogenous transition metal ions, Cu^{2+} and Ni^{2+} have been demonstrated to cause a decrease in water and glycerol permeability (P_f and P_{Gly}) in cells expressing human AQP3-GFP in a dose-dependent manner and the effect was rapid and reversible, while Pb^{2+} and Zn^{2+} ions had no effect in AQP3 permeability [4,21].

Moreover, the effect of Ni^{2+} was pH-dependent: at neutral and acidic pH, the AQP3-mediated water permeability was completely inhibited by 1 mM $NiCl_2$. At pH 7.4 and 8.0, the P_f in transfected cells was decreased by Ni^{2+}, but remained significantly higher than that in non-transfected cells. Site-directed mutagenesis studies identified three residues, Trp128 and Ser152 in the second extracellular loop and His241 in the third extracellular loop of AQP3, as determinants of Ni^{2+}

inhibition effects [4]. These Ni^{2+}-sensitive residues are the same as for Cu^{2+}, which suggests the same binding site and mechanism of inhibition [21]. Interestingly, Ser152 was identified as a common determinant of both Ni^{2+} and pH sensitivity.

Finally, considering the importance of glycerol in multiple vital physiological processes, regulation of its permeation across hydrophobic cell membranes via AQPs may be crucial for cell proliferation, adaptation and survival, and future research to untangle the biological relevance of aquaglyceroporins' pH gating in health and disease conditions ought to be conducted.

3.2.5 Experimental Section

Ethics Statement - Venous blood samples were obtained from healthy human volunteers following a protocol approved by the Ethics Committee of the Faculty of Pharmacy of the University of Lisbon. Informed written consent was obtained from all participants.

Strains, plasmids and growth conditions - Plasmid with *Rattus norvegicus* aquaporin-3 (rAQP3) cDNA (pcDNA3-AQP3), kindly provided by Dr. M. Eschevarria, Virgen del Rocio University Hospital-Seville, was used for AQP3 cDNA amplification. The centromeric plasmid pUG35 was used for cloning rat AQP3, conferring C-terminal GFP tagging, MET25 promoter and CYC1-T terminator. *Escherichia coli* DH5*α* [23] was used as host for routine propagation of the plasmids. *E. coli* transformants were maintained and grown in Luria-Bertani broth (LB) at 37 ˚C; ampicillin (100 μg/ml) [24]. Plasmid DNA from *E. coli* was isolated using a GenElute™ Plasmid Miniprep Kit (Sigma-Aldrich). *Saccharomyces cerevisiae*, 10560-6B *MATα leu2::hisG trp1::hisG his3::hisG ura352 aqy1D::KanMX aqy2D::KanMX* (YSH1770, further indicated as *aqy*-null) was used as a host strain for heterologous expression of rat AQP3. Yeast strains were grown at 28 ˚C with orbital shaking in YNB (yeast nitrogen base) without amino acids (DIFCO), with 2% (w/v) glucose supplemented with the adequate requirements for prototrophic growth.31 Yeast

transformants were maintained in the same YNB medium with 2% (w/v) agar. For stopped-flow assays, the same medium was used to yeast cells growth.

Cloning of rAQP3 and yeast transformation - *E. coli* DH5*α* was transformed with (pcDNA3_AQP3) and used for propagation of the plasmid. Plasmidic DNA was isolated and purified. rAQP3 specific primers modified to incorporate restriction sites for *Spe*I (underlined) and *Cla*I (underlined) (5′- GGACTAGTCCT ATG GGT CGA CAG AAG GAG TTG AT-3′ and 5′-CCAT CGATGGA GAT CTG CTC CTT GTG CTT CAT GT-3′ respectively) were designed and used for PCR amplification of *rAQP3* cDNA. PCR amplification was carried out in an Eppendorff thermocycler with Taq Change DNA polymerase (NZYTech). The PCR product was digested with *Spe*I and *Cla*I restriction enzymes (Roche Diagnostics®), purified using Wizard® SV Gel and PCR Clean-Up System kit (Promega) and cloned into the corresponding restriction sites of pUG35 digested with the same restriction enzymes, behind the MET25 promoter and in frame with GFP sequence and CYC1-T terminator, using T4 DNA Ligase (Roche), according to standard protocols [24], to construct the expression plasmid pUG35-rAQP3. The plasmid was used to transform DH5*α* *E. coli* strain, propagated and subjected to extraction and purification. Fidelity of constructs and correct orientation were verified by PCR amplification, restriction analysis and DNA sequencing. Agarose gel electrophoresis and restriction site mapping were performed according to standard methods [24,25]. Transformation of the *S. cerevisiae aqy*-null strain with pUG35-rAQP3 was performed by the lithium acetate method described in [25]. The same strain was also transformed with an empty pUG35 vector (which does not contain *rAQP3* cDNA) to be used as a control (further indicated as control). Transformants were selected on YNB medium without uracil as auxotrofic marker.

rAQP3 subcellular location by fluorescence microscopy - For subcellular localization of GFP-tagged rAQP3 in *S. cerevisiae*, yeast transformants in mid-exponential phase were observed with a Zeiss Axiovert 200 fluorescence microscope, at 495 nm excitation and 535

nm emission wavelengths. Fluorescence microscopy images were captured with a digital camera (CoolSNAP EZ, Photometrics, USA) and using the Metafluor software (Molecular Devices, Sunyvale, CA).

Cell sampling and preparation - Venous blood samples were collected in citrate anticoagulant (2.7% citric acid, 4.5% trisodium citrate and 2% glucose). Fresh blood was centrifuged at 750 x g for 5 min at 4 °C and plasma and buffy coat were discarded. Packed erythrocytes were washed three times in phosphate buffer saline solution (PBS; KCl 2.68 mM, NaCl 137 mM, KH_2PO_4 and Na_2HPO_4 concentration was varied in order to change the pH in the range 5 - 7.8 maintaining total osmolarity constant at 310 mOsM), diluted to 0.5% hematocrit and immediately used for experiments. Yeast transformants were grown up to OD_{640nm}≈1, harvested by centrifugation (5000 x g; 10 min; 4 °C), washed and re-suspended in ice cold sorbitol (1.4 M) K^+-citrate buffer (50 mM, pH 5 - 7.8) up to a concentration of 0.33 g ml^{-1} wet weight and kept on ice for at least 90 minutes. Prior to the osmotic challenges the cell suspension was pre-loaded with the nonfluorescent precursor 5-and-6-carboxyfluorescein diacetate (CFDA, 1 mM for 10 min at 30 °C) that is cleaved intracellularly by nonspecific esterases and generates the impermeable fluorescent form known to remain in the cytoplasm [26]. Cells were then diluted (1:10) in sorbitol 1.4 M buffer and immediately used for experiments.

Cell volume measurements - The equilibrium volume of RBC in PBS solutions at different pHs was determined using a CASY-1 Cell Counter (Scharfe System GmbH, Reutlingen, Germany) and was calculated as 86 fL for the experimental pH range used in the permeability assays. Mean volumes of yeast transformants equilibrated in sorbitol 1.4 M buffer were obtained by loading cells with carboxyfluorescein diacetate (CFDA) under a fluorescent microscope equipped with a digital camera as previously described [26]. Cells were assumed to have a spherical shape with a diameter calculated as the average of the maximum and minimum dimensions of each cell.

Stopped-flow experiments - Light scattering and fluorescence stopped-flow spectroscopy was used to monitor cell volume changes of respectively, RBC [8] and yeast transformants loaded with the concentration-dependent self-quenching CFDA fluorophore [26]. Experiments were performed on a HI-TECH Scientific PQ/SF-53 stopped-flow apparatus, which has a 2 ms dead time, temperature controlled, interfaced with an IBM PC/AT compatible 80386 microcomputer. After challenging cell suspensions with an equal volume of shock solution at 23 °C, the time course of volume change was measured by following the 90° scattered light intensity at 400 nm, or fluorescence intensity (excitation 470 nm and emission 530 nm). For each experimental condition, 5 to 7 replicates were analyzed. Baselines were acquired using the respective incubation buffers as isotonic shock solutions. For osmotic water permeability (P_f) measurements, a hyperosmotic shock solution containing a non-permeable solute was used (for RBC assays, sucrose 200 mM in PBS pH 5 to 7.8; for yeast assays, sorbitol 2.1 M in K^+-citrate pH 5 to 7.8) producing an inwardly directed gradient of solute. To measure glycerol permeability (P_{Gly}), a hyperosmotic shock solution containing glycerol was used (for RBC assays, glycerol 200 mM in PBS pH 5 to 7.8; for yeast assays, sorbitol 0.7 M, glycerol 1.4 M in K^+-citrate pH 5 to 7.8) creating an inwardly directed glycerol gradient. After the first fast cell shrinkage due to water outflow, glycerol influx in response to its chemical gradient was followed by water influx with subsequent cell re-swelling. In all the permeability assays the magnitude of the osmotic shocks (given by the ratio of the initial to final medium osmolarity after the applied osmotic challenges) is similar (tonicity of 1.25 to 1.5).

Data analysis - P_f was estimated by $P_f = k\ (V_o/A)(1/V_w(osm_{out}))$, where V_w is the molar volume of water, V_o/A is the initial cell volume to area ratio, (osm_{out}) is the final medium osmolarity after the applied osmotic gradient and k is the single exponential time constant fitted to the light scattering or fluorescence signal of yeast [26] or RBC shrinkage [8]. For RBC, P_{Gly} was calculated by $P_{Gly} = k\ (V_o/A)$, where V_o/A is the initial cell volume to area ratio and k is the single exponential time constant fitted to the light scattering signal of glycerol influx in erythrocytes. For yeast cells, fluorescence glycerol traces obtained were

corrected by subtracting the baseline slope that reflects the bleaching of the fluorophore. This was attained by fitting each signal to a double exponential with slope where the first process corresponds to cells shrinkage due to water outflow, the second process to cells swelling due to glycerol influx, and the slope corresponds to the baseline observed in all glycerol traces. The pattern of fitted slopes was confirmed for each experimental condition using baseline traces obtained with control stain under isotonic conditions.

Statistical Analysis - The results were expressed as mean ± SEM of n individual experiments. Statistical analysis between groups was performed by the unpaired t-test. P values < 0.05 were considered statistical significant.

Molecular modelling - The 3D structure of hAQP3 was obtained by homology modelling using the Molecular Operating Environment (MOE 2012.10) (CCG 2012) [17]. The choice of a template structure was based on the sequence identity between hAQP3 and the sequence of the AQPs with available resolved structures from human, bacteria and *Plasmodium falciparum*. The isoform showing the highest sequence similarity with hAQP3 is the bacterial isoform Glycerol Facilitator (GlpF), which was then chosen as a template structure to generate a homology model of hAQP3. Three resolved structures for bGlpF, crystallized either with or without glycerol and solved by X-Ray diffraction, were retrieved from the Protein Data Bank. Among them, the template was selected that had the best resolution (2.70 Å) without any substrate (pdb 1LDI) [27]. The tetrameric form was assembled and the structure was prepared and protonated at pH 7 by using the Amber12EHT force field [20]. Intermediate models of AQP3 were generated and averaged to obtain the final homology model. The model obtained was checked for reliable rotamers involving the side chains in the regions of ar/R SF and NPA, by comparison with the available crystal structures of all the other human and microbial AQP isoforms (pdb codes 1H6I, 36D8, 3D9S, 1RC2, 1LD1 and 3C02). The structure was protonated at pH 7 and an energy minimization refinement was performed, with fixed Cα atoms.

3.2.6 Supplementary Information

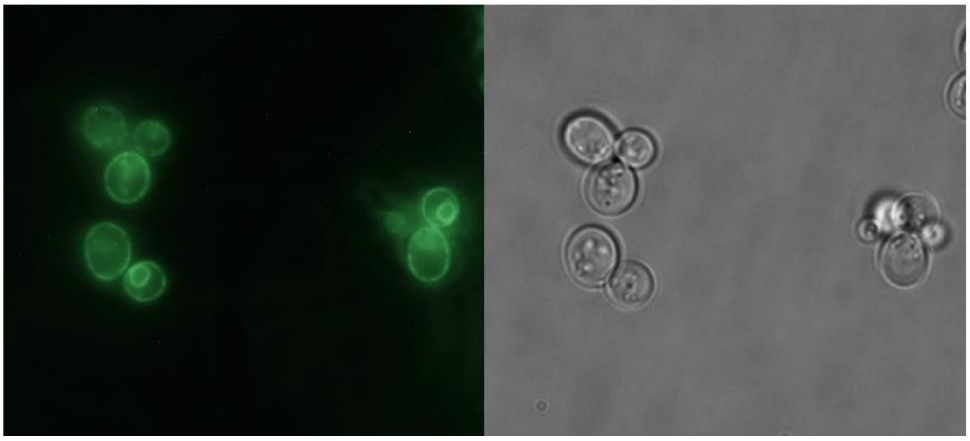

Supplementary Figure S3.2.1 | Localization of GFP-tagged rAQP3 expressed in *S. cerevisiae aqy*-null strain. Epifluorescence (left panel) and phase contrast (right panel) images of *S. cerevisiae aqy*-null strains transformed with rAQP3. [Data obtained jointly with Ana Paula Martins]

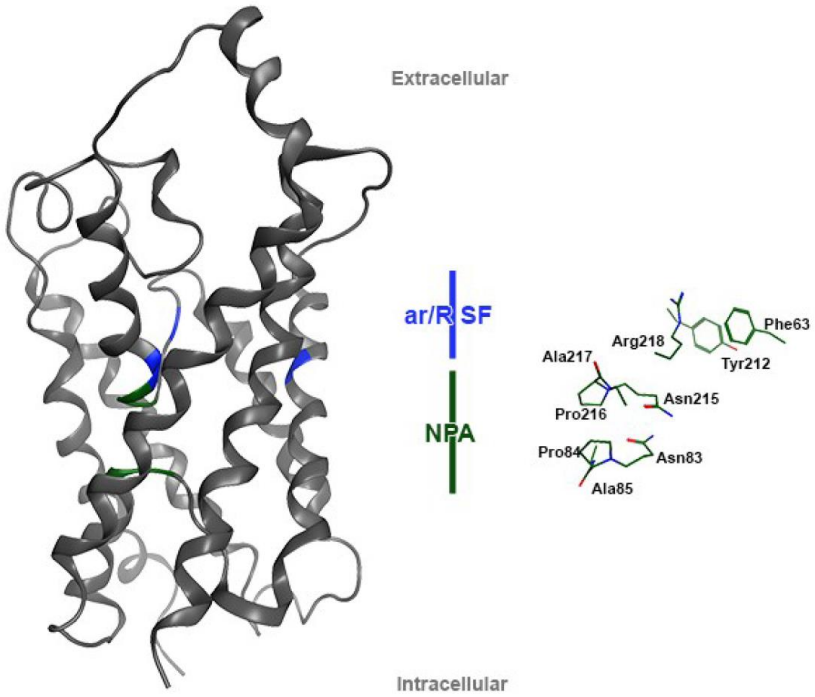

Supplementary Figure S3.2.2 | Homology model of human AQP3. Left panel: ribbon representation of the hAQP3 channel. Right panel: the represented residues compose the aromatic/Arginine selectivity filter (ar/R SF), in blue, and the NPA motif, in green. [Data obtained by Andreia de Almeida]

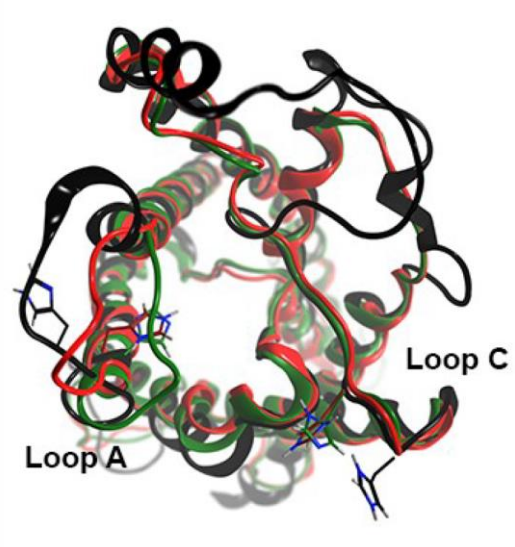

Supplementary Figure S3.2.3 | Ribbon representation of bovine AQP0 in an open (green, pdb 2B6P) and closed (red, pdb 1SOR), superposed with the homology model of hAQP3 (black). pH-sensitive histidines are represented in stick representation, with the color corresponding to the respective isoform: His40/53 in Loop A and His122/154 in Loop C. [Data obtained by Andreia de Almeida]

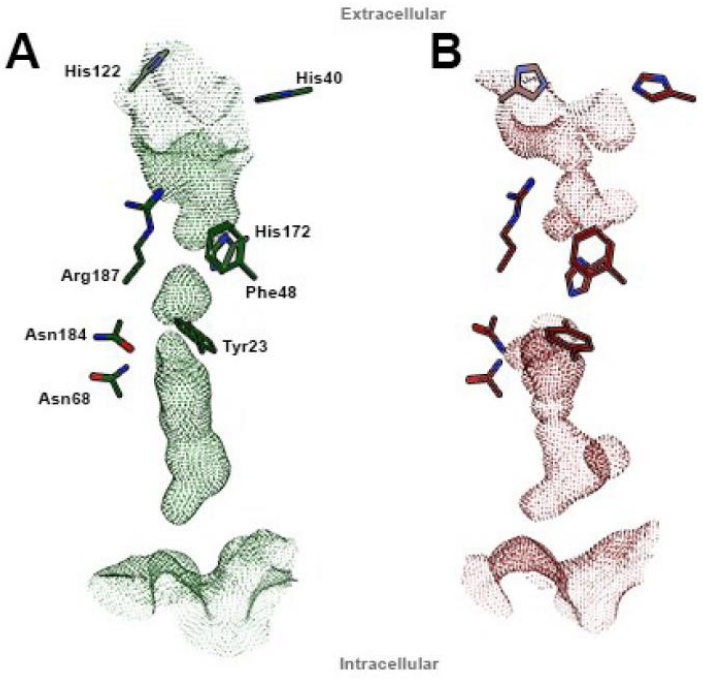

Supplementary Figure S3.2.4 | Molecular surface of bovine AQP0 in an open (green, pdb 2B6P) and closed (red, pdb 1SOR). Sidechains of residues in the channel lining, such as ar/R

SF residues, are depicted in stick representation, as well as the two pH-sensitive histidines, His122 and His40. [Data obtained by Andreia de Almeida]

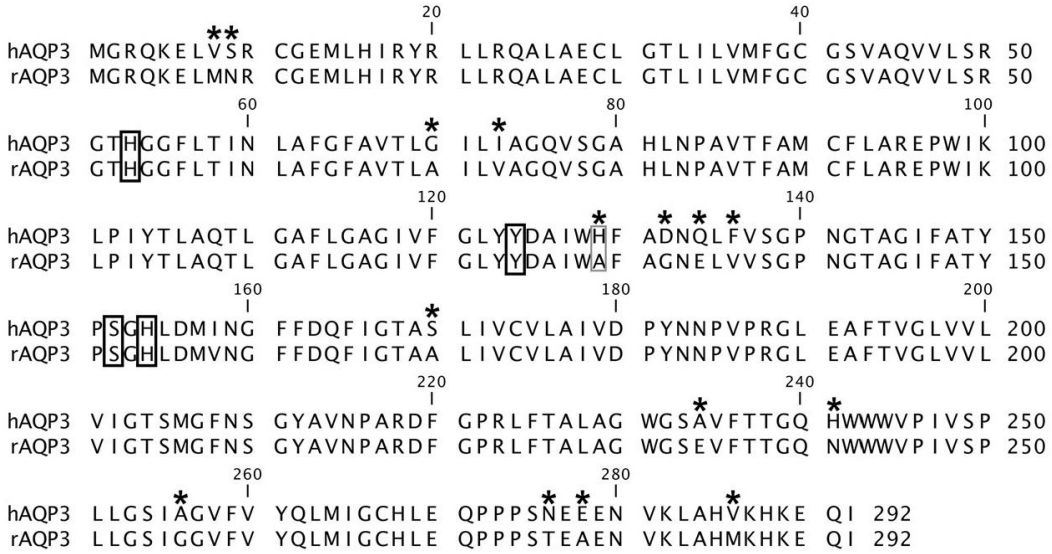

Supplementary Figure S3.2.5 | Sequence alignment of rat and human aquaporin-3. The black boxes highlight the pH-sensitive residues, while the grey box highlights His129 in hAQP3. * represents the residues that are not conserved in the two isoforms. [Data obtained by Andreia de Almeida]

3.2.7 References

[1] M. Hara, A.S. Verkman, Glycerol replacement corrects defective skin hydration, elasticity, and barrier function in aquaporin-3-deficient mice, Proc Natl Acad Sci U S A 100 (2003) 7360-7365.

[2] A. de Almeida, G. Soveral, A. Casini, Gold compounds as aquaporin inhibitors: new opportunities for therapy and imaging, MedChemComm 5 (2014) 1444-1453.

[3] T. Zeuthen, D.A. Klaerke, Transport of water and glycerol in aquaporin 3 is gated by H(+), J Biol Chem 274 (1999) 21631-21636.

[4] M. Zelenina, A.A. Bondar, S. Zelenin, A. Aperia, Nickel and extracellular acidification inhibit the water permeability of human aquaporin-3 in lung epithelial cells, J Biol Chem 278 (2003) 30037-30043.

[5] A.P. Martins, A. Marrone, A. Ciancetta, A. Galán Cobo, M. Echevarría, T.F. Moura, N. Re, A. Casini, G. Soveral, Targeting aquaporin function: potent inhibition of aquaglyceroporin-3 by a gold-based compound., PloS one 7 (2012) e37435.

[6] K.L. Nemeth-Cahalan, J.E. Hall, pH and calcium regulate the water permeability of aquaporin 0, J Biol Chem 275 (2000) 6777-6782.
[7] J. Nieto-Frausto, B. Kleutsch, A channel model with fluctuating barrier structures, Biochim Biophys Acta 1111 (1992) 81-92.
[8] E. Campos, T.F. Moura, A. Oliva, P. Leandro, G. Soveral, Lack of Aquaporin 3 in bovine erythrocyte membranes correlates with low glycerol permeation, Biochem Biophys Res Commun 408 (2011) 477-481.
[9] D. Fu, A. Libson, R. Stroud, The structure of GlpF, a glycerol conducting channel, Ion Channels - from atomic resolution physiology to functional genomics, 2002, pp. 51-65.
[10] Z.E. Newby, J. O'Connell, 3rd, Y. Robles-Colmenares, S. Khademi, L.J. Miercke, R.M. Stroud, Crystal structure of the aquaglyceroporin PfAQP from the malarial parasite Plasmodium falciparum, Nat Struct Mol Biol 15 (2008) 619-625.
[11] A. Spinello, A. de Almeida, A. Casini, G. Barone, The inhibition of glycerol permeation through aquaglyceroporin-3 induced by mercury(II): A molecular dynamics study, Journal of Inorganic Biochemistry (2016).
[12] A. Frick, M. Järvå, S. Törnroth-horsefield, Structural basis for pH gating of plant aquaporins, FEBS Letters 587 (2013) 989-993.
[13] L. Janosi, M. Ceccarelli, The gating mechanism of the human aquaporin 5 revealed by molecular dynamics simulations, PLoS One 8 (2013) e59897.
[14] S. Törnroth-Horsefield, Y. Wang, K. Hedfalk, U. Johanson, M. Karlsson, E. Tajkhorshid, R. Neutze, P. Kjellbom, Structural mechanism of plant aquaporin gating., Nature 439 (2006) 688-694.
[15] C. Tournaire-Roux, M. Sutka, H. Javot, E. Gout, P. Gerbeau, D.-T. Luu, R. Bligny, C. Maurel, Cytosolic pH regulates root water transport during anoxic stress through gating of aquaporins., Nature 425 (2003) 393-397.
[16] A. Madeira, M. Camps, A. Zorzano, T.F. Moura, G. Soveral, Biophysical assessment of human aquaporin-7 as a water and glycerol channel in 3T3-L1 adipocytes, PLoS One 8 (2013) e83442.
[17] M.O.E. (MOE), Chemical Computing Group Inc. Montreal, QC, Canada) 2012.10.
[18] D.G. Herries, Enzyme structure and mechanism (second edition), by Alan Fersht. Pp 475. W H Freeman, New York. 1984. £28.95 or £14.95 (paperback) ISBN 0–7167–1614–3 or ISBN 0–7167–1615–1 (pbk), Biochemical Education 13 (1985) 146-146.
[19] K.L. Nemeth-Cahalan, K. Kalman, J.E. Hall, Molecular basis of pH and Ca2+ regulation of aquaporin water permeability, J Gen Physiol 123 (2004) 573-580.
[20] T. Gonen, Y. Cheng, P. Sliz, Y. Hiroaki, Y. Fujiyoshi, S.C. Harrison, T. Walz, Lipid-protein interactions in double-layered two-dimensional AQP0 crystals, Nature 438 (2005) 633-638.
[21] M. Zelenina, S. Tritto, A.A. Bondar, S. Zelenin, A. Aperia, Copper inhibits the water and glycerol permeability of aquaporin-3, J Biol Chem 279 (2004) 51939-51943.
[22] S. Kaptan, M. Assentoft, H.P. Schneider, R.A. Fenton, J.W. Deitmer, N. MacAulay, B.L. de Groot, H95 Is a pH-Dependent Gate in Aquaporin 4, Structure 23 (2015) 2309-2318.

[23] D. Hanahan, Techniques for transformation of Escherichia coli, in: D.M. Glover (Ed.), DNA cloning: a practical approach,, IRL Press, Oxford, United Kingdom, 1985, pp. 109-135.
[24] J. Sambrook, E.F. Fritsch, T. Maniatis, Molecular Cloning: A Laboratory Manual, 2nd edn ed., Cold Spring Harbor, NY, 1989.
[25] R.D. Geitz, R.H. Schiestl, Transforming Yeast with DNA, Methods in Molecular and Cellular Biology 5 (1995) 255–269.
[26] G. Soveral, A. Madeira, M.C. Loureiro-Dias, T.F. Moura, Water transport in intact yeast cells as assessed by fluorescence self-quenching, Appl Environ Microbiol 73 (2007) 2341-2343.
[27] D. Fu, A. Libson, L.J. Miercke, C. Weitzman, P. Nollert, J. Krucinski, R.M. Stroud, Structure of a glycerol-conducting channel and the basis for its selectivity, Science 290 (2000) 481-486.

3.3 Regulation of Aquaporin-7 glycerol influx by acidic pH

3.3.1 Abstract

The aquaglyceroporin AQP7, a family member of aquaporin membrane channels, facilitates the permeation of water and glycerol though cell membranes and is crucial for body lipid and energy homeostasis. Regulation of glycerol permeability via AQP7 is considered a promising therapeutic strategy towards fat-related metabolic complications. We used a yeast expression system for heterologous expression and functional analysis of human AQP7 and investigated its regulation by pH. Using a combination of in vitro and in silico techniques, we found that AQP7 changes from fully permeable to virtually closed at acidic pH preventing glycerol influx but not efflux. Tyr135 and His165 are essential residues for pH sensing. Protonation further induces changes in protein surface electrostatic charges switching AQP7 from a bidirectional water/glycerol channel to a glycerol efflux channel. This mechanism of pH-regulation supports the role of AQP7 in adipose tissue and may help the design of selective modulators targeting aquaglyceroporin-related disorders.

3.3.2 Introduction

In this study we investigated pH regulation of human AQP7, the main aquaglyceroporin expressed in human adipocytes and particularly relevant to assure efficient glycerol fluxes in healthy adipose tissue, being involved in obesity and fat-related metabolic complications [1,2,3,4]. By expressing hAQP7 in our optimized yeast expression system [5], we were able to detect and characterize water and glycerol permeability corroborating hAQP7 channel function. Moreover, channel permeability was confirmed by inhibition with Auphen - $[Au(phen)Cl_2]Cl$ (phen = 1,10-phenanthroline) - a gold(III) compound reported by us as a potent

inhibitor of human aquaglyceroporins AQP3 and AQP7 in their native expression systems [6,7]. Using a combination of *in vitro* and *in silico* techniques, we showed for the first time that the bidirectional permeability of an aquaporin can be regulated differently upon pH changes, changing from a completely open bidirectional channel to a glycerol efflux channel at acidic pH. The mechanisms involved in hAQP7-pH regulation were investigated at a molecular level using site-directed mutagenesis combined with molecular modeling and molecular dynamics (MD) approaches. Knowledge on hAQP7 regulation can contribute to understand the roles of this isoform in physiology and pathology, helping in the development of aquaglyceroporin-targeted therapies.

3.3.3 Results and Discussion

hAQP7 is a functional water and glycerol channel when expressed in yeast

Yeast cells were transformed with either the empty plasmid (control cells) or the plasmid containing the human AQP7 gene (mentioned as hAQP7 cells for clarity). Expression and subcellular localization of hAQP7 at the yeast plasma membrane were confirmed by fluorescence microscopy using GFP-tagging (Supplementary Figure S3.3.1).

The activity of hAQP7 was assessed by stopped-flow fluorescence spectroscopy by challenging cells equilibrated in isosmotic solution at pH 7.4 (mammalian physiological pH) with hyperosmotic solutions of sorbitol (impermeant solute, inducing water efflux and cell shrinkage) or glycerol (after the initial fast water outflow, glycerol influx induces cell re-swelling [5]). Yeast expressing hAQP7 show faster volume equilibration and higher osmotic permeability coefficient P_f ((4.38 ± 0.23) x 10^{-4} cm s^{-1}) than control cells ((2.91 ± 0.12) x 10^{-4} cm s^{-1}) (Figure 3.3.1 A and B), evidencing water channeling. Regarding glycerol permeability, P_{Gly}, a marked

difference in the volume change rate between control and hAQP7 cells is observed (Figure 3.3.1 D), where the permeability P_{Gly} for hAQP7 cells was observed to be approximately 100-fold the control ((13.1 ± 1.80) $x10^{-6}$ and (0.12 ± 0.07) $x10^{-6}$ cm s^{-1} for hAQP7 and control cells respectively) (Figure 3.3.1 E). To confirm the contribution of hAQP7 for the observed P_f and P_{Gly}, the activation energies (E_a) for both water and glycerol permeation were measured (Figure 3.3.1 C and F). E_a is a crucial parameter that allows distinction between passive bilayer diffusion and protein-mediated diffusion through membranes. The observed E_a was lower in hAQP7 cells (9.16 ± 0.45 and 10.55 ± 0.41 kcal mol^{-1} for water and for glycerol) when compared to control cells (15.06 ± 0.46 and 23.20 ± 1.31 kcal mol^{-1} for water and for glycerol), indicating that hAQP7 expressed in yeast is a functional water and glycerol channel.

Previous studies by our group have detected the strong and selective inhibitory effect of a gold(III) coordination compound Auphen [Au(phen)Cl_2]Cl (phen=1,10-phenanthroline) on hAQP3 and hAQP7, expressed in human erythrocytes and mammalian cultured cells, respectively [6,7,8,9]. Here, we used Auphen to validate hAQP7 activity expressed in yeast and demonstrate that it is possible to detect small changes in channel permeation. Auphen induced a marked inhibitory effect of hAQP7 permeability (34% and 84% for P_f and P_{Gly} respectively) (Figure 3.3.1 G). Additionally, a dose-response curve for P_{Gly} inhibition by Auphen resulted in an inhibitory concentration (IC_{50}) of 12.95 ± 0.35 μM (Figure 3.3.1 H), in line with previously reported studies in hAQP7 expression in cultured adipocytes [6].

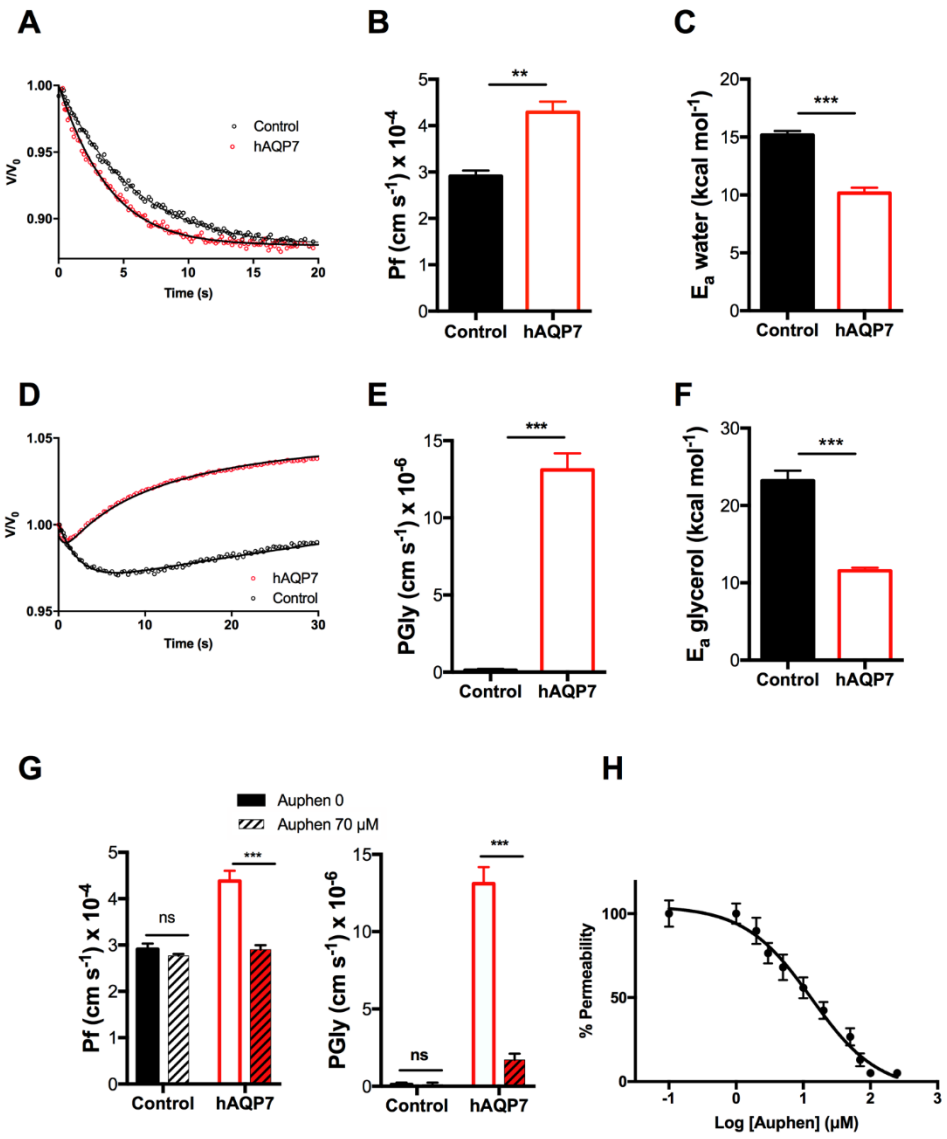

Figure 3.3.1 | Water and glycerol permeability in control and cells expressing hAQP7. **(A)** Representative time course of the relative cell volume (V/V_0) changes after a sorbitol hyperosmotic shock (pH 7.4, 23 °C) inducing water efflux and cell shrinkage. **(B)** Water permeability coefficient (P_f) and **(C)** Activation energy (E_a) for water permeation. **(D)** Representative time course of the relative cell volume (V/V_0) change after a glycerol hyperosmotic shock (pH 7.4). After the fast water outflow, glycerol influx induces cell reswelling. **(E)** Glycerol permeability (P_{Gly}) and **(F)** Activation energy (E_a) for glycerol permeation. **(G)** Water and glycerol permeability of cells upon treatment with Auphen (30 min, 70 µM). **(H)** Dose-response curve of glycerol permeability inhibition by Auphen, IC_{50} = 12.95 ± 0.35 µM. All permeability assays were performed at 23 °C, except for E_a assessment (described in Experimental Section). Data is shown as mean ± SEM of five independent experiments. ns, non significant; ** P < 0.01; *** P < 0.001.

hAQP7 is a pH-sensitive water and glycerol channel

hAQP7 pH-dependency has been previously evaluated in the Madin-Darby canine kidney (MDCKII) cells by measuring ^{14}C-glycerol uptake in the pH range 5.5 to 8 and, although glycerol uptake was significantly reduced at pH 5, no relevance was attributed to this effect with unclear meaningful physiological relevance [10]. A recent study also showed pH-dependence of murine AQP7 when expressed in yeast, with a loss of glycerol permeability at pH 4 and below [11]. This prompted us to investigate hAQP7 pH-sensitivity for both water and glycerol permeation using our optimized yeast-cell system where channel permeability was fully characterized as shown above.

Thus, P_f and P_{Gly} were evaluated by varying external pH from 7.4 to 5. (Figure 3.3.2 A and B). Data shows that, while at pH 7.4 hAQP7 is fully functional and has a maximal permeability at pH 6.5 and above, a marked reduction (more than 90% decrease) of P_f and P_{Gly} is observed at pH 5 (Figure 3.3.2 C and D). Interestingly, despite this clear reduction, P_f and P_{Gly} were still significantly higher than control cells, indicating that although the permeability is substantially reduced, the pore is not completely closed at pH 5. Remarkably, the pH-dependence profile was similar for both water and glycerol permeation, with pKa values estimated as 5.88 ± 0.01 and 5.85 ± 0.01 respectively. Additionally, the estimated E_a at three distinct pH values (pH 5, 6.5 and 7.5) corroborate the proposed channel regulation upon extracellular acidification (Supplementary Figure S3.3.2).

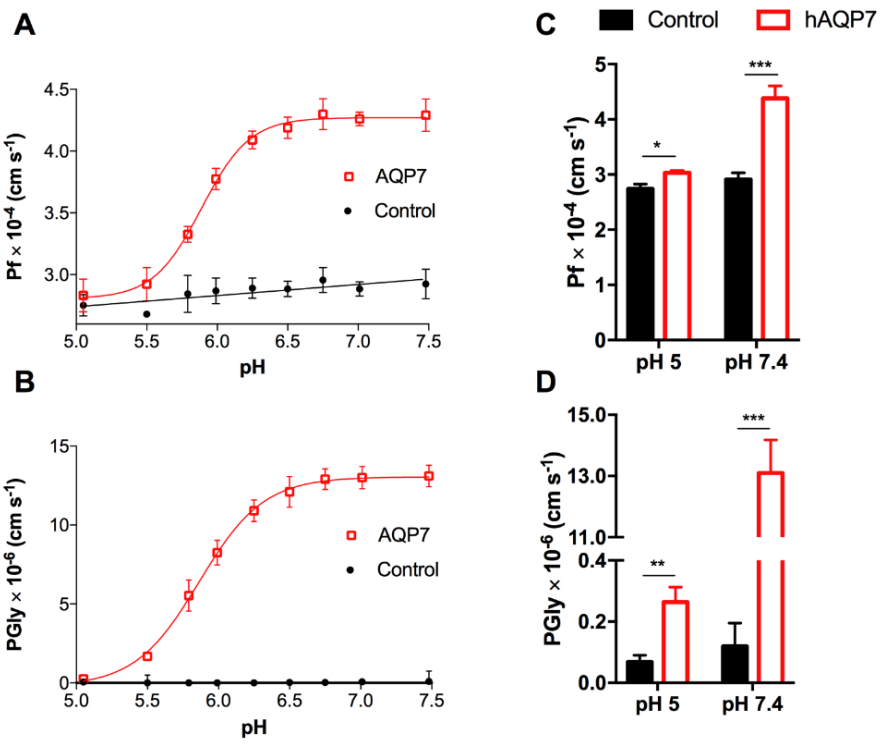

Figure 3.3.2 | pH-dependence of hAQP7 permeability. (A) P_f and **(B)** P_{Gly} dependency of control and hAQP7 cells at pH 5 – 7.5. **(C)** P_f and **(D)** P_{Gly} at pH 5 and pH 7.4. pH-dependence of hAQP7 was analyzed by fitting the experimental data to a Hill equation from where the pKa values were estimated. Permeability assays were performed at 23 ºC. Data are mean ± SEM of four independent experiments. * P < 0.05, ** P < 0.01, *** P < 0.001.

hAQP7 pore is not closed after pH decrease

To gain further insights into hAQP7's pH regulation, we used a molecular modeling approach previously developed by our group [12]. A homology model of hAQP7's tetramer, based on the available structure of the bacterial glycerol facilitator (GlpF, pdb code 1LDI) [13] was obtained using MOE software (MOE 2012.10; CCG 2012) [14], as described in the Experimental Section. In each protein monomer, the common fold shared by the aquaporin family was found: six transmembrane helices and two half-helices, with their N-terminal ends located in the centre of the pore (NPA motif). However, hAQP7 has NAA (Asn94, Ala95,

Ala96) and NPS (Asn226, Pro227, Ser228) motifs, rather than the common NPA found in other AQPs. A second selectivity filter, located near the extracellular entrance, named aromatic/arginine selectivity filter (ar/R SF), is an important distinctive and conserved feature of the aquaporin family. This is observed in our model of hAQP7, where Phe74, Tyr223 and Arg229 constitute the ar/R SF. The refined homology model of hAQP7 was protonated using the PROPKA 3.1 package [15] at pH 5 and 7.

Using the homology model prepared and protonated as described above, five independent MD simulations were run for 0.5 ns for each pH system (pH 5 and 7), as detailed in Experimental Section.

To investigate possible pore closure and conformational changes at low pH, the size and shape of the pore were analyzed using HOLE [16], from snapshots taken at five time points in each MD simulation. In Figure 3.3.3 is shown a HOLE surface representation of channel A, next to the average channel size of all monomers throughout the simulations. Interestingly, no differences were found in the size of the channels at the two pH values for both NPA and ar/R SF areas, indicating that the decrease in P_f and P_{Gly} may not be due to conformational changes and pore closure. However, there is an observable difference in the extracellular pocket (EP) (0.5 Å broader), just above the ar/R SF. This small variation may be due to system fluctuation during the simulation (as previously observed for other aquaporin isoforms [17]), as it was not detected in all individual cases (Supplementary Figure S3.3.3). Yet, such conformational difference at pH 7, leading to a broader extracellular glycerol binding pocket just above the ar/R SF, could favor its passage through the pore, leading to increased permeability.

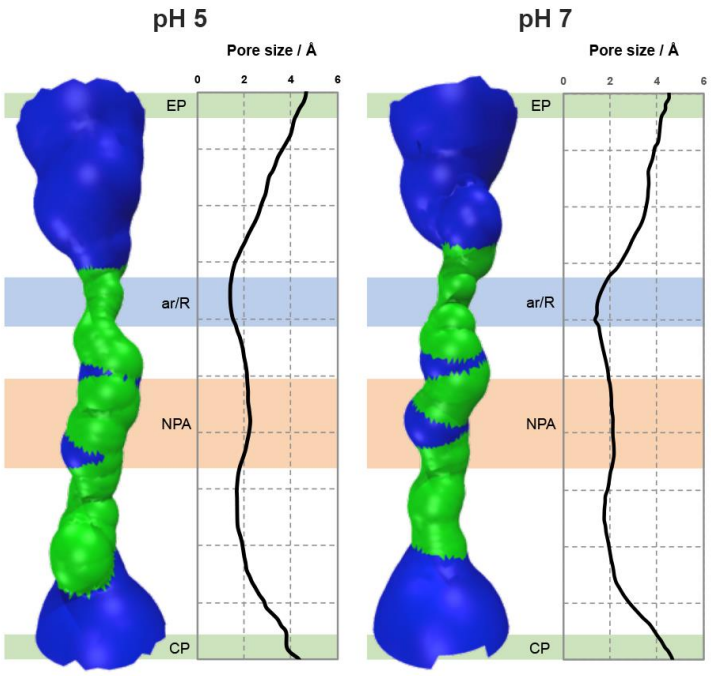

Figure 3.3.3 | Pore size of hAQP7 monomer A at pH 5 and pH 7. Surface of a representative snapshot of monomer A (based on VDW radii): red = smaller than single H_2O, green = single H_2O, blue = larger than single H_2O. Pore size represented as an average of all monomers in 5 simulations at each pH value. EP – extracellular pocket, ar/R – aromatic/arginine selectivity filter, NPA – NPA motif, CP – cytoplasmic pocket. Figure generated by HOLE [16] and VMD [18]. [Data obtained by Andreia de Almeida]

hAQP7 is a glycerol efflux channel at acidic pH

Since conformational analysis of the pore indicates that the protein does not alter pore size when protonated at pH 5, and the structure of the channel is not exactly symmetrical in both sides of the membrane (Figure 3.3.3), we decided to investigate if glycerol influx and efflux would similarly be affected by pH.

Therefore, as described in the Experimental Section, five independent MD simulations were run for 0.5 ns for each pH (pH 5 and 7) with four glycerol molecules, located in the intra or extracellular side of the membrane, pulled along the Z-axis in each direction, mimicking imposed glycerol gradients to simulate both influx and efflux. Hence, a total of 20 simulations were run to evaluate

glycerol permeability in both directions (see supplemental material for videos of the MD simulations). Afterwards, all simulations were analyzed and glycerol molecules monitored for successful permeation of hAQP7. In Figure 3.3.4 A, glycerol permeation is shown as an average number of glycerol molecules able to cross the tetramer via monomer channels. As expected, glycerol influx is significantly higher at pH 7 than at pH 5 corroborating the obtained experimental P_{Gly} (Figure 3.3.2 B), while surprisingly there is no significant difference between pH 5 and 7 for efflux.

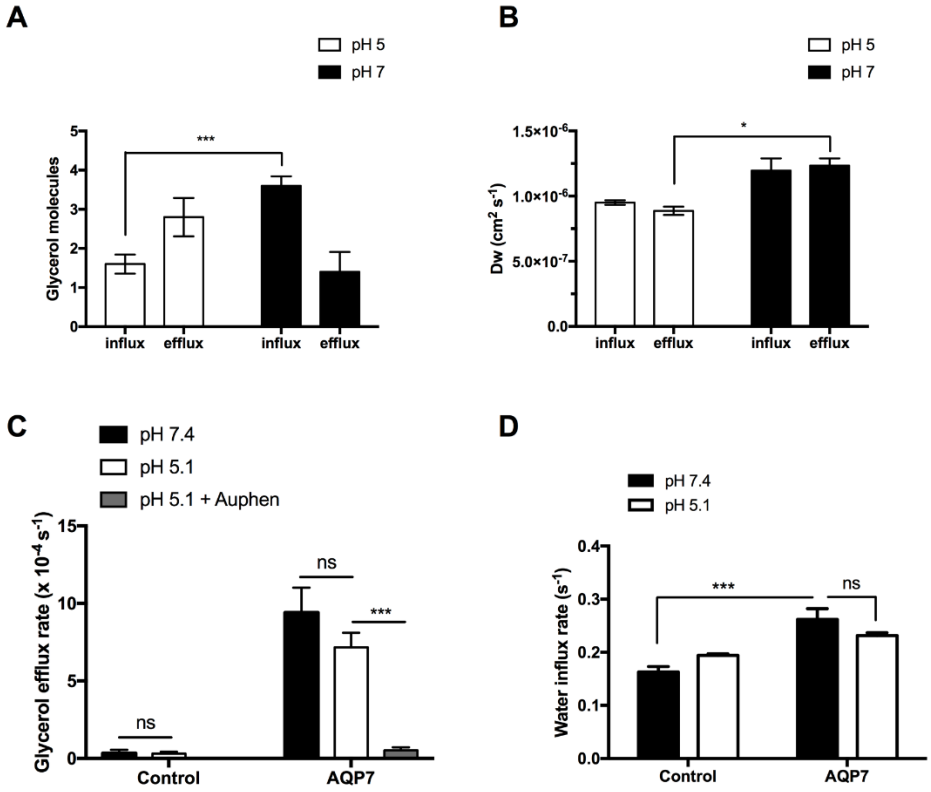

Figure 3.3.4 | Glycerol and water directional permeation across the hAQP7 channel (in silico and in vitro) as a function of pH. (A) Number of glycerol molecules crossing the AQP7 tetramer in MD studies, represented as mean ± SEM (n = 5). **(B)** Water diffusion coefficient calculated by MD simulations, represented as mean ± SEM (n = 3). n = number of simulations. **(C)** Glycerol efflux, and **(D)** water influx rates of hAQP7 cells by stopped-flow spectroscopy. Assays were performed at 23 °C, at pH 7.4 and pH 5.1. Glycerol efflux was also measured after incubation with 70 μM Auphen. Data are represented as mean ±

SEM of three independent experiments. ns, non-significant, * P < 0.05, ** P < 0.01, *** P < 0.001. [Data obtained jointly with Andreia de Almeida]

Since 0.5 ns MD simulations are too short to observe a net water movement, longer simulations (20 ns) were run at both pH values, without any pull code. The movement of water molecules between the two sides of the lipid bilayer was evaluated using a script, developed by us and based on previous work [19], that accounts for all water molecules moving from one side of the compartment to the other. For this purpose, only water molecules that completed the crossing through the AQP7 channel were counted, excluding all molecules crossing via the lipid bilayer. Moreover, we were able to discriminate between water molecules crossing in different directions of the Z-axis, allowing us to distinguish between influx and efflux. Water diffusion (D_w) was calculated as described in the experimental section and based on reference [20], simulating an equilibrium situation. It is important to note that, thermodynamically, due to the changes in protonation states, AQP7-pH7 and AQP7-pH5 are two different systems. For each of these systems separately, and as expected for an equilibrium situation, D_w evaluated for both water influx and efflux was identical (Figure 3.3.4 B). However, a significant difference between AQP7-pH7 and AQP7-pH5 was observed for water efflux. It should be noted that our MD simulations did not take into account the different ratio of charged species at the two pH values. Only neutral species permeate AQPs and, therefore, a decrease in pH will lead to decreased available neutral species, thus possibly reducing water permeability. This is a limitation of the MD approach, and in this respect further studies are necessary to fully disclose the gating mechanism for water permeation through aquaporins.

The obtained MD data on influx and efflux differences led us to explore this effect in vitro in yeast cells incubated with glycerol, promoting intracellular glycerol

accumulation [21]. The rate of glycerol efflux was measured after exposing glycerol-loaded cells to a sorbitol solution of identical osmolarity and following cell shrinkage. As depicted in Figure 3.3.4 C, glycerol efflux is 30-fold higher in hAQP7 cells compared to control and similar at both pH values, and, thus, not affected by pH as revealed by the above MD simulations. Importantly, we observed a full inhibition of glycerol efflux by Auphen, which validates the assay for hAQP7 activity. Regarding water influx, hAQP7 cells show significantly higher influx rates than control, but similar at both pH values (Figure 3.3.4 D); these data also corroborate our findings with the MD simulations.

Although the MD and stopped-flow spectroscopy data are not directly comparable, since the computational studies are not performed in conditions of osmotic shock, our in silico and in vitro data are in line in that only glycerol influx and water efflux are pH-regulated, while glycerol efflux and water influx are not affected within the tested pH range.

Tyr135 and His165 are key residues for glycerol permeability

Previous research on human AQP3 using site-directed mutagenesis [22], demonstrated that four residues (His53, Tyr124, Ser152 and His154) appear to be responsible for pH gating of this isoform. The relevance of these residues on hAQP3 was recently investigated by our group using MD and we proposed that gating occurs mainly due to protonation of His154 and its interaction with the neighboring His129 [12].

To investigate the mechanism of pH regulation, sequence alignment of hAQP3 and hAQP7 and superposition of the two homology models (the homology model of hAQP3 was prepared as described in reference [12]) showed that the corresponding residues in hAQP7 are Tyr64, Tyr135, His140, Pro163 and His165.

The location of residues Tyr135, His140 and His165 in the hAQP7 tetramer is shown in Figure 3.3.5 A and B.

Detailed analysis of the protonation sites at both pH values revealed that only four residues are protonated at pH 5, which are not at pH 7 (Supplementary Figure S3.3.4): on extracellular side, His140 (in all monomers), intracellularly, Glu40 (monomers A, C and D), His92 (monomers B, C and D) and Glu202 (in all monomers).

Based on the sequence/structural alignment and protonation studies, the residues facing the extracellular environment were chosen for further site-directed mutagenesis studies were Tyr135, His140 and His165. Additionally, as seen in Figure 3.3.3, changes in pore size are only observed in the extracellular side at pH 7, thus pointing at role of extracellular amino acids in pH-dependency. Since Pro163 does not have a protonable side chain, and Tyr64 was not protonated at pH 5, these residues were not further investigated.

Thus, to determine the importance of His165, His140 and Tyr135, the selected amino acids were substituted by alanine residues (Ala) and, due to the proposed role of His165 on AQP3 pH gating [12], double mutants were also generated. The relative membrane expression levels revealed that all the point-mutants could retain the same cellular distribution in the plasma membrane as the wild type AQP7 protein (WT). Additionally, no differences in membrane abundance were observed in cells incubated in media with different pH or osmolarity (Supplementary Figure S3.3.5). The permeability of the mutants was then further investigated under the same pH range as previously used for WT.

Data shows that the water permeability of all mutants remains equal or even slightly higher than WT above pH 7, indicating that the hAQP7 mutants are functional channels (Figure 3.3.5 C and E). Regarding glycerol permeation, while the single H140A mutant displays similar behavior to WT, all the other mutations

showed markedly reduced glycerol permeability at pH 7.4 (Figure 3.3.5 D and F). In fact, the mutants H165A and H165A+H140A reduced glycerol maximal permeability at pH 7.4 to 44% of the WT, inducing a shift in the pKa from 5.86 ± 0.01 to 6.30 ± 0.01 (Supplementary Table S3.3.2). Interestingly, the mutants Y135A and Y135A+H165A rendered the protein almost inactive, reducing the maximal P_{Gly} to 10% of the observed for WT (Figure 3.3.5 D and F). This suggests the key involvement of the Tyr135 and His165 residues in the channel pore permeability, while His140 does not appear to have any contribution to pH-dependency.

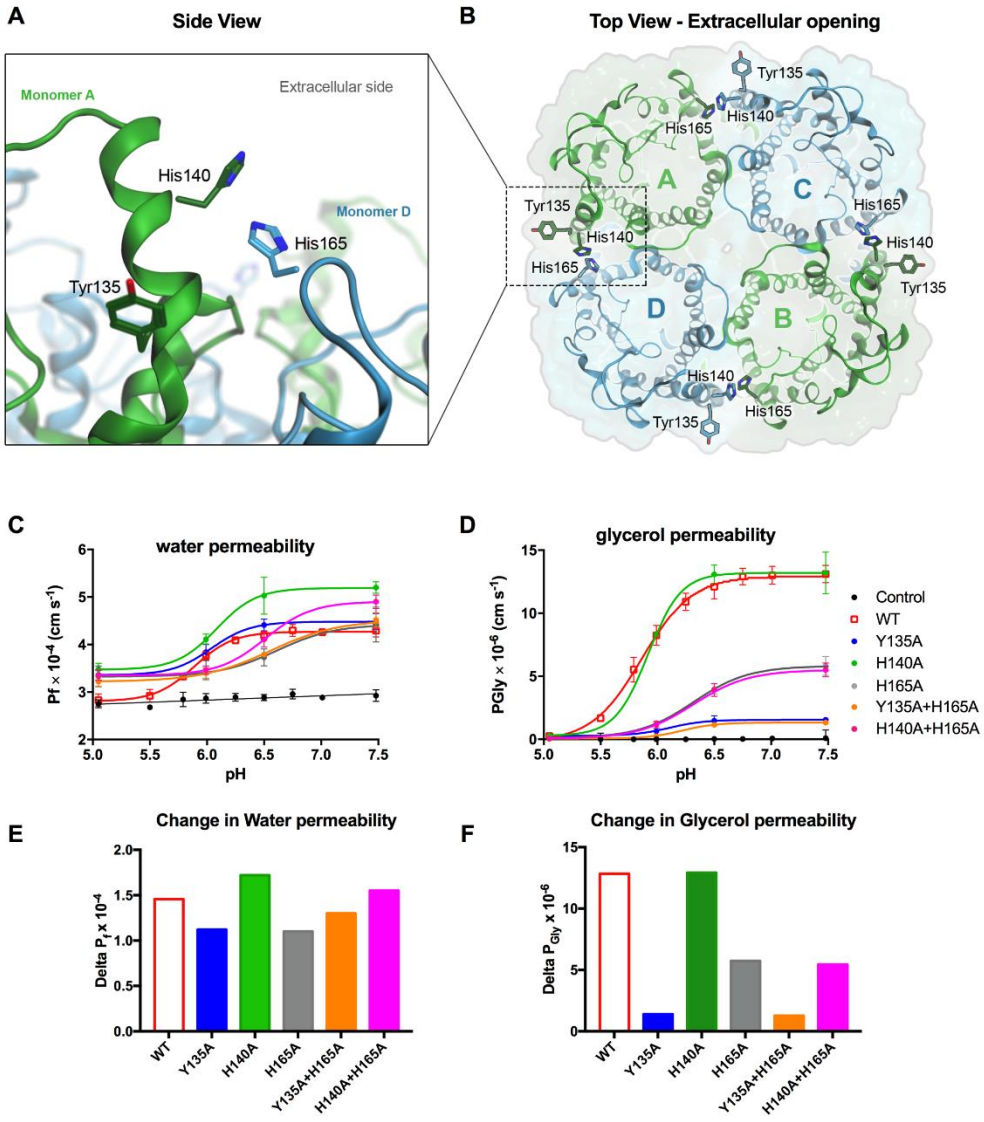

Figure 3.3.5 | Putative residues involved in hAQP7 pH regulation. (A) side and **(B)** top views of the refined homology model of human AQP7 in its tetrameric assembly, in cartoon representation of the tertiary structure, with ribbon representation of each monomer. Amino acid residues are shown in stick representation and backbone and hydrogens are hidden for clarity. Residues are colored according to the corresponding monomer, as shown in B. Figure generated with MOE [14]. **(C)** Water permeability (Pf) and **(D)** glycerol permeability (P_{Gly}) measured at pH 5.1-7.5, of control cells and cells expressing hAQP7-WT and -mutants. **(E)** Change in water (Delta P_f) and in **(F)** glycerol (Delta P_{Gly}) permeability (from pH 7.4 to pH 5.1). All permeability assays were performed at 23 ºC. Data (mean ± SEM, n=4 for each data set) were fitted according to the Hill equation. [Data obtained jointly with Andreia de Almeida]

Protonation of hAQP7 induces changes in protein surface electrostatic charges

Following the functional in vitro results, showing a clear role of Tyr135 and His165 in hAQP7 permeability, detailed analysis of the MD trajectories was performed. The MD trajectories of both glycerol and water permeation, did not allow to disclose a clear role for His165 in pH-gating of WT hAQP7. However, careful analysis of the hydrogen bond network during glycerol permeation at pH 7 shows that glycerol preferably forms hydrogen bonds with residues featuring protonable side chains (e.g. Lys63, Tyr64). Protonation of residues in the pore entrance, such as His165, at pH 5 may alter the hydrogen bond network, also affecting the residues responsible for glycerol passage.

Therefore, we postulate that the contribution of His165 and Tyr135 to AQP7 pore permeability is based on a network of hydrogen bonds that dynamically readapts to changes in external acidification. In order to support this hypothesis, we have prepared new homology models for all the mutants. The models were generated based on mutated sequences, refined and subsequently protonated at pH 5 and pH 7, using PROPKA 3.1 package [15], as performed for the WT model. Each model was further analyzed using HOLE [16] for pore size and the results for all models are shown in Supplementary Figure S3.3.6.

The main difference in size was found for the double mutant Y135A+H165A (Figure 3.3.6 A), which showed a decrease in pore size at the ar/R SF of approximately 1 Å when compared to the WT. All mutants show a pore size decrease in this region (Supplementary Figure S3.3.6), although not as marked (ca. 0.5 Å). Moreover, none of the mutants show relevant changes in size in the NPA region. A decrease in size of the ar/R SF, the first constriction site that solutes encounter when permeating AQPs from the extracellular side, may contribute to the observed loss of permeability of the mutants. However, His140A also shows a slight decrease in ar/R SF size, despite having the same permeability of the WT

protein. This indicates that pore size may not be the only factor playing a role in AQP7 permeability. In fact, as observed in Figure 3.3.5 and Supplementary Table S3.3.2, the studied mutants also appear to alter the pKa of water and glycerol permeation. This effect may be due to changes in the electrostatic surface of the mutants and also under different pH conditions. Therefore, in order to study the effects of pH and mutations in the electrostatic surface of hAQP7, surfaces were generated using the Adaptive Poisson-Boltzmann Solver (APBS) [23] plugin in Chimera [24], and are shown in Figure 3.3.6 B and Supplementary Figure S3.3.7.

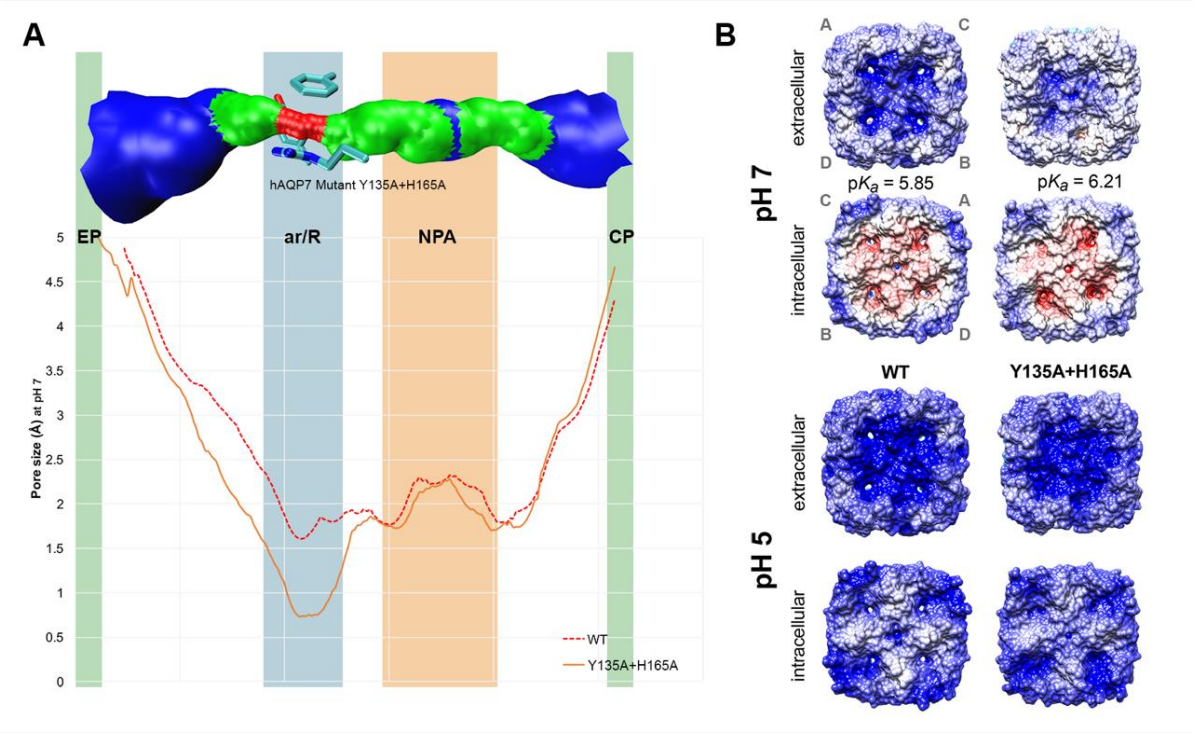

Figure 3.3.6 | Pore size and protein surface electrostatic charges. (A) Pore size of human AQP7-WT and double mutant Y135A+H165A, analyzed using HOLE [16]. Top channel surface represents the pore size of hAQP7 mutant Y135A+H165A (based on VDW radii): red = smaller than single H_2O, green = single H_2O, blue = larger than single H_2O. Figure generated by HOLE [16] and VMD [18]. **(B)** Electrostatic surfaces of hAQP7-WT and mutant Y135A+H165A, at pH 5 and 7, with the following color code: positive = blue, negative = red, neutral = white. Top views of both intra and extracellular sides, with the pKa of each protein indicated in the figure. Surfaces were generated using the Adaptive

Poisson-Boltzmann Solver (APBS) [23] plugin in Chimera [24]. Monomers labelled A-D are shown in grey to indicate their position in each view. [Data obtained by Andreia de Almeida]

Overall, the main observable difference is that the intracellular surface of all models appears to be much more negative (shown in red color) at pH 7 than at pH 5. At pH 7, the channel areas appear more positively charged, while the outer portion is more neutral than at the lowest pH. Interestingly, the H140A mutant is very similar to WT, both in charge distribution on the protein surface at both pH values and in terms of protonation (Supplementary Figure S3.3.7), which is in line with our experimental findings.

The most marked changes were observed for the H165A and Y135A single and double mutants, pointing at the crucial involvement of these two residues in pH gating and glycerol permeability. Remarkably, as observed for the glycerol permeability shown in Figure 3.3.5 C, Y135A mutation has the strongest effect on the double mutant, also shown to have the same protonated residues as the single mutant (Supplementary Figure S3.3.7). Similarly, H165A mutation appears to dominate the effects of the double His mutant, both in permeability and residue protonation.

Analysis of protonation reveals that the mutants do not induce changes in protonation of intracellular residues at pH 7. However, at pH 5 His92, an intracellular residue, is deprotonated in H165A and H140A+H165A mutants and partially deprotonated on the H140A mutant. Changes in protonation of this residue do not appear to affect the permeability at the lowest pH of any of the mutants, indicating that deprotonation of His92 is not a major player in the permeation mechanism. Despite the fact that none of the mutants induce protonation changes of intracellular residues at pH 7, it is possible to observe that

the intracellular charge distribution is altered in Y135A, H165A and the double mutants: surface of the channel area is more negative than WT. This indicates that changes in extracellular residues affect the overall electrostatic surface of the protein, including the intracellular surface. Thus, changes in extracellular pH may be able to affect the intracellular charge distribution, likely by altering the H-bond network of the protein, affecting the permeability.

Moreover, the pKa differences appear to be due to the changes in electrostatic protein surface, caused by the mutations, which can alter the protein's affinity for substrates. However, mutating these residues does not render the protein pH-insensitive. Interestingly, beside the residues mutated in this study, most of the protonable amino acids composing the protein surface are lysines and arginines, with pKa above 10, making them very unlikely players in pH-sensitivity in a physiological range. A likely scenario is that the protein rearranges its H-bonding network according to the newly inserted residues, redistributing the electrostatic potential and changing affinity for substrates, shifting the role of pH-sensitivity to other nearby residues.

hAQP7 regulation by acidic pH may contribute to an efficient glycerol efflux from adipocytes

Knowing that AQP7 is crucial for glycerol efflux from adipose tissue into blood circulation during lipolysis, to be used in gluconeogenesis in the liver [3,25], full hAQP7 activity for glycerol efflux at mammalian physiological pH would be expected. Notably, during intracellular lipolysis, diffusion of free fatty acids across adipocyte plasma membranes has been shown to release protons in a stoichiometric manner acidifying the intracellular pH [26,27,28]. In addition, it is

possible that significant levels of lipolysis with increased H^+ released into the adipose micro-circulation, create local acidic microenvironments [27].

Previous intracellular pH measurements of our yeast cells showed that an external acidification from pH 6.8 to 5 produces an intracellular pH drop from 6.8 to 6.1 [29]. Thus, in our experimental approach, lowering the extracellular pH from pH 7.4 to pH 5 may mimic the intracellular acidification observed in adipocytes during lipolysis.

Briefly, in basal conditions when intracellular pH is kept at a physiological range, water and glycerol movements via AQP7 are solely dependent on osmotic or glycerol gradients. However, during lipolysis, the occurring acidic pH prevents glycerol influx while efflux is not affected, transforming AQP7 in an efficient glycerol efflux channel able to dissipate the intracellular glycerol accumulation in the adipose tissue. Interestingly, we show that acidic pH also decreases water efflux via hAQP7. In fact, glycerol efflux driven by its outwardly directed gradient is followed by water to compensate the osmotic unbalance, which can permeate the membrane either via AQP7 or through the lipid bilayer. Competition between glycerol and water molecules for hydrogen bonding to the channel lining has already been reported using MD simulations [30,31]. As water and glycerol may compete for passage through the pore in a single-file, a mechanism excluding water from the pore and enabling glycerol to be the only molecular species inside the channel surely allows a higher efficiency of glycerol release during lipolysis.

3.3.4 Conclusions

Aquaglyceroporins have emerging roles in energy metabolism and adipose tissue homeostasis and have been implicated in obesity and metabolic-related complications, such as metabolic syndrome. AQP7 is the main glycerol channel

expressed in human adipose tissue, with a fundamental role in glycerol release from adipocytes during lipolysis, when triglycerides are hydrolysed to fatty acids and glycerol. During fasting, the intracellularly produced glycerol is channeled by AQP7 into the bloodstream to be taken up in the liver by AQP9 where it will be used for gluconeogenesis. Thus, the fine-tuning of AQP7 efficiency for glycerol release from the adipose tissue and its uptake by the liver might be the rate-limiting step for maintenance of normal blood glucose levels. While it appears evident that despite its bi-directionality, AQP7 may have selective directional permeation under certain conditions, this mechanism has never been explored. In fact, the channel structure is not symmetrical between intra and extracellular side, which may account for different solute affinity. Since acidification is a physiological consequence of triglyceride lipolysis in the human adipose tissue, we investigated the pH-regulation of human AQP7 permeability. Using *in vitro* and *in silico* approaches we found that residues Tyr135 and His165 facing the extracellular environment are crucial for channel permeability and, importantly, that protonation induces changes in protein surface electrostatic charges switching AQP7 from a bidirectional channel to a glycerol efflux channel. The selectivity model proposed supports the physiological role of human AQP7 in the adipose tissue as a glycerol efflux channel and opens new doors for the design of selective and potent modulators targeting AQP7.

3.3.5 Experimental Section

Strains, plasmids and growth conditions - Human AQP7 (hAQP7) cDNA was PCR amplified from pWPi-DEST-AQP7 plasmid [32] and C-terminally fused to GFP of the centromeric plasmid pUG35 [33]. *Escherichia coli* DH5α [34] was used as a host for routine propagation and purification of the plasmids with a GenElute™ Plasmid Miniprep Kit

(Sigma-Aldrich, USA). *E. coli* transformants were maintained and grown in Luria-Bertani broth (LB) at 37 ˚C, ampicillin (100 μg/ml) [35]. For functional studies, *Saccharomyces cerevisiae*, 10560-6B MAT*α* *leu2::hisG trp1::hisG his3::hisG ura352 aqy1D::KanMX aqy2D::KanMX* (YSH1770, further indicated as *aqy*-null) was used as a host strain for heterologous expression of hAQP7. Yeast strains were grown at 28 ˚C with orbital shaking in YNB (yeast nitrogen base) without amino acids (DIFCO), 2% (w/v) glucose supplemented with the adequate requirements for prototrophic growth [36].

Heterologous expression of hAQP7 in *S. cerevisiae*

Cloning of hAQP7 gene - *E. coli* DH5*α* was transformed with pWPi-DEST_lnAQP7 and used for propagation of the plasmid. Plasmidic DNA was isolated and purified. Specific primers modified to incorporate restriction sites for *Spe*I (bold) and *Cla*I (bold) were designed and used for amplification of hAQP7 cDNA (Supplementary Table S3.3.1). PCR amplification was carried out in an Eppendorff thermocycler with proofreading *Taq* Change DNA polymerase (NZYTech). A temperature gradient PCR was performed to determine the optimum annealing temperature. The amplified product was digested with *Spe*I and *Cla*I (Roche Diagnostics®) and purified using Wizard® SV Gel and PCR Clean-Up System kit (Promega). The purified product was cloned into the corresponding restriction sites of pUG35 digested with the same restriction enzymes, behind the MET25 promoter and in frame with GFP sequence and CYC1-T terminator, using T4 DNA Ligase (Roche). Cloning was performed according to standard protocols [35] to construct the expression plasmid pUG35-hAQP7. The plasmid was used to transform DH5*α* *E. coli* strain, propagated and subjected to extraction and purification. Fidelity of constructs and correct orientation was verified by PCR amplification, restriction analysis and DNA sequencing. Agarose gel electrophoresis and restriction site mapping were performed according to standard methods [35,37].

Transformation of the *S. cerevisiae aqy*-null strain - Transformation of the *aqy*-null strain with pUG35-hAQP7 was performed by the lithium acetate method described in [37]. The same strain was also transformed with the empty pUG35 vector (which does not contain hAQP7 cDNA) to be used as a control (further indicated as control cells). Transformants were selected on YNB medium without uracil as an auxotrophic marker.

Subcellular localization and membrane abundance analysis by fluorescence microscopy - For subcellular localization of GFP-tagged hAQP7 in *S. cerevisiae*, yeast transformants in mid-exponential phase were observed with a Zeiss Axiovert 200 fluorescence microscope, at 495 nm excitation and 535 nm emission wavelengths. Fluorescence microscopy images were captured with a digital camera (CoolSNAP EZ, Photometrics, USA) and using the Metafluor software (Molecular Devices, Sunyvale, CA). hAQP7 membrane expression was measured at pH 7.4 and pH 5.1 by measuring GFP-protein fluorescence intensity according to [38,39] and as previously reported by us [40]. A linear intensity profile across the cell membrane was generated and analyzed using the software ImageJ (https://imagej.net). The intensity profile along the line path from at least 30 cells in each experimental condition (n = 3) was recorded (Supplementary Figure S3.3.5), and for each cell three profile lines were taken. The background intensity along the same distance was measured and subtracted from the peak fluorescence intensity over each line, and the obtained difference divided by the maximal fluorescence to calculate the relative membrane expression (RME).

Site-directed mutagenesis - PCR-based site-directed mutagenesis was performed to introduce point mutations into wild-type hAQP7 cDNA, where Tyr135, His140 and His165 were replaced with Alanine residues (Ala), using the recombinant plasmid pUG35-hAQP7 as a template. The mutagenic primers used in this study and the respective substitutions introduced (underlined) are listed in Supplementary Table S3.3.1. Each mutation at the corresponding position was confirmed by DNA sequencing and, further PCR reactions were performed to create double mutations (Y135A+H165A and H140A+H165A). All PCR

mutagenized products were purified, digested and cloned in pUG35 and yeast cells were transformed as described above.

Permeability assays - Yeast transformants were grown up to $OD_{640nm} \approx 1$ (corresponding to $1x10^7$ cells/ml) and harvested by centrifugation (5000 ×g; 10 min; 4 °C). Afterwards, cells were washed and re-suspended in ice-cold sorbitol (1.4 M) K^+-citrate buffer (50 mM, pH 7.4), up to a concentration of 0.33 g ml^{-1} wet weight and kept on ice for at least 90 minutes. Prior to the osmotic challenges, the cell suspension was pre-loaded with the non-fluorescent precursor 5-and-6-carboxyfluorescein diacetate (CFDA, 1 mM for 10 min at 30 °C) that is cleaved intracellularly by nonspecific esterases and generates the impermeable fluorescent form carboxyfluorescein, known to remain in the cytoplasm [41].

Equilibrium cell volumes were obtained by loading cells with CFDA under a fluorescent microscope equipped with a digital camera as previously described [41]. Cells were assumed to have a spherical shape with a diameter calculated as the average of the maximum and minimum dimensions of each cell.

Stopped-flow was used to monitor cell volume changes of cells loaded with a concentration-dependent self-quenching fluorophore [41]. Experiments were performed on a HI-TECH Scientific PQ/SF-53 stopped-flow apparatus, which has a 2 ms dead time, temperature controlled, interfaced with an IBM PC/AT compatible 80386 microcomputer. Experiments were performed at 23 °C. Five runs were usually stored and analyzed in each experimental condition. In each run, 0.1 ml of cell suspension (1:10 dilution in resuspension buffer) was mixed with an equal amount of iso- (baseline) or hyperosmotic solutions (of sorbitol or glycerol) of 1.25 tonicity (($\Lambda = (osm_{out})_\infty/(osm_{out})_o$), 350 mM gradient). The fluorophore was excited using the light source with a 470 nm interference filter, detected using a 530 nm cut-off filter and the changes in fluorescence due to the carboxyfluorescein fluorescence quenching were recorded.

For efflux assays, cells were previously loaded with 1.4 M glycerol (pH 5.1 or pH 7.4) for 60 min on ice to prevent intracellular glycerol metabolism, and subsequently loaded with CFDA. In the stopped-flow, 0.1 ml of cell suspension were mixed with equal volume of

isosmotic sorbitol solution producing an outwardly gradient of 700 mM glycerol. The rate of glycerol efflux was followed by the decrease in fluorescence (self-quenching) due to cell shrinkage.

For inhibition experiments, cell suspensions equilibrated in an isotonic solution were incubated with CFDA in the absence or presence of Auphen (70 μM), at room temperature for 30 minutes at the selected pH.

Calibration of the fluorescence signals into relative volume - The fluorescence traces obtained were corrected by subtracting the baseline trace that reflects the bleaching of the fluorophore. The calibration of the resulting traces for the two strains followed our previous strategy [42], where a linear relationship between relative volume and F was obtained ($v_{rel} = a\ F/F_0 + b$); the values of a and b were estimated individually for each sorbitol osmotic shocks, considering the initial and final fluorescence values and the correspondent relative volumes obtained previously by our group for the same tonicity shock [41,42]. These values were then used for the calibration of the traces in the glycerol osmotic shock performed under the same experimental conditions, tonicity and temperature.

Permeability and activation energies evaluation - The experimental protocols to assess aquaporin function were designed to keep the membrane surface tension to a minimum, in order to maintain aquaporin activity at its maximum, as previously found in our laboratory [42]. This was accomplished by equilibrating cells in 1.4 M sorbitol solution (considering sorbitol as a non-diffusible solute) followed by the application of low tonicity hyperosmotic shocks (Λ = 1.25, 350 mM gradient) with sorbitol or glycerol. For this purpose, the calibrated experimental curves v_{rel} were fitted to their theoretical curves, considering the water and glycerol fluxes and the resulting changes in cell volume and intracellular concentrations of solutes. Optimization of permeability values was accomplished by numerical integrations using a mathematical model implemented in the Berkeley Madonna software (http://www.berkeleymadonna.com/).

The activation energy (E_a) of water and glycerol transport was evaluated by performing permeability assays at temperatures ranging from 7 to 38 °C. E_a values were obtained from the slope of Arrhenius plots (ln P_f or ln P_{Gly} as a function of 1/T).

pH dependency - In order to further characterize the pH-dependence of hAQP7 permeability, yeast transformants were incubated in an isotonic solution (sorbitol 1.4 M) with different pH (varying from 5 to 7.5) for at least 90 minutes. In these conditions, cells deprived of carbon sources and incubated on ice for a long period are considered in starvation and unable to maintain an internal pH gradient [43]. After the incubation with the fluorescence probe, stopped-flow experiments were performed at 23 °C for both water and glycerol transport at different external pH values.

Molecular Modeling and analysis - The 3D structure of hAQP7 was obtained by homology modelling using Molecular Operating Environment (MOE 2012.10) (CCG 2012) [14]. The choice of a template structure was based on the sequence identity between hAQP7 and the sequence of the AQPs with available resolved structures from human, bacteria and *Plasmodium falciparum* (UniProt 2013 codes O14520, C8TK05 and Q8WPZ6, respectively). The isoform that has the highest sequence similarity with hAQP7 is the bacterial isoform Glycerol Facilitator (GlpF), which was then chosen as a template structure. Three resolved structures for bGlpF, crystalized either with or without glycerol and solved by X-Ray diffraction, were retrieved from the Protein Data Bank [13]. Among them, the template was selected that had the best resolution (2.70 Å) without any substrate (pdb 1LDI). The tetrameric form was assembled according to directions given in the pdb file and the structure was prepared and protonated at pH 7 under forcefield Amber12EHT. Thus, the tetrameric form of the human AQP7 model was built: 50 intermediate models were generated and averaged to obtain the final homology model.

The obtained model was checked for more realistic rotamers of side chains in the regions of ar/R SF and NPA, by comparison with the available crystal structures of all the other AQP isoforms (pdb codes 1H6I, 36D8, 3D9S, 1RC2, 1LD1 and 3C02). The structure was

protonated at pH 7 and an energy minimization refinement was performed, also under the Amber12EHT force field, during which the Cα atoms were fixed. After identification of the residues of interest for the mechanism of pH gating, the same energy minimization procedure was used to further refine them. The refined homology model of hAQP7 was protonated using the PROPKA 3.1 package [15] at pH 5 and 7. Electrostatic surfaces were generated using the Adaptive Poisson-Boltzmann Solver (APBS) [23] plugin in Chimera [24].

Molecular Dynamics - Two model systems, using the above-described homology model, were produced using the PDB2PQR Server (version 2.0.0) [15], protonated at pH 7 and pH 5. The molecular systems consisted of the protonated tetrameric models of the AQP7 within a double layer of 175 palmitoyl-oleoyl-phosphatidyl-coline (POPC) lipid using the charm-gui online server [44]. Four glycerol molecules were placed into the system, one above each pore entrance on the extracellular side, at an approximate distance of 30 to 35 Å. To evaluate glycerol uptake, the system was solvated with 33151 (pH 7) and 33098 (pH 5) TIP3P water molecules and used a modified amber99sb-ildn forcefield, with the parameters for glycerol generated by the Automated Topology Builder and Repository (ATb, version 2.2) website using the B3LYP/6-31G* basis set [45]. A second system for each model was also created with the four glycerol molecules placed at an approximate distance of 30 to 35 Å from the pore entrance on the intracellular side, in order to evaluate efflux mechanisms.

All simulations were run using the GROMACS 5.1.2 simulation software with a 2fs time step. Particle-mesh Ewald method was used for calculating electrostatic interactions. The verlet cut-off scheme with a cut-off distance of 4.0 nm was used for short-range repulsive and attractive interactions and Lincs was used to constrain all bond lengths. Nose-hoover temperature coupling was used to maintain the temperature of the system (τ = 0.5 ps) at 310 K. The Parrinello-Rahman algorithm was used to maintain the pressure of the system at 1 bar with a coupling constant of τ = 1.0 ps. Simulations were equilibrated for 100 ps before production.

The four individual glycerol molecules were defined in the index and coupled in the pull code (e.g. gly_1 to chain_A). A total of 20 MD simulations, 10 in each direction (5 with the pH7 system and 5 with the pH5 system) were run using the direction COM pull procedure, in each case applying a separate yet equal harmonic restraint force to each solute molecule of 100 kJ $mol^{-1}nm^2$ with a rate of 0.02 nm ns^{-1} along the z-axis. Simulations were run for 250000 steps or 500 ps. Each pore radius was calculated using the Hole 2.0 program [16], which determines the internal surface based on atomic van der Waals radii. Snapshots at 100, 300,500,700 and 900 steps were taken of each simulation and coordinates for the centre of each pore (monomers A to D), at the ar/R SF, were used to generate the pore radius along the z-axis.

To test water permeation 6 MD simulations were performed, 3 for pH 7 and 3 for pH 5. Simulations were run for 10000000 steps or 20000 ps (20 ns) using the same two model systems and parameters. For these runs, the pull code was omitted, therefore removing any biasing of the system. Water molecules were counted using a python script, based on a Tcl script for tracking water molecules in a simulation [19], to determine each water molecule's position at each step and track its progress over the simulation time, registering full passage through the tetramer as well as the direction of movement. The upper and lower limits on the tetramer height were taken from the pore radius data calculated using the HOLE 2.0 program [16].

Water and glycerol permeation from Molecular Dynamics - Glycerol movement across hAQP7 was monitored by analyzing its trajectories for the whole duration of the simulations. For each simulation, glycerol molecules able to completely cross the hAQP7 channels were accounted for and all others excluded. The final data is represented as the mean ± SEM of total glycerol molecules crossing in each condition.

Due to the fact that the molecular dynamics used in this work represents an equilibrium simulation, only the diffusion constant (D_w) can be estimated, rather than the permeability coefficient. For this purpose, D_w of the single-file water molecules was estimated using the Einstein relation [46]:

$$D_w = \frac{k_0 z^2}{2}$$

where z represents the average distance between two water molecules in the single-file region and k_0 represents the transport rate. The transport rate was calculated as the total number of water molecules crossing the channel, given by the script, divided by the length of the simulation (in seconds). For uptake and efflux, the total number of water molecules was defined as the number of molecules going in either direction of the z-axis (positive direction for efflux and negative for uptake). The final data is represented as the mean ± SEM.

Statistical analysis - The results were expressed as mean ± SEM of *n* individual experiments. Statistical analysis between groups was performed by the unpaired Student's *t*-test using the Prism software (GraphPad Software Inc., San Diego, CA). *P* values < 0.05 were considered statistical significant.

3.3.6 Supplementary Information

Supplementary Table S3.3.1 – Human AQP7 specific primers for PCR amplification and mutagenic primers used in this study. Restriction sites for *Spe*I and *Cla*I are in bold and mutated nucleotides introduced are underlined. Each mutation was confirmed by DNA sequencing to ensure the fidelity of PCR reactions.

Primer name	***Sequence (5' to 3' direction)***
Cloning	
AQP7_FW	GG**ACTAGT**CCTATGGTTCAAGCATCCGGGCACAG
AQP7_REV	CC**ATCGAT**GGAGAAGTGCTCTAGGGCCATGGATTCAT
Site-directed mutagenesis	
Tyr135Ala_FW	GCTGCCACCATCTACAGTCTCTTCGCCACGGCCATTCTCCACTTTTCG
Tyr135Ala_REV	CGAAAAGTGGAGAATGGCCGTGGCGAAGAGACTGTAGATGGTGGCAGC
His140Ala_FW	CTCTTCTACACGGCCATTCTCGCCTTTTCGGGTGGACAGCTGATGGTG
His140Ala_REV	CACCATCAGCTGTCCACCCGAAAAGGCGAGAATGGCCGTGTAGAAGAG
His165Ala_FW	GCCACCTACCTTCCTGATGCCATGACATTGTGGCGGGGCTTCCTG
His165Ala_REV	CAGGAAGCCCCGCCACAATGTCATGGCATCAGGAAGGTAGGTGGC

Supplementary Table S3.3.2 - pH dependency (pKa values) of water and glycerol permeation via human AQP7 (wild-type and mutated). Data presented as mean ± SEM (n=4). *P < 0.05 vs wild type.

	Water	***Glycerol***
	pK_a	pK_a
Wild type	5.89 ± 0.02	5.86 ± 0.01
Y135A	6.06 ± 0.01	6.04 ± 0.01
H140A	6.11 ± 0.02	5.91 ± 0.01
H165A	6.65 ± 0.01*	6.30 ± 0.02*
Y135A+H165A	6.58 ± 0.01*	6.21 ± 0.02*
H140A+H165A	6.53 ± 0.01*	6.29 ± 0.01*

Values were compared to AQP7 wild type. *, P<0.05

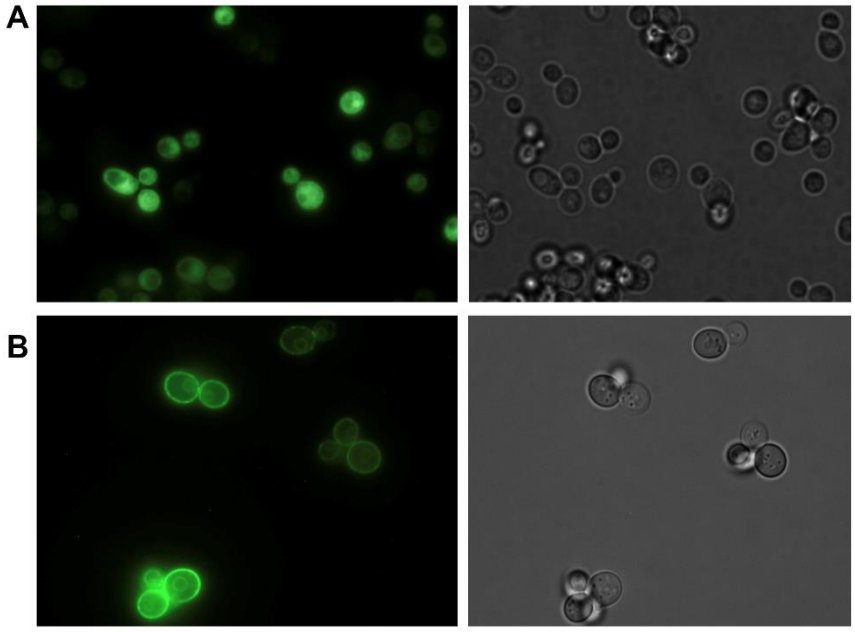

Supplementary Figure S.3.3.1 | Localization of GFP-tagged hAQP7 expressed in *S. cerevisiae aqy*-null strain. Epifluorescence (left panels) and phase contrast (right panels) images of *S. cerevisiae aqy*-null strains transformed with **(A)** the empty plasmid pUG35 (control cells) and **(B)** hAQP7. In control cells, GFP expression results in a homogeneous distribution of fluorescence in the cytoplasm, while yeast cells expressing hAQP7-GFP show membrane-localized fluorescence confirming hAQP7 localization at the plasma membrane.

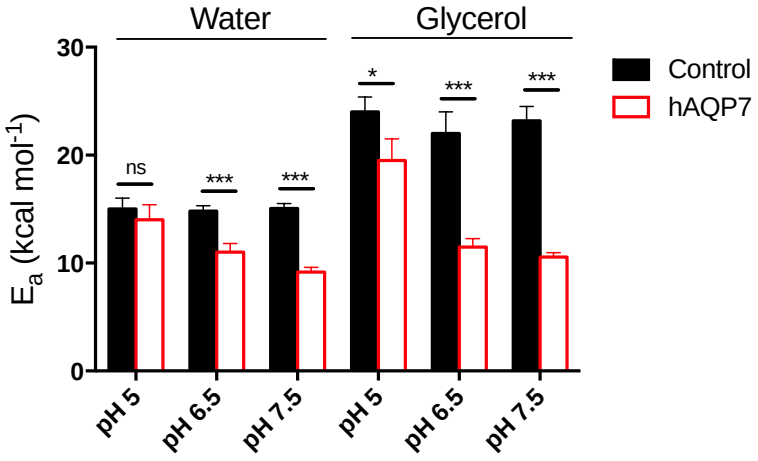

Supplementary Figure S.3.3.2 | Activation energy (E_a) for water and glycerol permeation at distinct pH values. E_a values estimated at three distinct pH values (pH 5, 6.5 and 7.5) significantly decreased from pH 5 (water 14.0 ± 1.4 kcal mol-1 and glycerol 19.5 ± 2.0 kcal

mol-1) to pH 6.5 (water 11.0 ± 0.8 kcal mol-1 and glycerol 11.5 ± 0.8 kcal mol-1) and pH 7.5 (water 9.2 ± 0.5 kcal mol-1 and glycerol 10.6 ± 0.4 kcal mol-1), corroborating the proposed channel pH regulation. Data is shown as mean ± SEM of three independent experiments. ns, non significant, * $p < 0.05$; *** $p < 0.001$.

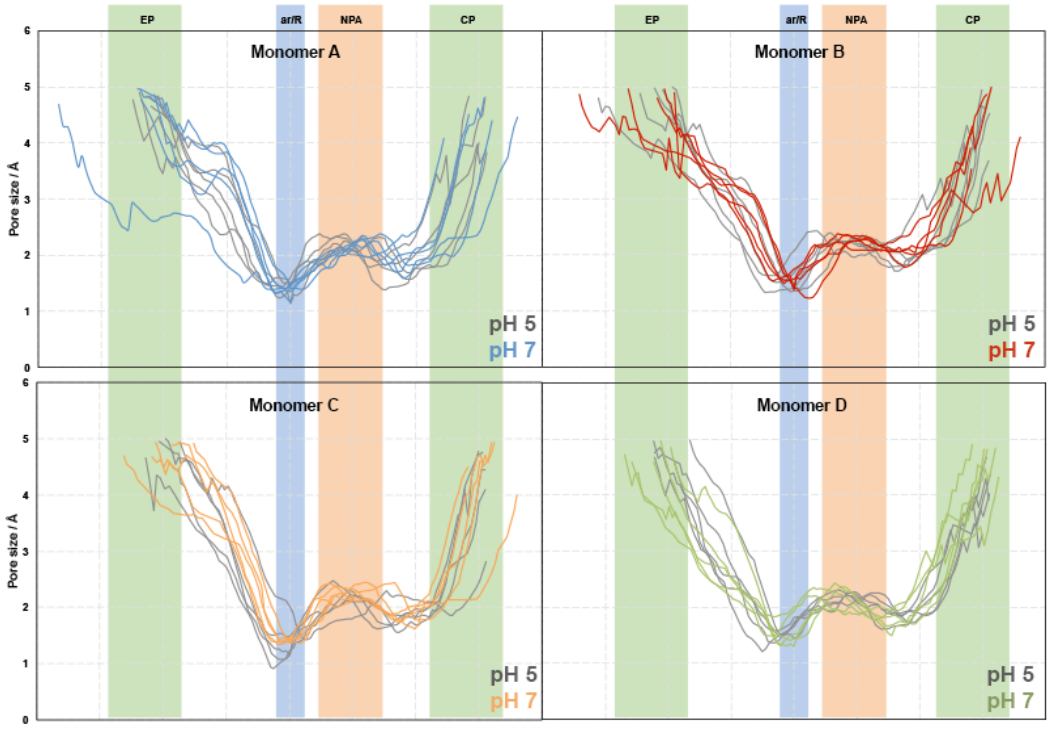

Supplementary Figure S3.3.3 | Pore size of the four AQP7 monomers at pH 5 and pH 7. Each line represents an average pore size for each simulation, by using the pore size taken from five snapshots of each simulation. EP – extracellular pocket, ar/R – aromatic/arginine selectivity filter, NPA – NPA motif, CP – cytoplasmic pocket. Pore size obtained with HOLE. [Data obtained by Andreia de Almeida]

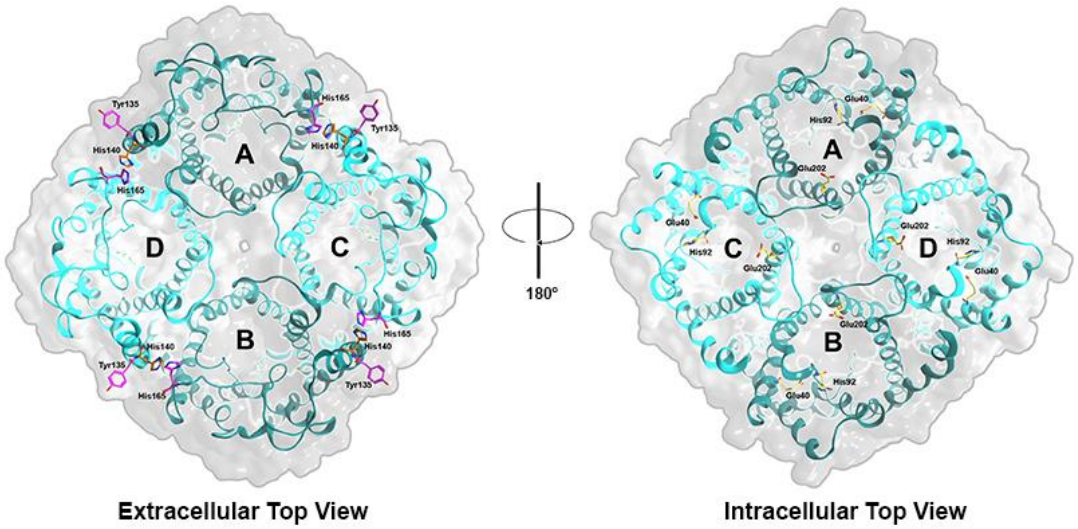

Supplementary Figure S3.3.4 | **(A)** Top extracellular and **(B)** intracellular views of the homology model of human AQP7 in its tetrameric assembly in cartoon representation of the tertiary structure, with ribbon representation (in blue) and surface representation of residues lining the channel (grey). Relevant amino acid residues are shown in stick representation. In yellow the residues that are protonated at pH 5 in the intracellular side are shown. His140 residues in each monomer are protonated at pH 5 and shown in orange, while His165 and Tyr135 are represented in magenta; all three residues were mutated for further studies. Figure generated with MOE. [Data obtained by Andreia de Almeida]

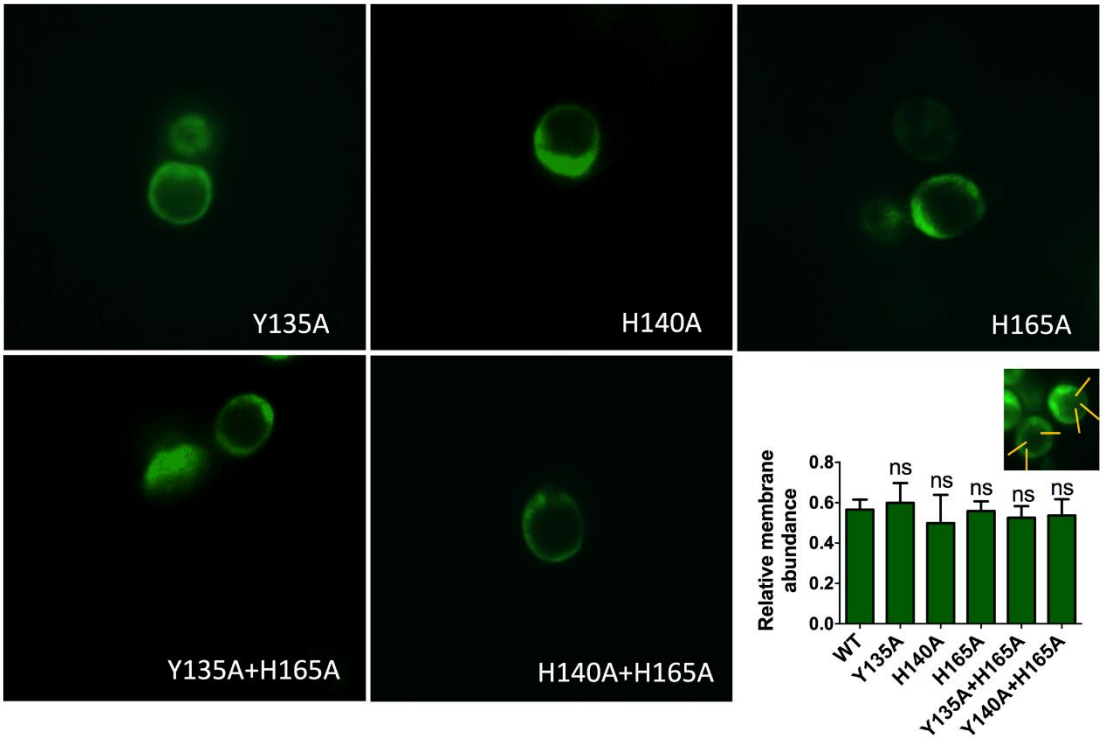

Supplementary Figure S3.3.5 | Plasma membrane localization and relative membrane abundance of GFP-tagged hAQP7 mutations in *S. cerevisiae aqy*-null strain. Photos are representative of cells incubated either in pH 7.4 or pH 5.1. Fluorescence was observed by fluorescence microscopy and the relative membrane abundance of each mutant (bar graph) was calculated from linear intensity profiles across cell membrane (yellow lines in the insert picture) from at least 30 cells (3 profiles lines per cell) using ImageJ software (https://imagej.net), according to [39,40]. Background fluorescence was subtracted from the maximal fluorescence intensity and the obtained difference was divided by the maximal fluorescence along the line scan to calculate the percentage of fluorescence at the membrane. No differences in membrane abundance were observed in cells incubated in media with different pHs or osmolarities. ns, non significant.

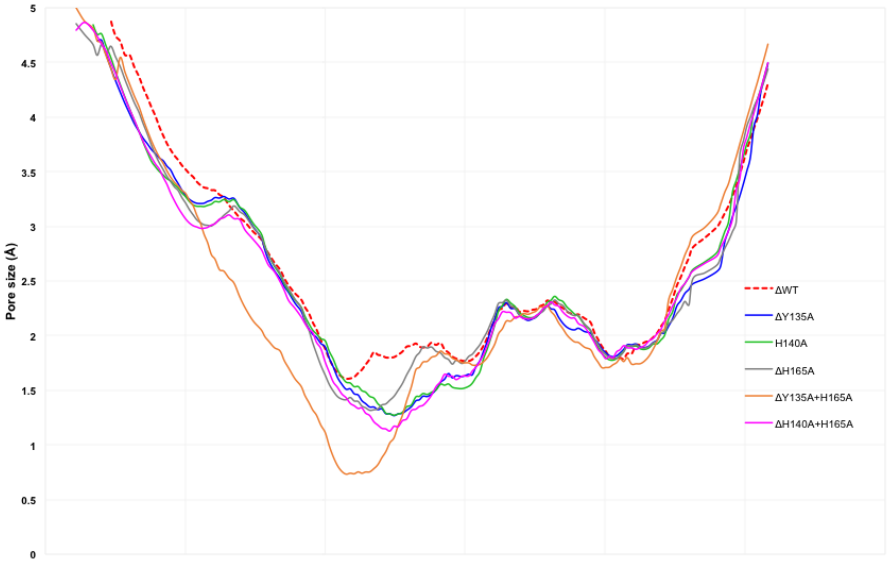

Supplementary Figure S3.3.6 | Pore size average of the four AQP7 monomers for each mutant and WT. Pore size obtained with HOLE. [Data obtained by Andreia de Almeida]

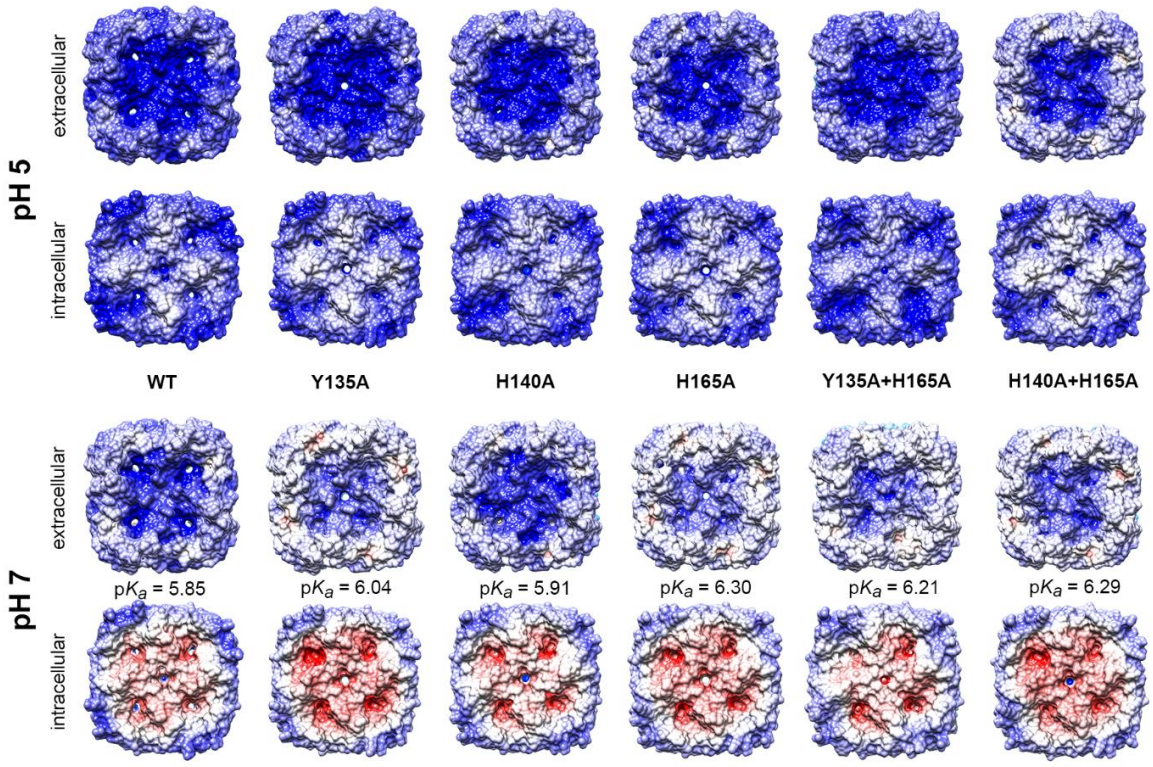

Supplementary Figure S3.3.7 | Electrostatic surfaces of hAQP7 WT and mutants, at pH 5 and 7. Protonation performed using PROPKA 3.1 package 3. Surfaces were generated using the Adaptive Poisson-Boltzmann Solver (APBS) plugin in Chimera. [Data obtained by Andreia de Almeida]

3.3.7 References

[1] I.V. da Silva, J.S. Rodrigues, I. Rebelo, J.P.G. Miranda, G. Soveral, Revisiting the metabolic syndrome: the emerging role of aquaglyceroporins, Cell Mol Life Sci (2018).

[2] I.V. da Silva, G. Soveral, Aquaporins in Obesity, Adv Exp Med Biol 969 (2017) 227-238.

[3] A. Madeira, T.F. Moura, G. Soveral, Aquaglyceroporins: implications in adipose biology and obesity, Cell Mol Life Sci 72 (2015) 759-771.

[4] A. Rodriguez, V. Catalan, J. Gomez-Ambrosi, G. Fruhbeck, Role of aquaporin-7 in the pathophysiological control of fat accumulation in mice, FEBS Lett 580 (2006) 4771-4776.

[5] A. Madeira, T.F. Moura, G. Soveral, Detecting Aquaporin Function and Regulation, Front Chem 4 (2016) 3.

[6] A. Madeira, A. de Almeida, C. de Graaf, M. Camps, A. Zorzano, T.F. Moura, A. Casini, G. Soveral, A gold coordination compound as a chemical probe to unravel aquaporin-7 function, Chembiochem 15 (2014) 1487-1494.

[7] A.P. Martins, A. Marrone, A. Ciancetta, A. Galán Cobo, M. Echevarría, T.F. Moura, N. Re, A. Casini, G. Soveral, Targeting aquaporin function: potent inhibition of aquaglyceroporin-3 by a gold-based compound., PloS one 7 (2012) e37435.

[8] A.P. Martins, A. Ciancetta, A. de Almeida, A. Marrone, N. Re, G. Soveral, A. Casini, Aquaporin inhibition by gold(III) compounds: new insights, ChemMedChem 8 (2013) 1086-1092.

[9] A. Serna, A. Galan-Cobo, C. Rodrigues, I. Sanchez-Gomar, J.J. Toledo-Aral, T.F. Moura, A. Casini, G. Soveral, M. Echevarria, Functional inhibition of aquaporin-3 with a gold-based compound induces blockage of cell proliferation, J Cell Physiol 229 (2014) 1787-1801.

[10] T. Katano, Y. Ito, K. Ohta, T. Yasujima, K. Inoue, H. Yuasa, Functional characteristics of aquaporin 7 as a facilitative glycerol carrier, Drug Metab Pharmacokinet 29 (2014) 244-248.

[11] M. Rothert, D. Ronfeldt, E. Beitz, Electrostatic attraction of weak monoacid anions increases probability for protonation and passage through aquaporins, J Biol Chem 292 (2017) 9358-9364.

[12] A. de Almeida, A.P. Martins, A.F. Mosca, H.J. Wijma, C. Prista, G. Soveral, A. Casini, Exploring the gating mechanisms of aquaporin-3: new clues for the design of inhibitors?, Molecular Biosystems 12 (2016) 1564-1573.

[13] E. Tajkhorshid, P. Nollert, M.O. Jensen, L.J. Miercke, J. O'Connell, R.M. Stroud, K. Schulten, Control of the selectivity of the aquaporin water channel family by global orientational tuning, Science 296 (2002) 525-530.

[14] M.O.E. (MOE), Chemical Computing Group Inc. Montreal, QC, Canada) 2012.10.

[15] C.R. Sondergaard, M.H. Olsson, M. Rostkowski, J.H. Jensen, Improved Treatment of Ligands and Coupling Effects in Empirical Calculation and Rationalization of pKa Values, J Chem Theory Comput 7 (2011) 2284-2295.

[16] O.S. Smart, J.G. Neduvelil, X. Wang, B.A. Wallace, M.S. Sansom, HOLE: a program for the analysis of the pore dimensions of ion channel structural models, J Mol Graph 14 (1996) 354-360, 376.

[17] L. Janosi, M. Ceccarelli, The gating mechanism of the human aquaporin 5 revealed by molecular dynamics simulations, PLoS One 8 (2013) e59897.
[18] W. Humphrey, A. Dalke, K. Schulten, VMD: visual molecular dynamics, J Mol Graph 14 (1996) 33-38, 27-38.
[19] T.O. Wambo, R.A. Rodriguez, L.Y. Chen, Computing osmotic permeabilities of aquaporins AQP4, AQP5, and GlpF from near-equilibrium simulations, Biochim Biophys Acta 1859 (2017) 1310-1316.
[20] A. Horner, F. Zocher, J. Preiner, N. Ollinger, C. Siligan, S.A. Akimov, P. Pohl, The mobility of single-file water molecules is governed by the number of H-bonds they may form with channel-lining residues, Sci Adv 1 (2015) e1400083.
[21] E. Nevoigt, U. Stahl, Osmoregulation and glycerol metabolism in the yeast Saccharomyces cerevisiae, FEMS Microbiol Rev 21 (1997) 231-241.
[22] M. Zelenina, A.A. Bondar, S. Zelenin, A. Aperia, Nickel and extracellular acidification inhibit the water permeability of human aquaporin-3 in lung epithelial cells, J Biol Chem 278 (2003) 30037-30043.
[23] N.A. Baker, D. Sept, S. Joseph, M.J. Holst, J.A. McCammon, Electrostatics of nanosystems: application to microtubules and the ribosome, Proc Natl Acad Sci U S A 98 (2001) 10037-10041.
[24] E.F. Pettersen, T.D. Goddard, C.C. Huang, G.S. Couch, D.M. Greenblatt, E.C. Meng, T.E. Ferrin, UCSF Chimera--a visualization system for exploratory research and analysis, J Comput Chem 25 (2004) 1605-1612.
[25] A. Rodriguez, V. Catalan, J. Gomez-Ambrosi, G. Fruhbeck, Aquaglyceroporins serve as metabolic gateways in adiposity and insulin resistance control, Cell Cycle 10 (2011) 1548-1556.
[26] H. Meisner, K. Tenney, pH as an indicator of free fatty acid release from adipocytes, J Lipid Res 18 (1977) 774-776.
[27] D. Rudman, P.W. Shank, Observations on the production of hydrogen ions during mobilization of fatty acids from adipose tissue, Endocrinology 79 (1966) 1100-1108.
[28] V.N. Civelek, J.A. Hamilton, K. Tornheim, K.L. Kelly, B.E. Corkey, Intracellular pH in adipocytes: effects of free fatty acid diffusion across the plasma membrane, lipolytic agonists, and insulin, Proc Natl Acad Sci U S A 93 (1996) 10139-10144.
[29] L. Leitao, C. Prista, T.F. Moura, M.C. Loureiro-Dias, G. Soveral, Grapevine aquaporins: gating of a tonoplast intrinsic protein (TIP2;1) by cytosolic pH, PLoS One 7 (2012) e33219.
[30] M.O. Jensen, E. Tajkhorshid, K. Schulten, The mechanism of glycerol conduction in aquaglyceroporins, Structure 9 (2001) 1083-1093.
[31] P. Grayson, E. Tajkhorshid, K. Schulten, Mechanisms of selectivity in channels and enzymes studied with interactive molecular dynamics, Biophys J 85 (2003) 36-48.
[32] A. Madeira, M. Camps, A. Zorzano, T.F. Moura, G. Soveral, Biophysical assessment of human aquaporin-7 as a water and glycerol channel in 3T3-L1 adipocytes, PLoS One 8 (2013) e83442.
[33] U. Guldener, S. Heck, T. Fielder, J. Beinhauer, J.H. Hegemann, A new efficient gene disruption cassette for repeated use in budding yeast, Nucleic Acids Res 24 (1996) 2519-2524.

[34] D. Hanahan, Techniques for transformation of Escherichia coli, in: D.M. Glover (Ed.), DNA cloning: a practical approach,, IRL Press, Oxford, United Kingdom, 1985, pp. 109-135.
[35] J. Sambrook, E.F. Fritsch, T. Maniatis, Molecular Cloning: A Laboratory Manual, 2nd edn ed., Cold Spring Harbor, NY, 1989.
[36] J.T. Pronk, Auxotrophic yeast strains in fundamental and applied research, Appl Environ Microbiol 68 (2002) 2095-2100.
[37] R.D. Geitz, R.H. Schiestl, Transforming Yeast with DNA, Methods in Molecular and Cellular Biology 5 (1995) 255–269.
[38] S.D. Joshi, L.A. Davidson, Live-cell imaging and quantitative analysis of embryonic epithelial cells in Xenopus laevis, J Vis Exp (2010).
[39] P. Kitchen, F. Oberg, J. Sjohamn, K. Hedfalk, R.M. Bill, A.C. Conner, M.T. Conner, S. Tornroth-Horsefield, Plasma Membrane Abundance of Human Aquaporin 5 Is Dynamically Regulated by Multiple Pathways, PLoS One 10 (2015) e0143027.
[40] C. Rodrigues, A.F. Mosca, A.P. Martins, T. Nobre, C. Prista, F. Antunes, A. Cipak Gasparovic, G. Soveral, Rat Aquaporin-5 Is pH-Gated Induced by Phosphorylation and Is Implicated in Oxidative Stress, Int J Mol Sci 17 (2016).
[41] G. Soveral, A. Madeira, M.C. Loureiro-Dias, T.F. Moura, Water transport in intact yeast cells as assessed by fluorescence self-quenching, Appl Environ Microbiol 73 (2007) 2341-2343.
[42] G. Soveral, A. Madeira, M.C. Loureiro-Dias, T.F. Moura, Membrane tension regulates water transport in yeast, Biochim Biophys Acta 1778 (2008) 2573-2579.
[43] M. Henriques, C. Quintas, M.C. Loureiro-Dias, Extrusion of benzoic acid in Saccharomyces cerevisiae by an energy-dependent mechanism, Microbiology 143 (1997) 1877-1883.
[44] S. Jo, T. Kim, V.G. Iyer, W. Im, CHARMM-GUI: a web-based graphical user interface for CHARMM, J Comput Chem 29 (2008) 1859-1865.
[45] A.K. Malde, L. Zuo, M. Breeze, M. Stroet, D. Poger, P.C. Nair, C. Oostenbrink, A.E. Mark, An Automated Force Field Topology Builder (ATB) and Repository: Version 1.0, J Chem Theory Comput 7 (2011) 4026-4037.
[46] F. Zhu, E. Tajkhorshid, K. Schulten, Collective diffusion model for water permeation through microscopic channels, Phys Rev Lett 93 (2004) 224501.

3.4 Cytoplasmic pH gate in Aquaporin-10

3.4.1 Abstract

Obesity is a major threat to global health and metabolically associated with glycerol homeostasis. Here we demonstrate that in human adipocytes, at the low pH observed during lipolysis (fat burning), glycerol release is achieved through stimulation of aquaglyceroporin AQP10. The crystal structure of human AQP10 determined at 2.3 Å resolution, representing the first structure of a mammalian aquaglyceroporin, unveils the molecular basis for pH modulation - an exceptionally wide selectivity (ar/R) filter and an unique cytoplasmic gate. Structural and functional (in vitro and in vivo) analyses disclose a glycerol-specific pH-dependence and pinpoint pore-lining His80 as the pH sensor. Molecular dynamics simulations indicate how gate opening is achieved. These findings unravel a novel type of aquaporin regulation important for controlling body fat mass. Thus, targeting the cytoplasmic gate to induce constitutive glycerol secretion may offer an attractive option for treating obesity and related complications.

3.4.2 Introduction

Uptake and release of glycerol from the small intestine (duodenal enterocytes), adipocytes and other cell types, are primarily facilitated by a subclass of aquaporins (AQP), the water and glycerol-conducting aquaglyceroporins (AQP3, 7, 9 and 10; Figure 3.4.1 A) [1,2,3]. Furthermore, mice aquaglyceroporin AQP7 knockouts accumulate glycerol and TAGs, and develop enlarged adipocytes and obesity with age. Thus, glycerol and aquaglyceroporin-induced glycerol flux are likely central elements of fat accumulation and the pathophysiology of obesity [4,5]. Nevertheless, the molecular principles that regulate glycerol flow across cellular membranes in the body remain enigmatic. The interplay between lipolysis

and glycerol flux is obscure, and human aquaglyceroporins are primarily believed to be controlled through trafficking (e.g. cathecolamine/insulin-dependent subcellular re-organisation of AQP7 in adipocytes [2,6], as structural information is available only for homologues from lower organisms [7,8,9]. Only a few reports hint at a pH-dependence of mammalian aquaglyceroporin-mediated flux [1,10,11].

3.4.3 Results and Discussion

We therefore assessed the pH effect on water and glycerol flow across membrane vesicles prepared from human adipocytes challenged with osmotic gradients (Figure 3.4.1 B and Supplementary Figure S3.4.1 A). Whereas the permeability to water (P_f) was pH-insensitive, glycerol passage (P_{Gly}) increased at low pH (pH 7.4 vs 5.5). To identify the responsible protein(s), all four human aquaglyceroporins and water-strict (orthodox) hAQP2 serving as control were isolated as green fluorescent protein (GFP)-fusions. Following reconstitution into biomimetic vesicles (polymersomes) [12], we investigated the flow rates at the equivalent pH upon osmotic stress (Figure 3.4.1 C and Supplementary Figure S3.4.1 B). The water permeability was unchanged for all tested AQPs, suggesting pH-insensitive water diffusion. Glycerol conductance was in contrast highly pH-dependent. As expected, orthodox hAQP2$_{GFP}$ displayed no glycerol transport. hAQP3$_{GFP}$, 7 and 9 were permeable to glycerol only at pH 7.4. Only hAQP10$_{GFP}$ allowed glycerol flux at pH 5.5, whereas the flow at pH 7.4 was markedly reduced, in agreement with the adipocyte-based data. As an additional control, we detected plasma membrane-localized hAQP10 in the adipose tissue through selective immunolabeling (Figure 3.4.1 D). Thus, our data suggest that adipocyte glycerol flux augmented at lower pH associated with e.g. lipolysis is mediated by hAQP10.

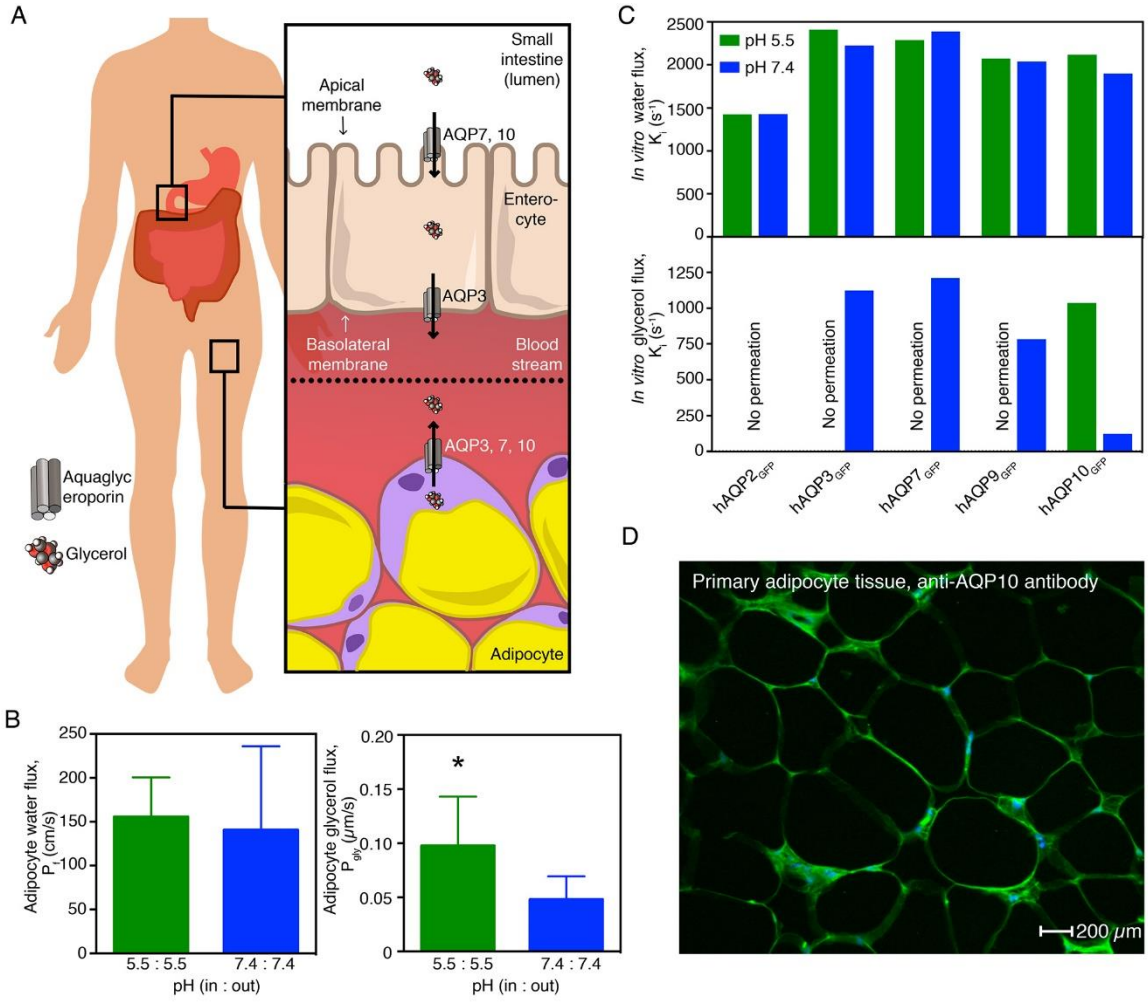

Figure 3.4.1 | Low pH stimulates human adipocyte glycerol flux through aquaglyceroporin AQP10. (A) Simplified overview of aquaglyceroporin-mediated regulation of human body glycerol homeostasis. Glycerol absorption in the small intestine (enterocytes) occurs through AQP7 and 10, and via AQP3-mediated excretion into the blood stream, whereas release into the circulation from fat tissue (adipocytes) involves AQP3, 7 and 10. **(B)** Water and glycerol permeability of human adipocyte plasma membrane vesicles exposed to glycerol gradient. Flux was measured using identical pH inside and outside: pH 7.4 (blue) or 5.5 (green). Water (P_f) and glycerol (P_{Gly}) permeability coefficients were calculated as described in Methods. Results are given as mean ± SD. *, P=0.037 vs. 7.4:7.4 (Student's t test; N=6). **(C)** Water and glycerol permeability of GFP-fused human aquaporins reconstituted into polymersomes. K_i rate constants (s^{-1}) were obtained at pH 7.4 (blue) and pH 5.5 (green). Each bar shows an average of N=10 measurements performed for the same proteopolymersome sample. **(D)** AQP10 is membrane-localized to subcutaneous human adipose tissue used for vesicle preparation. Representative immunofluorescence confocal microscopy images with anti-hAQP10

antibody (green) and DAPI staining for nuclei (blue). Scale bar: 200 µm. [Data obtained by Umberto Laforenza, Julie Winkel Missel and Mariana Spulber]

To resolve how hAQP10 is pH-gated, structural studies were initiated using polyhistidine (His)-tagged protein. However, full-length hAQP10 yielded no crystals and we continued with a variant ($hAQP10_{cryst}$; Figure 3.4.2 A) truncated in the termini (Δ1-10, Δ277-301) that crystallized at pH 6.0. The structure was determined at 2.3 Å resolution and reveals a tetramer fold highly reminiscent of other AQPs (Figure 3.4.2 B), with each monomer formed by six transmembrane helices (TM1-TM6) establishing a conducting channel (Figure 3.4.2 C). Strikingly, the region typically linked to selectivity in AQPs, the aromatic and arginine (ar/R) selectivity filter at the non-cytosolic end of the pore [13], is significantly wider (2.6 Å) than in previously structurally characterized AQPs (Figure 3.4.2 C and D), as revealed by HOLE analyses [14]. Furthermore, no glycerol molecule was identified at the ar/R filter, in contrast to the only available structure of a eukaryotic aquaglyceroporin, PfAQP (Figure 3.4.2 C and D) [9]. These observations raise questions if the functional role of the ar/R region is maintained in hAQP10. A single glycerol molecule is instead located adjacent to the AQP archetypical, central NPA-motif (N82-A84) in hAQP10 (Figure 3.4.2 C and E). This area and the presence of NPA glycerol molecule are highly conserved elements among structurally determined aquaglyceroporins (including GlpF and AqpM) [7,8]. However, towards the cytoplasm the glycerol molecule is rather positioned close to the unique F85 of loop B in hAQP10 (invariant as a valine/isoleucin in other AQPs). F85 has a side-chain configuration unfavorable for glycerol passage, forming a novel mechanistic feature. Moreover, the entire cytoplasmic pore region has adapted a tight arrangement not previously observed, achieved by the first part of loop B (G73-H80; loop layout likely allowed by the hAQP10-specific

G73G74-motif; Figure 3.4.2 E) with V76-S77 capping the cytoplasmic opening, F85, and R94 (of TM3), which seemingly stabilizes loop B in the closed configuration. Notably, HOLE analysis suggests that this narrowing (0.9 Å) permits water (0.8 Å at the ar/R filter in hAQP2) [14] but not glycerol (1.3 Å in AqpM) [8] flux, in agreement with the proteopolymersome data at relatively high pH. The most likely pH-sensor candidate in the region is H80, which lines the pore and structurally links loop B, F85 and R94. pH-dependent gating mechanisms have been proposed for human AQP3, 4 and 5 [10,15,16], but the available structures are open (for hAQP4 the H80 equivalent was pinpointed as a gate, but loop B in hAQP4 has a significantly different configuration as compared to hAQP10) [17,18]. Thus, this is to our knowledge the first structural evidence that human AQPs may be gated [19], and the first time that ligand-selective regulation is described for a membrane protein.

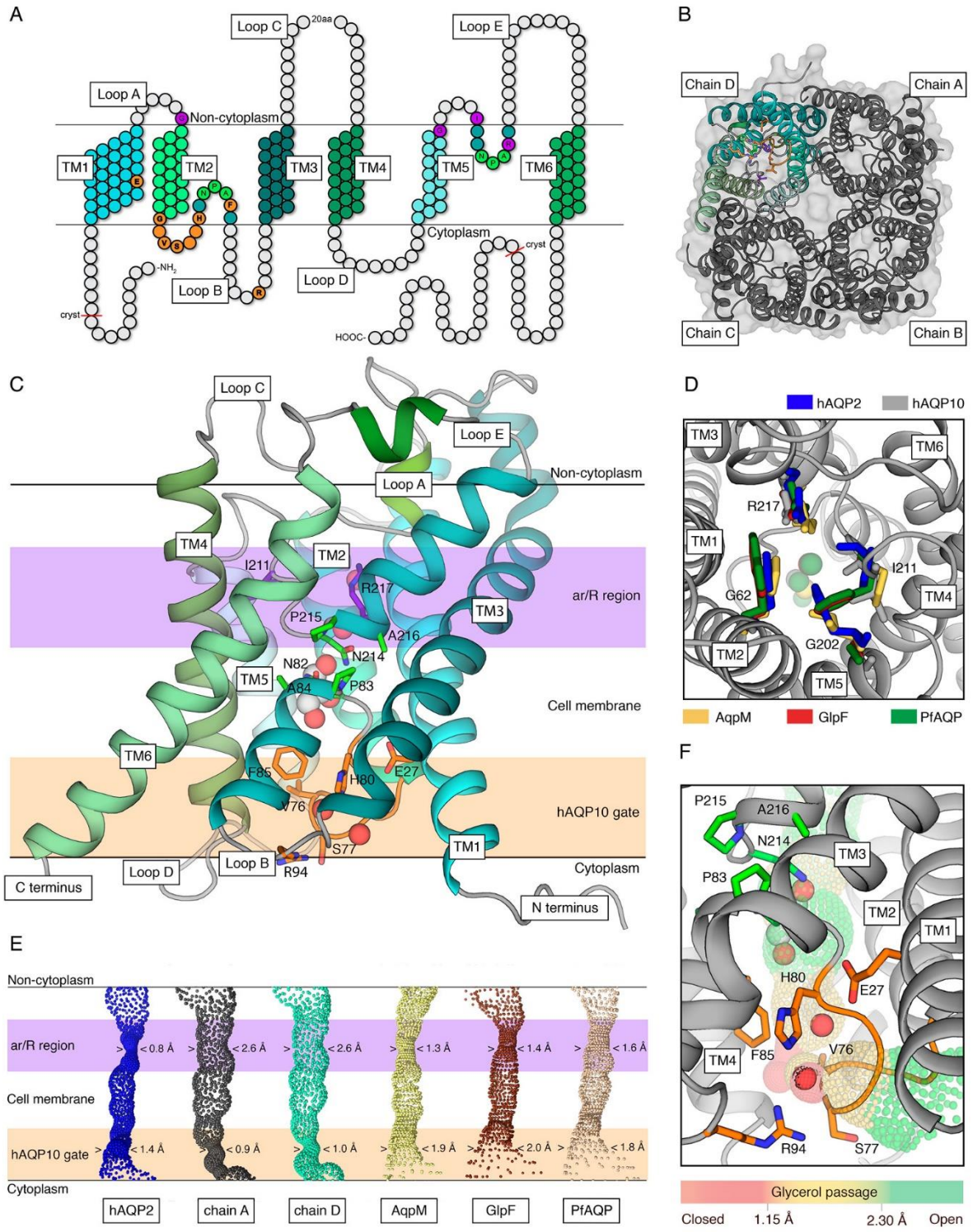

Figure 3.4.2 | Architecture of human AQP10 and the glycerol-specific gate. (A) Topology of hAQP10 monomer with six transmembrane helices (TM1-6) and five connecting stretches (loops A-E). Residues at the NPA-motives, the classical ar/R selectivity filter and the novel cytoplasmic gate are indicated in green, purple and orange

(throughout); hAQP10-specific residues in bold. The length of the crystallized form is also highlighted. **(B)** The hAQP10 tetramer from the cytoplasmic side, with chains A-C shown in gray and chain D in cyan tones. **(C)** Side view of the primed-to-open monomer (chain D). A single glycerol and four water molecules were identified. **(D)** The unusually wide ar/R selectivity region of hAQP10 (chain A, gray) compared to those in hAQP2 (blue, pdb-id 4NEF) [14], AqpM (yellow, pdb-id 2F2B) [8], GlpF (brown, pdb-id 1FX8) [20] and PfAQP (wheat, pdb-id 3C02) [9]. View from the non-cytoplasmic side. Glycerol molecules in the structures are shown as spheres in equivalent colors. **(E)** The channel profiles of selected aquaporins calculated using the software HOLE. hAQP10 chains A (gray) and D (cyan) are compared with increasing minimal diameter from left to right. The novel cytoplasmic gate and ar/R regions are marked in light orange and purple, respectively. **(F)** Close view of the novel cytoplasmic and glycerol-specific gate. H80 forms an interaction network work with E27, F85, R94, V76 and S77. [Data obtained by Kamil Gotfryd]

To assess the functional role and physiological importance of the novel cytoplasmic gate we investigated the functionality of hAQP10 and mutant forms using protepolymersome- (*in vitro*) and *S. cerevisiae*-based (*in-vivo*) assays (Supplementary Figure S3.4.1 B and C) [21]. In the reconstituted system, His-tag-fusions were assayed (Figure 3.4.3 A), revealing an overall similar pH-dependency permeation profile for water and glycerol as for GFP-fused counterparts (the crystallized variant, $hAQP10_{cryst}$, mimics full-length protein, hAQP10). Furthermore, our experiments unambiguously pinpoint H80 and F85 as critical for glycerol flux, and subtle effects of S77 and R94 substitutions. Subsequently, we measured glycerol (P_{gly}) and water (P_f) flow rates in yeast cells challenged with osmotic gradients (Figure 3.4.3 B and C and Supplementary Figure S3.4.2 and Supplementary Table S3.4.1). As in the proteopolymersome assay (Figure 3.4.1 C and 3.4.3 A), opposing pH effects were found for $hAQP3_{GFP}$ and hAQP10, increasing glycerol permeation at low pH in hAQP10. Most importantly, the detrimental effect of H80A in vitro was reproduced, suggesting a channel remaining closed independently of pH, in agreement with a pH-sensory role of the

histidine; scouting prove that the H80A mutant is impermeable to glycerol over large pH and temperature spectra (Figure 3.4.3 B, Supplementary Figure S3.4.2 and Supplementary Table S3.4.1). Impaired glycerol flux was also observed for mutations of H80-interaction network residues, S77 and R94 (both profoundly affected) and F85A (moderately influenced). Similarly, substitutions of G73, located distal to the channel, to valine and phenylalanine as in hAQP1 and 4, respectively, markedly reduced glycerol flux, supporting that the G73G74-motif is important to kink TM2, thereby allowing loop B to gate. In contrast, water-conducting flux remained unaffected in vivo for almost all hAQP10 forms (Supplementary Figure S3.4.2 E). This is congruent with the proteopolymersome data, substantiating that water diffusion through hAQP10 is pH-insensitive, maintained independently of the residues orchestrating glycerol flux. The moderate effect of G73A is exceptional, displaying increasing flux of glycerol and water only at low pH, indicating that this subtle alteration (mimicking the case in hAQP3, 7 and 9) maintains the gating-principles without achieving complete closure. We predict that the approximate loop configuration is maintained in other human aquaglyceroporins, but the pH-sensitivity is missing due to the valine replacement of F85.

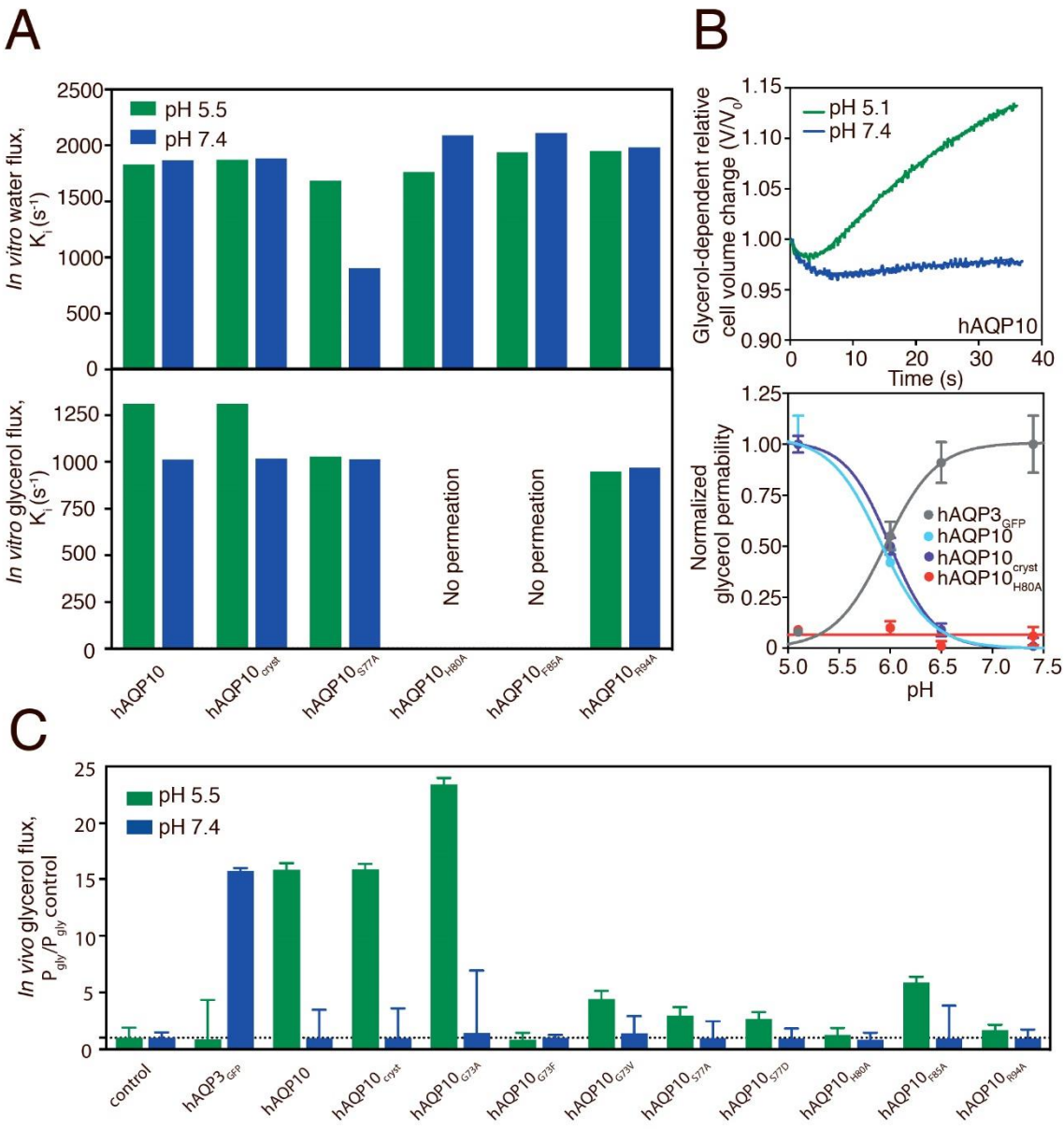

Figure 3.4.3 | Functional characterization of human AQP10. (A) Water and glycerol permeability of hAQP10 forms reconstituted into polymersomes. K_i rate constants (s^{-1}) were obtained at pH 7.4 (blue) and pH 5.5 (green). Each bar shows an average of N=10 measurements performed for the same proteopolymersome sample. **(B)** Upper plot: Representative time course of the relative cell volume (V/V_0) changes after glycerol osmotic shock at pH 5.1 (green) and 7.4 (blue) in hAQP10 expressing yeast cells. Lower plot: pH-dependence of glycerol permeability (P_{gly}) measured in cells expressing $hAQP3_{GFP}$ or different hAQP10 forms. P_{Gly} is normalized for each data set (P_{Gly}-P_{Gly} control/P_{Gly} max) and fitted with a Hill equation. **(C)** Glycerol permeability (P_{Gly}) ratio of yeast cells expressing $hAQP3_{GFP}$ or hAQP10 forms measured at pH 5.1 (green) and pH 7.4 (blue). Results are

normalized to P_{Gly} of the control strain at the respective pH. Results are given as mean ± SD of at least N=3 independent experiments. [Data obtained jointly with Mariana Spulber]

How then is hAQP10 opened at low pH? Crystallization attempts at lower pH to structurally decipher the opening mechanism were fruitless. Nevertheless, as the obtained crystal form contains the entire hAQP10 tetramer in the asymmetric unit, intermonomeric differences were analyzed. While overall highly similar, three chains (Figure 3.4.2 B dark grey) display an identical, closed, cytoplasmic arrangement. In contrast, a subtle shift of the pore-width (to 1.0 Å) is observed at H80 in chain D (Figure 3.4.2 B and D cyan). Hence, monomer D may represent a primed-to-open gate configuration (glycerol flux remains unanticipated at this pore-width). Equivalent examination reveals that the observed pore closure likely cannot be attributed to crystal packing or associated detergent molecules, as these interaction patterns differ between monomers. To unravel the molecular mechanism required for full opening we turned to molecular dynamics (MD) simulations of membrane-embedded hAQP10 tetramer in the presence of glycerol, assessing two different protonation states of H80 (mono(ε) and double), as a mimic of relatively high and low pH, respectively. All-in-all, based on structural, functional and MD simulation analyses, we propose a pH-dependent gating mechanism of hAQP10 triggered by protonation of H80, which at low pH reorients, stabilized by E27 (Figure 3.4.4). With this structural shift, F85 adapts a more open side-chain orientation, and the loop (including V76-S77) rearranges in conjunction with R94 to allow glycerol permeation.

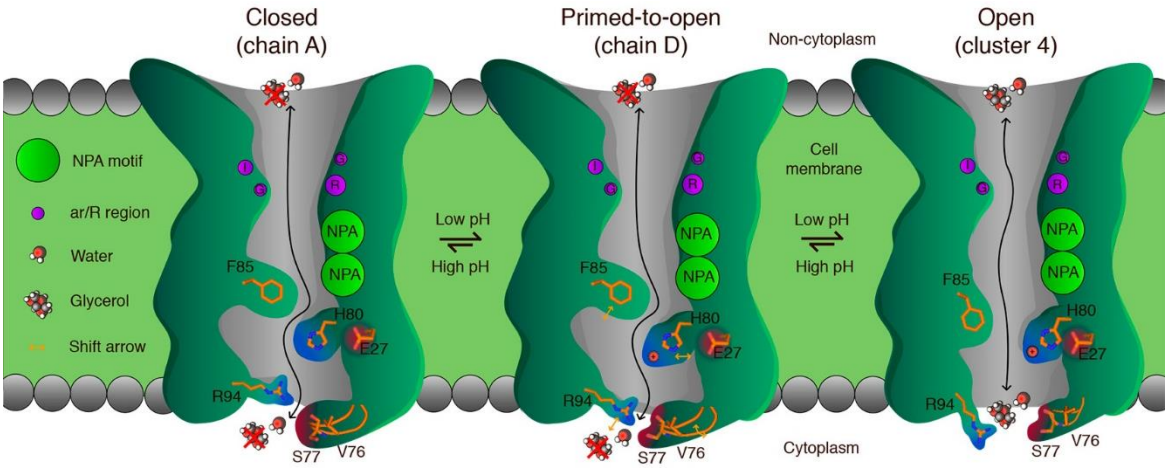

Figure 3.4.4 | Human AQP10 gate opening mechanism. Proposed hAQP10 pH-gated glycerol flux mechanism in adipocytes and likely other cell types. Glycerol, but not water, permeation is decreased at pH 7.4. AQP10 glycerol-specific opening is stimulated by pH reduction, triggering H80 protonation that renders the residue to interact with E27. Concerted structural changes of the nearby F85 and the cytoplasmic V76-S77 loop thereby allow glycerol passage. [Figure generated by Kamil Gotfryd and Julie Winkel Missel]

3.4.4 Conclusions

The present findings shed light on a key component of fat metabolism - how glycerol levels in the body are maintained through hAQP10-mediated influx (small intestine) and efflux (adipocyte tissue). Glycerol flux across plasma membranes of adipocytes (and likely duodenal enterocytes) is demonstrated to be stimulated by low pH and unarguably linked to hAQP10, a protein previously shown to be highly physiologically relevant for glycerol flow in these cell types [2,22]. The determined hAQP10 structure represents a paradigm shift for future studies of aquaglyceroporins. Our combined analyses reveal that pH regulation is achieved by a novel cytoplasmic, glycerol-specific gate and, likely, a widened ar/R filter, both unique to hAQP10, correlating with intracellular acidification of adipocytes observed during lipolysis [23]. Thus, hAQP10 has potential for therapeutic intervention of obesity and metabolic diseases, as targeting the pH gate to allow

constitutively high efflux of glycerol may prevent accumulation of TAGs inside adipocytes.

3.4.5 Experimental Section

Plasmids, site-directed mutagenesis and yeast strains - Codon-optimized human aquaporin cDNAs were purchased from GenScript, USA. Yeast-enhanced green fluorescent protein (GFP) was PCR amplified using a yeast codon-optimized version as template [24]. Briefly, for proteopolymersome reconstitution, each aquaporin was C-terminally fused to either a Tobacco Etch Virus (TEV) protease cleavage site attached to GFP and deca-histidine (His10) tag (yielding e.g. hAQP10$_{GFP}$), or to an octa-histidine (His8) stretch only (hAQP10, hAQP10$_{cryst}$ and hAQP10-derived mutant forms). Site-directed mutagenesis was performed as described previously [25] using AccuPol DNA polymerase (Amplicon, Denmark). For crystallization studies, the hAQP10cryst variant was derived from hAQP10 by removal of the first 10 (N-terminal) and last 24 (C-terminal) amino acids, respectively. All expression plasmids were assembled directly in the *S. cerevisiae* production strain PAP1500 by homologous recombination of *Hind*III-, *Sal*I- and *BamH*I-digested pPAP2259 [26] and aquaporin PCR products in presence or absence of a GFP PCR product [27]. Functional characterization in intact yeast cells was performed with wild-type aquaporins (tag-free) expressed from the methionine repressible promoter in pUG35 [28]. The plasmids were generated by homologous recombination directly in the *S. cerevisiae* assay strain YSH1770, silenced for endogenous aquaporins AQY1 and AQY2 (10560-6B MATa *leu2::hisG trp1::hisG his3::hisG ura352 aqy1D::KanMX aqy2D::KanMX*). Briefly, PCR amplified aquaporin cDNA fragments were co-transformed into YSH1770 strain with *BamH*I-, *Hind*III- and *Sal*I-digested pUG35 for synthetic cDNA-derived hAQP10 and its variants, or *Spe*I- and *Cla*I-digested pUG35 for genomic cDNA-derived hAQP3 and GFP PCR products yielding hAQP3$_{GFP}$ construct. The nucleotide sequence of all used constructs was verified by DNA sequencing.

Transport assay in human adipocyte plasma membrane vesicles - Subcutaneous adipose tissue was obtained from healthy donors during hip replacement surgery (males, age 53-78 years) following overnight fasting. The body mass index of the donors ranged from 24.4 and 37.5 kg m^{-2} (28.05 ± 4.8; mean ± SD, N=6). None of the subjects suffered from known metabolic or malignant diseases or were taking medications known to alter the adipose tissue metabolism. The conducted procedures were approved by the Institutional Review Board at "IRCCS Policlinico San Matteo Foundation" in Pavia, Italy, and in accordance with the Helsinki Declaration of 1975 as revised in 2008. Each patient gave written consent for participating in the study. Adipocyte plasma membrane vesicles were prepared as previously described [29]. Briefly, 3-8 g of freshly excised adipose tissue was homogenized in an ice-cold buffer containing 10 mM Tris-HCl pH 7.4, 250 mM sucrose, 1 mM EDTA. The homogenate was then centrifuged (3,000 × g, 15 min, 4 °C), the superficial solidified fat and pellet eliminated, and the infranatant centrifuged again (12,000 × g, 15 min, 4 °C). The resulting pellet consists of adipocyte plasma membrane vesicles, as assessed morphologically previously [2]. Water and glycerol permeabilities of isolated adipocyte plasma membranes were essentially measured exploiting stopped-flow light scattering as previously described [2]. Briefly, vesicles were suspended in solutions at pH 7.4 or 5.5 (10 mM KH_2PO_4/K_2HPO_4, 136 mM NaCl, 2.6 mM KCl) and incubated at RT for 30 min. Subsequently, vesicles were subjected to a 145 mM inwardly directed glycerol gradient (the solutions contained 10 mM $KH_2PO_4/K2HPO_4$ buffer at pH 7.4 or 5.5). Initially there is an increase in light scattering resulting from vesicle shrinkage caused by osmotic water efflux (water flux), followed by slower decrease resulting from vesicle swelling caused by glycerol entry triggering influx of water (glycerol flux). The water permeability coefficient (P_f) was calculated from the following equation as previously described [30]: $P_f = k \cdot V_0 / C \cdot V_w \cdot A$, where C is the osmotic gradient, V_w the molar water volume, V_0 the cell volume and A the vesicle surface area. The glycerol permeability coefficient (P_{Gly}) was calculated using the following equation: $P_{Gly} = 1/[(S/V)\tau]$, where S is the vesicle surface area, V the cell volume, and τ (K^{-1}) is the exponential time constant fitted to the vesicle swelling phase of the light scattering time course corresponding to glycerol entry [31]. Immunolocalization

of hAQP10 in human adipose tissue was performed using anti-hAQP10 rabbit polyclonal affinity isolated antibody (1:300 dilution; Sigma, USA) followed by incubation with AlexaFluor 488-conjugated goat anti-rabbit antibody (Molecular Probes, USA) as previously described [2]. The fluorescent dye diaminophenyl-indole (DAPI; Molecular Probes, USA) was used to visualize nuclei. Slides were examined with a TCS SP5 II LEICA confocal microscopy system (Leica Microsystems, Italy) equipped with a LEICA DM IRBE inverted microscope. Negative controls (not shown) were performed by incubating slices with the non-immune serum.

Protein production for proteopolymersome reconstitution and crystallization - TEV-GFP-His10- and His8-fusions were produced essentially as previously described [26,27]. Briefly, a single colony of transformed PAP1500 cells was grown until stationary phase in 5 mL of glucose minimal medium supplemented with leucine and lysine. Subsequently, 200 μL of the culture was propagated in 5 mL glucose minimal medium supplemented with lysine. Next day, 1 mL of this culture was used to inoculate 50 mL of the same medium. The following day this pre-culture was used to inoculate 1 L of glucose minimal medium supplemented with lysine. The overnight culture was subsequently transferred to 10 L of amino acid-supplemented minimal medium containing 3 % glucose and 3 % glycerol as carbon source, and propagated in an Applikon bioreactor equipped with an ADI 1030 Bio Controller connected to a PC running the BioExpert software (all from Applikon, Holland) as described previously [26]. The initial part of the fermentation was performed at 20 °C. The bioreactor was fed with glucose to a final concentration of 2 % when the initial glucose had been metabolized. The pH of the growth medium was maintained at 6.0 by computer-controlled addition of 1 M NH_4OH. The shift from growth on glucose to glycerol was monitored as a decrease in the rate of NH_4OH consumption. At this point the bioreactor was cooled to 15 °C and protein expression was induced by addition of galactose to a final concentration of 2 %. Cells were harvested 72 h post induction.

Protein was purified essentially as described previously [27]. Yeast cells were disrupted by glass bead homogenization (BioSpec, USA). Briefly, yeast cells were re-suspended in ice-cold lysis buffer (25 mM Tris-HCl pH 7.5, 500 mM NaCl, 20 % glycerol, 5 mM BME, 1 mM PMSF) supplemented with SIGMAFAST protease inhibitor cocktail (Sigma, USA). After mechanical disruption, cell debris was pelleted by centrifugation (3,000 rpm, 20 min, 4 °C) and the membranes were isolated from the supernatant by ultra-centrifugation (205,000 × g, 3 h, 4 °C). Crude membranes were re-suspended in solubilization buffer (20 mM Tris-HCl pH 7.5, 200 mM NaCl, 20 % glycerol, 5 mM BME, 1 mM PMSF) supplemented with SIGMAFAST protease inhibitor cocktail, homogenized in a Potter-Elvehjem homogenizer and stored at -80 °C until further use. Isolated membranes were solubilized in 2 % n-decyl-β-D-maltopyranoside (DM; Anatrace, USA) and each aquaporin was purified using immobilized metal affinity chromatography (IMAC). Briefly, detergent-solubilized material was clarified by ultra-centrifugation (120,000 × g, 1 h, 4 °C), diluted 2 × in IMAC buffer (20 mM Tris-HCl pH 7.5, 200 mM NaCl, 20 % glycerol, 5 mM BME and 0.2 % DM) and filtered using a 0.45 μm filter. Each sample was then bound to a nickel-charged affinity HisTrap HP column (GE Healthcare, Denmark), and bound protein was eluted in IMAC buffer using an imidazole gradient. GFP-TEV-His10- and His8-tagged variants used for proteopolymersome reconstitution were produced from membranes solubilized in 0.5 % n-hexadecyl-phosphocholine (FC-16; Glycon Biochemicals, Germany) and following the binding eluted in IMAC buffer containing 3 % lauryldimethylamine-N-oxide (LDAO; Anatrace, USA) and not subjected to size exclusion chromatography (SEC). Top IMAC fractions of the crystallization variant ($hAQP10_{cryst}$) were pooled, concentrated using Vivaspin 20 concentrators (MWCO 100 kDa; Sartorius, Germany), and subjected to SEC using a Superdex increase 200 10/300 GL column (GE Healthcare) equilibrated in SEC buffer (20 mM Tris-HCl pH 8, 100 mM NaCl, 10 % glycerol, 2 mM BME and 0.4 % n-nonyl-β-D-glucopyranoside (NG; Anatrace, USA)).

Functional characterization in proteopolymersomes - Poly (2-methyloxazoline)-block-poly (dimethyl siloxane) di-block copolymer PDMS34PMOXA11 (PDMS-PMOXA; DSM,

Denmark) polymersomes were prepared by the co-solvent method as previously described [32,33]. Briefly, 15 mg of PDMS-PMOXA copolymer was dissolved in 50 μL ethanol, and added dropwise to 4450 μL of 10 mM PBS pH 7.2, 136 mM NaCl, 2.6 mM KCl, followed by 24-h dialysis against PBS with 3 exchanges of the buffer. Proteopolymersomes were prepared in a similar manner where 15 mg of dissolved PDMS-PMOXA copolymer was mixed with PBS containing 25 μg of the respective purified aquaporin sample. After dialysis, all samples were extruded 15 times through a 200 nm polycarbonate filter (Whitman, USA). The dimensions of the extruded vesicles (hydrodynamic diameter) were determined at 20 °C by dynamic light scattering (DLS) using ZetaSizer NanoZs instrument (Malvern, UK). The water flux was measured employing a Bio-Logic SFM 300 stopped-flow device (Bio-Logic, France), with a monochromator at 517 nm and a cut off filter at 530 nm, respectively. For each individual stopped-flow test, 0.13 mL of extruded polymersomes or proteopolymersomes was quickly mixed with 0.13 mL of 0.5 M NaCl, which caused the vesicles to shrink due to osmotically driven water efflux. At least 10 tests were performed for each sample; the dead time for the mixing of stopped flow injection was 5 ms. Vesicle size changes were monitored and recorded in the form of an increasing signal in the DLS analysis. Obtained kinetic data were fitted with a double exponential equation, and the rate constant (s^{-1}) that is directly proportional to the water flux through polymeric membrane was determined. In the glycerol transport assay 3 mL of extruded polymersomes was incubated with 3 mL of 2 M glycerol overnight at 4 °C to mediate glycerol transport into the polymeric vesicles. After incubation, the dimensions of the polymeric vesicles were determined by DLS. Glycerol flux in proteopolymersomes was assessed using stopped-flow after mixing the samples with 0.5 M of NaCl (exhibiting the same osmotic pressure as 1 M glycerol).

Crystallization and structure determination - $hAQP10_{cryst}$ crystals were grown by hanging-drop vapor diffusion at 18 °C by mixing protein solution (~4 mg mL^{-1}) supplemented with 0.3 mM n-nonyl-β-D-thioglucoside (Hampton Research, USA) with a reservoir solution composed of 100 mM MES-monohydrate-NaOH pH 6.0, 19 % PEG 2k

MME and 5 % glycerol and flash frozen in liquid nitrogen. X-ray diffraction data were collected using an EIGER detector at the Paul Scherrer Institut, Villigen, Switzerland, beam line X06SA. Data processing was done using the software XDS [34]. Crystals belonged to space group P_{212121} with cell dimensions a = 97.07 Å, b = 116.84 Å, c = 138.55 Å. The initial phases were determined by molecular replacement with software PHASER using *E. coli* glycerol facilitator (GlpF) structure (pdb-id 1LDF [35]) yielding an entire tetramer in the asymmetric unit. Model building and refinement were done using COOT [36] and phenix.refine [37] iteratively. TLS refinement was introduced in the final refinement rounds [38]. All structure figures were generated using Pymol.

HOLE analysis of the pore dimensions - The software HOLE (version v2.2.005) was obtained from www.holeprogram.org [39]. Pore profiles were analyzed until the radius reached 5 Å, and van der Waals radii were subsequently determined. Analysis was performed after removal of water molecules and HETATOMS, with passage through S77, H80 and R94, and the pores colored according to the water permeability.

Functional characterization in yeast cells - YSH1770 strain was grown at 28 °C with orbital shaking in YNB (yeast nitrogen base) without amino acids (DIFCO), with 2 % (w/v) glucose and supplemented with the adequate requirements for prototrophic growth. Transformants were grown to $OD_{640nm} \approx 1$ (corresponding to 1×10^7 cells mL^{-1}), harvested by centrifugation (5,000 × g, 10 min, 4 °C), washed three times and resuspended in ice-cold sorbitol (1.4 M) K-citrate buffer (50 mM pH 5.1 or pH 7.4) up to a concentration of 0.33 g (wet weight) mL^{-1}, and kept on ice for at least 90 min. Prior to the osmotic challenges, the cell suspension was preloaded with the nonfluorescent precursor 5-and-6-carboxyfluorescein diacetate (CFDA, Sigma, USA; 1 mM for 20 min at 30 °C) that is cleaved intracellularly by nonspecific esterases, and generates the impermeable fluorescent form (CF) known to remain in the cytoplasm [40]. Cells were then diluted 1:10 in 1.4 M sorbitol buffer and immediately used for stopped-flow experiments. Equilibrium cell volumes (V_o) were obtained by loading cells with CFDA under a epifluorescence

microscope (Zeiss Axiovert, Zeiss, Jena, Germany) equipped with a digital camera as previously described [40]. Cells were assumed to have a spherical shape with a diameter calculated as the average of the maximum and minimum dimensions of each cell. Stopped-flow experiments were performed on a Hi-Tech Scientific PQ/SF-53 apparatus (Hi-Tech Scientific, UK) with 2 ms dead time, temperature-controlled, interfaced with a microcomputer. Permeability assays were performed at 23 °C, except for activation energy (E_a) assays where temperature ranged from 10 to 34 °C. Five runs were usually analyzed in each experimental condition. In each run 0.1 mL of cell suspension (1:10 dilution in the resuspension buffer) was mixed with an equal amount of iso (baseline) or hyperosmotic solution (sorbitol or glycerol 2.1 M, 50 mM K-citrate buffer pH 5.1 or pH 7.4) of 1.25 tonicity (($\Lambda = (osm_{out})_\infty/(osm_{out})_o$)). Fluorescence was excited using a 470 nm interference filter and detected using a 530 nm cut-off filter. The time course of cell volume change was followed by fluorescence quenching of the entrapped fluorophore (CF). The fluorescence traces obtained were corrected by subtracting baseline (reflecting the bleaching of the fluorophore). The calibration of the resulting traces was performed followed our previous strategy [41], where a linear relationship between relative volume and F was obtained ($v_{rel} = a\ F/F_0+b$), and the values of a and b were estimated individually for each osmotic shock. The permeability coefficients for water (P_f) and glycerol (P_{Gly}) transport were evaluated using the analysis described in [42]. The calibrated experimental data were fitted to theoretical curves, considering the water and glycerol fluxes and the resulting changes in cell volume and intracellular concentrations of solutes. Optimization of permeability values was accomplished by numerical integrations using the mathematical model implemented in the Berkeley Madonna software (http://www.berkeleymadonna.com/). Estimations of the internal pH (pH_{in}) were performed as previously described [43]. The activation energy (E_a) of glycerol permeation was evaluated from the slope of the Arrhenius plot (ln P_{Gly} as a function of T^{-1}) multiplied by the gas constant R. The results were expressed as mean ± SD of N individual experiments.

Molecular dynamics simulations - Molecular dynamics (MD) simulations were performed on the tetrameric hAQP10$_{cryst}$ structure embedded in a palmitoyloleoyl-phosphatidylethanolamine (POPE) bilayer. Two systems were built with the imidazole ring of H80 mono protonated at ε-nitrogen or double protonated, to mimic physiological and low pH, respectively. The detergent molecules, the three intermediate glycerol molecules located between the monomers and water molecules on the hydrophobic exterior side of the protein were removed from the system, while water molecules present inside the protein were kept. Missing atoms were added using the software VMD [44] with the PSFGEN plugin. Side chains were kept at their default protonation state including remaining H residues (protonated at ε-nitrogen). Additional water molecules were placed using the software DOWSER [45], according to an energy threshold of -12 kcal mol^{-1}. The protein was aligned in the XY plane using the VMD plugin ORIENT, and was subsequently solvated using the program SOLVATE. A partially hydrated POPE membrane of 127 Å × 127 Å bilayer patch was built using the VMD plugin MEMBRANE and aligned to the hydrophobic part of the protein. Lipids overlapping with the protein were removed to avoid steric clashes. The final solvation of the system was done by adding two 15 Å layers of water while water molecules in the hydrophobic part of the membrane were removed. To model the protein in natural ionic concentrations, the system was electroneutralized at 150 mM of Na^+ and Cl^- ions using the VMD plugin AUTOIONIZE. The H80 ε-nitrogen-protonated system consisted of 15177 protein atoms, 330 POPE lipid molecules, 18549 water molecules and 52 Na^+, 59 Cl^- ions for a total of 112241 atoms. The double protonated system consisted of 15,181 protein atoms, 326 POPE lipid molecules, 18,490 water molecules and 52 Na^+, 63 Cl^- ions for a total of 111,572 atoms. The two systems were simulated using the software NAMD2 [46] with the CHARMM27 parameter set [47,48] using TIP3P for water molecules. Glycerol was modeled with the CHARMM36 parameter set [49]. The lipid tails were initially minimized for 10,000 steps and simulated for 100 ps with the lipid heads (N and P) atoms, protein, water and ions fixed. Next, only glycerol and the protein atoms were restrained by 5 kcal mol^{-1} and the system was minimized for 1,000 steps and simulated for 500 ps. The restraints were

lowered to 1 kcal mol^{-1} and simulated for 5 ns to allow lipid membrane adjustment to the protein. Water molecules entering the hydrophobic part of the membrane was pushed out using the TCL script from the Membrane Proteins Tutorial during the membrane equilibration. Subsequently the protein was fully released and simulated for 250 ns, while saving coordinates every 2 ps. A constraint was applied on the glycerol center of mass with the NPA motif of residues 82-84 backbone atoms as reference in order to keep it the vicinity of the loop. For the first 100 ns, the restraint would allow the glycerol to move [-10;5] Å in the Z-direction, after which the restraint was updated to [-10;0] Å. A harmonic constant of 10 kcal mol^{-1} $Å^{-2}$ was used for maintaining the glycerol within the boundary with a width of 0.1 Å. The simulations were carried out at constant temperature (310 K) and pressure (1 atm) using Langevin dynamics with a damping coefficient of 5 ps^{-1} and a Langevin piston with a period and decay time of 2 ps, respectively. The Particle Mesh Ewald method was used for evaluating electrostatic forces with a resolution of at least 1 Å. A cutoff of 12 Å using a switching function beginning from 10 Å was employed. The integration time step was 2 fs and all hydrogen bonds were kept fixed with the SHAKE constraint and the Settle algorithm. Short- and long-range electrostatic forces were evaluated every 2 fs and 4 fs respectively.

Analysis of the trajectories was performed using the software VMD. During the simulations, the root mean square displacement (RMSD) on CA atoms and the area per lipid was monitored to ensure stable physical behavior. The total RMSD remained below 1.5 $Å^2$ while the area per lipid equilibrated towards 50 $Å^2$ within 50 ns. The analysis was performed on the 250 ns trajectories at every 10,000 steps, equivalent to every 20 ps. Clustering and principal component analysis (PCA) to determine the specific interactions and conformations of the loop and glycerol was performed using CPPTRAJ [50] on the combined mono and double protonated simulations. Each monomer was put in sequence yielding a combined 2 μs simulation. Both analyses were performed on CA atoms of 28 selected residues near the cytoplasmic region of the loop.

3.4.6 Supplementary Information

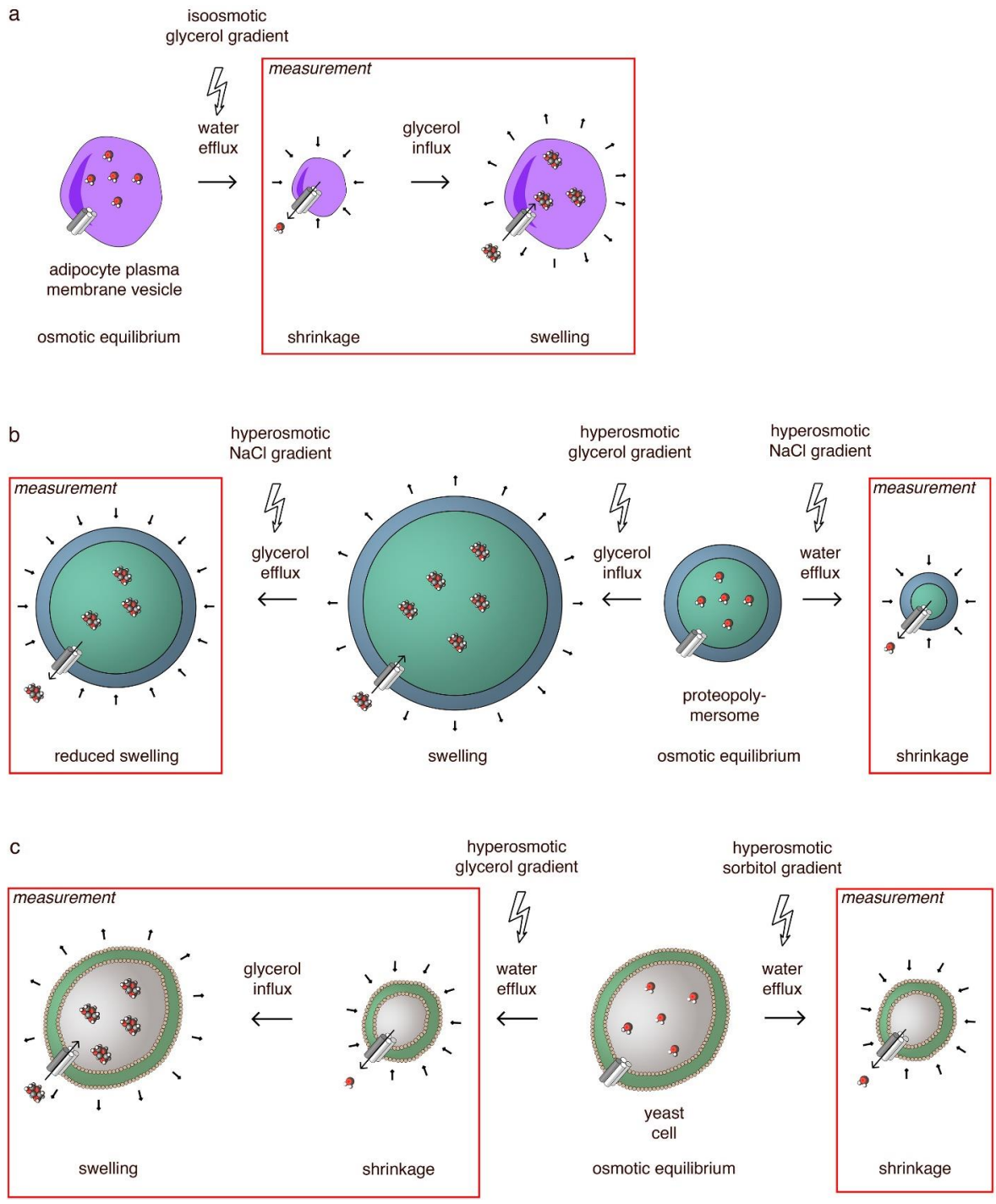

Supplementary Figure S3.4.1 | Overview of the three activity assays used for functional characterization of AQP-dependent fluxes. (a) Human adipocyte plasma membrane vesicle-based assay. Water and glycerol permeabilities of vesicles were induced

by isosmotic glycerol gradient and measured exploiting stopped-flow light scattering. Initially there is an increase in light scattering resulting from vesicle shrinkage caused by osmotic water efflux followed by a slower decrease resulting from vesicle swelling due to glycerol entry triggering water influx. **(b)** Proteopolymersome-bassed assay. Human AQPs were reconstituted into polymersomes and formed proteopolymersomes were exposed to either hyperosmotic NaCl gradient (to allow water efflux) or hyperosmotic glycerol gradient followed by NaCl osmotic stress to induce glycerol efflux. Permeation was measured using stopped-flow light scattering. **(c)** Intact yeast cell-based assay. Cells overexpressing respective human AQPs were preloaded with nonfluorescent dye that is intracellularly converted into impermeable fluorescent form. Water and glycerol permeabilities of cells were induced by hyperosmotic sorbitol or glycerol gradients, respectively and measured employing stopped-flow fluorescence. [Figure generated by Kamil Gotfryd and Julie Winkel Missel]

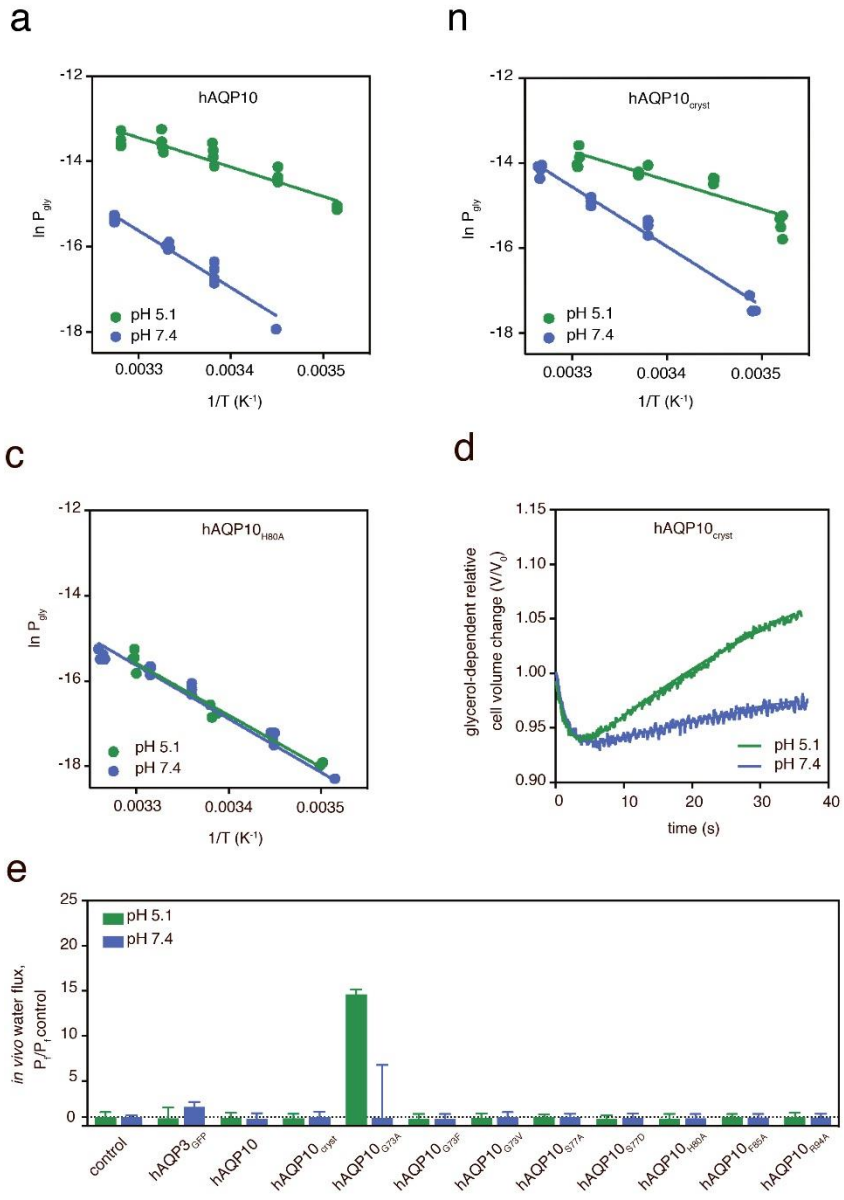

Supplementary Figure S3.4.2 | **Functional characterization of human AQP10 in vivo. (a-c)** Arrhenius plots for estimation of the activation energy (E_a) for glycerol permeability in cells expressing hAQP10 forms measured at pH 5.1 (green) and pH 7.4 (blue). Results are given as mean ± SD of at least N=3 independent experiments. **(d)** Representative time course of the relative cell volume (V/V_0) changes after glycerol hyperosmotic shock at pH 5.1 (green) and 7.4 (blue) in $hAQP10_{cryst}$ expressing intact yeast cells. After the fast water efflux, glycerol influx via $hAQP10_{cryst}$ induces cell reswelling. **(e)** Water permeability (P_f) ratio of yeast cells expressing $hAQP3_{GFP}$ or hAQP10 forms measured at pH 5.1 (green) and

pH 7.4 (blue). Results are normalized to P_f of the control strain (without plasmid) at the respective pH. Results are given as mean ± SD of at least N=3 independent experiments.

Supplementary Table S3.4.1 | Glycerol permeability (P_{Gly}) and activation energy (E_a) values obtained for pH-dependence transport measurements performed using *S. cerevisiae*-based *in vivo* assay. Results are given as mean ± SD of 3-6 independent experiments.

construct	pH 5.1		pH 7.4	
	P_{Gly} (23 °C) cm/s	E_a kcal/mol	P_{Gly} (23 °C) cm/s	E_a kcal/mol
control (empty pUG35)	6.69 e-9 ± 0.34	26.0 ± 2.1	11.9 e-8 ± 2.20	25.2 ± 2.0
hAQP3	6.13 e-8 ± 0.60	20.3 ± 1.8	1.87 e-6 ± 0.91	10.1 ± 1.8
hAQP10	1.40 e-6 ± 0.19	13.0 ± 1.2	6.03 e-8 ± 1.20	26.6 ± 1.9
$hAQP10_{cryst}$	1.40 e-6 ± 0.07	13.6 ± 1.7	9.19 e-8 ± 2.60	28.0 ± 1.2
$hAQP10_{H80A}$	8.27 e-8 ± 0.69	24.2 ± 1.6	9.90 e-8 ± 0.88	25.0 ± 1.6

3.4.7 References

[1] U. Laforenza, C. Bottino, G. Gastaldi, Mammalian aquaglyceroporin function in metabolism, Biochim Biophys Acta 1858 (2016) 1-11.

[2] U. Laforenza, M.F. Scaffino, G. Gastaldi, Aquaporin-10 represents an alternative pathway for glycerol efflux from human adipocytes, PLoS One 8 (2013) e54474.

[3] J. Lebeck, Metabolic impact of the glycerol channels AQP7 and AQP9 in adipose tissue and liver, J Mol Endocrinol 52 (2014) R165-178.

[4] T. Hibuse, N. Maeda, T. Funahashi, K. Yamamoto, A. Nagasawa, W. Mizunoya, K. Kishida, K. Inoue, H. Kuriyama, T. Nakamura, T. Fushiki, S. Kihara, I. Shimomura, Aquaporin 7 deficiency is associated with development of obesity through activation of adipose glycerol kinase, Proc Natl Acad Sci U S A 102 (2005) 10993-10998.

[5] A. Madeira, T.F. Moura, G. Soveral, Aquaglyceroporins: implications in adipose biology and obesity, Cell Mol Life Sci 72 (2015) 759-771.

[6] A. Rodriguez, V. Catalan, J. Gomez-Ambrosi, S. Garcia-Navarro, F. Rotellar, V. Valenti, C. Silva, M.J. Gil, J. Salvador, M.A. Burrell, G. Calamita, M.M. Malagon, G. Fruhbeck,

Insulin- and leptin-mediated control of aquaglyceroporins in human adipocytes and hepatocytes is mediated via the PI3K/Akt/mTOR signaling cascade, J Clin Endocrinol Metab 96 (2011) E586-597.
[7] D. Fu, A. Libson, L.J. Miercke, C. Weitzman, P. Nollert, J. Krucinski, R.M. Stroud, Structure of a glycerol-conducting channel and the basis for its selectivity, Science 290 (2000) 481-486.
[8] J.K. Lee, D. Kozono, J. Remis, Y. Kitagawa, P. Agre, R.M. Stroud, Structural basis for conductance by the archaeal aquaporin AqpM at 1.68 A, Proc Natl Acad Sci U S A 102 (2005) 18932-18937.
[9] Z.E. Newby, J. O'Connell, 3rd, Y. Robles-Colmenares, S. Khademi, L.J. Miercke, R.M. Stroud, Crystal structure of the aquaglyceroporin PfAQP from the malarial parasite Plasmodium falciparum, Nat Struct Mol Biol 15 (2008) 619-625.
[10] A. de Almeida, A.P. Martins, A.F. Mosca, H.J. Wijma, C. Prista, G. Soveral, A. Casini, Exploring the gating mechanisms of aquaporin-3: new clues for the design of inhibitors?, Molecular Biosystems 12 (2016) 1564-1573.
[11] M. Rothert, D. Ronfeldt, E. Beitz, Electrostatic attraction of weak monoacid anions increases probability for protonation and passage through aquaporins, J Biol Chem 292 (2017) 9358-9364.
[12] Y. Zhao, A. Vararattanavech, X. Li, C. Helixnielsen, T. Vissing, J. Torres, R. Wang, A.G. Fane, C.Y. Tang, Effects of proteoliposome composition and draw solution types on separation performance of aquaporin-based proteoliposomes: implications for seawater desalination using aquaporin-based biomimetic membranes, Environ Sci Technol 47 (2013) 1496-1503.
[13] A.S. Verkman, M.O. Anderson, M.C. Papadopoulos, Aquaporins: important but elusive drug targets, Nat Rev Drug Discov 13 (2014) 259-277.
[14] A. Frick, U.K. Eriksson, F. de Mattia, F. Oberg, K. Hedfalk, R. Neutze, W.J. de Grip, P.M. Deen, S. Tornroth-Horsefield, X-ray structure of human aquaporin 2 and its implications for nephrogenic diabetes insipidus and trafficking, Proc Natl Acad Sci U S A 111 (2014) 6305-6310.
[15] S. Kaptan, M. Assentoft, H.P. Schneider, R.A. Fenton, J.W. Deitmer, N. MacAulay, B.L. de Groot, H95 Is a pH-Dependent Gate in Aquaporin 4, Structure 23 (2015) 2309-2318.
[16] C. Rodrigues, A.F. Mosca, A.P. Martins, T. Nobre, C. Prista, F. Antunes, A. Cipak Gasparovic, G. Soveral, Rat Aquaporin-5 Is pH-Gated Induced by Phosphorylation and Is Implicated in Oxidative Stress, Int J Mol Sci 17 (2016).
[17] J.D. Ho, R. Yeh, A. Sandstrom, I. Chorny, W.E. Harries, R.A. Robbins, L.J. Miercke, R.M. Stroud, Crystal structure of human aquaporin 4 at 1.8 A and its mechanism of conductance, Proc Natl Acad Sci U S A 106 (2009) 7437-7442.
[18] R. Horsefield, K. Norden, M. Fellert, A. Backmark, S. Tornroth-Horsefield, A.C. Terwisscha van Scheltinga, J. Kvassman, P. Kjellbom, U. Johanson, R. Neutze, High-resolution x-ray structure of human aquaporin 5, Proc Natl Acad Sci U S A 105 (2008) 13327-13332.
[19] S. Kreida, S. Tornroth-Horsefield, Structural insights into aquaporin selectivity and regulation, Curr Opin Struct Biol 33 (2015) 126-134.

[20] N. Klein, J. Neumann, J.D. O'Neil, D. Schneider, Folding and stability of the aquaglyceroporin GlpF: Implications for human aqua(glycero)porin diseases, Biochim Biophys Acta 1848 (2015) 622-633.
[21] A. Madeira, T.F. Moura, G. Soveral, Detecting Aquaporin Function and Regulation, Front Chem 4 (2016) 3.
[22] H. Li, J. Kamiie, Y. Morishita, Y. Yoshida, E. Yaoita, K. Ishibashi, T. Yamamoto, Expression and localization of two isoforms of AQP10 in human small intestine, Biol Cell 97 (2005) 823-829.
[23] V.N. Civelek, J.A. Hamilton, K. Tornheim, K.L. Kelly, B.E. Corkey, Intracellular pH in adipocytes: effects of free fatty acid diffusion across the plasma membrane, lipolytic agonists, and insulin, Proc Natl Acad Sci U S A 93 (1996) 10139-10144.
[24] B.P. Cormack, G. Bertram, M. Egerton, N.A. Gow, S. Falkow, A.J. Brown, Yeast-enhanced green fluorescent protein (yEGFP): a reporter of gene expression in Candida albicans, Microbiology 143 (Pt 2) (1997) 303-311.
[25] S.N. Ho, H.D. Hunt, R.M. Horton, J.K. Pullen, L.R. Pease, Site-directed mutagenesis by overlap extension using the polymerase chain reaction, Gene 77 (1989) 51-59.
[26] P.A. Pedersen, J.H. Rasmussen, P.L. Joorgensen, Expression in high yield of pig alpha 1 beta 1 Na,K-ATPase and inactive mutants D369N and D807N in Saccharomyces cerevisiae, J Biol Chem 271 (1996) 2514-2522.
[27] F.B. Bjorkskov, S.L. Krabbe, C.N. Nurup, J.W. Missel, M. Spulber, J. Bomholt, K. Molbaek, C. Helix-Nielsen, K. Gotfryd, P. Gourdon, P.A. Pedersen, Purification and functional comparison of nine human Aquaporins produced in Saccharomyces cerevisiae for the purpose of biophysical characterization, Sci Rep 7 (2017) 16899.
[28] U. Guldener, S. Heck, T. Fielder, J. Beinhauer, J.H. Hegemann, A new efficient gene disruption cassette for repeated use in budding yeast, Nucleic Acids Res 24 (1996) 2519-2524.
[29] Y. Oka, T. Asano, Y. Shibasaki, M. Kasuga, Y. Kanazawa, F. Takaku, Studies with antipeptide antibody suggest the presence of at least two types of glucose transporter in rat brain and adipocyte, J Biol Chem 263 (1988) 13432-13439.
[30] H. Wiener, K. Turnheim, C.H. van Os, Rabbit distal colon epithelium: I. Isolation and characterization of basolateral plasma membrane vesicles from surface and crypt cells, J Membr Biol 110 (1989) 147-162.
[31] B. Yang, D. Zhao, A.S. Verkman, Evidence against functionally significant aquaporin expression in mitochondria, J Biol Chem 281 (2006) 16202-16206.
[32] B.M. Discher, Y.Y. Won, D.S. Ege, J.C. Lee, F.S. Bates, D.E. Discher, D.A. Hammer, Polymersomes: tough vesicles made from diblock copolymers, Science 284 (1999) 1143-1146.
[33] M. Kumar, M. Grzelakowski, J. Zilles, M. Clark, W. Meier, Highly permeable polymeric membranes based on the incorporation of the functional water channel protein Aquaporin Z, Proc Natl Acad Sci U S A 104 (2007) 20719-20724.
[34] W. Kabsch, Xds, Acta Crystallogr D Biol Crystallogr 66 (2010) 125-132.
[35] E. Tajkhorshid, P. Nollert, M.O. Jensen, L.J. Miercke, J. O'Connell, R.M. Stroud, K. Schulten, Control of the selectivity of the aquaporin water channel family by global orientational tuning, Science 296 (2002) 525-530.

[36] P. Emsley, B. Lohkamp, W.G. Scott, K. Cowtan, Features and development of Coot, Acta Crystallogr D Biol Crystallogr 66 (2010) 486-501.
[37] P.V. Afonine, R.W. Grosse-Kunstleve, N. Echols, J.J. Headd, N.W. Moriarty, M. Mustyakimov, T.C. Terwilliger, A. Urzhumtsev, P.H. Zwart, P.D. Adams, Towards automated crystallographic structure refinement with phenix.refine, Acta Crystallogr D Biol Crystallogr 68 (2012) 352-367.
[38] A. Urzhumtsev, P.V. Afonine, P.D. Adams, TLS from fundamentals to practice, Crystallogr Rev 19 (2013) 230-270.
[39] O.S. Smart, J.G. Neduvelil, X. Wang, B.A. Wallace, M.S. Sansom, HOLE: a program for the analysis of the pore dimensions of ion channel structural models, J Mol Graph 14 (1996) 354-360, 376.
[40] G. Soveral, A. Madeira, M.C. Loureiro-Dias, T.F. Moura, Water transport in intact yeast cells as assessed by fluorescence self-quenching, Appl Environ Microbiol 73 (2007) 2341-2343.
[41] G. Soveral, A. Madeira, M.C. Loureiro-Dias, T.F. Moura, Membrane tension regulates water transport in yeast, Biochim Biophys Acta 1778 (2008) 2573-2579.
[42] A. Madeira, M. Camps, A. Zorzano, T.F. Moura, G. Soveral, Biophysical assessment of human aquaporin-7 as a water and glycerol channel in 3T3-L1 adipocytes, PLoS One 8 (2013) e83442.
[43] L. Leitao, C. Prista, T.F. Moura, M.C. Loureiro-Dias, G. Soveral, Grapevine aquaporins: gating of a tonoplast intrinsic protein (TIP2;1) by cytosolic pH, PLoS One 7 (2012) e33219.
[44] W. Humphrey, A. Dalke, K. Schulten, VMD: visual molecular dynamics, J Mol Graph 14 (1996) 33-38, 27-38.
[45] L. Zhang, J. Hermans, Hydrophilicity of cavities in proteins, Proteins 24 (1996) 433-438.
[46] J.C. Phillips, R. Braun, W. Wang, J. Gumbart, E. Tajkhorshid, E. Villa, C. Chipot, R.D. Skeel, L. Kale, K. Schulten, Scalable molecular dynamics with NAMD, J Comput Chem 26 (2005) 1781-1802.
[47] A.D. MacKerell, D. Bashford, M. Bellott, R.L. Dunbrack, J.D. Evanseck, M.J. Field, S. Fischer, J. Gao, H. Guo, S. Ha, D. Joseph-McCarthy, L. Kuchnir, K. Kuczera, F.T. Lau, C. Mattos, S. Michnick, T. Ngo, D.T. Nguyen, B. Prodhom, W.E. Reiher, B. Roux, M. Schlenkrich, J.C. Smith, R. Stote, J. Straub, M. Watanabe, J. Wiorkiewicz-Kuczera, D. Yin, M. Karplus, All-atom empirical potential for molecular modeling and dynamics studies of proteins, J Phys Chem B 102 (1998) 3586-3616.
[48] A.D. Mackerell, Jr., M. Feig, C.L. Brooks, 3rd, Extending the treatment of backbone energetics in protein force fields: limitations of gas-phase quantum mechanics in reproducing protein conformational distributions in molecular dynamics simulations, J Comput Chem 25 (2004) 1400-1415.
[49] E. Hatcher, O. Guvench, A.D. Mackerell, Jr., CHARMM Additive All-Atom Force Field for Acyclic Polyalcohols, Acyclic Carbohydrates and Inositol, J Chem Theory Comput 5 (2009) 1315-1327.
[50] D.R. Roe, T.E. Cheatham, 3rd, PTRAJ and CPPTRAJ: Software for Processing and Analysis of Molecular Dynamics Trajectory Data, J Chem Theory Comput 9 (2013) 3084-3095.

CHAPTER 4

Gold compounds as aquaglyceroporins selective inhibitors

In the last decade, the discovery of AQPs modulators seed for drug design and with potential for novel therapeutics has attracted the scientific community. However, so far no reported small-molecule AQP inhibitors possess sufficient isoform selectivity to be good candidates for clinical development. Our recent studies in this area identified a gold(III) coordination complex as potent and selective AQP inhibitor, with potential use as a chemical probe to study AQPs function in biological systems. This chapter explores the mechanisms of AQPs inhibition by gold compounds at a molecular level via an integrated investigational approach. Additionally, aiming to optimize the drug design and achieve highly selective molecules with reduced risks of side effects, the inhibition properties of two new series of gold(III) compounds is described.

This chapter is adapted from one published manuscript:

de Almeida A*****, **Mósca AF***, Wragg D, Wenzel M, Kavanagh P, Barone G, Leoni S, Soveral G and Casini A. "The mechanism of aquaporin inhibition by gold compounds elucidated by biophysical and computational methods."
Chemical Communications (2017) 53, 3830-3833, DOI: 10.1039/C7CC00318H

*Equal contribution

4.1 The mechanism of aquaporin inhibition by gold-compounds

4.1.1 Abstract

The inhibition of water and glycerol permeation via aquaglyceroporin-3 (AQP3) endogenously expressed in human red blood cells (RBC) by four gold(III) complexes was studied by stopped-flow spectroscopy and, for the first time, its mechanism was described using molecular dynamics (MD) combined with density functional theory (DFT) and electrochemical studies. The obtained MD results showed that the most effective gold-based inhibitor of the series, anchored to Cys40 in AQP3, is able to induce shrinkage of pores preventing glycerol and water permeation. Moreover, the good correlation between the affinity of the Au(III) complex to Cys binding and AQP3 inhibition effects was highlighted, while no influence of the different oxidative character of the complexes could be observed.

4.1.2 Introduction

To validate the various roles of AQPs in health and disease, and to develop AQP-targeted therapies, in addition to genetic approaches, the use of selective inhibitors holds great promise. Sulfhydryl-reactive compounds such as $HgCl_2$ are typically used as AQP inhibitors, however, they are extremely toxic and nonspecific and thus not suitable for in vivo experiments and therapeutic application.

In this context, for the first time we reported on the potent and selective inhibition of human aquaglyceroporin-3 (AQP3) by a water-soluble Au(III) compound, $[Au(phen)Cl_2]Cl$ (phen = 1,10-phenanthroline) (Auphen, Figure 4.1.1 A) [1]. Using in silico approaches we revealed that the most favorable non-covalent binding site for Au(III) ions is the very accessible thiol group of Cys40 in the proximity of AQP3 channel pore, which is absent in AQP1 [1]. The involvement of this residue

in the inhibition mechanism by Auphen was further confirmed by site-directed mutagenesis studies [2].

Additional studies on other Au(III) compounds with different N^N ligand scaffolds allowed us to establish preliminary structure-activity relationships [3]. Notably, Quantum Mechanics/Molecular Mechanics (QM/MM) calculations showed that the ligand moiety may play a major role in orienting the selectivity towards a certain isoform [3], stabilizing the position of the inhibitor in the extracellular binding pocket and possibly blocking the solutes' fluxes. Interestingly, Molecular Dynamics (MD) simulations on the adducts of Hg^{2+} ions (benchmark inhibitors of all AQPs [4,5]) with AQP3 have allowed us to discover that pore closure may be due to protein conformational changes upon metal binding, other than direct steric blockage of the channel by the inhibitor [6].

We report here on the human AQP3 inhibition properties of four novel Au(III) complexes (Figure 4.1.1 B), including three coordination complexes with a dipyridin-2-ylamine (DipyAm) ligand $[Au(Dipyam)Cl_2]PF_6$ (**1**) [7], and with (pyridyl)benzimidazole type ligands – $[Au(PbIm)Cl_2]$ (**3**) (PbIm = 2-(pyridin-2-yl)-benzimidazole) [8] and $[Au(PbImMe)Cl_2]PF_6$ (**4**) (PbImMe = 1-methyl-2-(pyridin-2-yl)-benzimidazole), respectively. Moreover, for the first time, an organometallic Au(III) compound with a C^N cyclometalated 2-benzylpyridine (py^b-H) ligand (**2**) [9] was tested as AQP inhibitor. The mechanism of AQP3 inhibition by the most potent compound of this series was studied by MD simulations, allowing to disclose important structural changes leading to pore closure upon gold binding. Furthermore, the identification of structure-activity relationships that may link the electrochemical and electronic/structural properties of Au(III) compounds to their biological effects, was also explored. Thus, electrochemical methods were applied to define the compounds' electron-transfer abilities, while density functional

theory (DFT) calculations were performed to further substantiate and interpret the experimental biological effects.

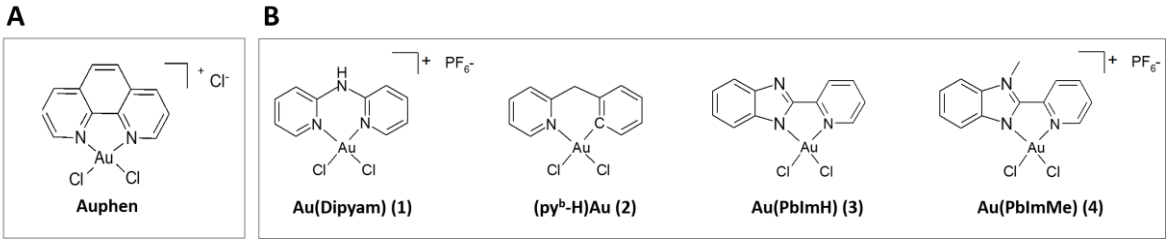

Figure 4.1.1 | Gold(III) compounds as human AQP3 inhibitors. (A) Auphen, from reference [1] **(B)** $[Au(Dipyam)Cl_2]PF_6$ (1), $[Au(PbIm)Cl_2]$ (3), $[Au(PbImMe)Cl_2]PF_6$**.**

4.1.3 Results and Discussion

Initially, four gold complexes (Figure 4.1.1 B) were tested for their AQP1 and AQP3 inhibition properties in RBC by stopped-flow spectroscopy. The obtained results are summarized in Table 4.1.1 and Figure 4.1.2 A. As previously observed for Auphen and related compounds [1,3] some of the new complexes act as inhibitors of glycerol permeation via AQP3, but do not affect water permeation via AQP1. The coordination complex **1** shows moderate inhibition of water and glycerol permeation (IC_{50} > 20 μM), which may be due to its poor stability in physiological environment [7]. The organometallic compound $[Au(py^{b}\text{-}H)Cl_2]$ **2** was also scarcely active up to 50 μM, maybe since the metal-carbon bond renders the Au(III) centre less prone to ligand exchange reactions. Interestingly, while the neutral complex **3** poorly inhibits glycerol transport (IC_{50} > 50 μM), the novel cationic compound $[Au(PbImMe)Cl_2]PF_6$ **4** is a very potent AQP3 inhibitor (IC_{50} = 0.6 ± 0.1 μM), even more effective than Auphen, and ca. 3 orders of magnitude more potent than **3**. The reversibility of AQP3 inhibition was also studied pre-treating hRBC with the compounds for 30 min at r.t. and subsequently washing the cells with either the thiol containing reducing agent β-mercaptoethanol (BME, 1

mM) [10] or with the sulfur donor L-Cys. In both cases, as shown in Figure 4.1.2 B, treatments with the competitor molecules led to an almost complete recovery of glycerol permeability, ruling out the possible oxidative modification of amino acid residues by the Au(III) complex.

Table 4.1.1 | IC_{50} (μM) values for the gold complexes as human AQP3 inhibitors.

Compound	IC_{50}[a] (μM)
Auphen	0.8 ± 0.1[b]
1	> 20
2	> 50
3	> 50
4	0.6 ± 0.1

[a] Mean ± SE of at least three independent experiments. [b] from reference [1].

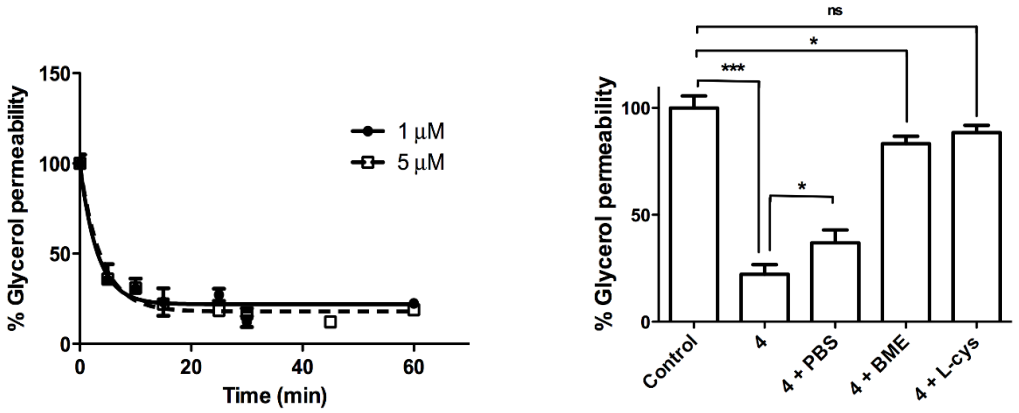

Figure 4.1.2 | **(A)** Time-dependence glycerol inhibition (% of control) for two concentrations of 4; **(B)** Inhibition of glycerol permeability (% of control) of RBCs after treatment with 4 (30 min at r.t., 1 μM), and reversibility by incubation with BME and L-Cys (1 mM for 30 min). The results represent the average of at least three independent experiments ± SE.

The mechanism of human AQP3 inhibition by complex **4** was analyzed using classical molecular dynamics (MD). The quaternary structure of AQP3 was prepared *via* homology modelling, following an approach previously described by us [6] and reported in the Experimental Section [11]. The compound was first parameterised using DFT and QM/MM to generate Au(III) parameters for the applied force field, and then directly bound to the thiolate of Cys40, in the form $[Au(PbImMe)Cl]^{2+}$. Geometry optimization was performed on this fragment (Supplementary Figure S4.1.1), which was subsequently embedded into monomer A of AQP3. The charge of Au was set to +3 (Au(III)). Afterwards, five independent MD simulations (0.5 ns) were conducted to determine the effect of **4** on water and glycerol permeation using either: (i) AQP3 or (ii) gold-bound AQP3 (AQP3-Au). Figure 4.1.3 shows the pore size comparison of the structures for monomer A obtained from the two representative simulations. Binding of complex **4** to Cys40 induces shrinkage of the pore, impeding both glycerol and H_2O permeability.

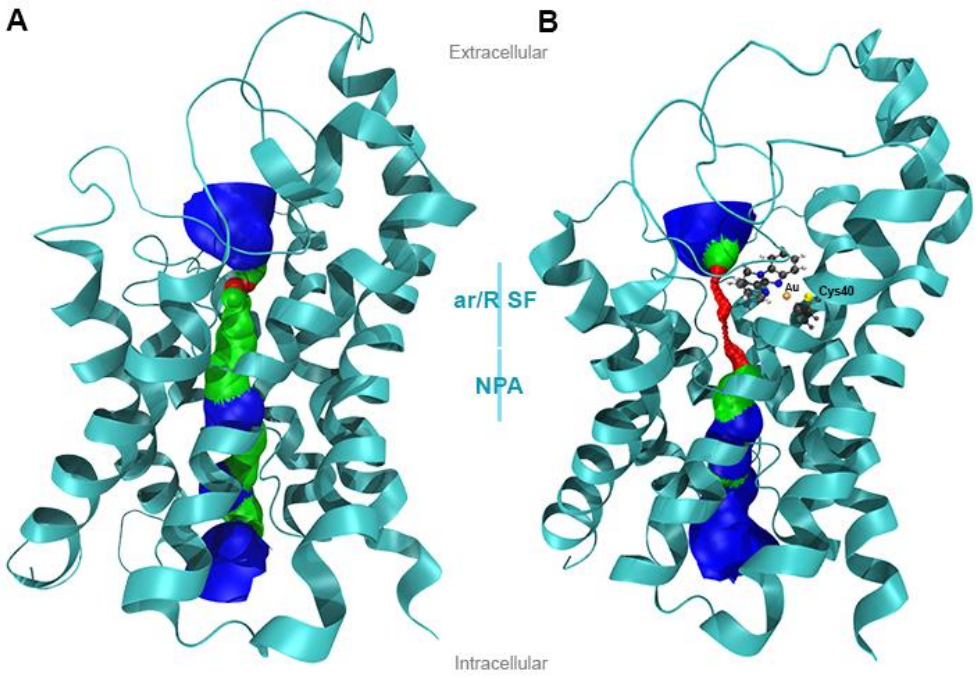

Figure 4.1.3 | **(A)** Human AQP3 monomer A and **(B)** AQP3 with modified Cys40 (AQP3-**4**), showing the effect on pore size (based on VDW radii): red = smaller than single H_2O, green = single H_2O, blue = larger than single H_2O. Complex **4** and Cys40 are shown in ball and stick representation, with atoms coloured by atom type. Generated with HOLE [12] and VMD [13]. [Data obtained by Andreia de Almeida]

From one simulation, 30 snapshots were taken and the pore size of each monomer was measured as detailed in the Supplementary Figure S4.1.2. Afterwards, in order to validate the observed trend, five snapshots were taken (100, 300, 450, 600 and 800 frames) from each of the five independent simulations, and the pore size was measured in each. The average of size fluctuations was obtained (Supplementary Figure S4.1.3), and allowed ruling out spontaneous pore geometry fluctuations during the simulation. Remarkably, from the average of the pore size analysis, it is seen that binding of complex **4** to monomer A also constricts monomer D, although

not sufficiently to hinder the solute permeability, but not B and C (Supplementary Figure S4.1.3).

The overall protein conformation is conserved upon gold binding, as shown by the root mean square displacement (RMSD) plots reported in Supplementary Figure S4.1.4. However, local conformational changes of both the protein surface (Supplementary Figure S4.1.5) and the pore lining can be observed. Specifically, binding of the complex induced rearrangement of the side chains of the ar/R SF (Figure 4.1.4). Compound **4** does not appear to be positioned in the channel in a way that could prevent glycerol or water to flow through. However, binding of the complex, just above Arg218, prevents this residue from forming a H-bond with the backbone, present in the native AQP3, pushing the side-chain into the channel area (Figure 4.1.4). These effects suggest that inhibition of AQP3's water and glycerol permeability is mainly due to protein conformational changes induced by binding of the gold complex to Cys40, rather than by the compound's steric hindrance, in line with the previous MD results on the binding of Hg^{2+} to AQP3 [6]. It is worth mentioning that similar effects were observed when a longer MD simulation was run (8 ns, Supplementary Figure S4.1.6).

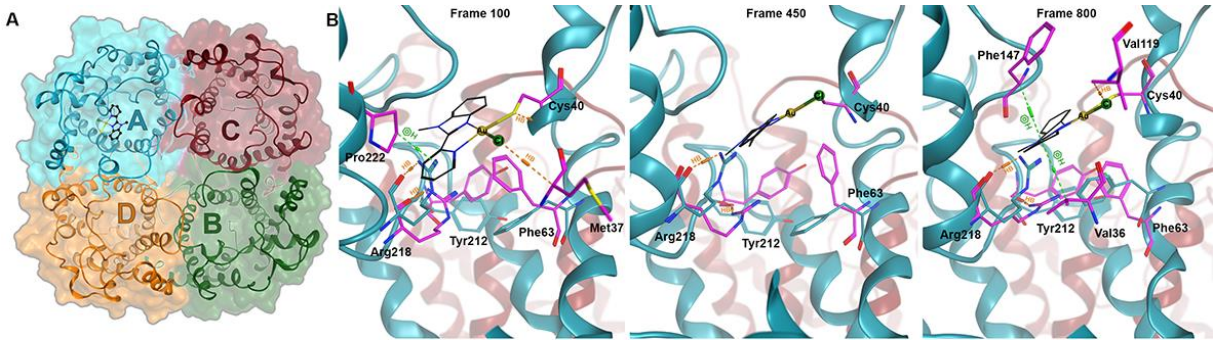

Figure 4.1.4 | **(A)** Tetrameric view of human AQP3 bound to complex 4. **(B)** Structure of the ar/R SF of AQP3 (blue) and upon binding of the gold complex (pink). The gold complex **4** is shown in black with thin sticks, gold in yellow-gold color and chloride in green, both in ball and stick representation. H-Bonds are shown using orange dashed lines (HB), while H-

arene interactions are shown using green dashed lines. Figures in panel B were generated with MOE. [Data obtained by Andreia de Almeida]

Moreover, the observed structural changes upon gold binding increase the hydrophobicity of the pore entrance of monomer A, due to increased exposure of hydrophobic side chains (Supplementary Figure S4.1.5). Overall, the symmetry of the tetramer is disrupted in the AQP3-Au model, as can be seen in Supplementary Figure S4.1.5, due to increased exposure of hydrophilic residues (e.g. Arg50 and Asp125). These relatively small changes appear to affect the approach of glycerol molecules to the channels.

To further investigate why the two complexes **3** and **4** have different AQP3 inhibitory effects, and assuming Cys40 as gold binding site as in the case of Auphen [2], DFT calculations were performed on the adducts between a cysteinato ligand and compounds **2**-**4**, as well as Auphen, obtained by substituting one of the two chlorido ligands (Supplementary Figure S4.1.7). The energy values of adduct formation are reported in Supplementary Table S4.1.1 and show that a larger formation energy is observed for positively charged Au(III) complexes with respect to neutral ones. These result supports the hypothesis that the cationic compounds, $[Au(phen)Cl_2]^+$ and $[Au(PbImMe)Cl_2]^+$ **4**, can be more easily complexed by cysteinato residues than the neutral complexes $[Au(py^b)Cl_2]$ **2** and $[Au(PbIm)Cl_2]$ **3**. Therefore, the corresponding AQP3 inhibition effects perfectly match this trend.

Finally, we used cyclic voltammetry (CV) to evaluate the electrochemical features of the Au(III) complexes. Previous reports have investigated the electrochemistry of square planar Au(III) complexes with chloride [14], N^N donor [15,16] and C^N^C donor [17,18] ligands. Typical responses involve the reduction of Au(III) to Au(I) at potentials which are heavily influenced by the coordinating ligand field

strength. Initially, we examined the electrochemical response of $HAuCl_4$ in DMSO containing 0.1 M TBAP as a supporting electrolyte by CV (Supplementary Figure S4.1.8 A). As expected, the introduction of strongly coordinating ligands, as in Auphen, shifts reduction potentials ($Au^{III/I}$ reduction process) to more positive values [19]. Supplementary Table S4.1.2 shows the values of redox potentials attributed to reductive (E_{red}) and oxidative (E_{ox}) electrochemical processes. A comparison of CVs of Auphen and $HAuCl_4$ clearly shows this effect (Supplementary Figure S4.1.8 B). Substitution of two chlorido ligands by a phen scaffold results in a shift of +0.33 V for the Au(III)→Au(I) process (peak I vs. peak I′). Similar voltammetric responses to Auphen were obtained for the complexes **2**-**4** (Supplementary Table S4.1.2 and Figure S4.1.9). As expected, complex **2** has the lowest reduction potential due to the C^N coordinating ligand.

Moreover, potentials are shifted to more negative values with increasing electron donating character. For example, the PbIm ligand is more electron donating than phen, so potentials are shifted by about -0.3 V [8]. Furthermore, the complexes yielded a second reduction peak (peak II) indicative of Au(I)→Au(0) reduction process. Interestingly, all peak II potentials are centred at *ca*. -1.26 V, with the exception of **2** (Supplementary Table S4.1.2). Similar responses were reported for a range of Au(III) monodentate pyridine complexes [20]. Interestingly, the organometallic complex **2** is predicted to form a C-Au-Cl complex after reduction. In fact, the voltammetric response of **2** differs from those of general formula $Au(N^N)Cl_2$, with two successive reduction peaks at -0.99 V and -1.72 V. The main conclusion drawn from the CV studies is that the electrochemical properties of the Au(III) compounds do not directly correlate to their AQP3 inhibition effects; for example, complexes **3** and **4** have similar redox potentials but markedly different effects on glycerol permeability.

4.1.4 Conclusions

Due to the broad range of functions of AQPs in physiology and in disease states, the development of selective modulators (inhibitors) of AQPs is indispensable, as these could be used as either chemical probes to detect their function in biological systems, or as innovative therapeutic agents in a variety of disease states.

Here, several Au(III) complexes has been studied for their AQP3 inhibition properties. In the first series, the cationic complex **4** was identified as the most potent inhibitor of glycerol permeation. Interestingly, the neutral complex **3**, with a similar ligand system, was scarcely active. DFT studies showed that a good correlation can be found between the compound's calculated affinity for cysteine residues and their AQP3 inhibitory activity. Instead, electrochemistry results suggest that the redox properties of the compounds do not influence their inhibition potency, excluding AQP3 inhibition by oxidative damage.

Remarkably, MD studies conducted for the first time on the Au(III) complex binding to AQPs have allowed discovering that protein conformational changes, upon metal binding to Cys40 in human AQP3, are mostly responsible for the observed inhibition of water and glycerol permeation. This finding has important implications for future inhibitor design, in that other amino acid residues could be targeted, if their modification leads to the necessary conformational changes to achieve channel closure. Interestingly, binding of the compound in one monomer also affects substrate permeability in an adjacent one, and alters the overall extracellular distribution of hydrophobic/hydrophilic surfaces of the tetramer, which, in turn, orients the approach of the substrates to the pore.

Of note, the Au(III) complexes described herein possess cytotoxic anticancer properties in vitro, and in recent years several gold compounds have shown promising anticancer effects related to the inhibition of different protein targets

[21]. In this context, we cannot exclude that inhibition of AQP3 might also contribute to the biological effects of the reported compounds towards cancer cells, although other studies are on-going in our labs to validate this hypothesis.

4.1.5 Experimental Section

Materials and Methods - Gold compounds **1**-**3** were prepared according to literature procedures [7,9,22,23]. The purity of the compounds was confirmed by elemental analysis, and all of them showed purity greater than 98%. 1,10-phenantroline and 2-mercaptoethanol were from Sigma. ^{1}H NMR spectra were recorded on a Bruker Avance II400 spectrometer at room temperature (r.t.). Elemental analyses were performed on a Carlo Erba EA 1110 CHN instrument. ESI-MS spectra were obtained in acetonitrile on a Thermo Finnigan LCQ DecaXPPlus quadrupole ion-trap instrument operated in positive ion mode over a mass range of m/z 150–2000. The absorption spectra of the complexes **3** and **4** in the UV-Visible region were recorded on a Cary 5000 UV-Visible NIR spectrophotometer.

Synthesis of Au(2-(pyridin-2-yl)-1H-benzo[d]imidazole)Cl$_2$ – 3 - To a solution of (2-(pyridin-2-yl)-benzimidazole) (0.195 g, 1.00 mmol) in MeCN (2 mL) was added an aqueous solution (12 mL) of potassium hydroxide (56 mg, 1.00 mmol). The reaction was stirred at r.t. for 15 minutes. Then, an aqueous solution of $NaAuCl_4$ (398 mg, 1.00 mmol) (12 mL) was added. The solution was allowed to stir overnight at r.t. in the dark. The brown solid was filtered off, washed with water, ethanol and diethyl ether and dried under vacuum. Yield: 0.419 g (91%). ESI-MS (MeCN, positive mode) exact mass for $C_{12}H_9AuCl_2N_3$ ($[M+H]^+$, theoretical m/z 461.9839): found m/z 461.9832 (err. -1.5 ppm). NMR ^{1}H (DMSO-d_6, 500 MHz): 9.24 (m, 1H, H^6), 8.46 (m, 1H, H^4), 8.36 (m, 2H, H^3 + $H^{3'}$), 7.86 (m, 1H, H^5), 7.74 (m, 1H, $H^{6'}$), 7.27 (m, 2H, $H^{4'}$ + $H^{5'}$). NMR ^{13}C{^{1}H} (DMSO-d^6, 126 MHz): 156.6 (C^{IV}), 149.1 (C^{IV}), 146.1 (CH^6), 144.7 (CH^4), 142.6 (C^{IV}), 140.6 (C^{IV}), 126.4 (CH^5), 124.4 (CH^3), 124.3 ($CH^{4'}$), 122.5 ($CH^{5'}$), 120.2 ($CH^{6'}$), 114.3 ($CH^{3'}$).

Synthesis of [Au(1-methyl-2-[2-pyridyl]-1H-benzo[d]imidazole)Cl2][PF_6] – 4 - To a solution of 1-methyl-2-[2-pyridyl]-benzimidazole (0.134 g, 0.64 mmol) in MeCN (2.5 mL) was added an aqueous solution of $NaAuCl_4$ (255 mg, 0.64 mmol) (15 mL) and solid KPF_6 (0.354 g, 1.92 mmol). The solution was allowed to stir for 3 h at room temperature. The solid was filtered off and washed with water, ethanol and diethyl ether. The light orange solid was recrystallized from acetone-diethyl ether. Yield: 0.327 g (82%). Anal. Calculated for $C_{13}H_{11}AuCl_2F_6N_3P$: C 25.10; H 1.78; N 6.75 %; found: C 25.54; H 1.55; N 6.63 %. ESI-MS (MeCN, positive mode) exact mass for $C_{13}H_{11}AuCl_2F_6N_3P$ ($[M\text{-}PF_6]^+$, theoretical m/z 475.9996): found m/z 475.9993 (err. -0.6 ppm). NMR ^1H (DMSO-d^6, 500 MHz): 8.93 (m, 1H, H^6), 8.30 (m, 1H, H^3), 8.22 (m, 1H, H^4), 8.02 (m, 1H, $H^{3'}$), 7.87 (m, 1H, $H^{6'}$), 7.81 (m, 1H, H^5), 7.60-7.63 (m, 2H, $H^{4'}$ + $H^{5'}$). NMR $^{13}C\{^1H\}$ (DMSO-d^6, 126 MHz): 150.4 (CH^6), 147.3 (C^{IV}), 143.6 (C^{IV}), 138.4 (CH^4), 134.2 (C^{IV}), 132.0 (C^{IV}), 127.1 (CH^5), 126.5 ($CH^{5'}$), 126.3 (CH^3), 126.2 ($CH^{4'}$), 115.3 ($CH^{6'}$), 113.3 ($CH^{3'}$).

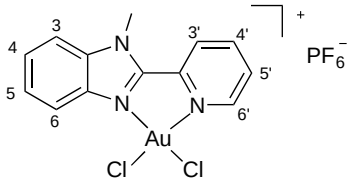

Ethics Statement - Venous blood samples were obtained from healthy human volunteers following a protocol approved by the Ethics Committee of the Faculty of Pharmacy of the University of Lisbon. Informed written consent was obtained from all participants.

Erythrocyte sampling and preparation - Venous blood samples were collected in citrate anticoagulant (2.7 % citric acid, 4.5 % trisodium citrate and 2% glucose). Fresh blood was centrifuged at 750 x *g* for 5 min at 4º C and plasma and buffy coat were discarded. Packed erythrocytes were washed three times in PBS (KCl 2.7 mM, KH_2PO_4 1.76 mM, Na_2HPO_4 10.1 mM, NaCl 137 mM, pH 7.4), diluted to 0.5 % haematocrit and immediately used for experiments. RBC mean volume in isotonic solution was determined using a CASY-1 Cell Counter (Schärfe System GmbH, Reutlingen, Germany) and was calculated as 82 fL.

Stopped-flow light scattering experiments - Stopped-flow experiments were performed on a HI-TECH Scientific PQ/SF-53 apparatus, with 2 ms dead time, temperature controlled and interfaced with a microcomputer. Experiments were performed at 23 °C for glycerol permeability (P_{Gly}) and for water permeability (P_f); for activation energy measurements temperatures were ranged from 10 °C to 37 °C. For each experimental condition, 5-7 replicates were analysed. For measuring the osmotic P_f, 100 μL of a suspension of fresh erythrocytes (0.5 %) was mixed with an equal volume of PBS containing 200 mM sucrose as a non-permeable osmolyte to produce a 100 mM inwardly directed sucrose gradient. The kinetics of cell shrinkage was measured from the time course of 90° scattered light intensity at 400 nm until a stable light scatter signal was attained. P_f was estimated by $P_f = k\ (V_o/A)(1/V_w(osm_{out})_\infty)$, where V_w is the molar volume of water, V_o/A is the initial cell volume to area ratio and $(osm_{out})_\infty$ is the final medium osmolarity after the applied osmotic gradient and k is the single exponential time constant fitted to the light scattering signal of erythrocyte shrinkage. For P_{Gly}, 100 μL of erythrocyte was mixed with an equal volume of hyperosmotic PBS containing 200 mM glycerol creating a 100 mM inwardly directed glycerol gradient. After the first fast cell shrinkage due to water outflow, glycerol influx in response to its chemical gradient was followed by water influx with subsequent cell reswelling. P_{Gly} was calculated as $P_{Gly} = k\ (V_o/A)$, where k is the single exponential time constant fitted to the light scattering signal of glycerol influx in erythrocytes. For inhibition experiments cells were incubated with different concentrations of complexes, from freshly prepared stock aqueous solutions, for various times at r.t. before stopped-flow experiments. A time dependent inhibition assay for all the tested compounds over several hours incubation with RBC showed no further increase of inhibition after 30 min at r.t. Inhibition reversibility was tested by 30 min incubation of RBCs with the compounds followed by further incubation with 1 mM 2-mercaptoethanol (EtSH) for 30 min at r.t.. The reversibility assays were also performed under the same conditions, using 1 mM L-cysteine. The inhibitor concentration necessary to achieve 50% inhibition (IC_{50}) was calculated by nonlinear regression of dose-response curves (Graph Pad Prism, Inc) to the

equation: $y=y_{min}+(y_{max}-y_{min})/(1+10((LogIC_{50}-Log[Inh])\ H))$, where y is the percentage inhibition obtained for each concentration of inhibitor [Inh] and H is the Hill slope. The activation energy (E_a) of water and glycerol permeation was calculated from the slope of the Arrhenius plot ($\ln P_f$ or $\ln P_{Gly}$ as a function of 1/T) multiplied by the gas constant *R*. All solution osmolarities were determined from freezing point depression on a semi-micro osmometer (Knauer GmbH, Berlin, Germany) using standards of 100 and 400 mOsM.

Statistical analysis - Data were presented as mean ± standard error of the mean (SEM) of at least four independent experiments, and were analysed with either the paired Student's t-test or one-way analysis of variance (ANOVA) followed by Tukey's test. A value of $P = 0.01$ was considered to be statistically significant.

Homology modelling and molecular dynamics – The 3D structure of hAQP3 was obtained by homology modelling using the Molecular Operating Environment (MOE 2013.08) [24]. The choice of a template structure was based on the sequence identity between hAQP3 and the sequence of the AQPs with available resolved structures. The isoform showing the highest sequence similarity with hAQP3 is the bacterial isoform GlpF, with 34.68% of sequence identity, which was then chosen as a template structure to generate a homology model of hAQP3. The template was selected among the structures with the best resolution (2.70 Å) without any substrate (pdb 1LDI) [25]. The tetrameric form was assembled and the structure was prepared and protonated at pH 7, with the Amber12EHT force field, as described in [6], using the Molecular Operating Environment (MOE 2013.08) [24]. 50 intermediate models of hAQP3 were generated and averaged to obtain the final homology model. The model obtained was checked for reliable rotamers involving the side chains in the region of ar/R SF and NPA, by comparison with the available crystal structures of all the other human and microbial AQP isoforms (pdb codes 1H6I, 3GD8, 3D9S, 1RC2, 1LD1 and 3C02). The structure was protonated at pH 7 and an energy minimization refinement was performed, with fixed Cα atoms.

Afterwards, the effect of binding of Au(III) complex **4** on AQP3 glycerol permeability was

investigated using classical molecular dynamics (MD). The molecular system consisted of the homology model of the hAQP3 tetramer within a double layer of 166 palmitoyl-oleyl-phosphatidyl-coline (POPC) lipid, prepared using the charmm-gui online server [26,27], using Amber99SB-ILDN in combination with Slipids (Stockholm lipids) force field for lipids [11,28]. Four glycerol molecules were placed into the system, one above each pore entrance, approximately 30 to 35 Å (to residue TRY212 at the pore entrance). The system was solvated with 35379 water molecules and used a modified amber99sb-ildn force field, with the parameters for glycerol and 1-methyl-2-(pyridine-2-yl)-benzimidazole generated by the Automated Topology Builder and Repository (ATb, version 2.2) website using the B3LYP/6-31G* basis set [29], using a combination of semi-empirical QM and DFT. Complex 4 was parameterized using DFT and QM/MM in order to obtain the parameters for the Au(III) ions in the force field. Afterwards, the complex was bound to the thiolate of a cysteine residue, to further integrate in the protein complex. The complex's geometry was further optimized and then incorporated into monomer A of AQP3.

All simulations were run using the GROMACS 5.1.2 simulation software [30]. Particle-mesh Ewald method was used for calculating electrostatic interactions. The verlet cut-off scheme with a cut-off distance of 4.0 nm was used for short range repulsive and attractive interactions and Lincs was used to constrain all bond lengths. Nose-hoover temperature coupling was used to maintain the temperature of the system (τ = 0.5 ps) at 310 K. The Parrinello-Rahman algorithm was used to maintain the pressure of the system at 1 bar with a coupling constant of τ = 1.0 ps. Simulations were equilibrated for 100 ps before production.

The four individual glycerol molecules were defined in the index and coupled in the pull code (e.g. gly_1 to chain_A). A total of 10 MD simulations (5 with the Au(III) complex present and 5 without) were run for 0.5 ns using the direction COM pull procedure, in each case applying a separate yet equal harmonic restraint force to each solute molecule of 600 kJ $mol^{-1}nm^{2}$ with a rate of 0.02 nm ns^{-1} along the z-axis. Two 4000000 step runs or 8 ns were run using the same two model systems and parameters. For these runs the pull code was omitted, therefore removing any biasing of the system.

Pore size measurements – Each pore radius was calculated using the Hole 2.0 program [12], which determines the internal surface based on atomic van der Waals radii. A snapshot at the beginning of each simulation was taken and coordinates for the centre of each pore (monomers A to D), at the ar/R SF, were used to generate the pore radius along the z-axis. In order to assess if the gold complex significantly affects the pore size by inducing protein conformational changes, five simulations, with and without gold complex, were performed. From these, 5 snapshots were taken (100, 300, 450, 600 and 800 frames) and the pore size was measured in each. For consistency, the narrowest part of the pore was considered to be the distance between the side chains of Tyr212 and Arg218 and, for each frame, the distance between the closest N atom of the side chain of Arg218 and C of the aromatic ring of Tyr212. The same methodology was used to assess the pore size of monomer A for the long (8 ns) simulation.

DFT calculations - DFT calculations were performed on the structures of cysteine, HCl, Auphen, **2**, **3**, **4** and on the adducts obtained by substituting one chlorido with a cysteinato ligand, by using the M06-L [31] functional, the Lanl2dz [32] basis set for Au, S and Cl atoms and the 6-31G(d,p) basis set for C, N, O and H atoms. Solvent effects were evaluated by full geometry optimization within the implicit water solvent, reproduced by the polarizable continuum model (PCM) [33]. Vibration frequency calculations, within the harmonic approximation, were performed to confirm that each optimized geometry corresponded to a minimum in the potential energy surface. Moreover, vibration frequency calculations allowed us to estimate the standard Gibbs free energy values, at 298.15 K, of each energy minimum structure, both in *vacuum* and in solution. All calculations were performed by the Gaussian 09 program package. The energy values of formation of the gold complex-Cys adducts were obtained by the following hypothetical reaction: $[Au(Ligand)Cl_2]^{n+} + HCys \rightarrow [Au(Ligand)ClCys]^{n+} + HCl$, where n is the charge of the metal complex, and calculated by the Eqn. 0 below, where E can be either the self-consistent field (SCF) energy or the standard Gibbs free energy in solution:

$$\Delta E = E[Au(Ligand)ClCys] + E[HCl] - E[Au(Ligand)Cl_2] - E[HCys] \qquad \text{Eq. 0}$$

Electrochemistry - Cyclic voltammograms were recorded using a PalmSens EmStat3+ potentiostat. Compounds (~ 2 mmol) were dissolved in DMSO containing 0.1 M tetrabutylammonium perchlorate (TBAP) as electrolyte and 1 mM ferrocene (Fc) used as internal reference. Measurements were recorded in a single compartment electrochemical cell (0.5 mL volume) containing a glassy carbon disk electrode (3mm diameter), a Ag/AgCl reference electrode and a platinum wire counter electrode. Prior to measurements, the glassy carbon disc electrode was polished on a microcloth pad in 0.05 μm alumina slurry. All measurements were carried out under nitrogen at r.t. Initially, we examined the electrochemical response of $HAuCl_4$ in DMSO containing 0.1 M TBAP as a supporting electrolyte. $HAuCl_4$ serves as a useful bench mark to evaluate the effect of the more strongly coordinating N^N and C^N ligands on the redox properties of the Au(III) complexes relative to weakly coordinating chlorido ligands. The electrochemical properties of $HAuCl_4$ have been extensively studied in aqueous [19,34,35,36], ionic liquids [37,38,39,40,41] and organic [14,15,16,42,43,44,45,46] electrolytes. In aqueous solution, the reduction of Au(III) to Au(0) takes place in a single three electron reduction process [34,35,36]. However, in aprotic organic media, reduction of Au(III) to Au(0) is postulated to occur in two distinct electrochemical steps [14,15,42,45]:

$AuCl_4^- + 2e^- \rightarrow AuCl_2^- + 2Cl^-$ (Eqn. 1)

$AuCl2^- + e^- \rightarrow Au + 2Cl^-$ (Eqn. 2)

Supplementary Figure S4.1.8 shows the CV of $HAuCl_4$ in DMSO containing 0.1 TBAP as supporting electrolyte. Due to the reactive nature of Au complexes at positive potentials (> +1.23 V vs. Ag/AgCl) [47], the scan was initiated at -0.1 V (indicated by *) to ensure that the Au metal centre was in the +3 oxidation state prior to measurement. Scanning to lower, more negative, potentials generated two successive reduction peaks centred at -0.35 V (peak I) and –1.26 V (peak II) which, in accordance with analogous studies [14,15,42,45], can be attributed to Au(III)→Au(I) and Au(I)→Au(0) transitions, respectively. The absence of defined oxidation peaks on the reverse scan, between -1.9 and 0 V vs. Fc, indicates that

both reduction processes are non-reversible. A broad oxidation peak (Peak III) centred at +0.31 V is evident at higher potentials. This oxidative process is consistently observed in aqueous [19], ionic liquids [37,38,39] and organic media [48] although its origin is unclear and has been attributed to both oxidation of free Cl^- ions [14,45] and electrodeposited Au(0) [16,43,48] at the electrode surface. In order to investigate this further, a scan was performed where the switching potential was reversed at -0.9 V, thus preventing subsequent reduction to Au(0) (Supplementary Figure S4.1.8 red scan). No evidence of the corresponding Au oxidation peak was observed indicating that the origin of the oxidation peak is dependent on the formation of Au(0) generated from the Au(I) reduction step. Furthermore, a thin layer of deposited Au(0) was visually observed on the working electrode surface after the two step reduction process. It is likely that this deposited Au(0) undergoes a anodic 'stripping' process at sufficiently positive potentials giving rise to the observed anodic peak [47]. Interestingly, the peak attributed to Au(I) reduction (Peak II') occurs at the same potential for that of $HAuCl_4$ complex. This suggests that the products of both reactions are similar in character. Indeed, this is reasonable as the postulated mechanism for Au(III) reduction results in liberation the free ligand to form $AuCl_2^-$ (Eqn 3). Therefore, it is likely that the $1e^-$ reduction of $AuCl_2$ to Au(0) gives rise to the reduction peak.

$Au(N\hat{}N)Cl_2 + 2e^- \rightarrow AuCl_2^- + N\hat{}N$ (Eqn. 3)

4.1.6 Supplementary information

Supplementary Table S4.1.1 | Formation energy of $[Au(ligand)ClCys]^{n+}$ adducts in H_2O solution (in kJ/mol, in terms of the SCF energy, ΔE, and of standard Gibbs free energy, ΔG°) calculated through DFT and by Eq. 0. [Data obtained by Giampaolo Barone]

Compound	ΔE	ΔG°
$[Au(phen)ClCys]^+$	-53.7	-45.0
2 $[Au(py^b)ClCys]$	-10.7	-0.2
3 [Au(PbIm)ClCys]	-27.8	-18.9
4 $[Au(PbImMe)ClCys]^+$	-53.0	-46.6

Supplementary Table S4.1.2 | List of electrochemical potentials attributed to reductive (E_{red}) and oxidative (E_{ox}) electrochemical processes. Potentials evaluated from cyclic voltammetric scans recorded in DMSO containing 0.1 M TBAP electrolyte at 0.1 V s^{-1} scan rate. All potentials measured against ferrocene/ferrocenium redox couple. [Data obtained by Stefano Leoni]

Compound	E_{red} (peak I)	E_{red} (peak II)	E_{ox} (peak III)
$HAuCl_4$	-0.35	-1.26	+0.31
$[Au(phen)Cl_2]$	-0.02	-1.26	+0.49
2 $[Au(py^b\text{-}H)Cl_2]$	-0.99	-1.72	+0.38
3 $[Au(PbIm)Cl_2]$	-0.30	-1.16	+0.41
4 $[Au(PbImMe)Cl_2]PF_6$	-0.33	-1.28	+0.52

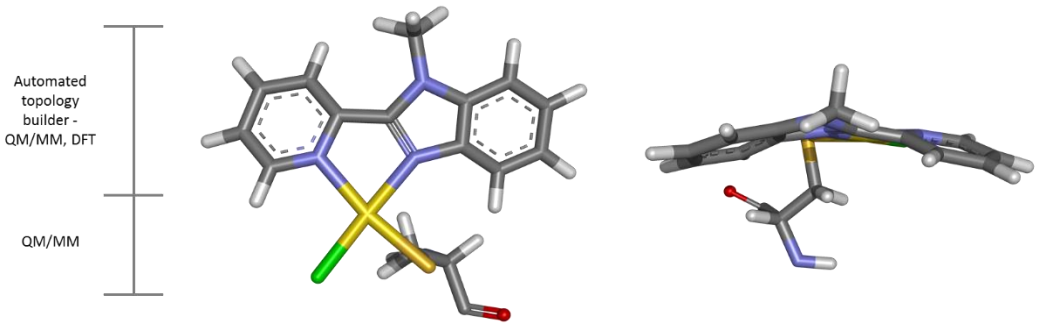

Supplementary Figure S4.1.1 | Geometry of modified Cys40 with complex **4** after energy minimization. [Data obtained by Giampaolo Barone]

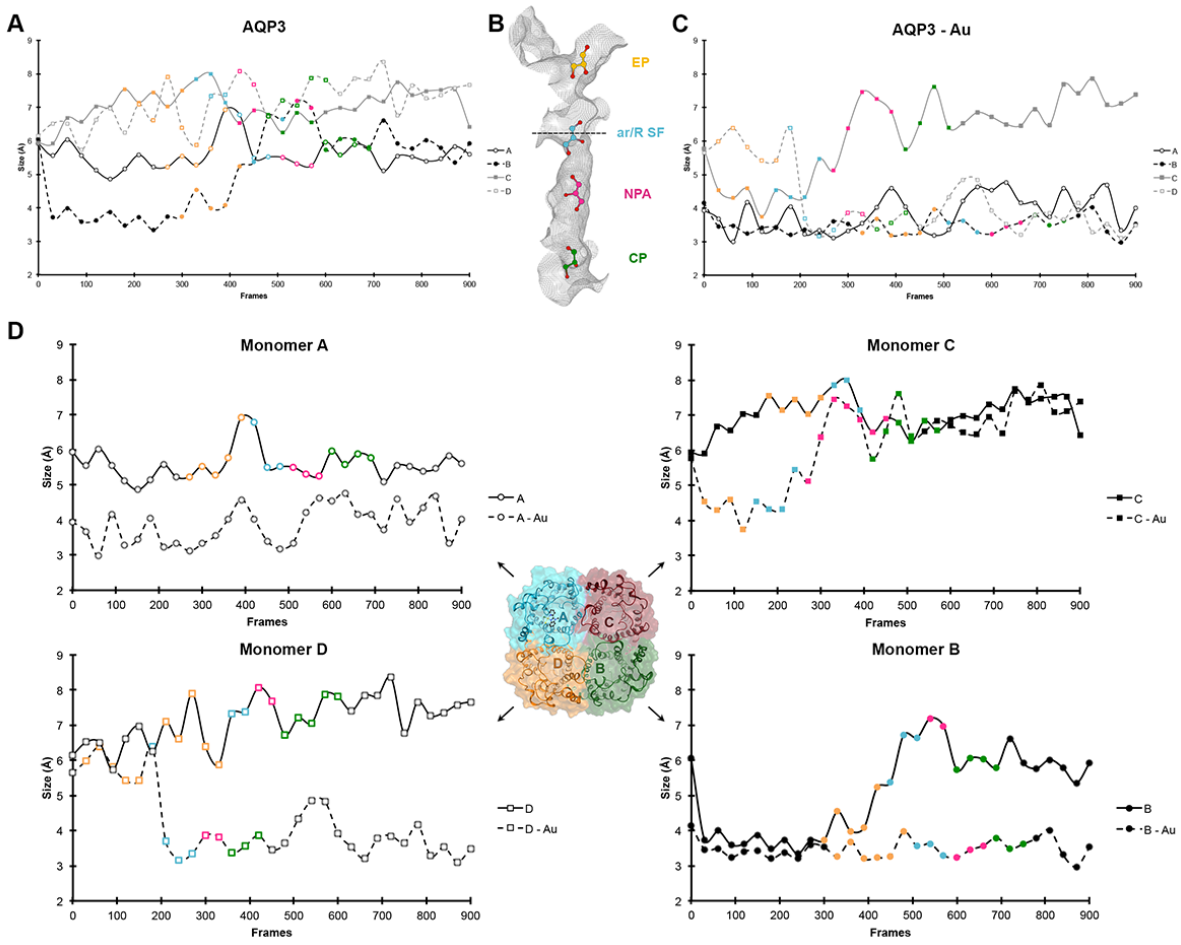

Supplementary Figure S4.1.2 | Pore size taken at the narrowest point of the channel (ar/R SF) from a representative simulation (0.5 ns) of AQP3 permeation by glycerol in the absence **(A)** or presence **(C)** of the gold complex. Each monomer is represented by a trace, and the colored markers indicate the glycerol passage from extracellular to cytoplasmic side. **(B)** Pockets for glycerol passage, indicated in yellow (extracellular pocket), blue (ar/R SF), pink (NPA motif) and green (cytoplasmic pocket). The narrowest point of the channel is indicated by a dashed line (approximate localization). In panel **D** the pore sizes of each monomer are shown with (dashed line) and without (full line) gold complex. The same color code of the point markers was used. [Data obtained by Andreia de Almeida]

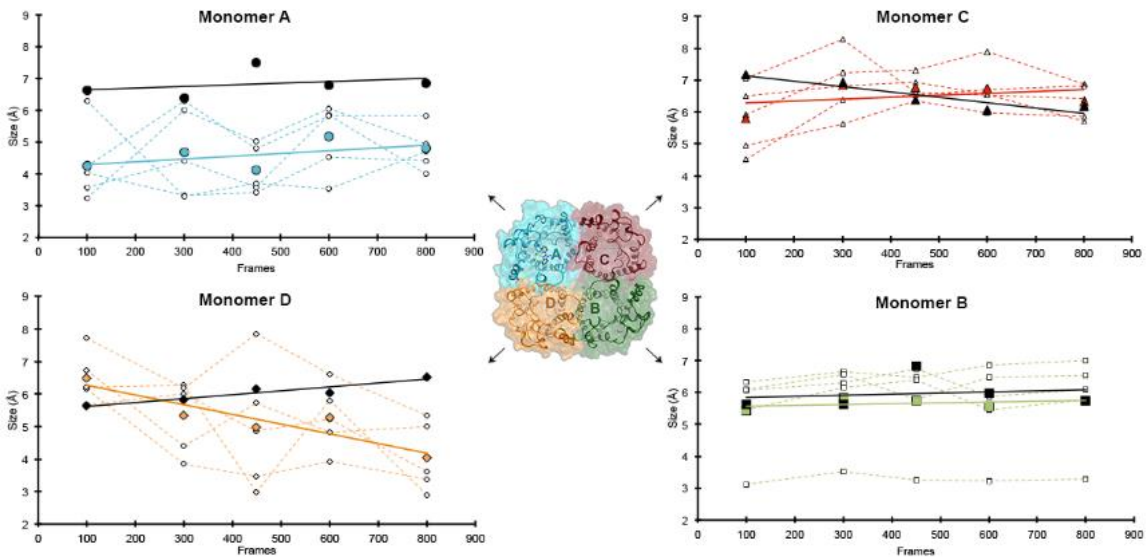

Supplementary Figure S4.1.3 | Pore size taken at the narrowest point of the channel (ar/R SF) from 10 independent simulations (0.5 ns) of AQP3 (5 without and 5 with gold complex) for each monomer. In black markers, the pore size of each monomer are show as an average of 5 independent simulations and with a linear trend line (shown in black). In colored dashed lines, with white markers, the results for each of the 5 individual simulations of AQP3 with the gold complex are shown. In colored markers is represented the average size for each point, for AQP3 with gold complex **4**, with an added linear trend line, shown in the respective color. [Data obtained by Andreia de Almeida]

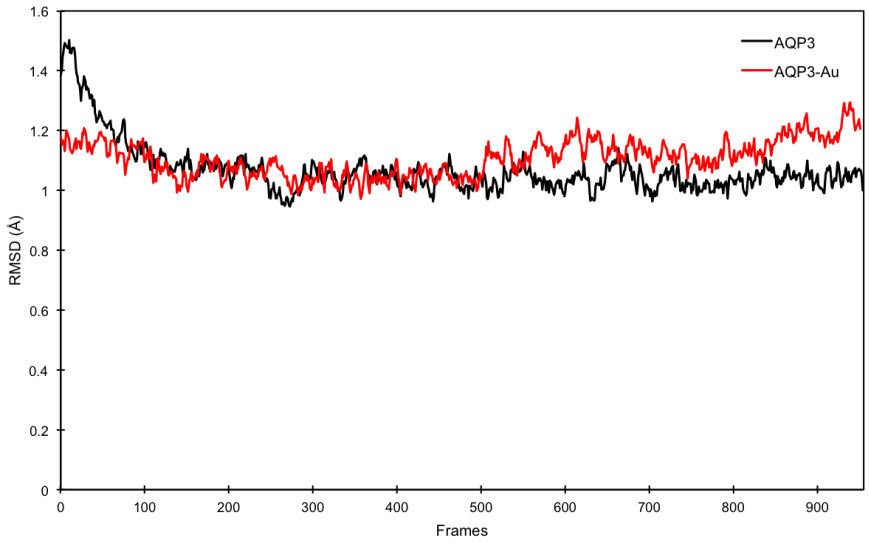

Supplementary Figure S4.1.4 | RMSD (Å) of the protein backbone atoms of AQP3 (black) and AQP3-Au (red). [Data obtained by Andreia de Almeida]

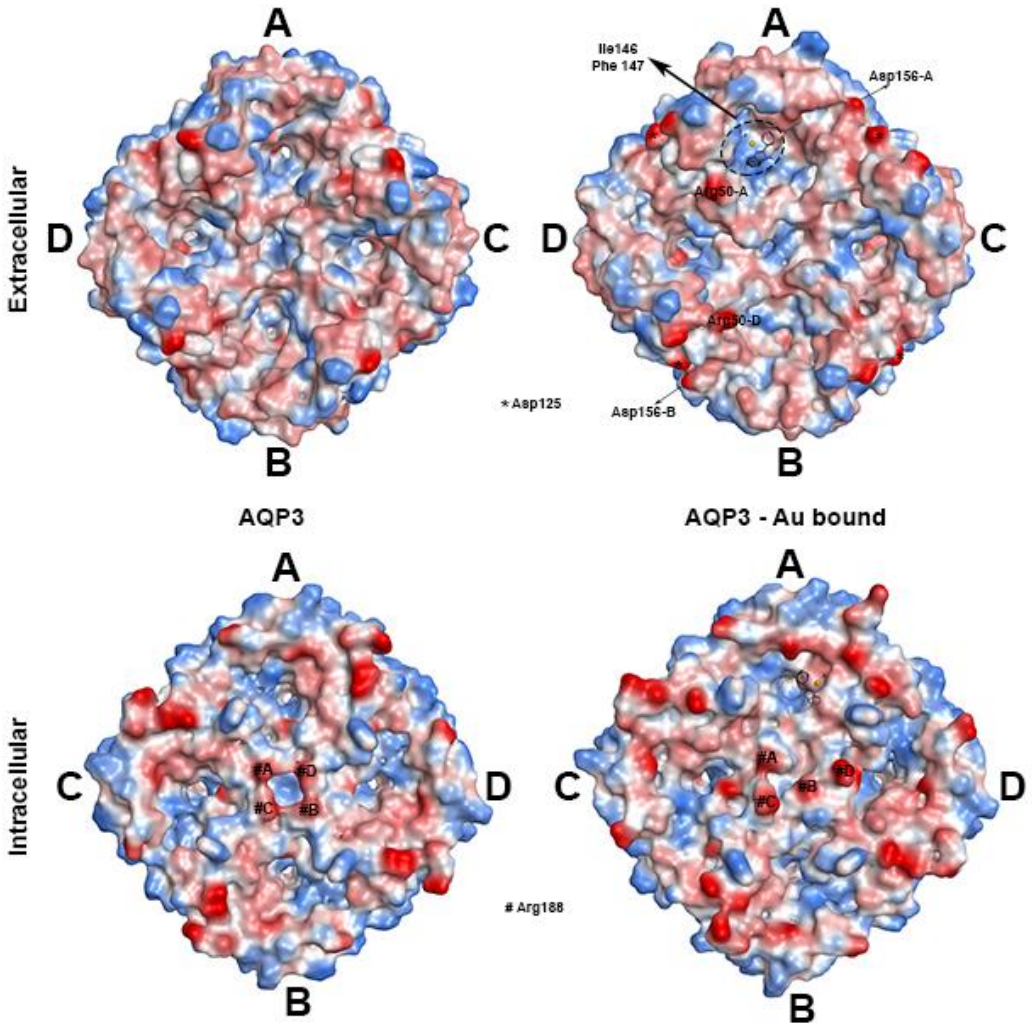

Supplementary Figure S4.1.5 - Top intra and extracellular view of AQP3 (left) and AQP3-Au bound (right) tetramers hydrophobic surfaces at the start of the simulation. Gold complex is shown over the surface only for indication of its relative position within the tetramer. This does not represent the compound's location across the z-axis. Blue = hydrophobic, red = hydrophilic. Generated with MOE. [Data obtained by Andreia de Almeida]

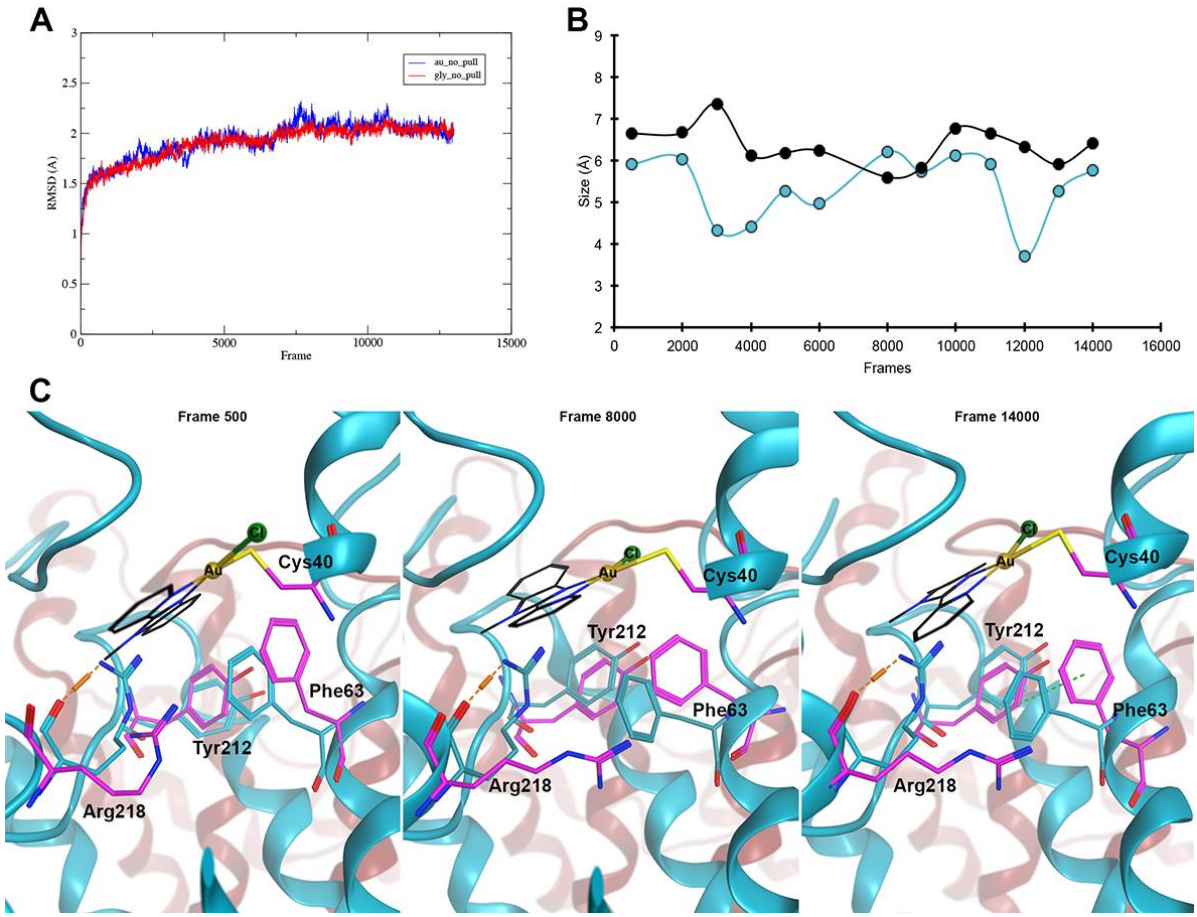

Supplementary Figure S4.1.6 | Molecular dynamics simulation of AQP3 permeation by glycerol in the presence and absence of the gold complex without pull (8 ns). During the time of the simulation, due to the absence of pull, any of the glycerol molecules crosses the AQP3 channels. **(A)** RMSD of the backbone of AQP3's simulation with (blue trace) and without (red trace) gold complex. **(B)** Pore size of monomer A, measured at the narrowest point of the channel. The simulation with gold complex is shown in blue markers and line, while the simulation without the complex is shown in black. **(C)** Structure of the ar/R SF of AQP3 (blue) and upon binding of the gold complex (pink). The gold complex 4 is shown in black with thin sticks, gold in yellow-gold color and chloride in green, both in ball and stick representation. H-bonds are shown in orange dashed lines, while H-arene interactions are shown in green dashed lines. The figures in panel C were generated with MOE. [Data obtained by Andreia de Almeida]

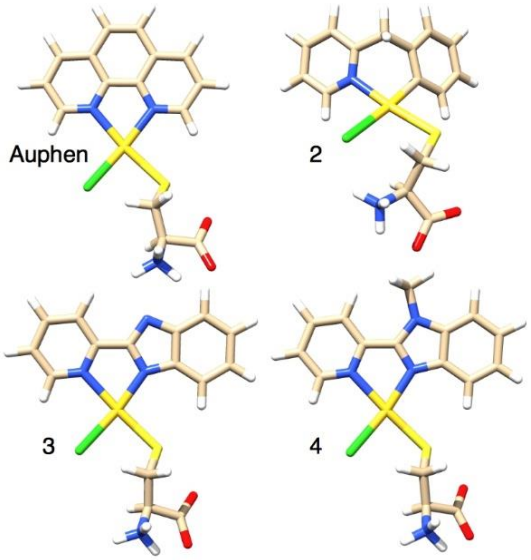

Supplementary Figure S4.1.7 | Structure of the cysteinato complexes [Au(ligand)ClCys]n+ obtained for Auphen, 2, 3 and 4, whose geometry was optimized by DFT calculations; n=1, 0, 0, 1 for the adducts of Auphen, 2, 3 and 4, respectively. [Data obtained by Giampaolo Barone]

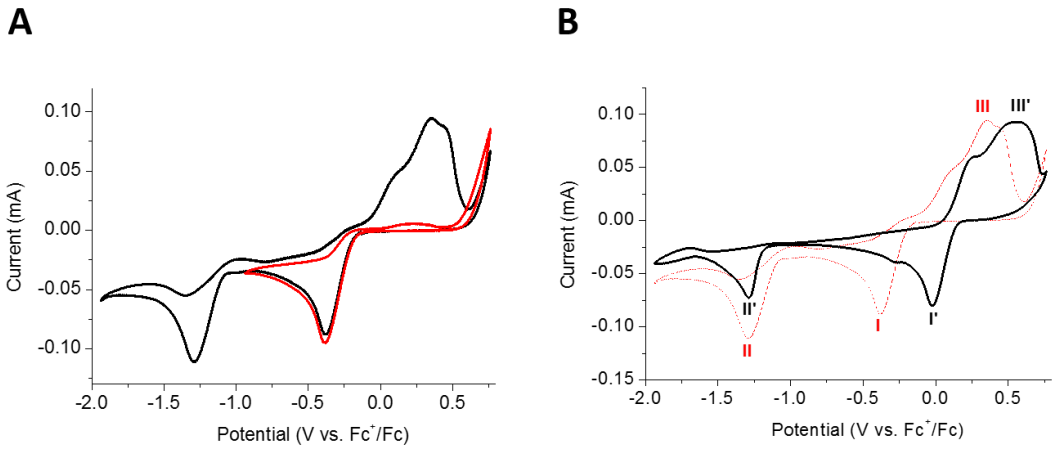

Supplementary Figure S4.1.8 | Cyclic voltammograms of **(A)** $AuCl_4^-$ in DMSO containing 0.1 M TBAP electrolyte at 0.1 V s^{-1} scan rate. Cathodic sweep initiated at -0.1 V vs Fc^+/FC. Switching potential -1.95 V vs Fc^+/FC (black scan) and -0.9 V vs Fc^+/FC (red scan); and of **(B)** Auphen (black) and $HAuCl_4$ (red dash) recorded in DMSO containing 0.1 M TBAP electrolyte at 0.1 V s^{-1} scan rate. [Data obtained by Stefano Leoni]

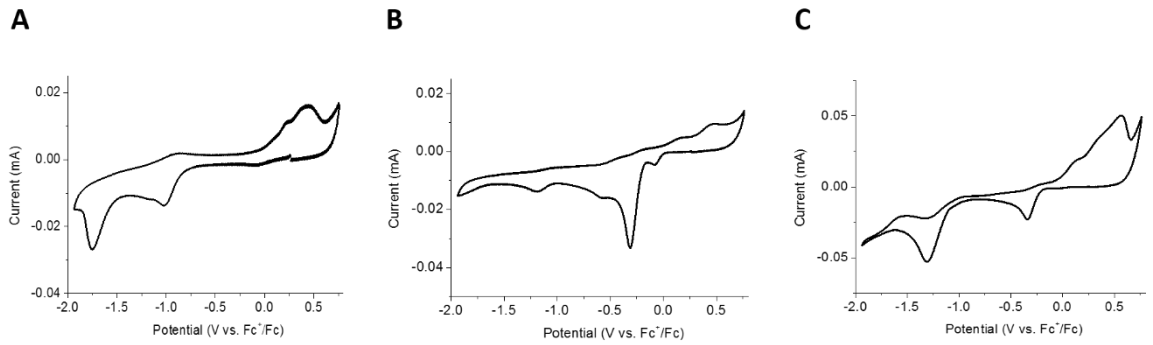

Supplementary Figure S4.1.9 | Cyclic voltammograms of **(A)** complex 2 **(B)** complex 3 and **(C)** complex 4. [Data obtained by Stefano Leoni]

4.1.7 References

[1] A.P. Martins, A. Marrone, A. Ciancetta, A. Galán Cobo, M. Echevarría, T.F. Moura, N. Re, A. Casini, G. Soveral, Targeting aquaporin function: potent inhibition of aquaglyceroporin-3 by a gold-based compound., PloS one 7 (2012) e37435.

[2] A. Serna, A. Galan-Cobo, C. Rodrigues, I. Sanchez-Gomar, J.J. Toledo-Aral, T.F. Moura, A. Casini, G. Soveral, M. Echevarria, Functional inhibition of aquaporin-3 with a gold-based compound induces blockage of cell proliferation, J Cell Physiol 229 (2014) 1787-1801.

[3] A.P. Martins, A. Ciancetta, A. de Almeida, A. Marrone, N. Re, G. Soveral, A. Casini, Aquaporin inhibition by gold(III) compounds: new insights, ChemMedChem 8 (2013) 1086-1092.

[4] R.I. Macey, R.E. Farmer, Inhibition of water and solute permeability in human red cells, Biochim Biophys Acta 211 (1970) 104-106.

[5] G.M. Preston, T.P. Carroll, W.B. Guggino, P. Agre, Appearance of water channels in Xenopus oocytes expressing red cell CHIP28 protein, Science 256 (1992) 385-387.

[6] A. Spinello, A. de Almeida, A. Casini, G. Barone, The inhibition of glycerol permeation through aquaglyceroporin-3 induced by mercury(II): A molecular dynamics study, Journal of Inorganic Biochemistry (2016).

[7] A. Casini, M.C. Diawara, R. Scopelliti, S.M. Zakeeruddin, M. Grätzel, P.J. Dyson, Synthesis, characterisation and biological properties of gold(III) compounds with modified bipyridine and bipyridylamine ligands., Dalton transactions 39 (2010) 2239-2245.

[8] M. Serratrice, M.A. Cinellu, L. Maiore, M. Pilo, A. Zucca, C. Gabbiani, A. Guerri, I. Landini, S. Nobili, E. Mini, L. Messori, Synthesis, structural characterization, solution behavior, and in vitro antiproliferative properties of a series of gold complexes with 2-(2'-pyridyl)benzimidazole as ligand: comparisons of gold(III) versus gold(I) and mononuclear versus binuclear derivatives, Inorg Chem 51 (2012) 3161-3171.

[9] M.A. Cinellu, A. Zucca, S. Stoccoro, G. Minghetti, M. Manassero, M. Sansoni, Synthesis and characterization of gold(III) adducts and cyclometallated derivatives with 6-benzyl- and 6-alkyl-2,2[prime or minute]-bipyridines, Journal of the Chemical Society, Dalton Transactions (1996) 4217-4225.
[10] D.F. Savage, R.M. Stroud, Structural basis of aquaporin inhibition by mercury, J Mol Biol 368 (2007) 607-617.
[11] J.P. Jambeck, A.P. Lyubartsev, An Extension and Further Validation of an All-Atomistic Force Field for Biological Membranes, J Chem Theory Comput 8 (2012) 2938-2948.
[12] O.S. Smart, J.G. Neduvelil, X. Wang, B.A. Wallace, M.S. Sansom, HOLE: a program for the analysis of the pore dimensions of ion channel structural models, J Mol Graph 14 (1996) 354-360, 376.
[13] W. Humphrey, A. Dalke, K. Schulten, VMD: visual molecular dynamics, J Mol Graph 14 (1996) 33-38, 27-38.
[14] L.M.A. Monzon, F. Byrne, J.M.D. Coey, Gold electrodeposition in organic media, Journal of Electroanalytical Chemistry 657 (2011) 54-60.
[15] A. Corma, I. Domínguez, A. Doménech, V. Fornés, C.J. Gómez-García, T. Ródenas, M.J. Sabater, Enantioselective epoxidation of olefins with molecular oxygen catalyzed by gold(III): A dual pathway for oxygen transfer, Journal of Catalysis 265 (2009) 238-244.
[16] L. Messori, F. Abbate, G. Marcon, P. Orioli, M. Fontani, E. Mini, T. Mazzei, S. Carotti, T. O'Connell, P. Zanello, Gold(III) complexes as potential antitumor agents: solution chemistry and cytotoxic properties of some selected gold(III) compounds, J Med Chem 43 (2000) 3541-3548.
[17] V.K. Au, W.H. Lam, W.T. Wong, V.W. Yam, Luminescent cyclometalated alkynylgold(III) complexes with 6-phenyl-2,2'-bipyridine derivatives: synthesis, characterization, electrochemistry, photophysics, and computational studies, Inorg Chem 51 (2012) 7537-7545.
[18] T. Dann, D.A. Rosca, J.A. Wright, G.G. Wildgoose, M. Bochmann, Electrochemistry of Au(II) and Au(III) pincer complexes: determination of the Au(II)-Au(II) bond energy, Chem Commun (Camb) 49 (2013) 10169-10171.
[19] S. Zhu, W. Gorski, D.R. Powell, J.A. Walmsley, Synthesis, structures, and electrochemistry of gold(III) ethylenediamine complexes and interactions with guanosine 5'-monophosphate, Inorg Chem 45 (2006) 2688-2694.
[20] R. Corbo, T.P. Pell, B.D. Stringer, C.F. Hogan, D.J. Wilson, P.J. Barnard, J.L. Dutton, Facile formation of homoleptic Au(III) trications via simultaneous oxidation and ligand delivery from [PhI(pyridine)2](2+), J Am Chem Soc 136 (2014) 12415-12421.
[21] A. De Almeida, B.L. Oliveira, J.D.G. Correia, G. Soveral, A. Casini, Emerging protein targets for metal-based pharmaceutical agents: An update, Coordination Chemistry Reviews 257 (2013) 2689-2704.
[22] B. Bertrand, S. Spreckelmeyer, E. Bodio, F. Cocco, M. Picquet, P. Richard, P. Le Gendre, C. Orvig, M.A. Cinellu, A. Casini, Exploring the potential of gold(III) cyclometallated compounds as cytotoxic agents: variations on the C^N theme, Dalton Trans 44 (2015) 11911-11918.

[23] L.S. Hollis, S.J. Lippard, Aqueous chemistry of (2,2',2"-terpyridine)gold(III). Preparation and structures of chloro(2,2',2"-terpyridine)gold dichloride trihydrate ([Au(terpy)Cl]Cl2.3H2O) and the mixed valence gold(I)-gold(III) salt bis[chloro(2,2',2"-terpyridine)gold] tris(dichloroaurate) tetrachloroaurate ([Au(terpy)Cl]2[AuCl2]3[AuCl4]), Journal of the American Chemical Society 105 (1983) 4293-4299.
[24] M.O.E. (MOE), Chemical Computing Group Inc. Montreal, QC, Canada) 2012.10.
[25] D. Fu, A. Libson, L.J. Miercke, C. Weitzman, P. Nollert, J. Krucinski, R.M. Stroud, Structure of a glycerol-conducting channel and the basis for its selectivity, Science 290 (2000) 481-486.
[26] S. Jo, T. Kim, V.G. Iyer, W. Im, CHARMM-GUI: a web-based graphical user interface for CHARMM, J Comput Chem 29 (2008) 1859-1865.
[27] E.L. Wu, X. Cheng, S. Jo, H. Rui, K.C. Song, E.M. Davila-Contreras, Y. Qi, J. Lee, V. Monje-Galvan, R.M. Venable, J.B. Klauda, W. Im, CHARMM-GUI Membrane Builder toward realistic biological membrane simulations, J Comput Chem 35 (2014) 1997-2004.
[28] J.P. Jambeck, A.P. Lyubartsev, Another Piece of the Membrane Puzzle: Extending Slipids Further, J Chem Theory Comput 9 (2013) 774-784.
[29] A.K. Malde, L. Zuo, M. Breeze, M. Stroet, D. Poger, P.C. Nair, C. Oostenbrink, A.E. Mark, An Automated Force Field Topology Builder (ATB) and Repository: Version 1.0, J Chem Theory Comput 7 (2011) 4026-4037.
[30] A. MJ, M. T, S. R, P. S, J. Smith, B. Hess, E. Lindahl, GROMACS: High performance molecular simulations through multi-level parallelism from laptops to supercomputers, SoftwareX 1-2 (2015) 19-25.
[31] Y. Zhao, D.G. Truhlar, A new local density functional for main-group thermochemistry, transition metal bonding, thermochemical kinetics, and noncovalent interactions, J Chem Phys 125 (2006) 194101.
[32] P.J. Hay, W.R. Wadt, Abinitio Effective Core Potentials for Molecular Calculations - Potentials for K to Au Including the Outermost Core Orbitals, Journal of Chemical Physics 82 (1985) 299-310.
[33] J. Tomasi, B. Mennucci, R. Cammi, Quantum mechanical continuum solvation models, Chem Rev 105 (2005) 2999-3093.
[34] C.J. Boxley, H.S. White, T.E. Lister, P.J. Pinhero, Electrochemical deposition and reoxidation of Au at highly oriented pyrolytic graphite. Stabilization of Au nanoparticles on the upper plane of step edges, Journal of Physical Chemistry B 107 (2003) 451-458.
[35] K.B. Holt, G. Sabin, R.G. Compton, J.S. Foord, F. Marken, Reduction of tetrachloroaurate (III) at boron-doped diamond electrodes: Gold deposition versus gold colloid formation, Electroanalysis 14 (2002) 797-803.
[36] L. Komsiyska, G. Staikov, Electrocrystallization of Au nanoparticles on glassy carbon from HClO4 solution containing [AuCl4](-), Electrochimica Acta 54 (2008) 168-172.
[37] L. Aldous, D.S. Silvester, C. Villagran, W.R. Pitner, R.G. Compton, M.C. Lagunas, C. Hardacre, Electrochemical studies of gold and chloride in ionic liquids, New Journal of Chemistry 30 (2006) 1576-1583.

[38] T. Oyama, T. Okajima, T. Ohsaka, Electrodeposition of gold at glassy carbon electrodes in room-temperature ionic liquids, Journal of the Electrochemical Society 154 (2007) D322-D327.
[39] T. Oyama, S. Yamaguchi, M.R. Rahman, T. Okajima, T. Ohsaka, N. Oyama, EQCM Study of the [(AuCl4)-Cl-III](-)-[(AuCl2)-Cl-I](-)-Au(0) Redox System in 1-Ethyl-3-methylimidazolium Tetrafluoroborate Room-Temperature Ionic Liquid, Langmuir 26 (2010) 9069-9075.
[40] N. Papaiconomou, N. Glandut, I. Billard, E. Chainet, Unusual electrochemical behaviour of AuBr4- in ionic liquids. Towards a simple recovery of gold(III) after extraction into an ionic liquid, Rsc Advances 4 (2014) 58910-58915.
[41] X.H. Xu, C.L. Hussey, The Electrochemistry of Gold at Glassy-Carbon in the Basic Aluminum Chloride-1-Methyl-3-Ethylimidazolium Chloride Molten-Salt, Journal of the Electrochemical Society 139 (1992) 3103-3108.
[42] B. Ballarin, L. Busetto, M.C. Cassani, C. Femoni, A new gold(III)-aminoethyl imidazolium aurate salt: Synthesis, characterization and reactivity, Inorganica Chimica Acta 363 (2010) 2055-2064.
[43] U. Koelle, A. Laguna, Electrochemistry of Au-complexes, Inorganica Chimica Acta 290 (1999) 44-50.
[44] K.N. Kouroulis, S.K. Hadjikakou, N. Kourkoumelis, M. Kubicki, L. Male, M. Hursthouse, S. Skoulika, A.K. Metsios, V.Y. Tyurin, A.V. Dolganov, E.R. Milaeva, N. Hadjiliadis, Synthesis, structural characterization and in vitro cytotoxicity of new Au(III) and Au(I) complexes with thioamides, Dalton Transactions (2009) 10446-10456.
[45] J.J. Li, J.L. Hu, Y.L. Gu, F.M. Mei, T. Li, G.X. Li, Catalytic activities and properties of Au(III)/Schiff-base complexes in methanol oxidative carbonylation, Journal of Molecular Catalysis a-Chemical 340 (2011) 53-59.
[46] M. Ongaro, A. Gambirasi, M. Favaro, A. Kuhn, P. Ugo, Asymmetrical modification of carbon microfibers by bipolar electrochemistry in acetonitrile, Electrochimica Acta 116 (2014) 421-428.
[47] L. Yu, A. Andriola, Quantitative gold nanoparticle analysis methods: A review, Talanta 82 (2010) 869-875.
[48] J.W. Zhang, P.F. Yan, G.M. Li, G.F. Hou, M. Suda, Y. Einaga, Systematic investigation of an array of TCNQ lanthanide complexes: synthesis, structure and magnetic properties, Dalton Transactions (2009) 10466-10473.

4.2 Expanding the series of gold(III) compounds

Furthermore, to expand the series of Au(III) coordination compounds, two different series based on Au(PbImMe) (**4**) and Auphen scaffolds (MNW and KAP series, respectively) (Figure 4.2.1) were synthesize and tested as AQP3 inhibitors, with the objective to improve our understanding on the structure-activity relationship of gold-based compounds as aquaglyceroporins inhibitors and increase inhibition potency. The compounds were synthesized at Cardiff University by the group of Prof. Angela Casini. MNW064 in the series resulted to be insoluble, therefore it was not further tested.

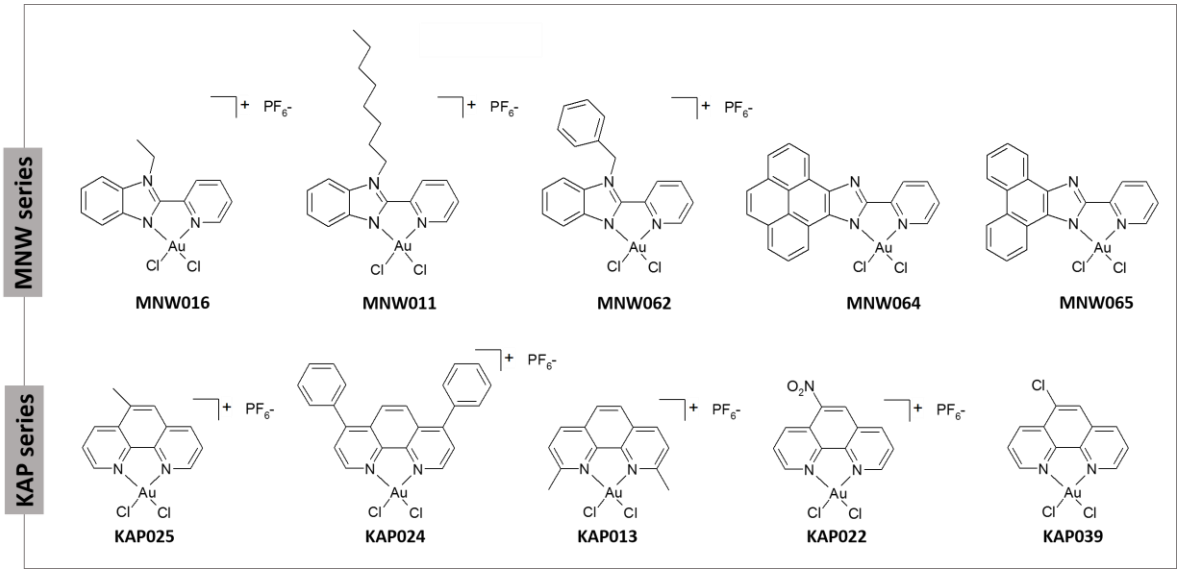

Figure 4.2.1 | **Gold(III) compounds as human AQP3 inhibitors.** Expanding the series with MNW and KAP compounds.

Table 4.2.1 | IC_{50} (μM) values for the gold complexes as human AQP3 inhibitors.

Compound	IC_{50}[a] (μM)
KAP025	0.73 ± 0.09
KAP024	0.43 ± 0.08
KAP013	0.89 ± 0.14
KAP022	0.57 ± 0.04
KAP039	0.57 ± 0.07
MNW011	1.83 ± 0.02
MNW016	0.88 ± 0.02
MNW062	0.85 ± 0.22
MNW065	0.81 ± 0.14

[a] Mean ± SE of at least three independent experiments

Briefly, all KAP compounds have equal or even better potency and selectivity towards AQP3 that Auphen. Within the KAP series, the most active compound is KAP024 featuring phenyls substituents on the phenanthroline ring (IC_{50} = 0.43 ± 0.08). Concerning the MWN series, no differences could be observed with respect to the AuPbImMe despite the different substitution patterns on the imidazole moiety of the ligand bound to Au(III).

Molecular dynamics studies are ongoing in the Cardiff lab to shed light into the different inhibitory effects of the KAP compounds at a molecular level and to define initial structure-activity relationships.

CHAPTER 5

Final remarks

This thesis presented different studies that investigated mechanisms of aquaporins regulation and possible physiologic outcome.

In the first part of this thesis (Chapter 2), hypothesizing for the expression of AQP5 in the adipose tissue, we disclosed a new physiological role of AQP5, as necessary for adipocyte differentiation. Downregulation of AQP5 in 3T3-L1 adipocytes led to an impairment of cell differentiation. Furthermore, overexpression of human AQP5 unveiled its activity as a functional water channel in adipocytes. Further studies are required to clarify the full involvement of AQP5 in adipose tissue biology and disclose if specific water transport through AQP5 is necessary for adipocyte differentiation and if it is involved in key protein–protein interactions.

The second part of this thesis (Chapter 3) was devoted to the functional characterization of AQPs and their regulatory mechanisms. For that purpose, we used a yeast heterologous expression system to evaluate water/glycerol transport of each individual AQP isoform. The yeast *Saccharomyces cerevisiae* is one of the best characterized eukaryotic models and considered to be an excellent model for the study of proteins in general due to the large library of strains available and

their easy and inexpensive genetic manipulation when compared with cultures of animal cells. This heterologous expression system is a valuable option due to the high functional homology between yeast and higher eukaryotes including mammals. Furthermore, contrary to animal cells, yeast cells can survive in severe external environments allowing establishing several experimental conditions that could not be applied to mammalian cells.

Using this approach, we showed that AQP3, AQP5, AQP7 and AQP10 channel permeability is regulated by pH and remarkably, all the isoforms presented distinct gating mechanisms, revealing that AQPs are subjected to an elaborated short-term regulation that might be coordinated at the tissue level to support its function.

The yeast system may also be used to investigate the involvement of intracellular signaling pathways on AQP regulation. The addition of glucose to starved yeast cells activating PKA pathway that mimics the well-known hormonal-induced phosphorylation in animal cells, is a clear example (Subchapter 3.1). Several studies demonstrated the effect of phosphorylation on AQP5 redistribution in the plasma membrane. Here, we showed for the first time that PKA phosphorylation significantly increases AQP5 individual channel permeability and that this activation is dependent on pH. Further studies are necessary to unveil the crucial residues for pH and the main phosphorylation sites involved in this peculiar gating mechanism.

Investigation of human and rat AQP3 pH regulation (Subchapter 3.2) revealed that acidic pH triggers the channel closure and consequently decreases permeability. Through molecular modelling studies, the pH dependent closure/opening of the hAQP3 channel at a molecular level was characterized.

Regulation of human AQP7, the main aquaglyceroporin expressed in the adipose tissue responsible for glycerol efflux during lipolysis, was investigated (Subchapter

3.3). Interestingly, we observed that protonation induces changes in protein surface electrostatic charges switching AQP7 from a bidirectional channel to a glycerol efflux channel. This selective directional permeation under certain conditions supports the physiological role of human AQP7 in the adipose tissue and reveals a fine-tuning mechanism of AQP7 efficiency for glycerol release from adipocytes. Using a combination of *in vitro* and *in silico* techniques, we were able also to identify Tyr135 and His165 as essential residues for pH sensing.

A multidisciplinary study revealed that AQP10, also abundantly expressed in adipocytes and proposed to be a second glycerol gateway in addition to AQP7, is stimulated by lipolysis induced acidification (Subchapter 3.4). In this study, the crystal structure of human AQP10, the first structure of a mammalian aquaglyceroporin, pinpointed His80 as the pH sensor and revealed an exceptionally wide selectivity (ar/R) filter and a novel cytoplasmic glycerol-specific gate, both unique to hAQP10.

Overall, the yeast expression system used in this thesis showed to be a valuable tool to assess individual AQP function and regulation and can be used to explore the remaining AQP isoforms. The results obtained and herein presented confirm that the physiological mechanisms of AQP regulation, in particular aquaporin pH-sensing and phosphorylation in mammalian cells, may offer new strategies to selectively target different AQPs.

The discovery of small molecule modulators of AQPs activity opens new opportunities for drug development. Following the recently reported gold(III) compound Auphen as aquaglyceroporin inhibitor, AQP3 inhibition properties of a new series of gold-based compounds were tested in RBC to achieve optimization of potency (Chapter 4). Among the series, Au(PbImMe) has stood out for its inhibitory potency for AQP3 glycerol permeability, with an IC_{50} even lower than Auphen. Molecular dynamics simulations combined with DFT calculations and

electrochemical studies, allowed to establish a structure-activity relationship by describing its inhibition mechanism. Binding of the gold(III) compound induces structural changes leading to shrinkage of the channel pore thus preventing glycerol and water permeation.

At the end of the work here described and discussed, particular questions remain to be addressed. A mammalian *in vitro* model able to validate the coordinated mechanisms of regulation of the several AQP isoforms is paramount. Concerning the AQP inhibitors, our group reported two potent inhibitors of human AQP3 (Auphen and Au(PbImMe)), that do not affect AQP1 water permeability, but the compounds selectivity towards other aquaglyceroporin isoforms remains to be explored. Although human red blood cells are a suitable screening model since only express one aquaglyceroporin (AQP3), a comparative study between the other human aquaglyceroporins (AQP7, 9 and 10) should be further investigated, allowing to optimize the drug design and to achieve highly selective molecules with reduced risks of side effects. To achieve this goal, the heterologous yeast system expressing human AQP3, AQP7, AQP9 and AQP10, seems to be the most appropriate to ascertain the selectivity and potency of the compounds. Future studies investigating AQP structure-function relationships taking advantage of structural differences between isoforms will broaden our knowledge of AQPs mechanisms of regulation and may help the design of novel and efficient compounds and their pharmaceutical formulations.

Acknowledgements

Em primeiro lugar gostaria de expressar a minha gratidão à minha orientadora, Dra. Graça Soveral, por ter aceite orientar-me neste tema e ter-me dado liberdade suficiente para ir experimentando coisas novas. Obrigada pelo encorajamento, paciência, sentido crítico, partilha de conhecimentos e por ter sempre encontrado tempo para mim. Obrigada pela enorme dedicação a escrever e rever artigos e a raciocinar sobre resultados que à partida nos eram estranhos. A sua orientação foi fundamental ao longo de todo o trabalho de investigação, bem como durante a escrita desta tese.

Quero também expressar o meu agradecimento à minha coorientadora, Dra. Angela Casini, por me ter dado a oportunidade de fazer parte do seu grupo de investigação onde, em conjunto com a Dra. Andreia de Almeida, fizemos descobertas muito entusiasmantes.

Agradeço também à Dra. Teresa Moura por todas as horas gastas comigo a analisar resultados e pelos conselhos. À Dra. Catarina Prista que me concedeu confiança ao longo de vários anos para desenvolver uma parte muito significativa deste trabalho no seu laboratório e à Dra. Ana Paula Martins por me ter transmitido toda a sua experiência.

Também gostaria de agradecer à Cláudia e à Inês, os outros dois vértices do triângulo, pessoas com a mesma dose de discernimento e que foram tapete de muitas situações científicas e pessoais. A minha sanidade mental fica grata por existirem.